

**New applications of continuous atmospheric O₂ measurements:
meridional transects across the Atlantic Ocean, and improved
quantification of fossil fuel-derived CO₂**

By

PENELOPE PICKERS

A thesis submitted to the
School of Environmental Sciences of the
University of East Anglia in partial
fulfilment of the requirements for the
degree of Doctor of Philosophy

School of Environmental Sciences
UNIVERSITY OF EAST ANGLIA

2016

© This copy of the thesis has been supplied on condition that anyone who consults it is understood to recognise that its copyright rests with the author and that use of any information derived there from must be in accordance with current UK Copyright Law. In addition, any quotation or extract must include full attribution.

In Memory of Greg Pickers (1949-2016)

Abstract

High precision, continuous measurements of atmospheric O₂ and CO₂ are a valuable tool for gaining insight into carbon cycle processes, and for separating land biospheric, oceanic and fossil fuel fluxes of CO₂. This thesis presents a new atmospheric O₂ and CO₂ measurement system that has been deployed on board a commercial container ship, travelling continuously between Germany (~55°N) and Argentina (~35°S). These data are the first ongoing atmospheric O₂ measurements across the Atlantic Ocean, closing a gap in the global atmospheric O₂ network.

The Atlantic meridional transects of atmospheric O₂ and CO₂ display latitudinally-varying seasonality. The annual mean latitudinal gradient in APO (Atmospheric Potential Oxygen; a tracer derived from O₂ and CO₂ measurements) does not show a pronounced bulge at the equator, in contrast to observations across the Pacific Ocean.

Atmospheric O₂ and CO₂ measurements from Norfolk, UK are used to demonstrate a novel method for quantifying fossil fuel derived CO₂ (ffCO₂), using APO data. This APO ffCO₂ quantification method is more precise than the frequently-used CO tracer method, owing to a smaller range of APO:CO₂ fossil fuel emission ratios compared to the CO:CO₂ range. A sensitivity analysis of the fossil fuel emission ratios also indicates that the APO method is very likely more accurate than the CO method, and can therefore be used independently of ¹⁴CO₂ measurements (unlike the CO method), which are costly and highly unreliable in many UK regions, owing to nuclear power plant influences.

These new applications of atmospheric O₂ measurements have significant future potential. The shipboard data can be used to test and improve global climate model estimates of meridional oceanic heat and carbon transport in the Atlantic. Using APO to quantify ffCO₂ has significant policy relevance, with the potential to provide more accurate and more precise top-down verification of fossil fuel emissions.

List of Contents

List of figures	xi
List of tables	xxiii
Acknowledgements	xxv
1 Introduction	1
1.1 Climate change and the carbon cycle	2
1.2 Atmospheric oxygen measurements as a tool for understanding the carbon cycle	8
1.3 The historical and current atmospheric oxygen measurement network	15
1.4 Objective and specific aims of this research	24
1.5 Outline of thesis	25
References	25
2 Methodology of atmospheric O₂ and CO₂ measurement	35
2.1 Introduction and outline of chapter	36
2.2 Measurement system design	40
2.2.1 Overview	40
2.2.2 O ₂ and CO ₂ analysers	41
2.2.3 Gas handling procedures	47
2.2.3.1 Air inlets	47
2.2.3.2 Drying system and diaphragm pumps	48
2.2.3.3 Flow and pressure control	53
2.2.3.4 Temperature considerations and leaks	54
2.3 Calibration procedures	56
2.3.1 Calibration gas handling	56
2.3.2 Analyser calibration procedures	57
2.3.3 High pressure cylinder standards	64
2.3.4 The role of the Zero Tank and Target Tank	66
2.4 Repeatability and compatibility of measurement system	71
2.5 Data acquisition and system software control	74
2.6 Improvements implemented	77
2.7 Experimental testing	79
2.8 Future improvements	82
2.9 Summary	84

References	86
3 Measurements of atmospheric O₂ and CO₂ in the North Atlantic Ocean on board the RRS James Cook	89
3.1 Introduction	90
3.1.1 Scientific background and chapter outline	90
3.1.2 Motivation for research cruise	91
3.1.3 Location of the cruise	92
3.2 Measurement system description, technical setbacks and complementary data	93
3.2.1 Description of O ₂ and CO ₂ measurement system	93
3.2.2 Technical issues that arose during the JC090 cruise	94
3.2.3 Complementary data used in analyses	97
3.3 Data flagging	98
3.3.1 Preliminary results	98
3.3.2 Flagging of CO ₂ , O ₂ and APO data based on analysis of diagnostic parameters	99
3.3.3 Flagging of CO ₂ , O ₂ and APO data contaminated by the ship's exhaust fumes	99
3.4 Results and data analysis	102
3.4.1 Comparison of CO ₂ mole fractions with those measured by PML, and consequences for CO ₂ flux estimates	102
3.4.2 Baseline data	105
3.4.3 Short-term events: correlations with meteorological parameters	107
3.4.4 Short-term events: NAME footprints	111
3.4.5 Short-term events: oxidative ratios	114
3.4.6 Short-term events: correlations with the JC090 underway data	115
3.4.7 Short-term events: evidence of eddies from satellite derived altimetry and sea surface temperature data	117
3.4.8 Short-term events: O ₂ flux estimate associated with a typical cold-core cyclonic eddy	120

3.4.9	Short-term events: modelling short-term variability in APO using NAME and NEMO-PlankTOM	125
3.5	Summary and conclusions	129
	References	131
4	Latitudinal variability in atmospheric O₂, CO₂ and APO across the Atlantic Ocean	135
4.1	Introduction	136
4.1.1	Installation of the shipboard atmospheric measurement system on board the Cap San Lorenzo	138
4.2	Meridional transects of atmospheric O ₂ , CO ₂ and APO across the Atlantic Ocean	140
4.2.1	Short-term variability: equator and open ocean	144
4.2.2	Short-term variability: The Channel and North Sea	148
4.2.3	Short-term variability: ocean upwelling and productivity events	150
4.2.4	Variability in the position of the ITCZ	154
4.3	Seasonality in atmospheric O ₂ , CO ₂ and APO across the Atlantic Ocean at different latitudes	157
4.4	Annual mean latitudinal gradients of atmospheric O ₂ , CO ₂ and APO across the Atlantic Ocean: the missing equatorial APO bulge	170
4.5	Summary and Conclusions	182
	References	186
5	Quantifying ffCO₂ using APO: a novel approach	191
5.1	Introduction	192
5.1.1	Outline of this chapter	195
5.2	Atmospheric O ₂ and CO ₂ measured from the Environmental Sciences building, University of East Anglia	196
5.3	Fossil fuel CO ₂ quantification using APO from sites in Norfolk, UK	205
5.3.1	Using 'fixed' fossil fuel emission ratios	205
5.3.2	Baseline and measurement uncertainty analysis	209
5.3.3	Using 'time-varying' fossil fuel emission ratios	212
5.3.4	Comparison of CO and APO fossil fuel quantification methods	214

5.3.5	Comparison of ffCO ₂ from 'top-down' atmospheric measurements with ffCO ₂ from 'bottom-up' inventories	220
5.4	Summary and future work	224
	References	227
6	Conclusions	231
6.1	Outline of major research findings	232
6.1.1	Shipboard atmospheric O ₂ and CO ₂ measurement system	232
6.1.2	Detecting short-term ocean O ₂ fluxes in atmospheric O ₂ data	233
6.1.3	The position of the ITCZ in the Atlantic Ocean	234
6.1.4	Seasonality variability and annual mean latitudinal distribution of atmospheric O ₂ , CO ₂ and APO across the Atlantic Ocean	234
6.1.5	Quantifying ffCO ₂ (fossil fuel-derived CO ₂) using APO	235
6.2	Summary of thesis and future work	236
	References	239
	Abbreviations	241
	Appendices	243

List of Figures

- Figure 1.1.** Radiative forcing estimates in 2011 relative to 1750, from IPCC (2013). Confidence level indicators correspond to: VH – very high, H – high, M – medium, L – low, VL – very low. Radiative forcing, in $W m^{-2}$, is defined as the change in energy flux caused by a driver, calculated either at the tropopause or the top of the atmosphere. 3
- Figure 1.2.** Model projections of (a) global mean surface temperature change relative to 1986-2005, (b) Arctic September sea-ice extent, and (c) global ocean surface pH, from 1950 to 2100 for the Representative Concentration Pathway (RCP) scenarios 2.6 and 8.5 of van Vuuren et al. (2011), with bars on the right indicating the 2081-2100 predictions for RCP4.5 and RCP6.0. Model projections are from the Coupled Model Intercomparison Project Phase 5 (CMIP5) multi-model ensemble simulations (Taylor et al., 2011). Black lines with grey shading represent modelled historical evolution of each parameter and its uncertainty, respectively. Likewise, for RCP2.6 and RCP 8.5, the uncertainty is shown by the blue and red shading, respectively. The black dashed line in (b) represents nearly ice-free conditions, while the dotted lines indicate the CMIP5 multi-model means. 4
- Figure 1.3.** A schematic of the global carbon cycle, from Ciais et al. (2013). Black numbers and arrows represent natural reservoirs and fluxes of carbon prior to 1750, and red numbers and arrows represent anthropogenic reservoirs and fluxes of carbon averaged over the 2000 – 2009 time period. Reservoir and flux values are given in units of PgC and $PgC yr^{-1}$ respectively. 5
- Figure 1.4.** The atmospheric CO_2 record measured at Mauna Loa Observatory, Hawaii, by Pieter Tans, NOAA/ESRL (National Oceanic and Atmospheric Administration/Earth System Research Laboratory, USA; www.esrl.noaa.gov/gmd/ccgg/trends/) and Ralph Keeling, Scripps Institution of Oceanography, USA (www.scrippsco2.ucsd.edu/). The red line shows the entire record, with the long-term trend represented by the black line. 7
- Figure 1.5.** Atmospheric O_2 and CO_2 time series data from Mauna Loa, Hawaii, USA, and the South Pole, Antarctica; northern hemisphere data are shown in green, while southern hemisphere data are shown in blue. CO_2 data are from Keeling et al. (2001) and O_2/N_2 data are from Ralph Keeling (personal communication; <http://scrippsco2.ucsd.edu/>). 11
- Figure 1.6.** A graphical representation of calculating the land and ocean carbon sinks using the method of Keeling and Manning (2014). Black dots are 6-monthly averages of $\delta(O_2/N_2)$ and CO_2 from Alert, Canada, La Jolla, California, USA, and Cape Grim, Tasmania, Australia. 13

Figure 1.7. The current status of the global high-precision O ₂ measurement network, as of May 2016. Note that aircraft and shipboard measurements are not shown for clarity. Stations where flask samples are collected are indicated by the red symbols, while continuous measurement stations are shown in blue. Stations that collect flask samples and make continuous measurements are shown as continuous stations (blue). Note that all atmospheric O ₂ stations also make concurrent measurements of CO ₂ .	23
Figure 2.1. Gas handling diagram of shipboard O ₂ and CO ₂ measurement system. 'Red' and 'blue' inlet lines are coloured accordingly in Unit 1, and the green colouring in Unit 2 denotes electrical cables.	42
Figure 2.2. Photograph showing the inside of the Li-6252 CO ₂ analyser.	43
Figure 2.3. Photograph showing the inside of the Oxzilla II O ₂ analyser. The MAX-250 fuel cells were originally housed inside the electronics box in the centre of the photograph, but were later moved to facilitate easier leak checking. The fuel cells have been insulated using glass wool. The inlet tubing shown in this photograph is 1/8" (external diameter), however, this was later replaced with 1/16" tubing to reduce the residence time of air in the tubing between V11 and the fuel cells (see Section 2.6 for details).	44
Figure 2.4 Top plot: Cell 1 (blue circles) and cell 2 (red triangles) O ₂ responses in [%] (uncalibrated Oxzilla II response units). Unfilled symbols represent data that are swept out and therefore ignored, while filled symbols represent data that are retained. 'WT' denotes periods when each cell is measuring the Working Tank, and 'S' denotes periods when each cell is measuring the air sample. Bottom plot: ΔO ₂ , in [%] *10 ⁴ (uncalibrated Oxzilla II response units), where unfilled symbols represent data that are swept out and ignored, while filled symbols represent data that are retained. 'WT-S' denotes periods when ΔO ₂ represents the Working Tank – air sample differential O ₂ signal, and 'S-WT' denotes periods when ΔO ₂ represents the air sample – Working Tank differential O ₂ signal. ΔΔO ₂ is calculated every minute from three V11 switch periods of ΔO ₂ (denoted by 'jog 1' and 'jog 2'), using Eq. 2.4. Note that ΔΔO ₂ could be calculated every 30 seconds, instead of every minute, however, this is not recommended, since successive jogs will share two thirds of the same data, instead of one third, and will therefore be less independent from each other.	46
Figure 2.5. Photograph (top) and annotated diagram (bottom) of the 'blue line' Aspirated Air Inlet (AAI) on board the Cap San Lorenzo Hamburg Süd container ship. The air to be measured (red arrows; 'sample air') is sampled from a moving air stream (blue arrows), which is generated by a waterproof blower. The blower prevents temperature gradients forming at the air inlet, and thus minimises fractionation of O ₂ relative to N ₂ at the inlet (Blaine et al., 2006).	47

Figure 2.6. Photograph of Unit 1, the drying unit of the O ₂ and CO ₂ measurement system.	50
Figure 2.7. Annotated diagram of the chiller trap, showing the dip tube, glass beads, and Swagelok Company quick connect stem and body fittings, which prevent the trap mistakenly being replaced the wrong way around in the chiller.	51
Figure 2.8. Drifts in the A and B coefficients of the quadratic CO ₂ fit (top and middle panels, respectively), and drift in the B coefficient of the linear O ₂ fit (bottom panel). Drifts represent the maximum possible drift in the calibration scales of CO ₂ and O ₂ . These data were constructed using a -8.9 mV ΔCO ₂ analyser response, equating to approximately 400 ppm, and using a 0.00444 % ΔO ₂ analyser response, equating to approximately -125 ppmEq (-700 per meg). Linear regression fits have been added to the plots to highlight the direction of the drift. Gaps in the time series are when the measurement system stopped working and could not be restarted until the next time the Cap San Lorenzo visited the London port.	62
Figure 2.9. Stability of the CO ₂ mole fraction (top panel) and O ₂ mole fraction (bottom panel) in the WTs over time. Each point represents the WT CO ₂ or O ₂ mole fraction as defined during a WSS calibration, minus the average WT CO ₂ or O ₂ mole fraction for each WT. Different coloured symbols represent different WTs. Typically, the lifetime of the air in a WT cylinder is about 18 days, with a starting pressure of about 300 bar and a final pressure of about 5 bar. Gaps in the time series in this figure, and Figures 2.11 and 2.12 below, are caused by system faults, predominantly drying problems, which could only be fixed each time the Cap San Lorenzo visited the London port.	63
Figure 2.10. Short-term drift in the ZT CO ₂ mole fraction, from the Cap San Lorenzo system for four days in Feb 2015. Blue symbols indicate ZT CO ₂ measurements that immediately follow a WSS calibration, and green symbols indicate the subsequent ZT CO ₂ measurements between WSS calibrations. Red symbols show the temperature measured in the room. Each ZT measurement is the mean of 11 one-minute averages of CO ₂ and O ₂ .	68
Figure 2.11. Stability of ZT CO ₂ and O ₂ mole fractions during deployment on board the Cap San Lorenzo between Sep 2014 and Sep 2015. Red and green symbols denote the CO ₂ and O ₂ mole fractions of ZTs D169300 and D064564 respectively. The red and green lines are linear regressions to the data, and indicate the direction of the long-term drift.	69
Figure 2.12. CO ₂ (top panel) and O ₂ (bottom panel) measurements of the TT cylinder on the Cap San Lorenzo. Data are shown as differences in mole fraction from the declared TT values. TT measurements that were made when the measurement system was experiencing known technical difficulties have been excluded. Each TT measurement shown is the mean of 13 consecutive one-minute averages of O ₂ and CO ₂ measurements.	70

- Figure 2.13.** Schematic tab of the Nemo software. The ‘Schematic’ tab allows the user to over-ride the default valve settings by clicking on the valve symbols on the gas handling diagram, displays the measurement system pressures, temperatures and flow rates, allows the user to set the desired system flow rate, displays the current calibrated O₂ and CO₂ mole fractions, displays whether the software is in ‘auto-run’ or ‘resting-state’ mode, and displays the status of the macro control, which determines the exact sequence for how the calibration cylinders and TT cylinder are purged and measured. Note that for internal CRAM research group reasons, the numbered designators for the valves, pressure transducers and flow meters on this schematic are not consistent with the numbering used in Fig. 2.1. 76
- Figure 2.14.** Allan deviation plot showing the optimum averaging period for the Oxzilla of about 14 seconds (black dot). This optimum averaging time represents the optimum trade-off between improved precision from averaging the signal noise and reduced precision owing to the inclusion of longer-term drifts in the differential O₂ signal. The Allan deviation for ΔO_2 with a ‘standard’ switching period of 1 minute is indicated by the pink dot (i.e. a jog length of 180 seconds), and the Allan deviation for ΔO_2 with a switching period of 30 seconds is indicated by the blue dot (i.e. a jog length of 90 seconds). 78
- Figure 2.15.** Histograms of 1-minute O₂ mole fraction when cylinder air was passed through a KNF Neuberger pump (left plot) and an Air Dimensions pump (right plot). 80
- Figure 2.16.** O₂ mole fraction of a 50 L cylinder (blue, left y-axis) and a 20 L cylinder (red, right y-axis) as a function of the number of hours since the cylinder was laid horizontally. 82
- Figure 3.1.** Bathymetric map showing the route of the RRS James Cook during the research cruise, from Vigo, Portugal, to the PAP site, and returning to Santander, Spain. Colours correspond to ordinal dates (where day 242 is 30Aug2013). The inset shows a zoomed version of the ship’s route in and around the PAP site. 92
- Figure 3.2.** Schematic of the RRS James Cook, showing the locations of the meteorological lab and ship’s exhaust stack, and the position of the AAls (image adapted from <http://noc.ac.uk/research-at-sea/ships/rrs-james-cook>). 93
- Figure 3.3.** Un-calibrated Oxzilla II fuel cell data during the JC090 cruise, showing the large variations caused by the ship’s motion superimposed on the 1-minute switching of the sample and working tank. Data are from the SEC file, recorded on 10Sep2013. Vertical grid lines are shown at 30 second intervals. 96

- Figure 3.4.** CO₂, δ(O₂/N₂) and APO data from the JC090 cruise (2-minute frequency). The y-axes have been scaled to be visually comparable on a mole per mole basis (since 1 ppm CO₂ ~ 5 per meg δ(O₂/N₂)). Gaps in the data correspond to periods when calibration cylinders were being analysed. 98
- Figure 3.5.** Unpolluted (black circles), statistically flagged (red triangles) and meteorologically flagged (green diamonds) CO₂, δ(O₂/N₂), and APO data. The CO₂, δ(O₂/N₂) and APO y-axes have been scaled to be visually comparable to each other on a mole per mole basis. 100
- Figure 3.6.** O₂:CO₂ ratio plot of the statistically and meteorologically flagged pollution spike data. δ(O₂/N₂) is given in ppm equivalent units (i.e. δ(O₂/N₂) ppm equivalent units = δ(O₂/N₂) per meg/4.77) to be comparable to CO₂ and enable correct calculation of the regression slope. The red dashed line indicates the major axis regression line, which has a slope of -1.38. The regression was weighted according to the difference in measurement uncertainty associated with the δ(O₂/N₂) and CO₂ data. 101
- Figure 3.7.** Atmospheric CO₂ data from the UEA O₂ and CO₂ measurement system (blue circles) and the PML pCO₂ measurement system (red triangles) during the JC090 cruise. 103
- Figure 3.8.** Difference between air-sea CO₂ flux calculated using UEA and PML atmospheric CO₂ mole fractions from the JC090 cruise. Positive values indicate that the UEA flux from the atmosphere into the ocean is greater than the PML flux. The overall mean CO₂ flux difference is 0.1731 mol m⁻² yr⁻¹. 104
- Figure 3.9.** Hourly-averaged CO₂, δ(O₂/N₂), and APO data, plotted alongside temperature and humidity data from the RRS James Cook meteorological instruments. The CO₂ y-axis has been scaled so that the data are visually comparable to the δ(O₂/N₂) and APO data. The pink lines on the CO₂, δ(O₂/N₂) and APO plots show the background mole fractions for Weybourne, UK, calculated using the 'rfbaseline' function from the 'IDPmisc' R package. 108
- Figure 3.10.** Wind rose showing wind speed and wind direction for event 1 data (red triangles), event 2 data (green diamonds), and all other data ('no event data'; black circles). 109
- Figure 3.11.** Correlation matrices for event 1 (top plot) and event 2 (bottom plot), created using the 'corPlot' function from the 'openair' package in R (Carslaw and Ropkins, 2012). Numbers indicate the correlation coefficients values from simple linear regressions of the variables. Strong positive correlations are shaded red, and strong negative correlations are shaded blue. The ellipsoids are more round in shape for weak correlations, and more elliptical in shape for strong correlations. 110

Figure 3.12. NAME footprint showing the origin of the air particles that were measured from the ship before event 1. At this time, NAME shows that the majority of the air particles originated from the northwest. Time-integrated particle concentrations are in units of gs m^{-3} .	112
Figure 3.13. NAME footprint showing the origin of the air particles that were measured from the ship during event 1. At this time, NAME shows that the majority of air particles originated from the west and southwest. Time-integrated particle concentrations are in units of gs m^{-3} .	112
Figure 3.14. NAME footprint showing the origin of the air particles that were measured from the ship after event 1, and before event 2. At this time, NAME shows that the majority of the air particles originate from the northwest. Time-integrated particle concentrations are in units of gs m^{-3} .	113
Figure 3.15. NAME footprint showing the origin of the air particles that were measured from the ship during event 2. This figure shows that the air particles were either very local at this time, or from the southwest. Time-integrated particle concentrations are in units of gs m^{-3} .	113
Figure 3.16. NAME footprint showing the origin of the air particles measured from the ship after event 2. NAME shows that most of the air particles originated from the north/northwest and west during this time. Time-integrated particle concentrations are in units of gs m^{-3} .	114
Figure 3.17. $\text{O}_2:\text{CO}_2$ ratio plot of background (i.e. non-event) data (black circles), event 1 data (red triangles), and event 2 data (green diamonds). As before, $\delta(\text{O}_2/\text{N}_2)$ is given in ppm equivalent units to be comparable to CO_2 and enable correct calculation of the regression slopes. The three lines indicates the major axis regression lines for background (black solid), event 1 (red dashed) and event 2 (green dashed-dotted) data. The regressions were weighted according to the difference in measurement uncertainty associated with the $\delta(\text{O}_2/\text{N}_2)$ and CO_2 data.	115
Figure 3.18. The top three panels show hourly averages of atmospheric CO_2 , $\delta(\text{O}_2/\text{N}_2)$ and APO, respectively. The bottom three panels show sea surface temperature, salinity and chlorophyll fluorescence data, respectively, measured by the James Cook underway system.	116
Figure 3.19. Gridded Sea Surface Height anomalies on 01Jan2014, produced from merged Jason-2/OSTM (Ocean Surface Topography Mission) and Cryosat-2 satellite data products (from: http://eddy.colorado.edu/ccar/ssh/nrt_global_grid_viewer). Blue areas are depressions in the mean sea surface height, which indicate cold core eddies, and red areas are elevations in the mean sea surface, which indicate warm core eddies.	119
Figure 3.20. Gridded Sea Surface Height anomalies on 13Sep2013 (from: http://eddy.colorado.edu/ccar/ssh/nrt_global_grid_viewer). The pink star indicates the position of the James Cook on this day.	119

Figure 3.21. A 7-day composite of SST from the MODIS aqua satellite (4 km resolution), centred around 13Sep2013 (from: http://eddy.colorado.edu/ccar/ssh/nrt_global_grid_viewer). The dashed lines indicate the contours of the sea surface height anomalies on 13Sep2013, as shown in figure 3.20. The pink ellipsoid indicates the location of the cyclonic cold-core eddy located to the east of the James Cook on the 13Sep2013. The SST colour scale has been limited to the range of 15 – 21 °C in order to visually emphasis temperature variations in the region of the cold-core eddy.	120
Figure 3.22. CTD cast dissolved O ₂ from the JC090 cruise (black circles). The CTD casts just before, during, and after event 2 are indicated by the yellow, orange and red triangles respectively. The pale blue and dark blue diamonds show dissolved O ₂ from an Argo float located southwest of the James Cook (at 44.5°N, 8.3°E), measured on 01Sep2013 and 11Sep2013, respectively.	123
Figure 3.23. A comparison of the 3-hourly-averaged detrended and deseasonalised measured Δ APO (blue circles) and modelled Δ APO (red triangles) for the JC090 cruise (where the Δ notation indicates that the APO values represent the difference from the APO baseline).	127
Figure 3.24. Modelled APO with all three variables changing as shown in Fig. 3.23 (red triangles), modelled APO with only the atmospheric footprint varying (green squares), modelled APO with only the BLH varying (pink diamonds), and modelled APO with only the O ₂ and N ₂ fluxes varying (cyan hexagons).	128
Figure 4.1. Schematic of the Cap San Lorenzo container ship, showing the location of the O ₂ and CO ₂ measurement system on G deck, the Aspirated Air Inlets, and the ship's engine exhaust stack.	139
Figure 4.2. Route of the Cap San Lorenzo from Hamburg to Buenos Aires and back.	140
Figure 4.3. Meridional transects of hourly-averaged atmospheric CO ₂ , δ (O ₂ /N ₂) and APO across the Atlantic Ocean. The equator is represented by the dashed line. Different northwards and southwards crossing are represented by the symbols and colours in the figure legend. Y-axes have been scaled to be visually comparable on a mole per mole basis.	142
Figure 4.4. Meridional transects of hourly-averaged atmospheric CO ₂ , δ (O ₂ /N ₂) and APO across the Atlantic Ocean, with polluted 'port air' data excluded. Y-axes have been scaled to be visually comparable on a mole per mole basis.	143
Figure 4.5. Atlantic equatorial variability in CO ₂ (top panel), δ (O ₂ /N ₂) (middle panel) and APO (bottom panel). Note that the y-axes have been scaled so that the APO and CO ₂ axes are 1.5 times and 2 times zoomed, respectively, compared to the δ (O ₂ /N ₂) axis on a mole per mole basis.	145

- Figure 4.6.** NAME footprint showing the air mass origin on 27Apr2015, as the Cap San Lorenzo was travelling south. The colour scale given is the log of the time-integrated concentration of air particles gs m^{-3} . 146
- Figure 4.7.** NAME footprint on 08Mar2015, showing the air mass origin as the Cap San Lorenzo crosses the ITCZ heading south. The colour scale given is the log of the time-integrated concentration of air particles gs m^{-3} . The footprint demonstrates that the air originates from both the northern and southern hemispheres simultaneously while the ship crosses the ITCZ. The ship's location is indicated by the black circle, and the position of the ITCZ is shown by the horizontal dashed black line. 148
- Figure 4.8.** Hourly-averaged atmospheric CO_2 (circles), $\delta(\text{O}_2/\text{N}_2)$ (squares) and APO (triangles) from two periods (top panel from Sep2014; bottom panel from Feb2015) when the Cap San Lorenzo was travelling between ports in Europe. Data collected when the ship's speed was less than 5 mph are shown in turquoise, bright green and yellow for CO_2 , O_2 , and APO respectively. Both plots are annotated with the names of the ports in which the ship made berth. The y-axes have been scaled to be visually comparable on a mole per mole basis. 149
- Figure 4.9.** HYSPLIT ensemble back trajectories for 08 Oct 2002 (left plot) and 25 Mar 2002 (right plot), consisting of eight 3-hourly trajectories 24 hours in length from Trinidad Head, California. The left plot corresponds to a period exhibiting low APO, and elevated CO_2 and N_2O , which was previously reported by Lueker and colleagues as being an ocean upwelling event, and the right plot corresponds to a period of little short-term variability in either APO, CO_2 or N_2O , which is of oceanic origin. 152
- Figure 4.10.** Short-term variability in N_2O (blue solid line), CFC-12 (green dashed-dotted line) and CFC-11 (red dashed line) from the AGAGE measurements at Trinidad Head. The orange shading indicates the approximate timing of the 'upwelling' events published in Lueker (2004). 153
- Figure 4.11.** Seasonal migration in the position of the ITCZ in the Atlantic Ocean. Positions obtained from the atmospheric CO_2 and O_2 from the Cap San Lorenzo (CSL) are shown in blue, positions obtained from atmospheric CO_2 and CH_4 data by Royal Holloway University of London (RHUL) on board the RRS James Clark Ross are shown in pink and cyan for 2013 and 2014 respectively, and positions obtained from rainfall maxima using NASA's Tropical Rainfall Measuring Mission (TRMM) are shown in red and green for 2014 and 2015 respectively. 155
- Figure 4.12.** Atmospheric CO_2 from the Cap San Lorenzo, binned into 5° latitude bands (black symbols). The curve fits were produced using HPspline (solid blue lines). For each latitude band, 400 ppm is shown by the dashed black horizontal line. 159

- Figure 4.13.** Atmospheric $\delta(\text{O}_2/\text{N}_2)$ from the Cap San Lorenzo, binned into 5° latitude bands (black symbols). The curve fits were produced using HPspline (solid red lines). For each latitude band, -600 per meg is shown by the dashed black horizontal line. 160
- Figure 4.14.** APO from the Cap San Lorenzo, binned into 5° latitude bands (black symbols). The curve fits were produced using HPspline (solid green lines). For each latitude band, -325 per meg is shown by the dashed black horizontal line. 161
- Figure 4.15.** CO_2 (top panel; blue circles and solid lines), $\delta(\text{O}_2/\text{N}_2)$ (bottom panel; red triangles and dashed lines) and APO (bottom panel; green squares and dash-dotted lines) seasonal amplitude as a function of latitude. Error bars show the uncertainty in the seasonal amplitude for each species, which was determined from the mean magnitude of the HPspline curve fit residuals at the seasonal inflexion points. Y-axes have been scaled to be visually comparable on a mole per mole basis. The equator is indicated by the vertical black dashed line. 166
- Figure 4.16.** Timing of the seasonal maxima (open symbols) and minima (filled symbols) in atmospheric CO_2 (top panel; blue circles and solid lines), $\delta(\text{O}_2/\text{N}_2)$ (bottom panel; red triangles and dashed lines) and APO (bottom panel; green squares and dash-dotted lines) as a function of latitude, determined from the detrended HPspline curve fits. The equator is indicated by the vertical black dashed line. 168
- Figure 4.17.** Annual mean latitudinal variability in detrended APO flask (left panel) and continuous (right panel) data from cargo ships crossing the Pacific Ocean, from Tohjima et al. (2015). Different colours correspond to data from different years, as shown in the legend, and the thick dark grey lines indicate the mean from all the years. 171
- Figure 4.18.** Latitudinally-varying annual mean CO_2 (top panel; blue circles), $\delta(\text{O}_2/\text{N}_2)$ (middle panel; red triangles) and APO (bottom panel; green diamonds) from the Cap San Lorenzo. Also shown in the top panel is the meridional variation in global annual mean CO_2 from the NOAA Marine Boundary Layer (MBL) reference product for 2015 (black squares), which was estimated by adding 2 ppm yr^{-1} to the 2014 values, because the 2015 data are not currently available. Error bars represent the mean standard error of the measurements at each latitude (see main text for justification). The vertical dashed line in each panel represents the equator. Note that y-axes for each panel have been scaled to be visually comparable on a mole per mole basis. 173
- Figure 4.19.** Latitudinal variability in annual mean APO calculated using 5° binned APO (green circles; same as in Fig. 5.17), and 2.5° binned APO (blue triangles). Error bars represent the mean standard error of the measurements at each latitude. The vertical dashed line represents the equator. 175

Figure 4.20. Annual mean latitudinal variability in APO from the Cap San Lorenzo measurements, binned into 5° latitude bands (green circles, solid lines) and 2.5° latitude bands (red triangles, dashed lines), as well as the annual mean variability in modelled APO using TM3 and low spatial resolution fluxes (blue diamonds, dotted and dashed lines) and high spatial resolution fluxes (pink squares, dotted lines). The vertical dashed line represents the equator.	176
Figure 4.21. Atlantic Ocean Air-sea O ₂ fluxes from the NEMO-PlankTOM model, binned into 10° latitude bands. The longitudinal range used in the latitudinal binning was 61°W to 20°E. Note that negative numbers indicate fluxes from the ocean to the atmosphere.	178
Figure 4.22. Comparison of annual mean latitudinal variability in Atlantic APO from the Cap San Lorenzo (green circles and solid lines; both panels) with annual mean latitudinal variability in Western Pacific APO from 2003-2012 flask data (pink squares and dashed line; top panel), 2010 only flask data (red triangles and dashed lines; top panel), and 2008-2012 continuous data (dark blue dash-dotted lines on the bottom panel, with uncertainties indicated by the turquoise dash-dotted lines). All western Pacific data are from Yasunori Tohjima (National Institute of Environmental Studies, Japan) and are published in (Tohjima et al., 2015).	179
Figure 4.23. Annual mean air-sea O ₂ flux for 2015 from the NEMO-PlankTOM model. Note that positive values indicate fluxes into the ocean (green to red shading), and negative values indicate fluxes out of the ocean (blue/purple shading). O ₂ fluxes are shown in units of mol m ⁻² s ⁻¹ .	181
Figure 4.24. NCEP2 vertical pressure velocity data (in Pa s ⁻¹) over the North Atlantic along a 22.5°E meridional transect. Note that positive values indicate downwards atmospheric transport, while negative values indicate upwards atmospheric transport.	182
Figure 5.1. Map showing the location of the University of East Anglia (UEA), and also the Tacolneston tall tower (TAC) and Weybourne Atmospheric Observatory (WAO).	196
Figure 5.2. Hourly-averaged atmospheric CO ₂ (top panel), δ(O ₂ /N ₂) (2 nd panel) and APO (3 rd panel) measured from the roof of the Environmental Sciences building at UEA. Note that the y-axes for δ(O ₂ /N ₂) and APO have been scaled to be visually comparable to the CO ₂ y-axis on a mole per mole basis, and 'bad' data caused by technical problems have been excluded prior to averaging. Also shown are 3-hourly model-derived GDAS meteorological data (NOAA): atmospheric temperature (4 th panel: dark red solid line), relative humidity (4 th panel: cyan short-dashed line), atmospheric pressure (4 th panel: pink dotted line), wind direction (bottom panel: dark navy long-dashed line), and wind speed (bottom panel: grey dashed/dotted line).	198

Figure 5.3. O ₂ :CO ₂ ratio of hourly-averaged data measured at UEA during the summer of 2014. $\delta(\text{O}_2/\text{N}_2)$ is given in ppm equivalent units to be comparable to CO ₂ on a mole per mole basis. The solid red line indicates the major axis regression line, which is weighted according to the difference in measurement precision (and therefore uncertainty) associated with the $\delta(\text{O}_2/\text{N}_2)$ and CO ₂ data, and has a slope of -1.1011. The negative value of the O ₂ :CO ₂ ratio indicates that the two species are anti-correlated.	199
Figure 5.4. Hourly-averaged CO ₂ (top panel) and $\delta(\text{O}_2/\text{N}_2)$ (bottom panel) with selected diurnal events coloured according to the O ₂ :CO ₂ ratio (see legend in figure). The y-axes have been scaled so that the $\delta(\text{O}_2/\text{N}_2)$ and CO ₂ panels are visually comparable on a mole per mole basis.	200
Figure 5.5. A polar plot of the variability in 2-minute O ₂ :CO ₂ ratios with wind speed (m s ⁻¹) and wind direction. Meteorological data are from NOAA's GDAS product. The polar plot was created in R using the 'polarPlot' function from the 'Openair' package (Carslaw and Ropkins, 2012).	201
Figure 5.6. Comparison of atmospheric CO ₂ at UEA and TAC (top panel), and comparison of atmospheric CO ₂ and $\delta(\text{O}_2/\text{N}_2)$ at UEA and WAO (middle panel and bottom panel). Y-axes have been scaled so that the $\delta(\text{O}_2/\text{N}_2)$ and CO ₂ panels are visually comparable on a mole per mole basis.	203
Figure 5.7. Comparison of hourly-averaged TAC CO and UEA APO data (top panel) and hourly-averaged WAO CO and APO data (middle panel), illustrating that a lot of the short-term variability in CO and APO is anti-correlated. Also shown is wind direction measured at WAO (bottom panel). The CO measurements at TAC are sampled from the 100 m tower inlet. It should be noted that the TAC CO data shown above are not the finalised, quality controlled data, due to an on-going calibration issue that is affecting the accuracy of the high CO values.	205
Figure 5.8. ffCO ₂ from CO at TAC and APO at UEA (top panel) and ffCO ₂ from CO and APO at WAO (bottom panel). Also shown is ffCO ₂ from ¹⁴ CO ₂ at TAC (top panel, black dots).	208
Figure 5.9. ffCO ₂ calculated from Co at TAC (top panel) and APO at UEA (bottom panel) using the moderately flexible baseline fits used in Fig. 4.8, as well as inflexible baseline fits (dashed pink and orange lines) and flexible baseline fits (dotted-dashed dark purple and dark red lines).	210
Figure 5.10. Moderately flexible, inflexible, and flexible baseline fits to CO from TAC (top panel) and APO from UEA (bottom panel).	211
Figure 5.11. ffCO ₂ (CO) and ffCO ₂ (APO) at TAC and UEA, respectively (top panel), and ffCO ₂ (CO) and ffCO ₂ (APO) at WAO (bottom panel), calculated using time-varying emission ratios and inflexible baselines. Shaded areas denote the respective uncertainties of the calculated ffCO ₂ . ffCO ₂ from ¹⁴ CO ₂ measurements at TAC are denoted by the black circles, of which the size represents the uncertainty of the ffCO ₂ (¹⁴ CO ₂) values.	216

Figure 5.12. ffCO ₂ from APO at UEA (top panel) and CO at TAC (bottom panel) calculated using a variety of emission ratios (see text above and figure legends). The ffCO ₂ from time-varying ratios is the same as the ffCO ₂ shown in Fig. 4.11 (top panel), only without the uncertainty shading, to aid visual comparison with the ffCO ₂ calculated using the other emission ratios. Also shown is ffCO ₂ from TAC ¹⁴ CO ₂ data (black symbols).	219
Figure 5.13. ffCO ₂ (CO) at TAC (top panel) and ffCO ₂ (APO) at UEA (bottom panel) compared to modelled ffCO ₂ from COFFEE (black lines) and the UK NAEI (orange lines).	221
Figure 5.14. WAO ffCO ₂ (CO) (top panel) and ffCO ₂ (APO) (bottom panel) compared to modelled ffCO ₂ from COFFEE (black lines) and the UK NAEI (orange lines).	222
Figure 5.15. Total CO ₂ (blue solid line), biosphere CO ₂ (green dashed line) and ffCO ₂ from APO (red dashed-dotted line) at UEA. Note that left and right y-axes are scaled to be visually comparable.	223
Figure 5.16. Total CO ₂ (blue solid line), biosphere CO ₂ (green dashed line) and ffCO ₂ from APO (red dashed-dotted line) at WAO. Note that left and right y-axes are scaled to be visually comparable.	224

List of Tables

Table 1.1. A record of the historical and current high-precision atmospheric O ₂ data from flask samples, continuous measurements, and campaigns.	16-22
Table 2.1 Shipboard measurement system WSS and TT cylinders. ‘# Fills’ indicates the number of previous fills of the cylinders, and is an indication of how well ‘conditioned’ the cylinder is. Note that D596276 was evacuated between Jan 2015 and Nov 2015, owing to the air inside getting ‘wet’. Evacuating a cylinder effectively removes all conditioning from the cylinder, and re-starts the ‘# Fills’ counter. The upper values in the ‘Dec. O ₂ ’ and ‘Dec. CO ₂ ’ columns refer to the declared values when the cylinders were prepared, while the bottom values refer to the declared values at the end of the cylinder lifetimes. Due to a technical issue with the cylinder filling system, it was not possible to prepare a 4 th WSS in time for January 2016.	66
Table 2.2. Repeatability of O ₂ and CO ₂ analysers of shipboard measurement system, determined from TT analyses. Repeatability is calculated as the mean of the $\pm 1\sigma$ standard deviations from all the TT runs (where a run consists of either 7 two-minute averages or 13 one-minute averages, as mentioned above), and hence is denoted as the mean of these $\pm 1\sigma$ standard deviations, reported to $\pm 1\sigma$ standard deviation, thus demonstrating how the repeatability of the O ₂ and CO ₂ measurements varies over time.	72
Table 2.3. Compatibility of O ₂ and CO ₂ measurements, determined from TT analyses. Compatibility is calculated as the mean difference from the UEA CRAM Laboratory ‘declared value’ of the TT. Note that there is no compatibility entry for the Wolfson Lab period when JT air was pass through the drying system, as unfortunately, it was not possible to measure the JT against the UEA calibration scales. The upper values in the ‘No. of TT runs’ column refer to the CRAM Laboratory declared values when the cylinders were prepared, while the bottom values refer to the declared values at the end of the cylinder lifetimes.	74
Table 2.4. Improvements in short-term precision from reduced V11 switching frequency. Values are means of the $\pm 1\sigma$ standard deviations of the TT and ZT runs, reported with $\pm 1\sigma$ standard deviation, and are in per meg units. The improvement for TT and ZT measurements correspond to a 40% and 60% reduction, respectively.	79
Table 3.1. Sensitivity of O ₂ fluxes calculated using the Jacob (1999) ‘Puff’ model to variations in vertical mixing height, <i>e</i> -folding time, and wind fetch. Note that the O ₂ flux values are in mol m ⁻² yr ⁻¹ , and negative flux values denote air-to-sea fluxes.	124

Table 4.1. Previous O ₂ and CO ₂ measurements from commercial container ships. NDIR refers to non-dispersive infrared, and GC/TCD refers to gas chromatograph equipped with a thermal conductivity detector. Latitude and longitude ranges are approximate. The container ship O ₂ and CO ₂ flask measurements of Battle et al. (2006) were continued on board the 'Ka' imimoana', a US NOAA (National Oceanic and Atmospheric Administration) research vessel, which serviced a series of moorings between 8°N and 8°S in the Pacific, from 2001 - 2007. Cont/Flask indicates continuous and flask sample measurements.	137
Table 4.2. Comparison of Cap San Lorenzo CO ₂ , O ₂ and APO seasonal cycle amplitudes with those from other O ₂ and CO ₂ measurement stations at similar latitudes. Data are either from the literature (please refer to the citations in Table 1.1) or are from personal communication with the measurement station personnel.	170
Table 5.1. Component and total uncertainties for the CO and APO ffCO ₂ quantification methods at TAC, WAO and UEA, given to 2 significant figures for easier comparison.	214
Table 5.2. Typical ffCO ₂ ranges from the literature, shown alongside the ffCO ₂ ranges for TAC, UEA and WAO presented in this work, calculated using CO, APO and ¹⁴ CO ₂ atmospheric data.	218
Table 5.3. Comparison of TAC ffCO ₂ values using the 'top-down' CO method and 'bottom-up' inventories. All units are in ppm. Average values are given ±1σ standard deviation.	222
Table 5.4. Comparison of UEA ffCO ₂ values using the 'top-down' APO method and 'bottom-up' inventories. All units are in ppm. Average values are given ±1σ standard deviation.	222
Table 5.5. Comparison of WAO ffCO ₂ values using the 'top-down' CO and APO methods and 'bottom-up' inventories. All units are in ppm. Average values are given ±1σ standard deviation.	222

Acknowledgements

Having now come to the end of my Ph.D., I can now say that there are two factors that are essential to Ph.D. success: a fair amount of luck, and also a lot of help. Hence, there are many people I would like to thank for the advice, help and support that has been offered to me throughout the last 3½ years.

Firstly, I would like to acknowledge and thank all of the people who helped me to design, build, and test the shipboard O₂ and CO₂ measurement system, in particular: Phil Wilson (UEA), for teaching me the basics of Swagelok in the CRAM lab, for building most of the shipboard system analyser rack and the Blue Box, both of which I inherited when I started my Ph.D., and for filling reference and calibration cylinders; Andy MacDonald (UEA), who introduced me to the art of beautiful tube bending, and who helped me to build the shipboard system regulator manifold and drying rack; Alex Etchells (UEA), who built the 'Nemo' software, and put up with my numerous requests for software 'upgrades'; Dave Blomfield (UEA), who built the ship system electronics box and the aspirated air inlets; Nick Griffin (UEA), who helped me out when I had a pre-cruise electronics emergency; Stuart Rix (UEA) and Gareth Flowerdew (UEA) from the workshop, who helped me to mount all the shipboard system components inside the 19-inch racks, and who also stopped the Blue Box from falling apart (!); and Marica Hewitt (UEA), who helped me with numerous complicated and/or problematic orders, and with all the logistical aspects of deploying and maintaining the shipboard measurement system. I would also like to thank all of the people who came with me to the London Gateway port for the installation and maintenance visits, and in doing so surrendered their Friday evening plans. I am also very grateful to my international colleagues, who provided information that allowed me to compile Table 1.1 in Chapter 1.

With respect to the JC090 cruise, I would like to thank Alberto Naveira Garabato (University of Southampton, UK), for allowing myself and Andrew Manning to 'piggy-back' onto the OSMOSIS project cruise, Alex Forryan (National Oceanography Centre, Southampton, UK), for sharing the JC090 underway data with me, and Dan Comben (National Oceanography Centre, Southampton, UK) who helped to install the inlet lines from the Monkey Island and foremast down to the Met Lab, Martin Bridger (National Environment Research Council, UK) for providing the meteorological data and for I.T. support during the cruise, and Steve Woodward (National Oceanography Centre, Southampton, UK) for arranging the shipping to

Portugal and for helping with other logistical aspects of preparing for the JC090 cruise. I would also like to thank Vas Kitidis (Plymouth Marine Laboratory, UK) for helping to arrange for the pCO₂ measurement system to be turned on for the JC090 cruise, and who provided the pCO₂ data shown in Chapter 3, and Zoë Fleming (National Centre for Atmospheric Science, UK), who produced the NAME footprints for the JC090 cruise. The NEMO-PlankTOM model output presented in Chapters 3 and 5 was provided by Clare Enright (UEA), to whom I am very grateful.

In relation to Chapter 4, I would like to thank Christoph Gerbig (Max Planck Institute for Biogeochemistry, Jena, Germany), for updating the COFFEE dataset to 2014 and providing the data. I would also like to thank the UK Met Office, particularly Andrew Jones and Laura Burgin, for the NAME model training and help that I received when I was getting started with NAME. Leo Earl (UEA) and Mike Salmon (UEA) were very helpful when I was struggling to get NAME set up at UEA and working smoothly, and Zoë Fleming provided me with some sample input files, which were very useful when I was figuring out how to set up my own NAME runs. The Tacolneston data were provided by Dave Oram (CO data; UEA) and Angelina Wenger (ffCO₂ from ¹⁴CO₂ data; University of Bristol, UK), and measurements are managed by Simon O'Doherty (University of Bristol, UK) and Bill Sturges (UEA). The Weybourne CO data are maintained by Grant Forster (UEA), who also provided the data.

The shipboard measurements shown in Chapter 5 would not have been possible without the continued generous co-operation of Hamburg Süd and the Cap San Lorenzo crew, who have been extremely helpful throughout the project, and even allowed me to stay on board the ship for a week when I was deploying the shipboard measurement system for the first time. In particular, I would like to thank Nils Klemme, who made the installation on board the Cap San Lorenzo possible, Andreas Buhl, who installed the synflex tubing and cables for the inlet lines, and the engineers who have been changing the chiller traps for me. I would also like to thank the staff at the London Gateway port, DP World and John Good Shipping, especially Colin Hitchcock, Billy Dey, and Helen Woolford, who allow us to visit the ship when it makes berth in the UK, and arrange for the calibration cylinders to be lifted on and off the ship every 8 weeks, so that we can keep the measurement system running. I am also very grateful to Sara Mikaloff-Fletcher (National Institute of Water and Atmospheric Research Ltd, New Zealand) who provided the modelled APO data, and to Yasunori Tohjima (National Institute for Environmental Studies, Japan), for sharing the western Pacific shipboard data with me.

I have been very lucky to have been surrounded by excellent colleagues during my Ph.D., and I would like to thank Thomas ‘Barney’ Barningham (UEA) for being a great sounding board, when I needed to talk a problem through with someone, Sander van der Laan for some interesting discussions that were very helpful, particularly relating to Chapter 4, and Grant Forster for helping us to keep the measurements at Weybourne running. I would also like to thank Britt Stephens (National Center for Atmospheric Research, Colorado, USA) for his very useful advice about shipboard O₂ measurements, and for all the help with fixing the CRAM Lab VUV analyser.

I have been very fortunate to form some great friendships during my time in 01.37W, in particular Anna Ridley, who introduced me to indoor bouldering (which I highly recommend!), helped to cheer me up when the measurement system was ‘broken again’, and is as bad as me about talking aloud to oneself in the office. Also, Amanda Hopes, who is the only person I know who is crazier about knitting than me. And of course, I am very grateful to my Mum, for her lasting support and encouragement since I moved to Norwich, and to my Dad, who I am sure would have been very proud.

Last, but certainly not least, I would like to thank my supervisory team: Corinne Le Quéré, who is an incredibly inspiring role model and who helped me to see the ‘bigger picture’ in my research; Bill Sturges, who has been a fantastic supervisor throughout, always making the time to listen to my measurement system technical woes, and offering insightful advice and lots of encouragement along the way; and finally, Andrew Manning, who is a wonderful person to work with, and to whom I owe the greatest thanks of all.

Chapter 1

Introduction

1.1 Climate change and the carbon cycle

There is now an overwhelming consensus amongst the scientific community that human activities are the major contributing factor to recent climate change (Cook et al., 2013); the ongoing scientific climate change debate is no longer about whether climate change is happening or not, but rather is about how the climate will change in the future, and what should or can be done about it. Numerous 'fingerprints' of anthropogenic climate change in long-term datasets provide the evidence of humanity's influence on the planet. Examples include: a rise in the global land and ocean surface temperature by approximately 0.8 °C since 1850, a 1971-2010 mean rate of warming in the oceans of 0.11 °C per decade, considerable decline in mass observed in the world's ice sheets, particularly in Greenland, the Arctic and in West Antarctica, and sea level that has risen by about 0.18 m since 1900 (IPCC, 2013).

The natural greenhouse effect that arises from water vapour and other infrared radiation absorbing gases in the atmosphere is an important and beneficial component of the Earth's system, which helps to maintain a higher mean global surface temperature that is more favourable to both human existence and life itself on Earth. Large increases in anthropogenic greenhouse gas concentrations in the atmosphere are now perturbing this natural greenhouse effect and causing global temperatures to rise, which will very likely have negative consequences for humanity and many other species on Earth (IPCC, 2013). Atmospheric concentrations of the two most important anthropogenically-produced greenhouse gases, carbon dioxide (CO₂) and methane (CH₄), are now 40% and 150% higher than pre-industrial concentrations respectively (IPCC, 2013). Figure 1.1 shows natural and anthropogenic radiative forcing relative to 1750, and demonstrates that anthropogenic greenhouse gases in the atmosphere, in particular CO₂ and CH₄, are by far the dominant positive contributors.

In addition to the radiative forcing estimates shown in Fig. 1.1, there are several other lines of evidence demonstrating that recent climate change is caused by anthropogenic greenhouse gases in the atmosphere, and not by natural forcings, such as changes in solar radiation or volcanic emissions. These lines of evidence include: satellite measurements detecting changes in the planet's outgoing long-wave radiation spectra (Harries et al., 2001); a long term decrease in the global ¹³C/¹²C ratio of atmospheric CO₂ (Keeling et al., 1979); and a long-term decrease in the global ¹⁴C/¹²C ratio of atmospheric CO₂ (Suess, 1955). The key uncertainties with respect to

climate change are now focused on regional climate changes and future predictions: how much will global temperatures rise and at what rate? How much sea level rise will occur? How much fossil fuel CO₂ will be emitted? What are the options for safely geoengineering the climate?

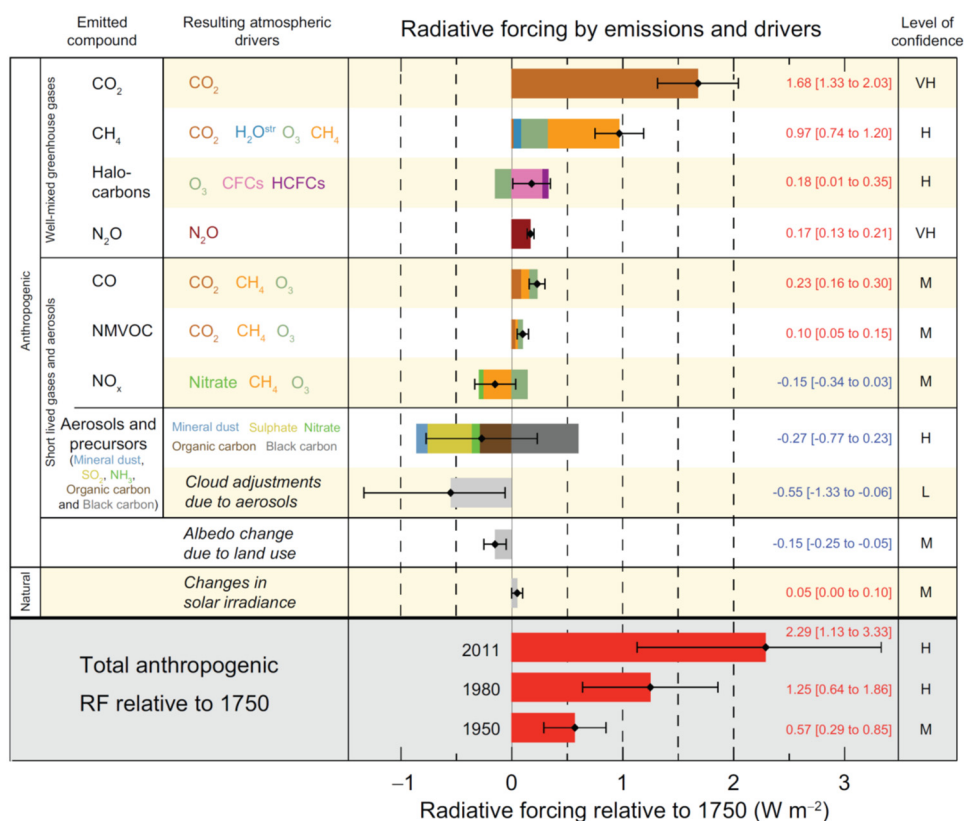


Figure 1.1. Radiative forcing estimates in 2011 relative to 1750, from (IPCC, 2013). Confidence level indicators correspond to: VH – very high, H – high, M – medium, L – low, VL – very low. Radiative forcing, in W m⁻², is defined as the change in energy flux caused by a driver, calculated either at the tropopause or the top of the atmosphere.

Figure 1.2 shows model projections of global mean surface temperature change (Fig. 1.2a), Arctic September sea-ice extent (Fig. 1.2b), and global surface ocean pH (Fig. 1.2c) from 1950 to 2100, for different scenarios of anthropogenic forcings, known as Representative Concentration Pathways, or RCPs (IPCC, 2013; van Vuuren et al., 2011). Only the model projections for RCP2.6 and RCP8.5 are shown in full in Fig. 1.2 for clarity, which represent the two most extreme pathways, corresponding to the lowest (RCP2.6) and highest (RCP8.5) anthropogenic forcings. It is clear that there is a large degree of uncertainty regarding future climate change, which is largely dependent upon the RCP that is followed. Each RCP projection itself is also associated with a large uncertainty, particularly for global mean surface temperature and Arctic September sea-ice extent, as indicated by the blue and red shading in Fig. 1.2. This is because the climate system is extremely complex, with

multiple positive and negative feedback processes that may act to either amplify or attenuate any perturbation in climate. Many of these feedback processes are not currently fully understood, particularly those associated with the global carbon cycle. Therefore, improving our understanding of the global carbon cycle is crucial for limiting atmospheric greenhouse gas concentrations to levels that will prevent or reduce severe impacts of climate change on Earth.

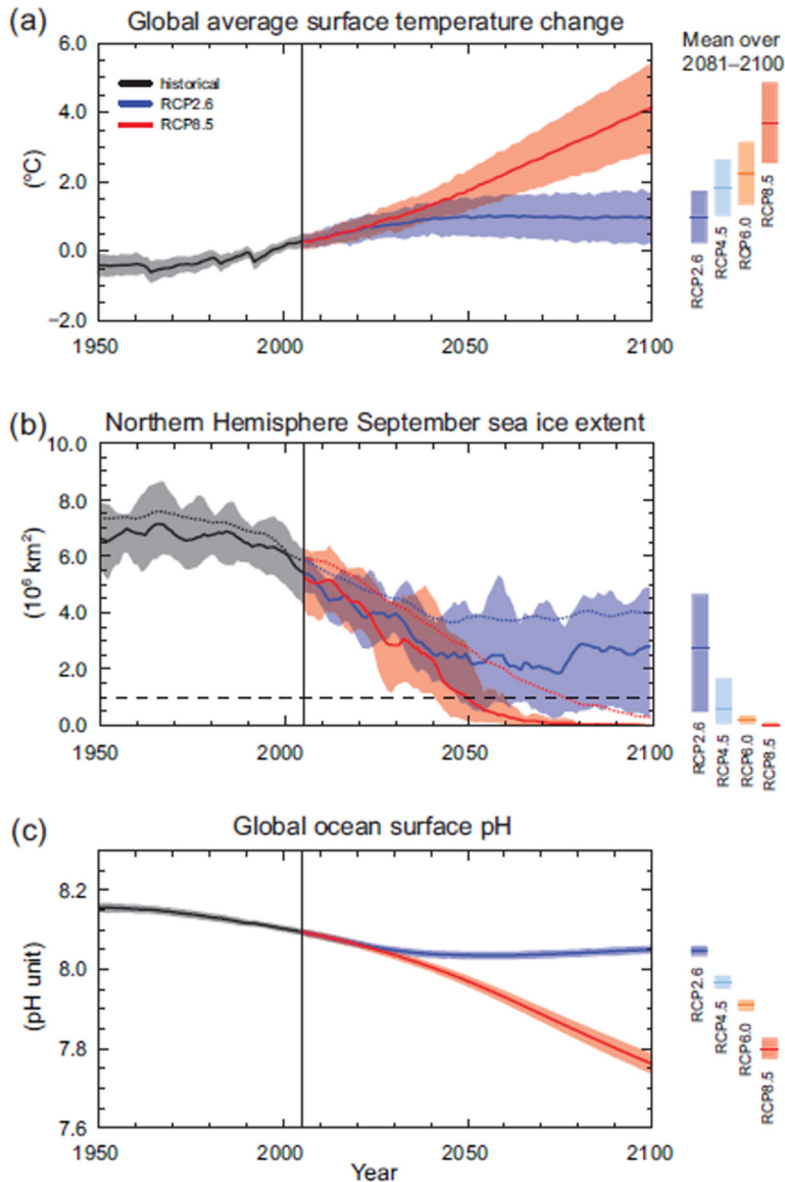


Figure 1.2. Model projections of (a) global mean surface temperature change relative to 1986-2005, (b) Arctic September sea-ice extent, and (c) global ocean surface pH, from 1950 to 2100 for the Representative Concentration Pathway (RCP) scenarios 2.6 and 8.5 of (van Vuuren et al., 2011), with bars on the right indicating the 2081-2100 predictions for RCP4.5 and RCP6.0. Model projections are from the Coupled Model Intercomparison Project Phase 5 (CMIP5) multi-model ensemble simulations (Taylor et al., 2011). Black lines with grey shading represent modelled historical evolution of each parameter and its uncertainty, respectively. Likewise, for RCP2.6 and RCP 8.5, the uncertainty is shown by the blue and red shading, respectively. The black dashed line in (b) represents nearly ice-free conditions, while the dotted lines indicate the CMIP5 multi-model means. Figure 1.2 is from IPCC (2013).

The global carbon cycle, shown in Figure 1.3, consists of four main carbon reservoirs: the oceans (comprising of the surface, intermediate and deep oceans, and the marine biota and dissolved organic carbon pool), atmosphere, terrestrial biosphere (comprising of vegetation and soils, including permafrost) and fossil fuels. In general, carbon fluxes between the rock reservoir and the other carbon reservoirs occur over time scales of thousands to millions of years, and are therefore not relevant to the timescales over which recent anthropogenic climate change is occurring; hence, the rock reservoir is not shown in Fig. 1.3, but is an important component of the carbon cycle on millennial timescales.

As shown by the red arrows and values in Fig. 1.3, it is clear that there has been a substantial flux of carbon to the atmosphere from anthropogenic fossil fuel burning and land use change. Approximately 56% of fossil fuel carbon released to the atmosphere has remained there, while the other 44% has been taken up approximately equally by the ocean and terrestrial biosphere (Sarmiento et al., 2010), known as the ocean and land carbon sinks respectively.

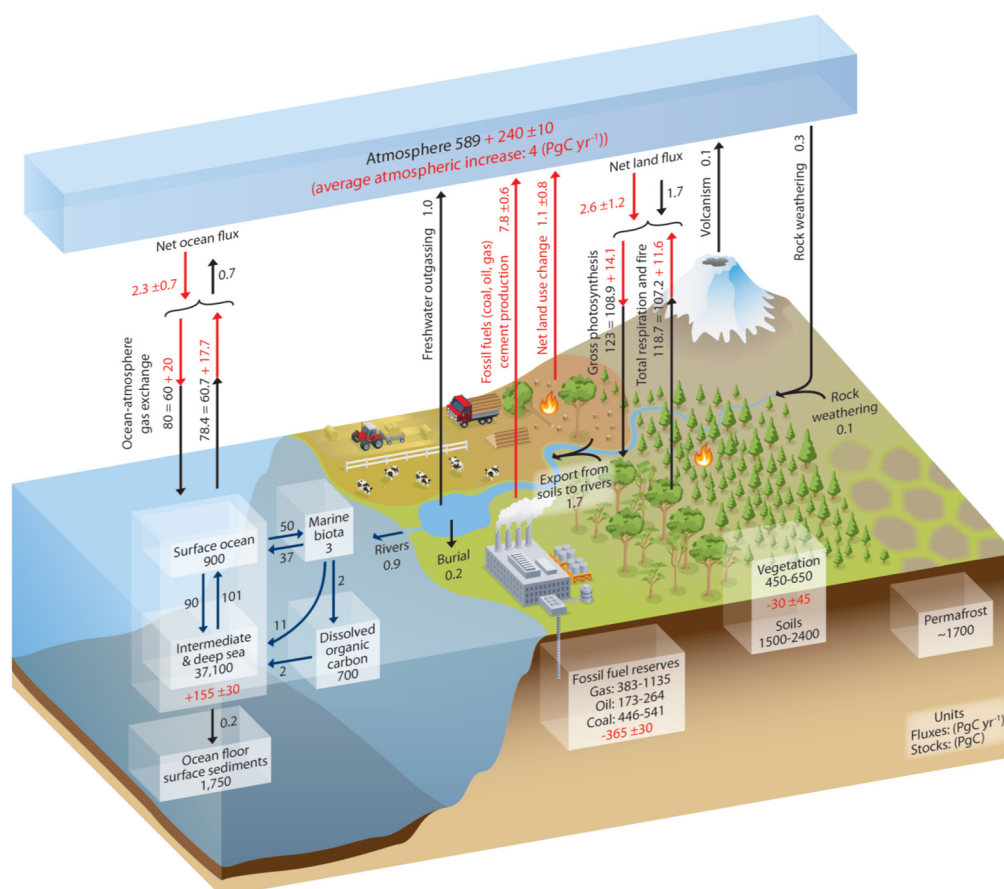


Figure 1.3. A schematic of the global carbon cycle, from (Ciais et al., 2013). Black numbers and arrows represent natural reservoirs and fluxes of carbon prior to 1750, and red numbers and arrows represent anthropogenic reservoirs and fluxes of carbon averaged over the 2000 – 2009 time period. Reservoir and flux values are given in units of PgC and PgC yr⁻¹ respectively.

Most gases are not very soluble in water, however, when CO₂ dissolves in seawater it dissociates to bicarbonate and carbonate ions. This changes the balance of carbon between the atmosphere and the oceans due to Henry's Law, resulting in a higher proportion of carbon being stored in the ocean than otherwise would be, if CO₂ did not dissociate in seawater. In addition, the uptake of CO₂ from the surface ocean by marine biological primary productivity, and the subsequent transport of organic carbon from dead organisms to the deep ocean also acts to increase the proportion of carbon stored in the oceans (Riebesell et al., 2007). These processes are partially offset by the marine inorganic carbon pump, whereby the formation of calcium carbonate by marine phytoplankton in surface ocean waters results in a flux of CO₂ from the ocean to the atmosphere. Another offsetting process is a shift in the Revelle factor (Ciais et al., 2013), whereby an increase in dissolved CO₂ in the ocean increases the Revelle factor, resulting in less CO₂ dissociation to bicarbonate and carbonate ions, which in turn reduces the CO₂ uptake of the oceans due to Henry's Law. The overall result of these ocean processes is that approximately 98.5% of pre-industrial carbon in the ocean-atmosphere system remains in the ocean (Houghton, 2007), and there is an overall net flux of anthropogenic carbon from the atmosphere to the oceans. Owing to the Revelle buffer factor, the oceans are only expected to take up ~70% of anthropogenic carbon from the atmosphere, not ~98.5%, because the addition of anthropogenic carbon to the oceans reduces ocean pH, which reduces the CO₂ dissociation in seawater to other species, and thus reduces the ocean's capacity to take up atmospheric CO₂.

Fluxes of carbon between the terrestrial biosphere and the atmosphere largely arise from respiration, which results in a flux of CO₂ to the atmosphere, and photosynthesis, which results in a flux of CO₂ out of the atmosphere. Land use change and other disturbances, such as forest fires also contribute to fluxes of CO₂ between the atmosphere and the land (Houghton, 2007). Currently, the net global flux of carbon is from the atmosphere to the terrestrial biosphere, although some studies indicate that the land carbon sink may be changing (Barichivich et al., 2013; Graven et al., 2013; Keeling et al., 1996; Piao et al., 2008). There is also large interannual variability in the global land carbon sink, owing to climatic variability (e.g. interannual variability in temperature and precipitation, and El Niño-Southern Oscillation variability), which can have large impacts on ecosystem uptake and release of carbon (Sarmiento et al., 2010).

The ocean and land carbon sinks play an important role in mitigating anthropogenic climate change, however, the future roles of these two carbon sinks are highly uncertain, due to climate-carbon feedback processes (Houghton, 2007). For example, under warmer conditions, some studies show that carbon release from the terrestrial biosphere due to increased respiration will exceed carbon uptake by photosynthesis, and thus the land biosphere may in fact become a source of carbon to the atmosphere (Ciais et al., 2013; Friedlingstein et al., 2014). Similarly, changes in ocean temperature, circulation, stratification and primary productivity may reduce the effectiveness of the ocean as a carbon sink, which will have implications for future climate change (Fay and McKinley, 2013; Houghton, 2007; Le Quéré et al., 2009).

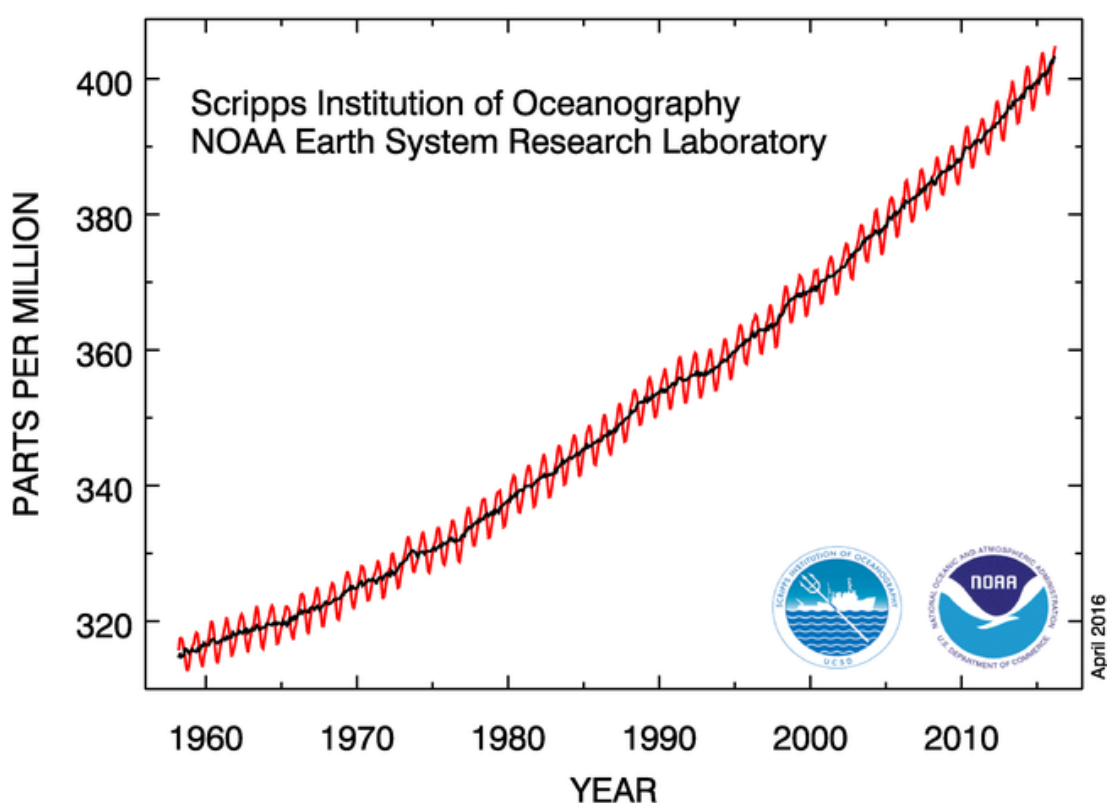


Figure 1.4. The atmospheric CO₂ record measured at Mauna Loa Observatory, Hawaii, by Pieter Tans, NOAA/ESRL (National Oceanic and Atmospheric Administration/Earth System Research Laboratory, USA; www.esrl.noaa.gov/gmd/ccgg/trends/) and Ralph Keeling, Scripps Institution of Oceanography, USA (scrippsco2.ucsd.edu/). The red line shows the entire record, with the long-term trend represented by the black line.

The accumulation of CO₂ in the atmosphere has been monitored accurately since the late 1950s at the Mauna Loa Observatory, Hawaii, USA (see Figure 1.4). The atmospheric CO₂ record shown in Fig. 1.4 has several features, including a long-term trend caused by fossil fuel combustion and land use change, and a seasonal cycle, which demonstrates the dominance of northern hemisphere terrestrial biosphere

photosynthesis over respiration in summer, and vice versa in winter. Interannual variability in both the seasonal and long-term variations in CO₂ are due to climatic variability (e.g. El Niño–Southern Oscillation), volcanic eruptions, and variability in fossil fuel emissions (Keeling et al., 1995).

1.2 Atmospheric oxygen as a tool for understanding the carbon cycle

In order to gain better understanding of specific carbon cycle processes and feedbacks, it is necessary to separate out individual components, such as the land and ocean carbon sinks. There are three types of methods for distinguishing between the land and ocean carbon sinks: those that are based on measurements, those that are based on modelling studies, and those that are based on accounting or inventory techniques.

Measurement-based carbon sink separation methods include using dissolved ocean CO₂ measurements from ships and buoys to estimate changes in the ocean carbon sink (Takahashi et al., 2002; Takahashi et al., 2009), although this method requires significant extrapolation to fill data gaps, and is limited by uncertainties in gas transfer velocities (Liss and Merlivat, 1986). Measurements of atmospheric ¹³CO₂/¹²CO₂ ratios can also be used to estimate changes in the land carbon sink, since plants preferentially photosynthesize ¹²CO₂ molecules over ¹³CO₂ molecules, yet there is almost no isotopic preference for ocean carbon uptake (e.g. Gruber and Keeling, 2001; Heimann and Meier-Reimer, 1996). This method is limited by the very small changes in isotopic signature of atmospheric CO₂, which are very challenging to measure. Additionally, C₃ and C₄ plant carbon fixation pathways have different isotopic preferences, and different parts of the land biosphere act as carbon sinks over varying time scales, from hours to years, which adds significant complexity to this method (Manning and Keeling, 2006).

Modelling-based carbon sink estimation methods include using ocean modelling techniques to estimate the ocean carbon sink, and then calculating the land carbon sink by subtraction (e.g. Le Quéré et al., 2003; Sarmiento et al., 2010). This method is difficult to validate with observations, and different models can produce significantly different estimates. Alternatively, one can apply an inverse modelling method, such as (Stephens et al., 2007b), who used a range of atmospheric transport models and vertical profile atmospheric CO₂ measurements to calculate land CO₂

fluxes, although vertical mixing biases were found to affect the land flux estimates. Additionally, the authors found that the atmospheric transport models that performed well for calculating land CO₂ fluxes did not agree on ocean CO₂ fluxes, and the uncertainty estimates were large compared to other methods.

'Bottom-up' methods using inventory or process model approaches (e.g. Pan et al., 2011) provide an alternative method for quantifying the land sink, but some studies have not been able to detect large carbon land uptake in the mid- to high-latitude northern hemisphere, and do not show a land carbon source in the tropics (e.g. Baker et al., 2004; McGuire et al., 2001). Such methods are also typically only performed about once per decade, and so have relatively coarse temporal resolution.

An additional method, which is used in this thesis, is to use high-precision atmospheric O₂ measurements, in conjunction with concurrent atmospheric CO₂ measurements, to separate out land and ocean carbon fluxes. Fluxes of CO₂ and O₂ from fossil fuel combustion are strongly anti-correlated, as shown in Equation 1.1:



where C_xH_y represents the composition of the fuel.

The molar oxidative ratio (O₂:CO₂ ratio) of fossil fuel combustion is in the range of -1.17 to -1.95, depending on fuel type (Keeling, 1988; Steinbach et al., 2011). Note that in this thesis, a negative O₂:CO₂ ratio denotes anti-correlation between O₂ and CO₂ fluxes, whereas a positive O₂:CO₂ ratio denotes correlation. Fluxes of CO₂ and O₂ between the atmosphere and terrestrial biosphere are also strongly anti-correlated (see Equation 1.2), with a mean global O₂:CO₂ ratio of about -1.1 (Severinghaus, 1995), although the regional value can vary from approximately -0.9 to -1.2 depending on vegetation and soil properties (Masiello et al., 2008; Worrall et al., 2013). O₂ and CO₂ fluxes between the atmosphere and terrestrial biosphere are represented by:



where CH₂O represents the very approximate composition of terrestrial organic matter.

For ocean-atmosphere fluxes, however, CO₂ and O₂ are uncoupled, owing to the differences in solubility properties and seawater chemistry between CO₂ and O₂. As mentioned previously, CO₂ dissociates to bicarbonate and carbonate ions in seawater so that 98.5% of carbon in the atmosphere-ocean system is in the oceans; however, O₂ is very insoluble in water, and so only 1% of O₂ in the ocean-atmosphere system is in the oceans, with 99% in the atmosphere (Bender and Battle, 1999). The difference in the relationship of O₂ and CO₂ between land and ocean fluxes with the atmosphere enables the calculation of the global land and ocean carbon sinks, as presented most recently in (Keeling and Manning, 2014), and which is not possible using CO₂ measurements alone (Keeling et al., 1993).

Figure 1.5 shows time series representative of both northern hemisphere (green) and southern hemisphere (blue) atmospheric O₂ and CO₂. Measurements of atmospheric O₂ are reported as changes in the O₂/N₂ ratio (see Equation 1.3), because O₂ is not a trace gas, and its mole fraction is therefore affected by small changes in other gases, such as CO₂ (Keeling et al., 1998a). It is also difficult to detect very small changes of O₂ in the atmosphere (Stephens et al., 2003), however, N₂ is not as variable as O₂, so O₂/N₂ changes should mainly reflect changes in O₂ (Keeling and Shertz, 1992). Throughout this thesis, the term ‘O₂’ has been used when describing atmospheric O₂ in the text, and the term ‘δ(O₂/N₂)’ has been used for figure axes. Changes in the O₂/N₂ ratio are reported as:

$$\delta\left(\frac{O_2}{N_2}\right) = \left(\frac{O_2/N_{2\text{sample}}}{O_2/N_{2\text{reference}}} - O_2/N_{2\text{reference}} \right) \quad (\text{Eq. 1.3})$$

As for Fig. 1.4, both CO₂ time series plotted in Fig. 1.5 show a long-term increase from fossil fuel combustion, as well as a seasonal cycle that represents exchange of CO₂ with the terrestrial biosphere (Keeling and Shertz, 1992). The seasonal cycle amplitude in the northern hemisphere is much greater than in the southern hemisphere, owing to a greater proportion of land masses in the northern hemisphere.

As expected, both O₂ time series show a long-term decreasing trend caused by fossil fuel combustion (Bender et al., 1996). There is also a seasonal cycle apparent in the O₂ data, which is partly due to O₂ exchange with the terrestrial biosphere, but also caused by seasonality in the air-sea exchange of O₂. This seasonality in atmosphere-ocean O₂ exchange is due to three seasonal processes that reinforce each other: the

seasonal cycle in O₂ produced by the marine biosphere (see Equation 1.4); the seasonal cycle in ocean surface temperature, which affects the solubility of O₂ in seawater; and the seasonal cycle in ocean stratification, which affects the ventilation of O₂-depleted deeper waters (Bender and Battle, 1999; Keeling and Shertz, 1992).

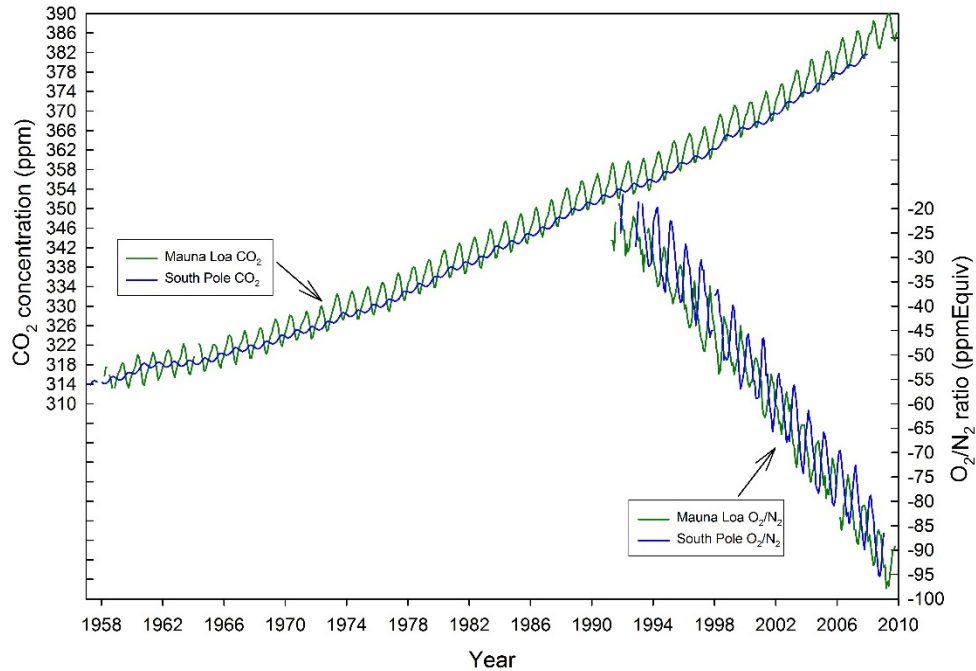
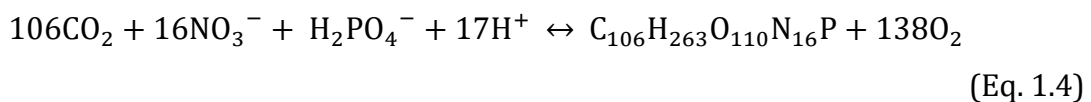


Figure 1.5. Atmospheric O₂ and CO₂ time series data from Mauna Loa, Hawaii, USA, and the South Pole, Antarctica; northern hemisphere data are shown in green, while southern hemisphere data are shown in blue. CO₂ data are from (Keeling et al., 2001) and O₂/N₂ data are from Ralph Keeling (personal communication; <http://scrippsco2.ucsd.edu/>, 2016).



where C₁₀₆H₂₆₃O₁₁₀N₁₆P represents the average composition of marine organic matter (Redfield et al., 1963).

Unlike CO₂, the O₂ seasonal cycle amplitude is similar in both the northern and southern hemispheres, because the atmospheric O₂ seasonal cycle reflects both land and ocean processes, and thus the larger proportion of land in the northern hemisphere is balanced by a larger proportion of ocean in the southern hemisphere. There is no ocean component in the CO₂ seasonal cycle, partly because the three reinforcing processes mentioned above for O₂ counteract each other for CO₂, thus seasonal CO₂ fluxes are relatively small, but more importantly, because the equilibration time between the ocean and atmosphere for CO₂ is slow (~ 1 year)

(Broecker and Peng, 1974), owing to the atmosphere-ocean distribution of CO₂ and the dissociation of CO₂ in seawater (Keeling et al., 1993; Keeling and Shertz, 1992; Manning and Keeling, 2006). In contrast, the O₂ equilibration time between the ocean and atmosphere is less than a month (Keeling and Shertz, 1992).

One can see from Fig. 1.5 that the decreasing trend in atmospheric O₂ is greater than the increasing trend in atmospheric CO₂; this is owing to the existence of two sinks for atmospheric CO₂ (the land and the ocean), but only one significant source for O₂ (the land). The oceans are also warming due to climate change; thus, it is expected that some O₂ is being released from the oceans to the atmosphere as a small long-term source (Keeling and Garcia, 2002; Manning and Keeling, 2006). Fig 1.5 also shows that the interhemispheric O₂ and CO₂ gradients are increasing over time. This is caused by the accelerating rate of fossil fuel emissions, combined with the fact that the majority of fossil fuel emissions are in the northern hemisphere, and the interhemispheric atmospheric mixing time is relatively slow (~ 1 year).

In order to isolate the ocean influences on atmospheric O₂ variability, it can be useful to use the tracer, Atmospheric Potential Oxygen (APO), which is defined as:

$$\text{APO} = \delta \frac{\text{O}_2}{\text{N}_2} - \alpha_B \text{CO}_2 \quad (\text{Eq. 1.5})$$

where α_B is the mean O₂:CO₂ ratio of terrestrial biosphere-atmosphere exchange (typically the global average value of -1.1 is used) (Stephens et al., 1998).

Note that Equation 1.5 is a simplified version of the equation from (Stephens et al., 1998), as it excludes the influences of CH₄ and CO oxidation on APO, which are negligible for most applications. APO is therefore conservative with respect to terrestrial biosphere processes, and thus mainly reflects air-sea exchange of O₂, N₂ and CO₂, with a minor influence from fossil fuel combustion.

The global O₂ and CO₂ budgets are as follows:

$$\Delta \text{O}_2 = \alpha_F F - \alpha_B B + Z \quad (\text{Eq. 1.6})$$

$$\Delta \text{CO}_2 = F - O - B \quad (\text{Eq. 1.7})$$

where ΔO_2 and ΔCO_2 are the respective changes (in moles) of O_2 and CO_2 in an air parcel, α_F is the mean $O_2:CO_2$ ratio of fossil fuel combustion, F is the atmospheric CO_2 source from fossil fuels, B is the atmospheric CO_2 sink due to the terrestrial biosphere, O is the atmospheric CO_2 sink due to the ocean, and Z is the net O_2 air-sea exchange (Manning and Keeling, 2006).

By substituting Equations 1.6 and 1.7 into Eq. 1.5, the global APO budget can also be determined (Manning and Keeling, 2006):

$$\Delta APO = (\alpha_F - \alpha_B)F + \alpha_B O + Z \quad (\text{Eq. 1.8})$$

F is relatively well known and Z can be estimated using oceanic heat fluxes and knowledge of air-sea O_2 out-gassing per Joule of heat flux (Bopp et al., 2002; Keeling and Garcia, 2002). Solving Equation 1.8 for O , and then substituting this into Eq. 1.7 to solve for B enables one to calculate the land and ocean carbon sinks. A graphical representation of calculating the land and ocean sinks using the method of (Keeling and Manning, 2014) is shown in Figure 1.6.

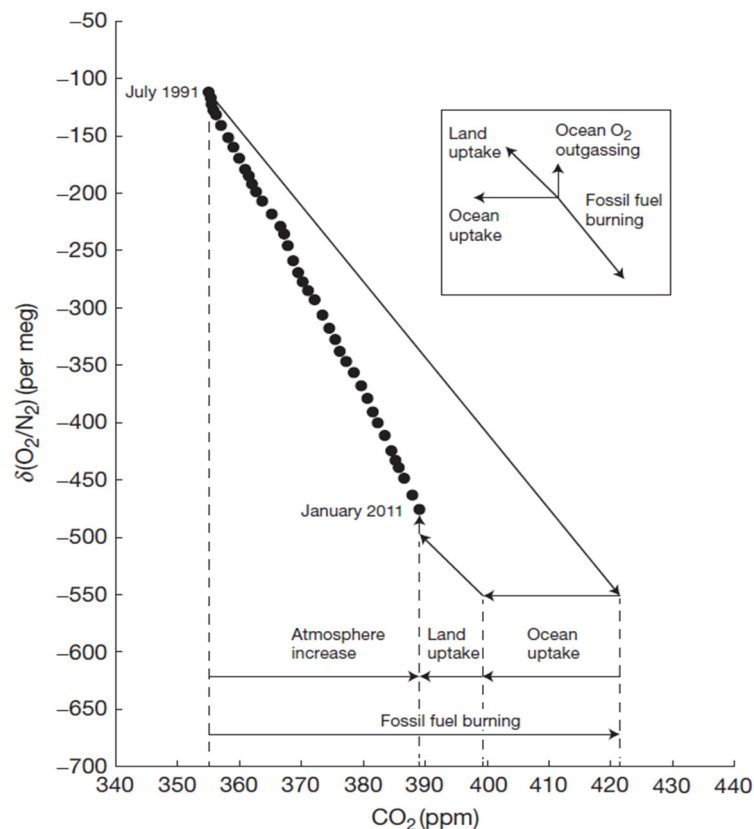


Figure 1.6. A graphical representation of calculating the land and ocean carbon sinks using the method of (Keeling and Manning, 2014). Black dots are 6-monthly averages of $\delta(O_2/N_2)$ and CO_2 from Alert, Canada, La Jolla, California, USA, and Cape Grim, Tasmania, Australia.

Calculation of the land and ocean carbon sinks using atmospheric O₂ and CO₂ measurements was first carried out by (Keeling and Shertz, 1992), and later by (Battle et al., 2000). The main limitation of the APO method for calculating the land and ocean carbon sinks is the large uncertainty in the ocean out-gassing term Z. Also, (Worrall et al., 2013) have suggested that the value of -1.1 for α_B might be over-estimated, and that this would cause an under-estimation of the global land and ocean carbon sinks; however, the carbon sinks calculated using a lower value of α_B are still within the uncertainties of the values calculated by (Battle et al., 2000).

In addition to quantifying the land and ocean carbon sinks, atmospheric O₂ and CO₂ measurements have been used to further scientific understanding about a wide range of atmospheric transport and oceanic processes. Early studies used atmospheric O₂ and CO₂ measurements to calculate ocean biological productivity (Keeling and Shertz, 1992), constrain the open ocean gas exchange velocity for O₂ (Keeling et al., 1998b), and test ocean model parametrisations of interhemispheric transport of O₂ and CO₂ in the oceans (Stephens et al., 1998).

Later studies have used atmospheric O₂ and CO₂ measurements to test the effectiveness of atmospheric transport models in representing the atmospheric rectifier effect (Blaine, 2005), and, in conjunction with atmospheric N₂O measurements, to infer Southern Ocean ventilation of water masses (Nevison et al., 2005). More recently, atmospheric O₂ and CO₂ measurements have been used to determine spatial and temporal features in oceanic air-sea O₂ fluxes, such as the effect of ENSO (El Niño – Southern Oscillation) on O₂ out-gassing from ventilation in equatorial regions using an atmospheric inversion model (Rödenbeck et al., 2008) and shipboard O₂ and CO₂ measurements in the Pacific (Tohjima et al., 2015), and the discovery of an oceanic O₂ sink in the northwest Pacific Ocean (Tohjima et al., 2012). (Nevison et al., 2012) used atmospheric N₂O and satellite-derived ocean colour data in conjunction with atmospheric O₂ and CO₂ measurements to separate out oceanic thermal, ventilation and biological productivity signals, and hence estimate net community production in the Southern Ocean. Using this separation technique, (Nevison et al., 2015) tested six Earth system models from the CMIP5 (Coupled Model Intercomparison Project Phase 5) project, and found that most of the models underestimated net primary productivity and/or ventilation, particularly in northern hemisphere oceans. In summary, concurrent atmospheric measurements of O₂ and CO₂ have proven to be a useful tool for learning about ocean carbon cycle processes,

and will continue to be important for monitoring and understanding current and future climate change.

1.3 The historical and current atmospheric oxygen measurement network

The very first atmospheric O₂ measurements were made simultaneously by Joseph Priestley and Carl Wilhelm Scheele in the late 1770s, with the first accurate atmospheric O₂ measurements to the percent level made by Humboldt and Gay-Lussac in the early 1800s, using a Volta eudiometer (Benedict, 1912). A study by (Benedict, 1912) found that atmospheric O₂ concentration was constant, a conclusion that was reinforced by (Machta and Hughes, 1970) many years later, although both studies were limited by the precision of the analytical techniques employed. Continuous measurements of atmospheric O₂ to the parts per million (ppm) precision level were first conducted by (Keeling, 1988) in Cambridge, Massachusetts, using an interferometric technique. (Keeling, 1988) observed strong anti-correlation between atmospheric O₂ and concurrent measurements of CO₂ caused by fossil fuel combustion processes, and recognised the potential of concurrent atmospheric O₂ and CO₂ measurements in studying the global carbon cycle. Since this first study, high-precision atmospheric measurements of O₂ and CO₂ have been made all over the world from a variety of platforms, including ships (e.g. Patecki and Manning, 2007; Stephens et al., 2003; Thompson et al., 2007; Tohjima et al., 2005), aircraft (e.g. Ishidoya et al., 2012a; Ishidoya et al., 2014; Sturm et al., 2005; Wofsy et al., 2011), and tall towers (e.g. Kozlova et al., 2008; Thompson et al., 2009), using several analytical techniques. Table 1.1 presents a record of all of the known published and unpublished high-precision atmospheric O₂ data, including flask sample data, continuous data, and data from campaigns.

Table 1.1. A record of the historical and current high-precision atmospheric O₂ data from flask samples, continuous measurements, and campaigns.

Time Period	Location	Flask/Continuous/ Other	Institution	Measurement Technique	Example Publications
Flask Measurements					
1978-2002	Cape Grim, Australia	Cape Grim Air Archive (Flask)	CSIRO ¹	Mass spectrometric	(Langenfelts, 2002)
1989, 1991- present	Alert, Canada	Flask	Scripps ²	Interferometric/ Mass spectrometric	(Manning, 2001)
2004-present			MPI-BGC ³	Mass spectrometric	-
1989-present	La Jolla, California, USA	Flask	Scripps	Interferometric/ Mass spectrometric	(Manning, 2001)
1998-2009			Princeton ⁴	Mass spectrometric	(Battle et al., 2006)
2010-present			NIES ⁵	GC/TCD ²²	-
1991-1994	Baring Head, New Zealand	Flask	Princeton	Mass spectrometric	(Bender et al., 1996)
1991-present	Cape Grim, Australia	Flask	Scripps	Interferometric/ Mass spectrometric	(Manning, 2001)
1991-2010			Princeton	Mass spectrometric	(Bender et al., 2005)
1996-2002			CSIRO	Mass spectrometric	(Langenfelts, 2002)
1991-present	Mauna Loa, Hawaii, USA	Flask	Scripps	Interferometric/ Mass spectrometric	(Manning, 2001)
1991-1993	Niwot Ridge, Colorado, USA	Flask	Scripps	Interferometric/ Mass spectrometric	(Manning, 2001)
1991-present	South Pole, Antarctica	Flask	Scripps	Interferometric/ Mass spectrometric	(Manning, 2001)
1992-1994	Macquarie Island, Australia	Flask	Scripps	Interferometric/ Mass spectrometric	(Manning, 2001)
1998-2010			Princeton	Mass spectrometric	(Bender et al., 2005)
1993-present	American Samoa, USA	Flask	Scripps	Interferometric/ Mass spectrometric	(Manning, 2001)
1993-2009			Princeton	Mass spectrometric	(Bender et al., 2005)
1993-2008	Barrow, Alaska, USA	Flask	Princeton	Mass spectrometric	(Bender et al., 2005)

Time Period	Location	Flask/Continuous/ Other	Institution	Measurement Technique	Example Publications
1993-present	Cape Kumukahi, Hawaii, USA	Flask	Scripps	Interferometric/ Mass spectrometric	(Manning, 2001)
1994-2007	Sable Island, Canada	Flask	Princeton	Mass spectrometric	(Battle et al., 2006)
1994-2009	Syowa, Antarctica	Flask	Princeton	Mass spectrometric	(Bender et al., 2005)
2000-present			Tohoku ⁶ /NIPR ⁷	Mass spectrometric	(Ishidoya et al., 2012b)
1995-present	Cold Bay, Alaska, USA	Flask	Scripps	Interferometric/ Mass spectrometric	(Manning, 2001)
1996-2009	Amsterdam Island, France	Flask	Princeton	Mass spectrometric	(Bender et al., 2005)
1996-present	Palmer Station, Antarctica	Flask	Scripps	Interferometric/ Mass spectrometric	(Manning, 2001)
1996-2007	Pacific Ocean (VOS ²⁴ and Ka'imimoana research vessel)	Flask	Princeton	Mass spectrometric	(Battle et al., 2006)
1997-present	Hateruma Island, Japan	Flask	NIES	GC/TCD	(Tohjima et al., 2008)
2008-2009			Princeton	Mass spectrometric	-
1998-2001, 2003-2008	Fyodorovskoye, Russia (aircraft)	Flask	CIO-RuG ⁸	Mass spectrometric	(van der Laan et al., 2014)
1999, 2003- 2005	Syktyvakar, Russia (aircraft)	Flask	CIO-RuG	Mass spectrometric	(van der Laan-Luijkx, 2010)
1998-present	Mace Head, Ireland	Flask	CIO-RuG	Mass spectrometric	(van der Laan-Luijkx et al., 2010a)
1998-present	Ochi-Ishi, Japan	Flask	NIES	GC/TCD	(Tohjima et al., 2008)
1999-present	Aobayama, Sendai, Japan	Flask	Tohoku	Mass spectrometric	(Ishidoya et al., 2003)
1999-present	Sendai, Japan and Sendai to Fukuoka/Sapporo, Japan (aircraft)	Flask	Tohoku	Mass spectrometric	(Ishidoya et al., 2012a)
1998-2001	Zotino, Siberia, Russia (aircraft)	Flask	CIO-RuG	Mass spectrometric	(van der Laan-Luijkx, 2010)
2000-present	Jungfrauoch, Switzerland	Flask	UBERN ⁹	Mass spectrometric	(Valentino et al., 2008)
2007-2014			CIO-RuG	Mass spectrometric	(van der Laan-Luijkx et al., 2013)

Time Period	Location	Flask/Continuous/ Other	Institution	Measurement Technique	Example Publications
2007-present			MPI-BGC	Mass spectrometric	(van der Laan-Luijkx et al., 2013)
2000-present	Lutjewad, The Netherlands	Flask	CIO-RuG	Mass spectrometric	(van der Laan-Luijkx et al., 2010a)
2001-present	Ny Ålesund, Svalbard, Norway	Flask	Tohoku/NIPR/AIST ¹⁰	Mass spectrometric	(Ishidoya et al., 2012b)
2001-present	Puy de Dôme, France	Flask	UBERN	Mass spectrometric	(Valentino et al., 2008)
2001-present	Pacific Ocean (VOS)	Flask	NIES	GC/TCD	(Tohjima et al., 2015)
2003-2004	Griffin Forest, UK (aircraft)	Flask	UBERN	Mass spectrometric	(Sturm et al., 2005)
2003-present	Ochsenkopf, Germany	Flask	MPI-BGC	Mass spectrometric	-
2003-present	Shetland Islands, UK	Flask	MPI-BGC	Mass spectrometric	(Kozlova, 2010)
2003-2006	Ubs Nur, Siberia, Russia (aircraft)	Flask	CIO-RuG	Mass spectrometric	(van der Laan-Luijkx, 2010)
2004-2006, 2011-2012	Takayama, Japan	Chamber and Branch Bag/Flask	AIST/Tohoku	Mass spectrometric	(Ishidoya et al., 2013)
2004-present		Flask			
2005-present	Białystok, Poland	Flask	MPI-BGC	Mass spectrometric	-
2006-2011, 2015 - present	F3 platform, North Sea	Flask	CIO-RuG	Mass spectrometric	(van der Laan-Luijkx et al., 2010a)
2006-present	Zotino, Siberia, Russia	Flask	MPI-BGC	Mass spectrometric	-
2007-2009	Cape Point, South Africa	Flask	Princeton	Mass spectrometric	-
2007-present	Cape Verde	Flask	MPI-BGC	Mass spectrometric	-
2011-present	Minamitorishima, Japan	Flask	NIES	GC/TCD	-
2012-present	Gobabeb, Namibia	Flask	MPI-BGC	Mass spectrometric	(Morgan et al., 2015)
2012-present	Western North Pacific (aircraft)	Flask	AIST/JMA-MRI ¹¹	Mass spectrometric	(Ishidoya et al., 2014)
2013-present	Halley Base, Antarctica	Flask	CIO-RuG	Mass spectrometric	-
2015-present	Kjølnes, Norway	Flask	MPI-BGC	Mass spectrometric	-
Continuous Measurements					
1999-present	Baring Head, New Zealand	Continuous	NIWA ¹² /Scripps	Paramagnetic	(Manning, 2001)

Time Period	Location	Flask/Continuous/ Other	Institution	Measurement Technique	Example Publications
1999-2004	Trinidad Head, California, USA	Continuous	Scripps	Paramagnetic	(Lueker et al., 2003)
2000-2003	Wisconsin, USA	Continuous	NCAR ¹³ /NOAA ¹⁴	Fuel cell	(Stephens et al., 2007a)
2002-2003, 2006-present	Ochsenkopf, Germany	Continuous	MPI-BGC	Fuel cell	(Thompson et al., 2009)
2004-present	Bern, Switzerland	Continuous	UBERN	Mass spectrometric	(Uglietti, 2009)
2005-present	Białystok, Poland	Continuous	MPI-BGC	Fuel cell	(Popa et al., 2010)
2005-present	Jungfrauoch, Switzerland	Continuous	UBERN	Fuel cell/ paramagnetic	(Uglietti, 2009)
2005-present	Ochi-Ishi, Japan	Continuous	NIES	GC/TCD	(Yamagishi et al., 2008)
2005-2006	Zotino, Siberia, Russia	Continuous	MPI-BGC	Paramagnetic	(Kozlova et al., 2008)
2006-present	Hateruma Island, Japan	Continuous	NIES	GC/TCD	(Minejima et al., 2012)
2007-2012	Aobayama, Sendai, Japan	Continuous	Tohoku/NIPR	Fuel cell	(Goto et al., 2013)
2007-present	Cape Verde	Continuous	Exeter ¹⁵ /MPI-BGC	Paramagnetic	-
2007-2014	Ivittuut, Greenland, Denmark	Continuous	LSCE ¹⁶	Paramagnetic	(Bonne, 2015)
2007-present	Pacific Ocean (VOS)	Continuous	NIES	GC/TCD	(Tohjima et al., 2015)
2008-present	Enoshima Island, Japan	Continuous	Tohoku/NIPR	Fuel cell	-
2008-2011	F3 platform, North Sea	Continuous	CIO-RuG	Fuel cell	(van der Laan-Luijkx et al., 2010b)
2008-present	Syowa, Antarctica	Continuous	Tohoku/NIPR	Fuel cell	-
2008-present	Weybourne, Norfolk, UK	Continuous	UEA ¹⁷	Fuel cell	(Wilson, 2013)
2012-present	Gobabeb, Namibia	Continuous	MPI-BGC	Fuel cell	(Morgan et al., 2015)
2012-present	Lutjewad, The Netherlands	Continuous	CIO-RuG	Fuel cell	(Van Leeuwen, 2015)
2012-present	Ny Ålesund, Svalbard, Norway	Continuous	Tohoku/NIPR	Fuel cell	(Goto et al., 2013)
2012-present	Southern Ocean (Laurence M. Gould research vessel)	Continuous	NCAR	Fuel cell	(Stephens et al., 2007a)
2012-2013	Takayama, Japan	Continuous	AIST	Fuel cell	(Ishidoya et al., 2015)

Time Period	Location	Flask/Continuous/ Other	Institution	Measurement Technique	Example Publications
2012-present	Tsukuba, Japan	Continuous	AIST	Mass spectrometric	(Ishidoya and Murayama, 2014)
2014-2015	Mace Head, Ireland	Continuous	UEA	Fuel cell	(Evans, 2016)
2014-present	Atlantic Ocean (VOS)	Continuous	UEA	Fuel cell	This thesis
2015-present	Minamitorishima, Japan	Continuous	AIST/JMA-MRI	Paramagnetic	-
2016-present	Halley Base, Antarctica	Continuous	UEA	Fuel cell	(Barningham, in prep)
2016 – present	Indian, Pacific and Southern Ocean (Investigator research vessel)	Continuous	CSIRO/NCAR	Fuel cell	-
2016-present	Tokyo (Yoyogi), Japan	Continuous	AIST/NDA ¹⁸	Paramagnetic	-
2006 - 2010	Harvard Forest, Massachusetts, USA	Continuous	Bowdoin College ¹⁹	Fuel cell	-
Campaign Measurements					
25-26 Oct 1986	Cambridge, Massachusetts, USA	Continuous	Harvard ²⁰	Interferometric	(Keeling, 1988)
1993	Biosphere 2, Arizona, USA	Chamber (Transient)	Columbia University ²¹ /Scripps	GC/TCD	(Severinghaus, 1995)
1993	Various USA sites (see thesis for details)	Chamber (Steady-state)	Columbia University/Scripps	Interferometric	(Severinghaus, 1995)
1995-2000	Bass Strait, Australia (aircraft)	Flask	CSIRO	Mass spectrometric	(Langenfels, 2002)
April-May 1998	Equatorial Pacific (Ka'imimoana research vessel)	Continuous	Scripps	VUV ²³	(Stephens et al., 2003)
1998 (1 month during summer)	Harvard Forest, Massachusetts, USA	Continuous	Scripps	VUV	(Stephens, 1999)
October 1998	Southern Ocean (Laurence M. Gould research vessel)	Continuous	Scripps	VUV	(Stephens et al., 2003)

Time Period	Location	Flask/Continuous/ Other	Institution	Measurement Technique	Example Publications
1999-2002, 2004, 2006, 2007	Sanriku, Japan (balloon)	Flask	AIST/Tohoku	Mass spectrometric	(Ishidoya et al., 2006)
2001-2002	Alice Holt, UK	Flask	UEA	Mass spectrometric	(Marca, 2004)
2002	Japan/Arctic stratosphere (aircraft)	Flask	Tohoku/NIES	Mass spectrometric	(Ishidoya et al., 2008)
2003, 2004	Southern Ocean (Tangaroa research vessel)	Continuous	NIWA	Fuel cell	(Thompson et al., 2008)
2004	Syowa, Antarctica (balloon)	Flask	Tohoku	Mass spectrometric	(Ishidoya et al., 2006)
2005	Hainich Forest, Germany	Flask	MPI-BGC	Mass spectrometric	(Kozlova, 2010)
2006	Northwest Atlantic Ocean (RRS Discovery)	Continuous	UEA	Fuel cell	(Patecki and Manning, 2007)
Apr-Jun 2008	Colorado, USA (HIAPER aircraft)	Flask & Continuous	NCAR/Scripps	Mass Spectrometer & VUV	-
2009-2011	Pole-to-Pole observations over the Pacific Ocean (HIAPER aircraft)	Flask & Continuous	NCAR/Scripps	Mass Spectrometer & VUV	(Bent, 2014)
2010, 2015	Taiki, Japan (balloon)	Flask	AIST/Tohoku	Mass spectrometric	(Ishidoya et al., 2013)
2012-present (Autumn only)	Northern North Pacific and the Arctic Ocean	Flask	AIST/NIPR	Mass spectrometric	(Ishidoya et al., 2016)
Sep 2013	North Atlantic Ocean (RRS ²⁵ James Cook)	Continuous	UEA	Fuel cell	This thesis
2014	The Netherlands (CCS mobile system)	Continuous	CIO-RuG	Fuel cell	(van Leeuwen and Meijer, 2015)
2014, 2015	Norwich, UK	Continuous	UEA	Fuel cell	This thesis; (Barningham, in prep)
Jan-Mar 2016	Southern Ocean (HIAPER aircraft)	Flask & Continuous	NCAR/Scripps	Mass Spectrometer & VUV	-
Aug 2016	Pole-to-Pole observations over the Pacific and	Flask & Continuous	NCAR/Scripps	Mass Spectrometer & VUV	-

Time Period	Location	Flask/Continuous/ Other	Institution	Measurement Technique	Example Publications
	Atlantic Oceans (HIAPER aircraft)				

¹Commonwealth Scientific and Industrial Research Organisation, Australia.

²Scripps Institution of Oceanography, San Diego, USA.

³Max Planck Institute for Biogeochemistry, Jena, Germany.

⁴Princeton University, Princeton, USA. Note that measurements were formerly of the University of Rhode Island, Kingston, USA.

⁵National Institute for Environmental Studies, Tsukuba, Japan.

⁶Tohoku University, Sendai, Japan.

⁷National Institute of Polar Research, Tokyo, Japan.

⁸Centre for Isotope Research, University of Groningen, Groningen, The Netherlands.

⁹University of Bern, Bern, Switzerland.

¹⁰National Institute of Advanced Industrial Science and Technology, Tsukuba, Japan.

¹¹Meteorological Research Institute, Japan Meteorological Agency, Tsukuba, Japan.

¹²National Institute of Water and Atmospheric Research, Wellington, New Zealand.

¹³National Center for Atmospheric Research, Boulder, USA.

¹⁴National Oceanic and Atmospheric Administration, Washington DC, USA.

¹⁵University of Exeter, Exeter, UK.

¹⁶Laboratoire des Sciences du Climat et de l'Environnement, Paris, France.

¹⁷University of East Anglia, Norwich, UK.

¹⁸National Defense Academy, Yokosuka, Japan.

¹⁹Bowdoin College, Brunswick, USA

²⁰Harvard University, Cambridge, USA.

²¹Columbia University, New York, USA.

²²Gas chromatograph equipped with a thermal conductivity detector

²³Vacuum-ultraviolet

²⁴Voluntary observing ship

²⁵Royal research ship

Note that Table 1.1 was last updated November 2016

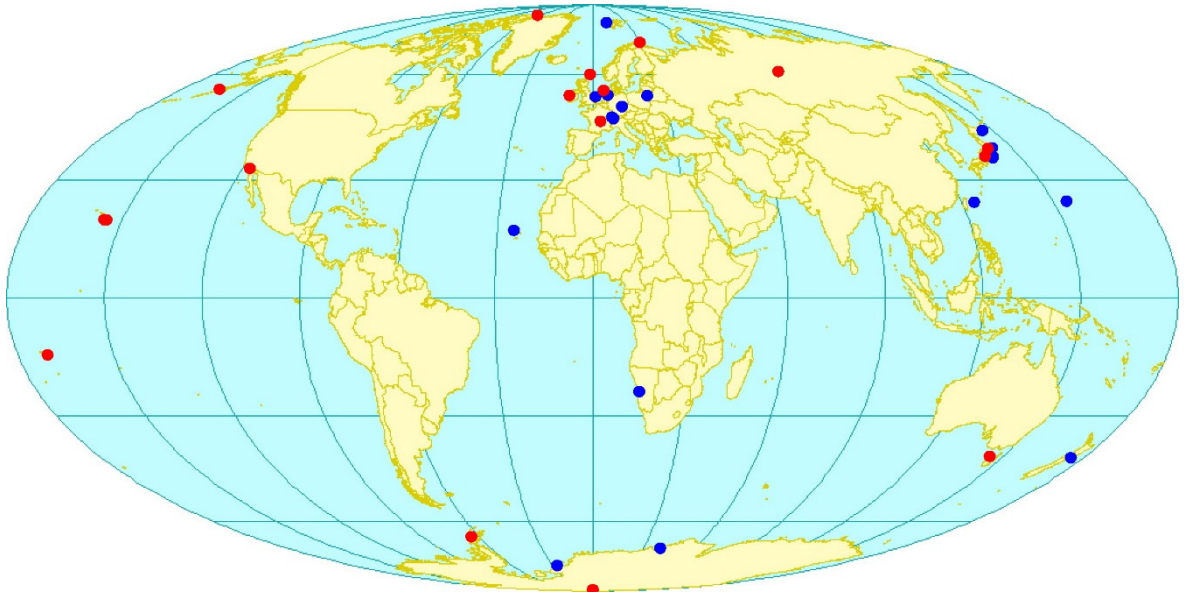


Figure 1.7. The current status of the global high-precision O_2 measurement network, as of May 2016. Note that aircraft and shipboard measurements are not shown for clarity. Stations where flask samples are collected are indicated by the red symbols, while continuous measurement stations are shown in blue. Stations that collect flask samples and make continuous measurements are shown as continuous stations (blue). Note that all atmospheric O_2 stations also make concurrent measurements of CO_2 .

There are only approximately 35 stations globally that measure atmospheric O_2 (as shown in Fig. 1.7), whereas there are more than 100 atmospheric CO_2 concentration measurement stations. Many regions of the world are significantly under-sampled for atmospheric O_2 , such as continental Asia, Antarctica and the Southern Ocean, Africa, South America, and the ocean interiors. Additionally, many of the routine atmospheric O_2 and CO_2 measurement stations shown in Fig. 1.7 collect flask samples only, where data are collected weekly or fortnightly. Although these data are useful for determining long-term trends, and seasonal and interannual variability, continuous measurements can also detect short-term variability on daily and hourly time scales, and can therefore provide a more detailed view of carbon cycle processes.

It is important to consider the value of atmospheric measurements for climate change research: it will never be possible to directly measure the air today again, other than right now. Thus, every day without atmospheric greenhouse gas measurements in a region represents a loss of data to future climate science that can never be recovered. Atmospheric O_2 and CO_2 measurements inform us on the current state of the atmosphere, and provide a ‘top-down’ view of fluxes in and out of the atmosphere, which is central to understanding future anthropogenic climate change.

Such measurements are also very useful for verifying emissions estimates from 'bottom-up' accounting approaches, which involve applying emissions factors to activity data, and then extrapolating over entire regions and countries, and can therefore be very inaccurate. (Stephens et al., 2011) state that our ability to infer surface CO₂ fluxes from atmospheric CO₂ data is currently hampered by a lack of data, and errors in atmospheric transport modelling. In addition, long-term observations of atmospheric O₂ and CO₂ are required for reliable estimates of the global carbon budget, since there are large interannual variations in air-sea fluxes (Nevison et al., 2008). The lack of high-precision, continuous atmospheric O₂ and CO₂ measurements in oceanic regions, particularly in the Atlantic sector, provides the main motivation for the research presented in this thesis.

1.4 Objective and specific aims of this research

The overall objective of this research was two-fold: firstly, to design, build, test and deploy a continuous, high-precision, atmospheric O₂ and CO₂ measurement system on board a commercial container ship travelling across the Atlantic Ocean; secondly, to develop a method for quantifying the fossil fuel component of atmospheric CO₂ using continuous O₂ and CO₂ measurements. The shipboard data presented in Chapter 4 of this thesis represent the first on-going continuous measurements of atmospheric O₂ and CO₂ over the Atlantic Ocean; hence, the dataset provides a valued contribution to the global atmospheric O₂ and CO₂ measurement network, and can be used to gain further insight into carbon cycle processes in the Atlantic Ocean, and how the Atlantic carbon sink may be changing over time. The specific aims of this research were:

1. To measure atmospheric O₂ and CO₂ across a wide latitudinal range over the Atlantic Ocean to assess latitudinal variability in both species.
2. To assess short-term (i.e. hourly to daily) variability in atmospheric O₂ and CO₂ over the Atlantic Ocean.
3. To measure atmospheric O₂ and CO₂ across the Atlantic Ocean for a period of one year or more, to assess seasonal variability in both species.
4. To investigate equatorial out-gassing of O₂ and CO₂ in the Atlantic Ocean, and compare to equatorial out-gassing signals in atmospheric O₂ and CO₂ data from the western Pacific Ocean.

5. To develop and test a method for quantifying fossil fuel CO₂ using APO data from Norfolk, UK.

1.5 Outline of thesis

The outline of this thesis is as follows. Chapter 2 presents the atmospheric O₂ and CO₂ measurement methodology used to obtain the data presented in the latter chapters. In Chapter 3, I present the first results from the shipboard measurement system when it was tested during a research cruise in the North Atlantic Ocean. In Chapter 4, I present atmospheric O₂, CO₂ and APO data measured on board the Cap San Lorenzo container ship, including meridional transects, seasonal variability, and annual mean distribution across the Atlantic Ocean. Chapter 5 demonstrates a new methodology for quantifying fossil fuel CO₂, using continuous APO data in Norfolk. Finally, In Chapter 6, I summarise the key research findings and conclusions, and outline future research directions and potential applications for high-precision atmospheric O₂ measurements.

References

- Baker, T. R., Phillips, O. L., Malhi, Y., Almeida, S., Arroyo, L., Di Fiore, A., Erwin, T., Higuchi, N., Killeen, T. J., Laurance, S. G., Laurance, W. F., Lewis, S. L., Monteagudo, A., Neill, D. A., Vargas, P. N., Pitman, N. C. A., Silva, J. N. M., and Martinez, R. V.: Increasing biomass in Amazonian forest plots, *Philosophical Transactions of the Royal Society of London Series B-Biological Sciences*, 359, 353-365, 2004.
- Barichivich, J., Briffa, K. R., Myneni, R. B., Osborn, T. J., Melvin, T. M., Ciais, P., Piao, S. L., and Tucker, C.: Large-scale variations in the vegetation growing season and annual cycle of atmospheric CO₂ at high northern latitudes from 1950 to 2011, *Global Change Biology*, 19, 3167-3183, 2013.
- Barningham, S. T.: Elucidating Southern Ocean carbon sink variability by establishing continuous atmospheric O₂ and CO₂ observations at the Halley Research station, Antarctica, Ph.D. thesis, School of Environmental Sciences, University of East Anglia, Norwich, UK, in prep.
- Battle, M., Bender, M. L., Tans, P. P., White, J. W. C., Ellis, J. T., Conway, T., and Francey, R. J.: Global carbon sinks and their variability inferred from atmospheric O₂ and $\delta^{13}\text{C}$, *Science*, 287, 2467-2470, 2000.
- Battle, M., Fletcher, S. E. M., Bender, M. L., Keeling, R. F., Manning, A. C., Gruber, N., Tans, P. P., Hendricks, M. B., Ho, D. T., Simonds, C., Mika, R., and Paplawsky, B.: Atmospheric potential oxygen: New observations and their implications for some atmospheric and oceanic models, *Global Biogeochemical Cycles*, 20, 2006.
- Bender, M. and Battle, M. O.: Carbon cycle studies based on the distribution of O₂ in air, *Tellus Series B-Chemical and Physical Meteorology*, 51, 165-169, 1999.

- Bender, M., Ellis, T., Tans, P., Francey, R., and Lowe, D.: Variability in the O₂/N₂ ratio of southern hemisphere air, 1991-1994: Implications for the carbon cycle, *Global Biogeochemical Cycles*, 10, 9-21, 1996.
- Bender, M. L., Ho, D. T., Hendricks, M. B., Mika, R., Battle, M. O., Tans, P. P., Conway, T. J., Sturtevant, B., and Cassar, N.: Atmospheric O₂/N₂ changes, 1993-2002: Implications for the partitioning of fossil fuel CO₂ sequestration, *Global Biogeochemical Cycles*, 19, 2005.
- Benedict, F. G.: *The Composition of the Atmosphere with Special Reference to its Oxygen Content*, Carnegie Institute of Washington, Washington, D.C., USA, 1912.
- Bent, J. D.: *Airborne Oxygen Measurements over the Southern Ocean as an Integrated Constraint of Seasonal Biogeochemical Processes*, Ph.D. thesis, University of California, San Diego, USA, 2014.
- Blaine, T. W.: *Continuous Measurements of Atmospheric Ar/N₂ as a Tracer of Air-Sea Heat Flux: Models, Methods and Data.*, Ph.D. thesis, University of California, San Diego, California, USA, 2005.
- Bonne, J. L.: *Continuous monitoring of the atmospheric composition in southern Greenland*, Ph.D. thesis, Laboratoire des sciences du climat et l'environnement, 2015.
- Bopp, L., Le Quere, C., Heimann, M., Manning, A. C., and Monfray, P.: Climate-induced oceanic oxygen fluxes: Implications for the contemporary carbon budget, *Global Biogeochemical Cycles*, 16, 2002.
- Broecker, W. S. and Peng, T. H.: Gas-exchange rates between air and sea, *Tellus*, 26, 21-35, 1974.
- Ciais, P., Sabine, C., Bala, G., Bopp, L., Brovkin, B., Canadell, J., Chhabra, A., DeFries, R., Galloway, J., Heimann, M., Jones, C., Le Quéré, C., Myneni, R. B., Piao, S., and Thornton, P.: Carbon and Other Biogeochemical Cycles. In: *Climate Change 2013: The Physical Science Basis. Contribution of Working Group I to the Fifth Assessment Report of the Intergovernmental Panel on Climate Change*, Stocker, T. F., Qin, D., Plattner, G.-K., Tignor, M., Allen, S. K., Boschung, J., Nauels, A., Xia, Y., Bex, V., and Midgley, P. M. (Eds.), Cambridge University Press, Cambridge, United Kingdom and New York, NY, USA, 2013.
- Cook, J., Nuccitelli, D., Green, S. A., Richardson, M., Winkler, B., Painting, R., Way, R., Jacobs, P., and Skuce, A.: Quantifying the consensus on anthropogenic global warming in the scientific literature, *Environmental Research Letters*, 8, 2013.
- Evans, B.: *Investigating terrestrial biosphere activity and fossil fuel CO₂ emissions with atmospheric potential oxygen measurements at Mace Head, Ireland*, M.Sci. thesis, School of Environmental Sciences, University of East Anglia, Norwich, UK, 2016.
- Fay, A. R. and McKinley, G. A.: Global trends in surface ocean pCO₂ from in situ data, *Global Biogeochemical Cycles*, 27, 541-557, 2013.
- Friedlingstein, P., Meinshausen, M., Arora, V. K., Jones, C. D., Anav, A., Liddicoat, S. K., and Knutti, R.: Uncertainties in CMIP5 Climate Projections due to Carbon Cycle Feedbacks, *Journal of Climate*, 27, 511-526, 2014.
- Goto, D., Morimoto, S., Ishidoya, S., Ogi, A., Aoki, S., and Nakazawa, T.: Development of a High Precision Continuous Measurement System for the Atmospheric O₂/N₂ Ratio and Its Application at Aobayama, Sendai, Japan, *Journal of the Meteorological Society of Japan*, 91, 179-192, 2013.
- Graven, H. D., Keeling, R. F., Piper, S. C., Patra, P. K., Stephens, B. B., Wofsy, S. C., Welp, L. R., Sweeney, C., Tans, P. P., Kelley, J. J., Daube, B. C., Kort, E. A., Santoni, G. W., and Bent, J. D.: Enhanced Seasonal Exchange of CO₂ by Northern Ecosystems Since 1960, *Science*, 341, 1085-1089, 2013.

- Gruber, N. and Keeling, C. D.: An improved estimate of the isotopic air-sea disequilibrium of CO₂: Implications for the oceanic uptake of anthropogenic CO₂, *Geophysical Research Letters*, 28, 555-558, 2001.
- Harries, J. E., Brindley, H. E., Sagoo, P. J., and Bantges, R. J.: Increases in greenhouse forcing inferred from the outgoing longwave radiation spectra of the Earth in 1970 and 1997, *Nature*, 410, 355-357, 2001.
- Heimann, M. and Meier-Reimer, E.: On the relations between the oceanic uptake of CO₂ and its carbon isotopes, *Global Biogeochemical Cycles*, 10, 89 - 110, 1996.
- Houghton, R. A.: Balancing the global carbon budget, *Annual Review of Earth and Planetary Sciences*, 35, 313 - 347, 2007.
- IPCC: Summary for policy makers. In: *Climate Change 2013: The Physical Science Basis. Contribution of Working Group I to the Fifth Assessment Report of the Intergovernmental Panel on Climate Change*, Stocker, T. F., Qin, D., Plattner, G.-K., Tignor, M., Allen, S. K., Boschung, J., Nauels, A., Xia, Y., Bex, V., and Midgley, P. M. (Eds.), Cambridge University Press, Cambridge, United Kingdom and New York, NY, USA, 2013.
- Ishidoya, S., Aoki, S., Goto, D., Nakazawa, T., Taguchi, S., and Patra, P. K.: Time and space variations of the O₂/N₂ ratio in the troposphere over Japan and estimation of the global CO₂ budget for the period 2000-2010, *Tellus Series B-Chemical and Physical Meteorology*, 64, 2012a.
- Ishidoya, S., Aoki, S., and Nakazawa, T.: High precision measurements of the atmospheric O₂/N₂ ratio on a mass spectrometer, *Journal of the Meteorological Society of Japan*, 81, 127-140, 2003.
- Ishidoya, S., Morimoto, S., Aoki, S., Taguchi, S., Goto, D., Murayama, S., and Nakazawa, T.: Oceanic and terrestrial biospheric CO₂ uptake estimated from atmospheric potential oxygen observed at Ny-Alesund, Svalbard, and Syowa, Antarctica, *Tellus Series B-Chemical and Physical Meteorology*, 64, 2012b.
- Ishidoya, S., Morimoto, S., Sugawara, S., Watai, T., Machida, T., Aoki, S., Nakazawa, T., and Yamanouchi, T.: Gravitational separation suggested by O₂/N₂, δ¹⁵N of N₂, δ¹⁸O of O₂, Ar/N₂ observed in the lowermost part of the stratosphere at northern middle and high latitudes in the early spring of 2002, *Geophysical Research Letters*, 35, 2008.
- Ishidoya, S. and Murayama, S.: Development of a new high precision continuous measuring system for atmospheric O₂/N₂ and Ar/N₂ and its application to the observation in Tsukuba, Japan, *Tellus Series B-Chemical and Physical Meteorology*, 66, 2014.
- Ishidoya, S., Murayama, S., Kondo, H., Saigusa, N., Kishimoto-Mo, A., and Yamamoto, S.: Observation of O₂:CO₂ exchange ratio for net turbulent fluxes and its application to forest carbon cycles, *Ecological Research*, 30, 225-234, 2015.
- Ishidoya, S., Murayama, S., Takamura, C., Kondo, H., Saigusa, N., Goto, D., Morimoto, S., Aoki, N., Aoki, S., and Nakazawa, T.: O₂:CO₂ exchange ratios observed in a cool temperate deciduous forest ecosystem of central Japan, *Tellus Series B-Chemical and Physical Meteorology*, 65, 2013.
- Ishidoya, S., Sugawara, S., Hashida, G., Morimoto, S., Aoki, S., Nakazawa, T., and Yamanouchi, T.: Vertical profiles of the O₂/N₂ ratio in the stratosphere over Japan and Antarctica, *Geophysical Research Letters*, 33, 2006.
- Ishidoya, S., Tsuboi, K., Matsueda, H., Murayama, S., Taguchi, S., Sawa, Y., Niwa, Y., Saito, K., Tsuji, K., Nishi, H., Baba, Y., Takatsuji, S., Dehara, K., and Fujiwara, H.: New Atmospheric O₂/N₂ Ratio Measurements over the Western North Pacific Using a Cargo Aircraft C-130H, *Sola*, 10, 23-28, 2014.
- Ishidoya, S., Uchida, H., Sasano, D., Kosugi, N., Taguchi, S., Ishii, M., Morimoto, S., Tohjima, Y., Nishino, S., Murayama, S., Aoki, S., Ishijima, K., Fujita, R., Goto, D.,

- and Nakazawa, T.: Ship-based observations of Atmospheric Potential Oxygen and regional air-sea O₂ flux in the Northern North Pacific and the Arctic Ocean, *Tellus B*, 68, 2016.
- Keeling, C. D., Chin, J. F. S., and Whorf, T. P.: Increased activity of northern vegetation inferred from atmospheric CO₂ measurements, *Nature*, 382, 146-148, 1996.
- Keeling, C. D., Mook, W. G., and Tans, P.: Recent trends in the ¹³C/¹²C ratio of atmospheric carbon dioxide, *Nature*, 277, 1979.
- Keeling, C. D., Piper, S. C., Bacastow, R. B., Wahlen, M., Whorf, T. P., Heimann, M., and Meijer, H. A. J.: Exchanges of atmospheric CO₂ and ¹³CO₂ with the terrestrial biosphere and oceans from 1978 to 2000 Global aspects, S. R. S., No. 01-06 (Ed.), Scripps Institution of Oceanography, San Diego, 2001.
- Keeling, C. D., Whorf, T. P., Wahlen, M., and Vanderpligt, J.: Interannual extremes in the rate of rise of atmospheric carbon-dioxide since 1980, *Nature*, 375, 666-670, 1995.
- Keeling, R. F.: Measuring correlations between atmospheric oxygen and carbon-dioxide mole fractions - a preliminary study in urban air, *Journal of Atmospheric Chemistry*, 7, 153-176, 1988.
- Keeling, R. F. and Garcia, H. E.: The change in oceanic O₂ inventory associated with recent global warming, *Proceedings of the National Academy of Sciences of the United States of America*, 99, 7848-7853, 2002.
- Keeling, R. F. and Manning, A. C.: 5.15 - Studies of Recent Changes in Atmospheric O₂ Content. In: *Treatise on Geochemistry (Second Edition)*, Holland, H. D. and Turekian, K. K. (Eds.), Elsevier, Oxford, 2014.
- Keeling, R. F., Manning, A. C., McEvoy, E. M., and Shertz, S. R.: Methods for measuring changes in atmospheric O₂ concentration and their application in southern hemisphere air, *Journal of Geophysical Research-Atmospheres*, 103, 3381-3397, 1998a.
- Keeling, R. F., Najjar, R. P., Bender, M., and Tans, P. P.: What atmospheric oxygen measurements can tell us about the global carbon cycle, *Global Biogeochemical Cycles*, 7, 37-67, 1993.
- Keeling, R. F. and Shertz, S. R.: Seasonal and interannual variations in atmospheric oxygen and implications for the global carbon cycle, *Nature*, 358, 723-727, 1992.
- Keeling, R. F., Stephens, B. B., Najjar, R. G., Doney, S. C., Archer, D., and Heimann, M.: Seasonal variations in the atmospheric O₂/N₂ ratio in relation to the kinetics of air-sea gas exchange, *Global Biogeochemical Cycles*, 12, 141-163, 1998b.
- Kozlova, E. A.: Multi-Species Atmospheric Continuous Measurements as a Tool to Study Changes in the Carbon Cycle, Ph.D. thesis, School of Environmental Sciences, University of East Anglia, Norwich, UK, 2010.
- Kozlova, E. A., Manning, A. C., Kisilyakhov, Y., Seifert, T., and Heimann, M.: Seasonal, synoptic, and diurnal-scale variability of biogeochemical trace gases and O₂ from a 300m tall tower in central Siberia, *Global Biogeochemical Cycles*, 22, 2008.
- Langenfelds, R. L.: Studies of the global carbon cycle using atmospheric oxygen and associated tracers, Ph.D. thesis, University of Tasmania, 2002.
- Le Quéré, C., Aumont, O., Bopp, L., Bousquet, P., Ciais, P., Francey, R., Heimann, M., Keeling, C. D., Keeling, R. F., Khesghi, H., Peylin, P., Piper, S. C., Prentice, I. C., and Rayner, P. J.: Two decades of ocean CO₂ sink and variability, *Tellus Series B-Chemical and Physical Meteorology*, 55, 649-656, 2003.
- Le Quéré, C., Raupach, M. R., Canadell, J. G., Marland, G., Bopp, L., Ciais, P., Conway, T. J., Doney, S. C., Feely, R. A., Foster, P., Friedlingstein, P., Gurney, K., Houghton, R. A., House, J. I., Huntingford, C., Levy, P. E., Lomas, M. R., Majkut, J., Metzl, N.,

- Ometto, J. P., Peters, G. P., Prentice, I. C., Randerson, J. T., Running, S. W., Sarmiento, J. L., Schuster, U., Sitch, S., Takahashi, T., Viovy, N., Van Der Werf, G. R., and Woodward, F. I.: Trends in the sources and sinks of carbon dioxide, *Nature Geoscience*, 2, 831-836, 2009.
- Liss, P. S. and Merlivat, L.: Air-sea gas exchange rates: Introduction and synthesis In: *The Role of Air-Sea Exchange in Geochemical Cycling* Buat-Menard, P. (Ed.), D Reidel Norwell, Massachusetts, USA, 1986.
- Lueker, T. J., Walker, S. J., Vollmer, M. K., Keeling, R. F., Nevison, C. D., Weiss, R. F., and Garcia, H. E.: Coastal upwelling air-sea fluxes revealed in atmospheric observations of O₂/N₂, CO₂ and N₂O, *Geophysical Research Letters*, 30, 2003.
- Machta, L. and Hughes, E.: Atmospheric Oxygen in 1967 to 1970, *Science*, 168, 1582- &, 1970.
- Manning, A. C.: Temporal variability of atmospheric oxygen from both continuous measurements and a flask sampling network: Tools for studying the global carbon cycle, Ph.D. thesis, Scripps Institution of Oceanography, University of California, 2001.
- Manning, A. C. and Keeling, R. F.: Global oceanic and land biotic carbon sinks from the scripps atmospheric oxygen flask sampling network, *Tellus, Series B: Chemical and Physical Meteorology*, 58, 95-116, 2006.
- Marca, A.: A new instrument for precise atmospheric O₂ measurements and its use to study uptake and release of O₂ and CO₂ by terrestrial vegetation, Ph.D. thesis, School of Environmental Sciences, University of East Anglia, Norwich, UK, 2004.
- Masiello, C. A., Gallagher, M. E., Randerson, J. T., Deco, R. M., and Chadwick, O. A.: Evaluating two experimental approaches for measuring ecosystem carbon oxidation state and oxidative ratio, *Journal of Geophysical Research-Biogeosciences*, 113, 2008.
- McGuire, A. D., Sitch, S., Clein, J. S., Dargaville, R., Esser, G., Foley, J., Heimann, M., Joos, F., Kaplan, J., Kicklighter, D. W., Meier, R. A., Melillo, J. M., Moore, B., Prentice, I. C., Ramankutty, N., Reichenau, T., Schloss, A., Tian, H., Williams, L. J., and Wittenberg, U.: Carbon balance of the terrestrial biosphere in the twentieth century: Analyses of CO₂, climate and land use effects with four process-based ecosystem models, *Global Biogeochemical Cycles*, 15, 183-206, 2001.
- Minejima, C., Kubo, M., Tohjima, Y., Yamagishi, H., Koyama, Y., Maksyutov, S., Kita, K., and Mukai, H.: Analysis of $\Delta O_2/\Delta CO_2$ ratios for the pollution events observed at Hateruma Island, Japan, *Atmospheric Chemistry and Physics*, 12, 2713-2723, 2012.
- Morgan, E. J., Lavric, J. V., Seifert, T., Chicoine, T., Day, A., Gomez, J., Logan, R., Sack, J., Shuuya, T., Uushona, E. G., Vincent, K., Schultz, U., Brunke, E. G., Labuschagne, C., Thompson, R. L., Schmidt, S., Manning, A. C., and Heimann, M.: Continuous measurements of greenhouse gases and atmospheric oxygen at the Namib Desert Atmospheric Observatory, *Atmospheric Measurement Techniques*, 8, 2233-2250, 2015.
- Nevison, C. D., Keeling, R. F., Kahru, M., Manizza, M., Mitchell, B. G., and Cassar, N.: Estimating net community production in the Southern Ocean based on atmospheric potential oxygen and satellite ocean color data, *Global Biogeochemical Cycles*, 26, 2012.
- Nevison, C. D., Keeling, R. F., Weiss, R. F., Popp, B. N., Jin, X., Fraser, P. J., Porter, L. W., and Hess, P. G.: Southern Ocean ventilation inferred from seasonal cycles of atmospheric N₂O and O₂/N₂ at Cape Grim, Tasmania, *Tellus, Series B: Chemical and Physical Meteorology*, 57, 218-229, 2005.

- Nevison, C. D., Mahowald, N. M., Doney, S. C., Lima, I. D., and Cassar, N.: Impact of variable air-sea O₂ and CO₂ fluxes on atmospheric potential oxygen (APO) and land-ocean carbon sink partitioning, *Biogeosciences*, 5, 875-889, 2008.
- Nevison, C. D., Manizza, M., Keeling, R. F., Kahru, M., Bopp, L., Dunne, J., Tiputra, J., Ilyina, T., and Mitchell, B. G.: Evaluating the ocean biogeochemical components of Earth system models using atmospheric potential oxygen and ocean color data, *Biogeosciences*, 12, 193-208, 2015.
- Pan, Y. D., Birdsey, R. A., Fang, J. Y., Houghton, R., Kauppi, P. E., Kurz, W. A., Phillips, O. L., Shvidenko, A., Lewis, S. L., Canadell, J. G., Ciais, P., Jackson, R. B., Pacala, S. W., McGuire, A. D., Piao, S. L., Rautiainen, A., Sitch, S., and Hayes, D.: A Large and Persistent Carbon Sink in the World's Forests, *Science*, 333, 988-993, 2011.
- Patecki, M. and Manning, A. C.: First results from shipboard atmospheric O₂ and CO₂ measurements over the North Atlantic Ocean, New York, 2007.
- Piao, S., Ciais, P., Friedlingstein, P., Peylin, P., Reichstein, M., Luyssaert, S., Margolis, H., Fang, J., Barr, A., Chen, A., Grelle, A., Hollinger, D. Y., Laurila, T., Lindroth, A., Richardson, A. D., and Vesala, T.: Net carbon dioxide losses of northern ecosystems in response to autumn warming, *Nature*, 451, 49-52, 2008.
- Popa, M. E., Gloor, M., Manning, A. C., Jordan, A., Schultz, U., Haensel, F., Seifert, T., and Heimann, M.: Measurements of greenhouse gases and related tracers at Bialystok tall tower station in Poland, *Atmospheric Measurement Techniques*, 3, 407-427, 2010.
- Redfield, A. B., Ketchum, B. H., and Richards, F. A.: The influence of organisms on the composition of seawater. In: *The Sea*, Hill, M. N. (Ed.), Wiley Interscience, New York, 1963.
- Riebesell, U., Schulz, K. G., Bellerby, R. G. J., Botros, M., Fritsche, P., Meyerhofer, M., Neill, C., Nondal, G., Oschlies, A., Wohlers, J., and Zollner, E.: Enhanced biological carbon consumption in a high CO₂ ocean, *Nature*, 450, 545-U510, 2007.
- Rödenbeck, C., Le Quere, C., Heimann, M., and Keeling, R. F.: Interannual variability in oceanic biogeochemical processes inferred by inversion of atmospheric O₂/N₂ and CO₂ data, *Tellus Series B-Chemical and Physical Meteorology*, 60, 685-705, 2008.
- Sarmiento, J. L., Gloor, M., Gruber, N., Beaulieu, C., Jacobson, A. R., Fletcher, S. E. M., Pacala, S., and Rodgers, K.: Trends and regional distributions of land and ocean carbon sinks, *Biogeosciences*, 7, 2351-2367, 2010.
- Severinghaus, J. P.: Studies of the terrestrial O₂ and carbon cycles in sand dunes gases and in Biosphere 2, Ph.D. thesis, Columbia University, 1995.
- Steinbach, J., Gerbig, C., Rodenbeck, C., Karstens, U., Minejima, C., and Mukai, H.: The CO₂ release and Oxygen uptake from Fossil Fuel Emission Estimate (COFFEE) dataset: effects from varying oxidative ratios, *Atmospheric Chemistry and Physics*, 11, 6855-6870, 2011.
- Stephens, B. B.: Field-based Atmospheric Oxygen Measurements and the Ocean Carbon Cycle, Ph.D. thesis, University of California, San Diego, California, USA, 1999.
- Stephens, B. B., Bakwin, P. S., Tans, P. P., Teclaw, R. M., and Baumann, D. D.: Application of a differential fuel-cell analyzer for measuring atmospheric oxygen variations, *Journal of Atmospheric and Oceanic Technology*, 24, 82-94, 2007a.
- Stephens, B. B., Gurney, K. R., Tans, P. P., Sweeney, C., Peters, W., Bruhwiler, L., Ciais, P., Ramonet, M., Bousquet, P., Nakazawa, T., Aoki, S., Machida, T., Inoue, G., Vinnichenko, N., Lloyd, J., Jordan, A., Heimann, M., Shibistova, O., Langenfelds, R. L., Steele, L. P., Francey, R. J., and Denning, A. S.: Weak northern and strong

- tropical land carbon uptake from vertical profiles of atmospheric CO₂, *Science*, 316, 1732-1735, 2007b.
- Stephens, B. B., Keeling, R. F., Heimann, M., Six, K. D., Murnane, R., and Caldeira, K.: Testing global ocean carbon cycle models using measurements of atmospheric O₂ and CO₂ concentration, *Global Biogeochemical Cycles*, 12, 213-230, 1998.
- Stephens, B. B., Keeling, R. F., and Paplawsky, W. J.: Shipboard measurements of atmospheric oxygen using a vacuum-ultraviolet absorption technique, *Tellus Series B-Chemical and Physical Meteorology*, 55, 857-878, 2003.
- Stephens, B. B., Miles, N. L., Richardson, S. J., Watt, A. S., and Davis, K. J.: Atmospheric CO₂ monitoring with single-cell NDIR-based analyzers, *Atmospheric Measurement Techniques*, 4, 2737-2748, 2011.
- Sturm, P., Leuenberger, M., Moncrieff, J., and Ramonet, M.: Atmospheric O₂, CO₂ and δC¹³ measurements from aircraft sampling over Griffin Forest, Perthshire, UK, *Rapid Communications in Mass Spectrometry*, 19, 2399-2406, 2005.
- Suess, H. E.: Radiocarbon Concentration in Modern Wood, *Science*, 122, 415-417, 1955.
- Takahashi, T., Sutherland, S. C., Sweeney, C., Poisson, A., Metzl, N., Tilbrook, B., Bates, N., Wanninkhof, R., Feely, R. A., Sabine, C., Olafsson, J., and Nojiri, Y.: Global sea-air CO₂ flux based on climatological surface ocean pCO₂, and seasonal biological and temperature effects, *Deep-Sea Research Part II-Topical Studies in Oceanography*, 49, 1601-1622, 2002.
- Takahashi, T., Sutherland, S. C., Wanninkhof, R., Sweeney, C., Feely, R. A., Chipman, D. W., Hales, B., Friederich, G., Chavez, F., Sabine, C., Watson, A., Bakker, D. C. E., Schuster, U., Metzl, N., Yoshikawa-Inoue, H., Ishii, M., Midorikawa, T., Nojiri, Y., Kortzinger, A., Steinhoff, T., Hoppema, M., Olafsson, J., Arnarson, T. S., Tilbrook, B., Johannessen, T., Olsen, A., Bellerby, R., Wong, C. S., Delille, B., Bates, N. R., and de Baar, H. J. W.: Climatological mean and decadal change in surface ocean pCO₂, and net sea-air CO₂ flux over the global oceans, *Deep-Sea Research Part II-Topical Studies in Oceanography*, 56, 554-577, 2009.
- Taylor, K. E., Stouffer, R. J., and Meehl, G. A.: An Overview of CMIP5 and the Experiment Design, *Bulletin of the American Meteorological Society*, 93, 485-498, 2011.
- Thompson, R. L., Gloor, M., Manning, A. C., Lowe, D. C., Rodenbeck, C., and Le Quere, C.: Variability in atmospheric O₂ and CO₂ concentrations in the southern Pacific Ocean and their comparison with model estimates, *Journal of Geophysical Research-Biogeosciences*, 113, 2008.
- Thompson, R. L., Manning, A. C., Gloor, E., Schultz, U., Seifert, T., Hansel, F., Jordan, A., and Heimann, M.: In-situ measurements of oxygen, carbon monoxide and greenhouse gases from Ochsenkopf tall tower in Germany, *Atmospheric Measurement Techniques*, 2, 573-591, 2009.
- Thompson, R. L., Manning, A. C., Lowe, D. C., and Weatherburn, D. C.: A ship-based methodology for high precision atmospheric oxygen measurements and its application in the Southern Ocean region, *Tellus Series B-Chemical and Physical Meteorology*, 59, 643-653, 2007.
- Tohjima, Y., Minejima, C., Mukai, H., Machida, T., Yamagishi, H., and Nojiri, Y.: Analysis of seasonality and annual mean distribution of atmospheric potential oxygen (APO) in the Pacific region, *Global Biogeochemical Cycles*, 26, 2012.
- Tohjima, Y., Mukai, H., Machida, T., Nojiri, Y., and Gloor, M.: First measurements of the latitudinal atmospheric O₂ and CO₂ distributions across the western Pacific, *Geophysical Research Letters*, 32, 2005.
- Tohjima, Y., Mukai, H., Nojiri, Y., Yamagishi, H., and Machida, T.: Atmospheric O₂/N₂ measurements at two Japanese sites: estimation of global oceanic and land

- biotic carbon sinks and analysis of the variations in atmospheric potential oxygen (APO), *Tellus Series B-Chemical and Physical Meteorology*, 60, 213-225, 2008.
- Tohjima, Y., Terao, Y., Mukai, H., Machida, T., Nojiri, Y., and Maksyutov, S.: ENSO-related variability in latitudinal distribution of annual mean atmospheric potential oxygen (APO) in the equatorial western Pacific, *Tellus B*, 67, 2015.
- Uglietti, C.: Understanding the Carbon Cycle through Atmospheric Carbon Dioxide and Oxygen Observations, Ph.D. thesis, Physikalisches Institut der Universität Bern, Switzerland, 2009.
- Valentino, F. L., Leuenberger, M., Uglietti, C., and Sturm, P.: Measurements and trend analysis of O₂, CO₂ and $\delta^{13}\text{C}$ of CO₂ from the high altitude research station Junfgraujoch, Switzerland - A comparison with the observations from the remote site Puy de Dome, France, *Science of the Total Environment*, 391, 203-210, 2008.
- van der Laan-Luijkx, I. T.: Atmospheric oxygen and the global carbon cycle: Observations from the new F3 North Sea platform monitoring station and 6 additional locations in Europe and Siberia, Ph.D. thesis, University of Groningen, The Netherlands, 2010.
- van der Laan-Luijkx, I. T., Karstens, U., Steinbach, J., Gerbig, C., Sirignano, C., Neubert, R. E. M., van der Laan, S., and Meijer, H. A. J.: CO₂, $\delta\text{O}_2/\text{N}_2$ and APO: observations from the Lutjewad, Mace Head and F3 platform flask sampling network, *Atmospheric Chemistry and Physics*, 10, 10691-10704, 2010a.
- van der Laan-Luijkx, I. T., Neubert, R. E. M., van der Laan, S., and Meijer, H. A. J.: Continuous measurements of atmospheric oxygen and carbon dioxide on a North Sea gas platform, *Atmospheric Measurement Techniques*, 3, 113-125, 2010b.
- van der Laan-Luijkx, I. T., van der Laan, S., Uglietti, C., Schibig, M. F., Neubert, R. E. M., Meijer, H. A. J., Brand, W. A., Jordan, A., Richter, J. M., Rothe, M., and Leuenberger, M. C.: Atmospheric CO₂, $\delta\text{O}_2/\text{N}_2$ and $\delta^{13}\text{CO}_2$ measurements at Jungfraujoch, Switzerland: results from a flask sampling intercomparison program, *Atmospheric Measurement Techniques*, 6, 1805-1815, 2013.
- van der Laan, S., van der Laan-Luijkx, I. T., Rodenbeck, C., Varlagin, A., Shironya, I., Neubert, R. E. M., Ramonet, M., and Meijer, H. A. J.: Atmospheric CO₂, $\delta(\text{O}_2/\text{N}_2)$, APO and oxidative ratios from aircraft flask samples over Fyodorovskoye, Western Russia, *Atmospheric Environment*, 97, 174-181, 2014.
- Van Leeuwen, C.: Highly precise atmospheric oxygen measurements as a tool to detect leaks of carbon dioxide from carbon capture and storage sites, Ph.D. thesis, University of Groningen, The Netherlands, 2015.
- van Leeuwen, C. and Meijer, H. A. J.: Detection of CO₂ leaks from carbon capture and storage sites with combined atmospheric CO₂ and O₂ measurements, *International Journal of Greenhouse Gas Control*, 41, 194-209, 2015.
- van Vuuren, D. P., Edmonds, J., Kainuma, M., Riahi, K., Thomson, A., Hibbard, K., Hurtt, G. C., Kram, T., Krey, V., Lamarque, J. F., Masui, T., Meinshausen, M., Nakicenovic, N., Smith, S. J., and Rose, S. K.: The representative concentration pathways: an overview, *Climatic Change*, 109, 5-31, 2011.
- Wilson, P. A.: Insight into the Carbon Cycle from Continuous Measurements of Oxygen and Carbon Dioxide at Weybourne Atmospheric Observatory, UK, Ph.D. thesis, University of East Anglia, Norwich, UK, 2013.
- Wofsy, S. C., Team, H. S., Cooperating Modellers, T., and Satellite, T.: HIAPER Pole-to-Pole Observations (HIPPO): fine-grained, global-scale measurements of climatically important atmospheric gases and aerosols, *Philosophical*

Transactions of the Royal Society a-Mathematical Physical and Engineering Sciences, 369, 2073-2086, 2011.

Worrall, F., Clay, G. D., Masiello, C. A., and Mynheer, G.: Estimating the oxidative ratio of the global terrestrial biosphere carbon, *Biogeochemistry*, 115, 23-32, 2013.

Yamagishi, H., Tohjima, Y., Mukai, H., and Sasaoka, K.: Detection of regional scale sea-to-air oxygen emission related to spring bloom near Japan by using in-situ measurements of the atmospheric oxygen/nitrogen ratio, *Atmospheric Chemistry and Physics*, 8, 3325-3335, 2008.

Chapter 2

Methodology of atmospheric O₂ and CO₂ measurement

2.1 Introduction and outline of chapter

The natural variability of O_2 in the atmosphere is very small (Keeling et al., 1993). In order to provide meaningful information for carbon cycle studies, atmospheric O_2 measurements must be precise enough to capture the long-term decrease in atmospheric O_2 , interannual variability in O_2 seasonal cycles, and small variations owing to short-term ‘events’ in ocean–atmosphere and biosphere–atmosphere exchange. Achieving precise measurements of atmospheric O_2 is very challenging, since O_2 is not a trace gas, and has an atmospheric background of $\sim 20.95\%$, that is, $\sim 209,500$ ppm. For example, to measure a change of 1 ppm O_2 against this background would require a relative O_2 measurement precision of 0.0005%. In comparison, to measure a change of 1 ppm CO_2 against an atmospheric background of 400 ppm CO_2 only requires a relative CO_2 measurement precision of 0.25%.

The World Meteorological Organization (WMO) recommendation for CO_2 measurement compatibility is ± 0.1 ppm (in the northern hemisphere, and ± 0.05 ppm in the southern hemisphere, owing to smaller variability in CO_2 over vast regions, such as the Southern Ocean) (Tans and Zellweger, 2013), where the term ‘measurement compatibility’ refers to the acceptable level of agreement required between two different field stations or laboratories when measuring the same air sample. Since atmospheric O_2 variability tends to be greater than atmospheric CO_2 variability on a mole per mole basis, an O_2 measurement compatibility equivalent to ± 0.4 ppm is recommended by the WMO (Brailsford, 2012). In order to meet these compatibility goals, the rule of thumb is that a measurement system’s analytical precision should not exceed half of the compatibility goal for a given species. Thus, the measurement imprecision for CO_2 and O_2 should not be greater than ± 0.05 ppm (± 0.025 ppm for southern hemisphere) and ± 0.2 ppm, respectively. With very careful gas handling protocols in place, routinely attaining a CO_2 measurement precision of ± 0.025 ppm is challenging but achievable. Routinely attaining an O_2 measurement precision of ± 0.2 ppm, however, is not yet an achievable goal for most laboratories and field stations making precise atmospheric O_2 measurements.

As mentioned in Section 1.2, atmospheric O_2 measurements are reported as $\delta(O_2/N_2)$ ratios (see Eq. 2.1), because O_2 mole fractions are sensitive to mole fraction changes in trace gases, such as CO_2 (Manning and Keeling, 2006). For example, an addition of 1 μmol CO_2 to 1 mole of air will result in a 0.2 μmol decrease in O_2 mole

fraction, because even though the amount of O₂ has remained the same, the total number of moles of air has increased. A 1 μmol addition of CO₂ to 1 mole of air will not have any influence on the δ(O₂/N₂) ratio, however (Manning and Keeling, 2006).

$$\delta \left(\frac{O_2}{N_2} \right) = \frac{\left(\frac{O_2}{N_2} \right)_{sam} - \left(\frac{O_2}{N_2} \right)_{ref}}{\left(\frac{O_2}{N_2} \right)_{ref}} \times 10^6 \quad (\text{Eq. 2.1})$$

where δ(O₂/N₂) is expressed in 'per meg' units, (O₂/N₂)_{sam} is the ratio of O₂ to N₂ in the air sample, and (O₂/N₂)_{ref} is the ratio of O₂ to N₂ in an arbitrary reference.

'Per meg' is a dimensionless unit equivalent to 0.001 per mil (Coplen, 2011), and refers to a one millionth change in a ratio (Keeling et al., 1993). Since N₂ is approximately four times as abundant as O₂ in the atmosphere, and variability in atmospheric N₂ is much smaller than variability in atmospheric O₂ (by several orders of magnitude), variations in N₂ are assumed to have a negligible effect on δ(O₂/N₂), with the exception of air-sea N₂ exchange caused by thermally-induced solubility changes (Manning and Keeling, 2006).

It is easy to incorrectly convert from per meg to ppm units, and vice versa, owing to the fact that O₂ is not a trace gas (Kozlova et al., 2008). For example, an addition of 1 μmol O₂ mole fraction to 1 mole of dry air will increase the δ(O₂/N₂) ratio by 4.77 per meg. However, since O₂ is not a trace gas, such an addition increases the total of number of moles, thus in actual fact, 0.79 ppm of O₂ has been added, not 1 ppm. In contrast, adding 1 μmol of a trace gas, such as CO₂, to 1 mole of dry air increases the mole fraction of that trace gas by almost exactly 1 ppm, but has no effect on the δ(O₂/N₂) ratio. Thus, the 'conversion factor' of 4.77 per meg per ppm applies when converting a change in δ(O₂/N₂) ratio to an equivalent change in trace gas mole fraction (Brailsford, 2012; Keeling et al., 1998). It should be emphasised that the conversion factor of 4.77 per meg per ppm should only be used where O₂ and CO₂ changes are anti-correlated with approximately the same magnitude (e.g. for land biosphere and fossil fuel related O₂ and CO₂ fluxes). For example, when calculating O₂:CO₂ ratios, or scaling O₂ and CO₂ plot axes to be visually comparable, a conversion factor of 4.77 can be used. In a few cases it may, however, also be useful to convert a change in δ(O₂/N₂) ratio to an equivalent change in O₂ mole fraction when there is no corresponding change in CO₂, in which case a conversion factor of 6.04 per meg per

ppm should be used (since $4.77/0.79 = 6.04$) (Brailsford, 2012). One such case would be when ‘spiking’ a high pressure cylinder of air with pure O₂, which causes a change in the total amount of O₂ within the cylinder with no corresponding change in CO₂. It can be seen from Eq. 2.2 below, that the conversion factor of 6.04 per meg per ppm will be applicable in any case where there is a change in O₂ but no change in CO₂. For any other conversions of changes in the $\delta(O_2/N_2)$ ratio in per meg to O₂ mole fraction in ppm, where O₂ and CO₂ are either not anti-correlated (e.g. in air-sea gas exchange), or are anti-correlated but with differing magnitudes (e.g. the long-term decrease in atmospheric O₂ and corresponding long-term increase in atmospheric CO₂), one should refer to Eq. 2.2 in order to calculate the correct ppm change in O₂ mole fraction. It should also be noted that a correction should be made to thermally-driven ocean influences on the $\delta(O_2/N_2)$ ratio resulting from corresponding thermally-driven ocean fluxes in N₂.

$$\delta \left(\frac{O_2}{N_2} \right) (\text{per meg}) = \frac{\delta O_2 (\text{ppm}) + (CO_2 - 363.29) \times S_{O_2}}{S_{O_2} \times (1 - S_{O_2})} \quad (\text{Eq. 2.2})$$

where S_{O_2} is the standard mole fraction of O₂ in dry air (a value of 0.2094 is used throughout this thesis, based on Tohjima et al. (2005)), and 363.29 is an arbitrary reference value for CO₂ in ppm, which is based on the mean CO₂ mole fraction of the reference cylinders that define ‘zero’ on the Scripps Institution of Oceanography (SIO) O₂ calibration scale (Stephens et al., 2007).

There are now six different analytical techniques for making precise measurements of atmospheric O₂. The first high precision atmospheric O₂ measurements were made using an interferometric technique, whereby small differences in the refractivity of light in air are correlated with atmospheric O₂ and N₂ changes, thus directly measuring the $\delta(O_2/N_2)$ ratio (Keeling, 1988). A second method, developed in the mid-1990s, employs isotope ratio mass spectrometry to simultaneously measure masses 29 (¹⁵N¹⁴N) and 32 (¹⁶O₂) (Bender et al., 1994), therefore also directly measuring the $\delta(O_2/N_2)$ ratio (more recently this technique is used to measure masses 28 and 32). Two further techniques were developed in the late 1990s: a paramagnetic technique, which utilises the paramagnetic properties of O₂ gas molecules to determine the O₂ mole fraction (Manning, 2001), and a vacuum ultraviolet absorption technique (VUV), whereby O₂ mole fraction is measured via the

absorption of ultraviolet radiation in a beam of light (Stephens et al., 2003). Unlike the interferometric and mass spectrometric methods, the paramagnetic and VUV methods do not measure the $\delta(\text{O}_2/\text{N}_2)$ ratio directly, but rather measure the change in O_2 mole fraction and calculate the $\delta(\text{O}_2/\text{N}_2)$ ratio using Eq. 2.2, assuming no change in N_2 .

The most recently developed analytical techniques for measuring atmospheric $\delta(\text{O}_2/\text{N}_2)$ ratios are a gas chromatographic technique, which measures the $\delta(\text{O}_2/\text{N}_2)$ ratio directly using a thermal conductivity detector (Tohjima, 2000), and a differential fuel cell technique, whereby changes in O_2 mole fraction are detected via an electrochemical reaction of O_2 with a lead electrolyte solution (Stephens et al., 2007), and no change in N_2 is assumed (similar to the paramagnetic and VUV techniques).

Each of the six analytical techniques has inherent advantages and disadvantages. For example, the paramagnetic and VUV techniques are the most precise; however, the paramagnetic technique is extremely sensitive to motion and vibrations (Manning, 2001), and is thus not suitable for mobile measurement systems and platforms, while the VUV is not currently commercially available, which limits its widespread application. For my shipboard O_2 and CO_2 measurement system, a differential fuel cell O_2 analyser was the optimum choice for several reasons. Firstly, although not as precise as the paramagnetic or VUV techniques, the differential fuel cell technique has the advantages of being suitable for mobile platforms, and being commercially available (and cheaper and smaller than a gas chromatograph or an isotope ratio mass spectrometer). The differential fuel cell technique also has the potential to be more precise than the interferometric, mass spectrometric, and gas chromatographic techniques, and has a proven record of being used successfully at sea on board research vessels (e.g. Patecki and Manning, 2007; Thompson et al., 2007).

This chapter describes in detail the shipboard atmospheric O_2 and CO_2 measurement system used to obtain the data that are discussed in the following chapters of this thesis. Section 2.2 of this chapter outlines the overall design of the O_2 and CO_2 measurement system, and describes in detail the key components, including the O_2 and CO_2 analysers and gas handling procedures. In Section 2.3, I describe the calibration procedures and present results from some calibration data. In Section 2.4, I describe the performance of the measurement system, in terms of repeatability and compatibility. Section 2.5 describes the data acquisition and software, and Section 2.6

presents the main methodological change that I implemented, which resulted in a significant improvement in the short-term O₂ precision. Section 2.7 presents the results from experimental testing of individual components of the measurement system in the laboratory and at sea, and Section 2.8 discusses the potential future improvements that could be made. Lastly, Section 2.9 provides a short summary of this chapter.

2.2 Measurement system design

2.2.1 Overview

The shipboard O₂ and CO₂ atmospheric measurement system, shown in Figure 2.1, is comprised of three units: drying, measurement, and calibration. The drying unit is where the sample air is drawn into the system and dried to less than 1 ppm of water, using a three stage drying system. The measurement unit comprises of a 'Li-6252' CO₂ analyser (Li-Cor Inc.) and an 'Oxzilla II' O₂ analyser (Sable Systems International Inc.) in series. The calibration unit comprises of an insulated 'Blue Box', which contains a suite of high pressure calibration cylinders filled with air of known O₂ and CO₂ mole fractions, as well as some high pressure reference air cylinders, known as 'Working Tanks' (WTs).

The measurement system was designed specifically with deployment on board a container ship in mind. The three units are easy to disconnect from each other, and can be separated into sections that are small enough to hand-carry and to fit through relatively small doorways and narrow staircases. Where possible, heavy equipment has been replaced with smaller or lighter alternatives. The custom-built software (see Section 2.5) has been modified to enhance the likelihood of the measurement system running continuously for 8 weeks (the time taken to complete a full 'Europe - South America - Europe' circuit) without any human intervention (since there is no remote access via an internet connection).

This chapter describes the O₂ and CO₂ measurement system as it is setup on board the Cap San Lorenzo, run by the Hamburg Süd Group. For details relating to the setup while on the RRS James Cook and when measuring from the University of East Anglia (UEA) roof, refer to Chapters 3 and 5 of this thesis, respectively. The O₂ and CO₂ measurement system was constructed mostly by myself, however, several other colleagues also contributed significantly. Their contributions are recognised in the acknowledgements of this thesis, and also in the text of this chapter.

2.2.2 O₂ and CO₂ analysers

Atmospheric CO₂ mole fraction is measured using a commercially available 'Li-6252' analyser (Li-Cor Inc.), which uses non-dispersive infrared (NDIR) technology. The Li-6252 is operated in differential mode, whereby the analyser measures the difference in the absorption of infrared radiation through two cells: a sample air cell, and a reference, or working tank (WT) air cell (see Figure 2.2). By measuring CO₂ differentially, any variability owing to changes in the ambient temperature or pressure in the room in which the equipment is situated will be largely mitigated by the differential CO₂ measurements (denoted as ΔCO_2), since each cell will respond to the temperature or pressure change in a similar way, and these differences will largely cancel out. In addition, measuring the CO₂ in the sample air relative to CO₂ in the WT air, where the WT air CO₂ mole fraction is close to the sample air CO₂ mole fraction, reduces the uncertainty in the 'span' variable of the CO₂ calibration, which improves the accuracy of the measurements (see Section 2.3.2).

The Li-6252 CO₂ analyser is specifically tuned to the 4.26 μm absorption band for CO₂ using a 150 nm optical filter, which enables the analyser to be insensitive to other infrared absorbing gases, and also insensitive to vibration, which is important for a shipboard measurement system (LI-COR Inc, 1996). According to the Beer-Lambert law, the infrared absorption in each cell is proportional to the CO₂ mole fraction of the cell gas. The calibrated CO₂ mole fraction in the sample and WT air is determined following the calibration procedures described in Section 2.3.2, which determine the span and baseline response of the Li-6252. In order to improve CO₂ accuracy, the Li-6252 internal plastic tubing was replaced with steam-cleaned stainless steel $1/16''$ (external diameter) tubing (VICI Valco Instruments Co. Inc.) by Lena Kozlova. Plastics are known to be semi-permeable to CO₂, and differentially permeable to O₂ and N₂, which will affect the O₂ measurements, because the Oxzilla II is located downstream of the Li-6252.

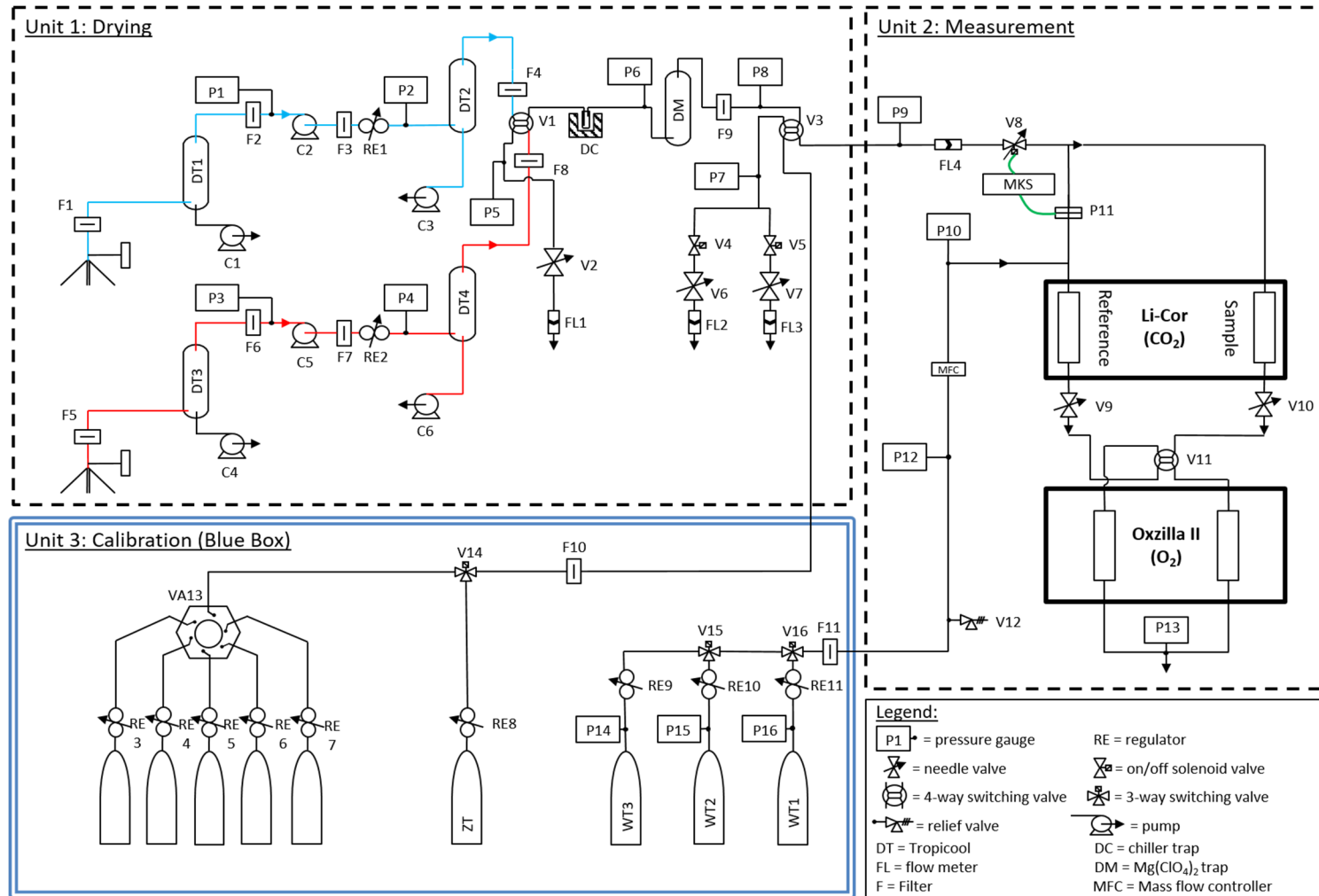


Figure 2.1. Gas handling diagram of shipboard O₂ and CO₂ measurement system. 'Red' and 'blue' inlet lines are coloured accordingly in Unit 1, and the green colouring in Unit 2 denotes electrical cables.

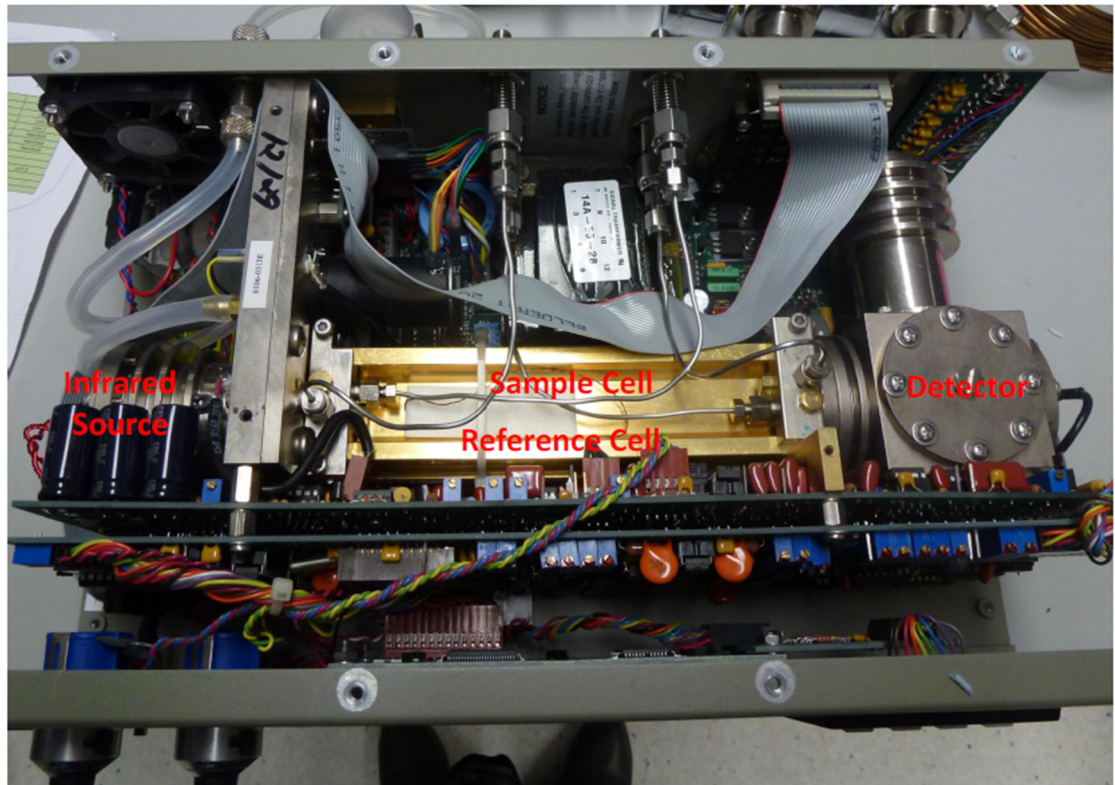
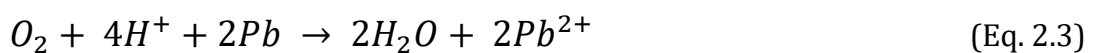


Figure 2.2. Photograph showing the inside of the Li-6252 CO₂ analyser.

Atmospheric O₂ mole fraction is measured using a commercially available 'Oxzilla II' analyser (Sable Systems International Inc.), which employs two 'MAX-250' lead fuel cell O₂ sensors (Maxtec Inc.). The MAX-250 is a galvanic type O₂ sensor, consisting of a lead anode, a gold oxygen cathode, and a weak acid electrolyte (Maxtec). A non-porous Teflon membrane, which is bonded to the gold cathode, separates the air from the weak acid electrolyte. O₂ from the air permeates the membrane and undergoes electrochemical reduction in the cell, according to:



This reaction generates a current that is directly proportional to the partial pressure of O₂ at the cell sensing surface (Maxtec). Ultimately, PbO is produced, which dissolves into the weak acid electrolyte until the electrolyte becomes saturated, at which point the lifetime of the cell expires. The MAX-250 O₂ sensor is sensitive to temperature changes, however, this is largely mitigated by employing active temperature control of the Oxzilla II housing, as well as differential sample/reference measurements analogous to that employed with the CO₂ analyser.

As with the Li-6252, the internal plastic tubing inside the Oxzilla II was replaced with steam-cleaned stainless steel $\frac{1}{8}$ " external diameter tubing (VICI Valco Instruments Co. Inc.), since differential permeation of O_2 and N_2 through plastic tubing will affect the O_2 mole fraction. Additionally, the outlet sample and WT tubing was joined immediately downstream of the fuel cells to minimise pressure differences between the two cells, and the internal SenSym SCX-Series pressure sensor (Sensortech GmbH; P13 in Fig. 2.1) was moved so that instead of measuring the ambient pressure inside the Oxzilla II housing, it measures the pressure at the point where the sample and WT tubing meet (see Fig 2.4), and thus is a more accurate indicator of fuel cell pressure. These Oxzilla II modifications were carried out by Phil Wilson.

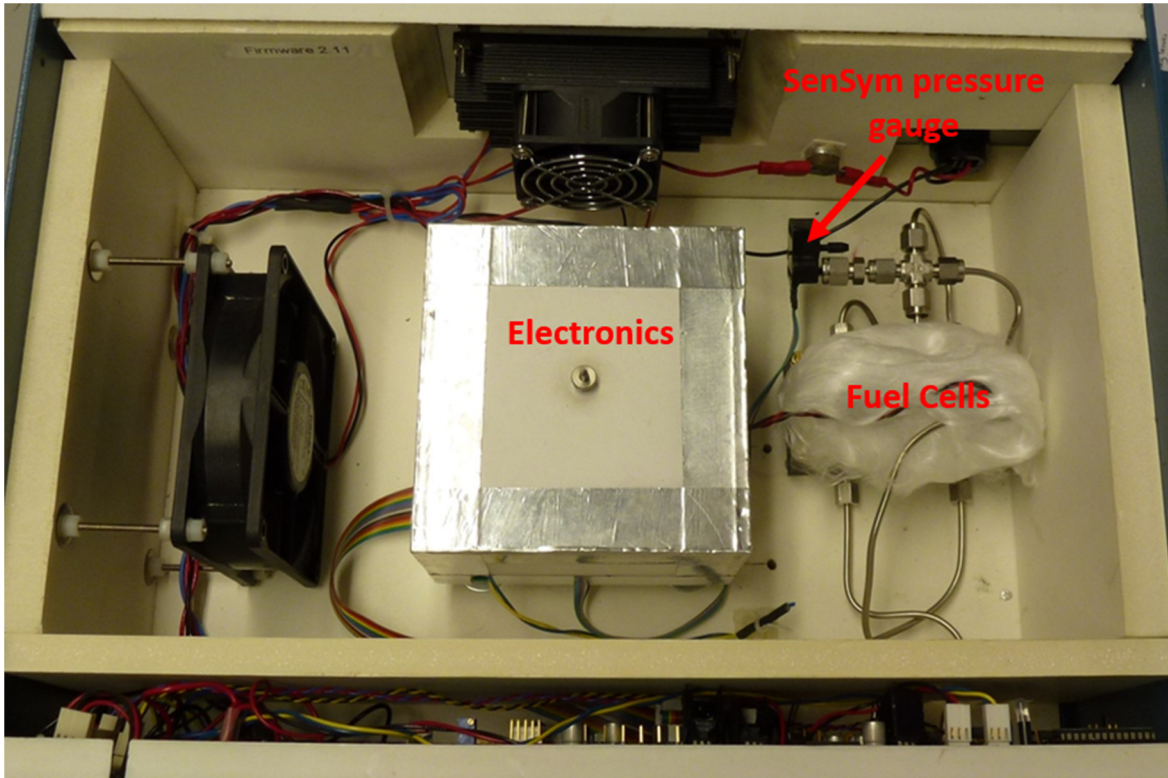


Figure 2.3. Photograph showing the inside of the Oxzilla II O_2 analyser. The MAX-250 fuel cells were originally housed inside the electronics box in the centre of the photograph, but were later moved to facilitate easier leak checking. The fuel cells have been insulated using glass wool. The inlet tubing shown in this photograph is $\frac{1}{8}$ " (external diameter), however, this was later replaced with $\frac{1}{16}$ " tubing to reduce the residence time of air in the tubing between V11 and the fuel cells (see Section 2.6 for details).

Similarly to the Li-6252 analyser, the Oxzilla II measures O_2 mole fraction differentially, i.e. the difference between the sample air O_2 and the WT air O_2 (denoted as ΔO_2), so that most sources of long-term drift in the signals are eliminated (Stephens et al., 2007). Unlike the Li-6252 analyser, however, a 4-way valve

(comprised of two miniature three-way solenoid valves; Numatics, TM series) upstream of the Oxzilla II analyser (V11 in Fig. 2.1) switches the sample and WT air between each fuel cell every 30 seconds. The 90% response time of the MAX-250 fuel cells is up to 15 seconds; hence, the first 15 seconds after every V11 switch is ignored (referred to as the 'sweepout time', which also allows for the tubing between V11 and the fuel cells to be flushed, or 'swept out'), with the latter 15 seconds from the 30 second switching period retained and averaged (see Fig. 2.4). Therefore, the ΔO_2 signal represents 'sample - WT' and 'WT - sample' alternately, and so a double differential, denoted as $\Delta\Delta O_2$, is calculated from three V11 switching periods of ΔO_2 , known as a 'jog' whereby:

$$\Delta\Delta O_2 = \frac{(A_1 - B_1) + (A_3 - B_3)}{2} - (B_2 - A_2) \quad (\text{Eq. 2.4})$$

where A_n refers to either the sample air or the WT air passing through fuel cell 'A', and B_n refers to either the WT air or the sample air passing through fuel cell 'B'. Each A_n or B_n is a 15 second average of 5 Hz measurements, taken after the 15 second sweepout is discarded within the jog. Both $(A_n - B_n)$ and $(B_n - A_n)$ represent ΔO_2 , where 'n' denotes the switching period number within the 'jog'. For example, if A_1 refers to sample air passing through fuel cell 'A', then B_1 refers to WT air passing through fuel cell 'B' at the same time, A_2 refers to WT air passing through fuel cell 'A' during the next switching period, B_2 refers to sample air passing through fuel cell 'B' in this next switching period, and so on. Effectively, $\Delta\Delta O_2$ linearly interpolates the fuel cell difference $(A_n - B_n)$ between switching periods 1 and 3, and subtracts this value from the fuel cell difference of switching period 2 $(B_2 - A_2)$. The uncertainty in $\Delta\Delta O_2$ is calculated by summing the $\pm 1\sigma$ standard deviations of the averages of the three ΔO_2 switching periods (1, 2, and 3) in quadrature. To illustrate the concept of $\Delta\Delta O_2$, both of the cell O_2 responses, ΔO_2 , and $\Delta\Delta O_2$ are shown graphically using real data in Fig. 2.4.

Switching the sample and WT air streams between the fuel cells in this manner helps to eliminate short-term drift on time scales longer than the switching period (30 seconds), and also increases the sensitivity of the O_2 measurements by a factor of two, since the amplitude of the difference between the fuel cells has doubled, but the 'noise' (short-term uncertainty) of the O_2 measurements for each fuel cell has remained the same (see Fig. 2.4).

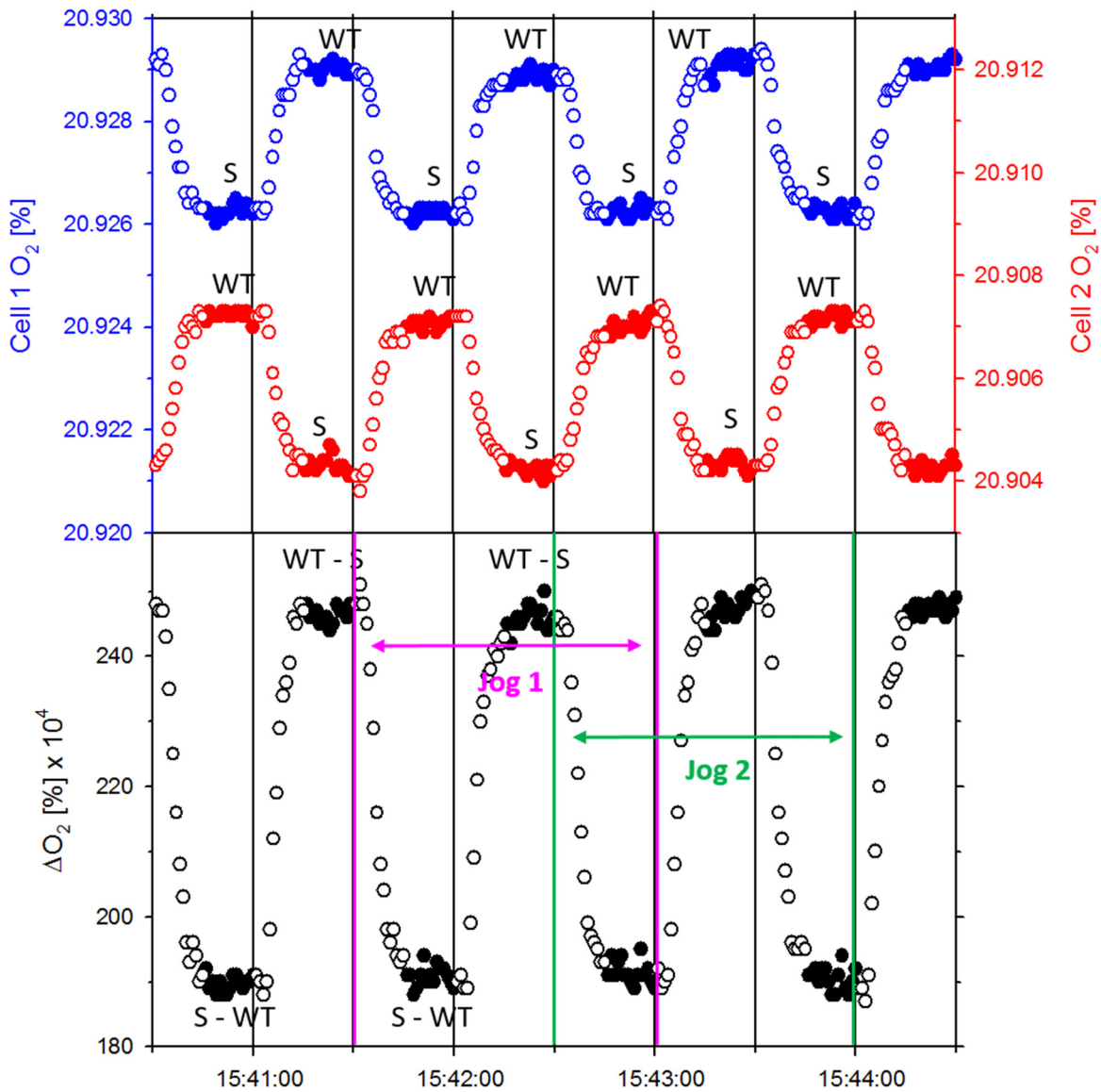


Figure 2.4 Top plot: Cell 1 (blue circles) and cell 2 (red triangles) O₂ responses in [%] (uncalibrated Oxzilla II response units). Unfilled symbols represent data during the sweepout time and are therefore ignored, while filled symbols represent data that are retained and averaged. 'WT' denotes periods when each cell is measuring the Working Tank, and 'S' denotes periods when each cell is measuring sample air. Bottom plot: ΔO_2 , in [%] $\times 10^4$ (uncalibrated Oxzilla II response units), where unfilled symbols represent data during the sweepout time, while filled symbols represent data that are retained and averaged. 'WT-S' denotes periods when ΔO_2 represents the Working Tank – air sample differential O₂ signal, and 'S-WT' denotes periods when ΔO_2 represents the air sample – Working Tank differential O₂ signal. $\Delta \Delta O_2$ is calculated every minute from three V11 switching periods of ΔO_2 (denoted by 'jog 1' and 'jog 2'), using Eq. 2.4. Note that $\Delta \Delta O_2$ could be calculated every 30 seconds, instead of every minute, however, this is not recommended, since successive jogs will share two thirds of the same data, instead of one third, and will therefore be less independent from each other.

2.2.3 Gas handling procedures

2.2.3.1 Air inlets

As shown in Fig. 2.1, the O₂ and CO₂ measurement system comprises of two identical air inlet lines, known as ‘blue line’ and ‘red line’, which are switched alternately at V1 every hour, where one line continues on to the analysers, and the other is purged to the room. Having two identical inlet lines has been shown to be very beneficial for diagnosing leaks (Chapter 3, Section 3.2.2), as well as faults in the system such as blockages in the first stage of the drying system or failed aspirated inlet fans.

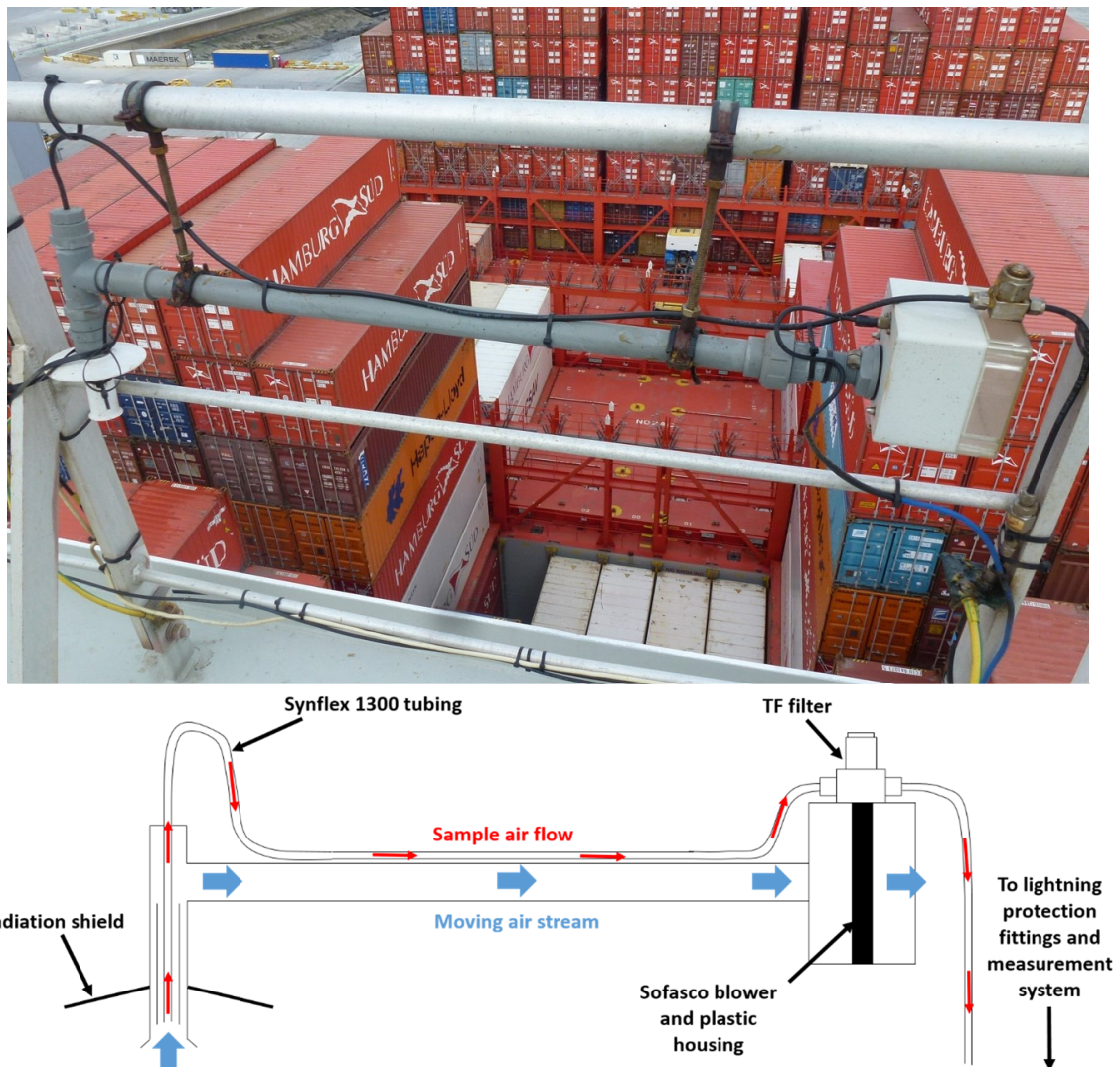


Figure 2.5. Photograph (top) and annotated diagram (bottom) of the ‘blue line’ Aspirated Air Inlet (AAI) on board the Cap San Lorenzo Hamburg Süd container ship. The air to be measured (red arrows; ‘sample air’) is sampled from a moving air stream (blue arrows), which is generated by a waterproof blower. The blower prevents temperature gradients forming at the air inlet, and thus minimises fractionation of O₂ relative to N₂ at the inlet (Blaine et al., 2006).

Air is sampled from the roof of the bridge of the Cap San Lorenzo Hamburg Süd container ship, which is about 40 m above sea level. Since $\delta(O_2/N_2)$ ratios are sensitive to fractionation of O_2 and N_2 molecules, the air is sampled using two aspirated air inlets (AAIs), which were custom-built at UEA by Dave Blomfield and Stuart Rix (see Fig. 2.5). As mentioned in (Blaine et al., 2006), the effects of thermal fractionation are substantially reduced when there is a steady flow of air; hence, the air is sampled with ¼" external diameter Synflex 1300 tubing from a moving air stream, which is generated with a Sofasco water-proof blower. Additionally, radiation shields are used to prevent direct sunlight warming the Synflex tubing. A Swagelok Company TF Series 40 μm filter is placed on each AAI to prevent particulate matter being drawn into the Synflex tubing.

Just downstream of each AAI, a Swagelok Company dielectric fitting (part number SS-8-DE-6) is placed in-line, as well as a bulkhead union, which is attached to a copper plate, and electrically grounded to the ship using thick copper earthing cable. These fittings act to protect the equipment in the event of a lightning strike. Synflex 1300 is comprised of two layers: an outer polyethylene based plastic coating, and an intermediate aluminium layer; hence, the inner aluminium layer is deliberately intersected at the dielectric and bulkhead union fittings using Serto AG sleeve inserts, in order to ground the Synflex tubing to the ship, and prevent electricity from travelling down the tubing to the equipment, should a lightning strike occur.

2.2.3.2 Drying system and diaphragm pumps

Air is drawn down from the bridge roof at 100 ml min^{-1} to the equipment, which is located in the ship's electronics server room two floors below the bridge. The residence time of air travelling from the AAIs to the first stage drying is calculated to be about 4 minutes (due to the relatively low flow rate), and the calculated pressure drop is less than 1 mbar (see Appendix A for details). The sample air makes two passes through the first stage drying, which is a Peltier element thermo-electric cooler (Tropicool XC3000A; DT1 – DT4 in Fig. 2.1), and is set at about 1°C , that is, just above freezing (see Fig 2.6). The Tropicool effectively performs the same function as a refrigerator (employed in other *in situ* O_2 and CO_2 systems, e.g. Kozlova and Manning, 2009), with the advantages of being both smaller and lighter than a refrigerator, and therefore more suitable for a shipboard measurement system.

The tubing from this point onwards is $1/8$ " external diameter steam-cleaned stainless steel Valco tubing, unless otherwise stated. The Tropicool consists of $1/2$ " external diameter stainless steel tubes (known as 'traps') filled with 4 mm diameter glass beads, which simultaneously aid the condensation of water vapour from the air stream by increasing the surface area within the trap, and also reduce the trap volume, and hence the residence time of air passing through the measurement system.

The Tropicool traps are drained by peristaltic pumping units (Masterflex model, Cole Parmer Instrument Co. Ltd.), with a 1 rpm rotation speed and employing 1.6 mm internal diameter tubing. The diaphragm sample pumps (C2 and C5 in Fig. 2.1), which draw the sample air down from the inlets, are located between the first and second passes of the air through the Tropicool; hence, the air in the first pass through the Tropicool is at a very slight vacuum, whilst the air in the second pass through the Tropicool is at elevated pressure, set to ~ 1650 mbar absolute by the forward pressure regulators (RE1 and RE2 in Fig. 2.1). The over-pressure of the air while it makes a second pass through the Tropicool helps to remove additional water vapour from the air stream, while the air passing through the first pass of the Tropicool prevents excess water from collecting in the pump heads. After each Tropicool trap and after both of the diaphragm pumps, Swagelok Company 2 μm FW Series filters are placed in-line, to prevent particles generated by the diaphragm pumps, or small pieces of glass from the Tropicool traps, from travelling through the tubing to the analysers.

As shown in Fig. 2.6, the two diaphragm pumps are situated near the top of Unit 1, and oriented upside-down, in order to prevent water collecting inside the pump heads and tubing, which caused pump failures during the JC090 cruise (see Chapter 3, Section 3.2.2). Initially, two KNF Neuberger Inc. KNF N05-ATI diaphragm pumps were used, but owing to the permanent failure of one of these pumps during the JC090 cruise (described in Section 3.2.2), an Air Dimensions Inc. J-Series Dia-Vac pump was used on the 'blue line' instead. To my knowledge, this brand of pump has never been used in a high precision O_2 and CO_2 atmospheric measurement system before, hence it was tested for possible O_2 or CO_2 artefacts (see Section 2.7).

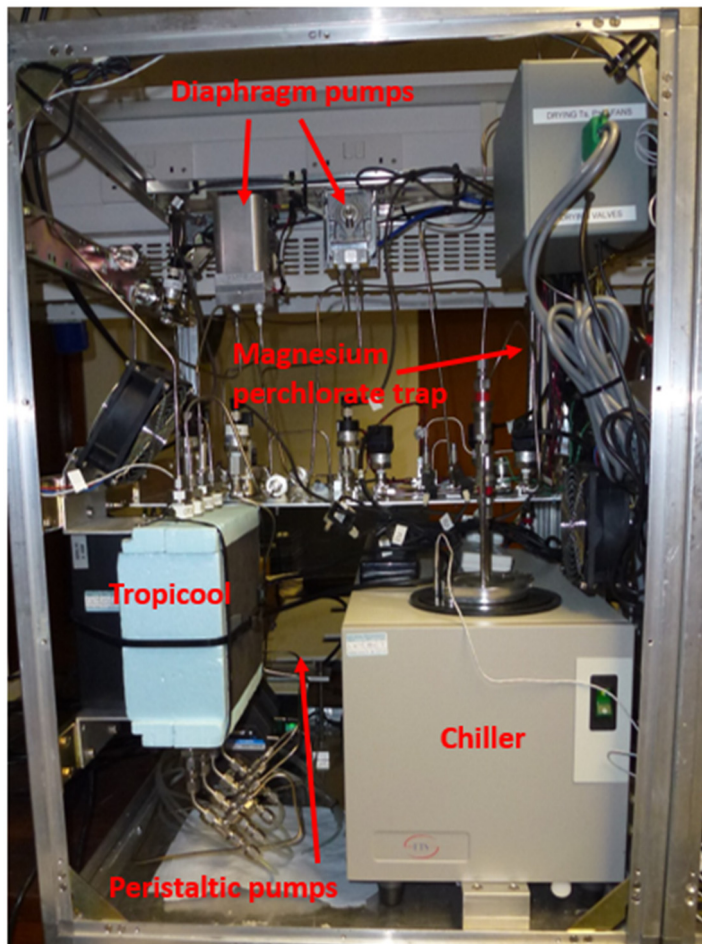


Figure 2.6. Photograph of Unit 1, the drying unit of the O_2 and CO_2 measurement system.

The second stage of drying employs an FTS VT255D model cryogenic cooler (SP Scientific), referred to here as a ‘chiller’ (DC in Fig. 2.1), which can achieve a dew point of about -50 to -55°C . The chiller has a 2 L bath, which is filled with a non-flammable coolant (H Galden ZT130, from Solvay Solexis Inc.; to comply with Hamburg Süd health and safety regulations), into which a tapered trap is placed, through which the sample air passes. As with the Tropicool traps, the chiller trap is filled with 4 mm diameter glass beads (see Fig. 2.7). However, unlike the Tropicool traps, the purpose of the glass beads is not to increase the surface area for condensation, and is also more subtle than simply reducing the residence time of the air within the trap. As described in (Manning, 2001), temperature gradients within the chiller trap will lead to fractionation of O_2 and N_2 , because O_2 will accumulate in the coldest part of the trap. Any small disturbance in flow rate or pressure (e.g. caused by unavoidable valve switches) will therefore cause a ‘spike’ of O_2 from the trap to travel downstream, and will create an artefact in the O_2 measurements. The recovery time from this O_2 spike has been shown to be proportional to the volume of

the chiller trap (Manning, 2001); hence, filling the trap with glass beads is an effective way of reducing the recovery time, which therefore reduces the amount of data that needs to be 'flagged' as not representing outside air.

Figure 2.7 also shows that the chiller trap has a ¼" external diameter dip tube on the outlet, but not on the inlet. The existence of the dip tube is important for ensuring that the sample air travels to the bottom of the trap, and therefore is sufficiently cooled by the chiller. The dip tube also helps to prevent air accumulating in the bottom of the trap without passing through to the analysers downstream. Placing the dip tube on the trap inlet results in the trap blocking only after a few days, because ice forms more easily at the top of the dip tube as the relatively 'wet' air enters the trap, owing to the relatively narrow internal diameter of the tube, whereas placing the dip tube on the trap outlet, the air entering the bottom of the dip tube is already relatively 'dry' compared to the air that entered the trap, and so the trap will not block for typically 6-8 weeks.

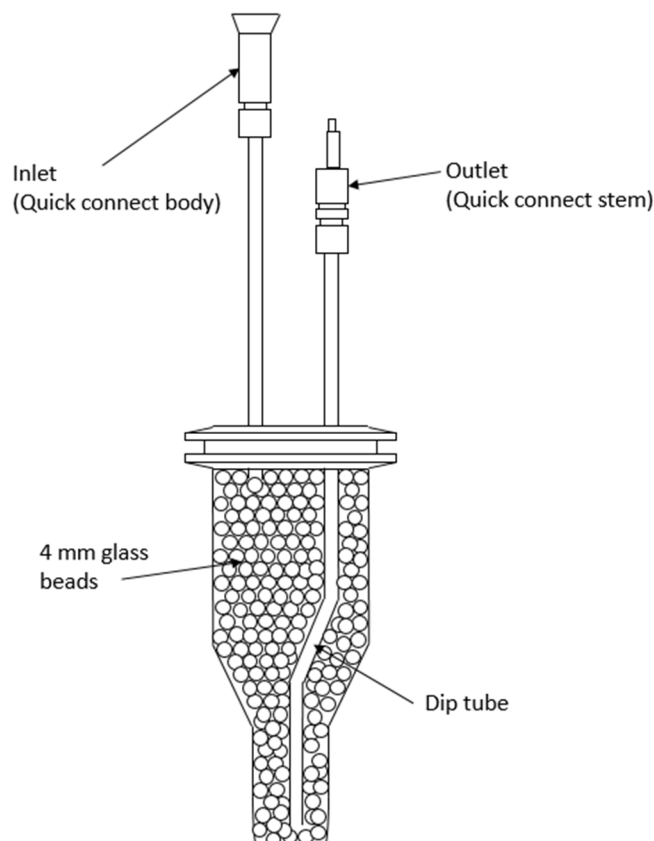


Figure 2.7. Annotated diagram of the chiller trap, showing the dip tube, glass beads, and Swagelok Company quick connect stem and body fittings, which prevent the trap mistakenly being replaced the wrong way around in the chiller.

The VT255D chiller in the second drying stage was chosen specifically for the ship system because it is much smaller and lighter than the VT490 and VT890 models

(which are used in other O₂ and CO₂ measurement systems). This, however, meant that a third stage of drying was required for the shipboard measurement system, since the -55°C level of drying achieved by the VT255D is not sufficient for high precision O₂ measurement (in contrast, the VT490 and VT890 achieve -90°C drying). For the third drying stage, a magnesium perchlorate trap is used (DM in Fig 2.1), because it is small, light, and has been shown to be effective in achieving a very low dew point of air. As shown in Fig. 2.1, another 2 µm Swagelok Company FW series filter is placed after the magnesium perchlorate trap, so that no particulate matter from the second and third stages of the drying system can travel downstream to the analysers.

Magnesium perchlorate, Mg(ClO₄)₂, is an oxidising agent, and therefore might introduce O₂ artefacts when the magnesium perchlorate reacts with water (Langenfelds, 2002). Using Mg(ClO₄)₂ as a drying agent when filling glass flasks has been shown to produce elevated O₂, compared to filling flasks using a cryogenic drying technique, owing to the pressure variations that occur during flask purging and filling (Shigeyuki Ishidoya, personal communication, 2013). Under conditions of strict pressure control, however, Mg(ClO₄)₂ has been shown to be a very stable drying agent for O₂ and CO₂, with negligible effects on the sample air compared to other drying methods (Langenfelds, 2002).

The purpose of employing a three stage drying system was to ensure that the sample air was dried to ≤1 ppm water vapour. The theoretical water content of air after the Tropicool and chiller, based on temperature and assuming sufficient residence time in the traps, is ~6900 ppm and ~20 ppm, respectively, the latter of which is acceptable for CO₂ measurement, but not for O₂. The water content of the sample air was measured after the Mg(ClO₄)₂ trap using a Meeco Inc. Accupoint 2 moisture transmitter, which showed that the three stage drying system was able to dry the sample air to <1 ppm water. As mentioned in (Stephens et al., 2007), the sample air should be dried to less than 1 ppm water in order to prevent dilution effects biasing the O₂ measurements (1 ppm water vapour content will dilute the O₂ mole fraction by 1.3 per meg). Ideally, one would also pass the WT and calibration gas air through the last drying stages, to ensure that both the sample air and cylinder air have exactly the same dew point, and are treated in the same way. With my shipboard system, however, this was deliberately not done, since the chiller and Mg(ClO₄)₂ traps could potentially cause 're-wetting' of the cylinder air. As such, it is important that the water content of the WT and calibration cylinders is measured when these cylinders

are filled in the Cylinder Filling Facility (CFF) at UEA, to ensure that the cylinders contain very dry air (<1 ppm water).

2.2.3.3 Flow and pressure control

Atmospheric O₂ and CO₂ measurements are very sensitive to changes in the flow rate and pressure of the air stream through the measurement system; hence it is very important to ensure that flow rate and pressure changes are minimal, and also that the flow rate and pressure of the sample air gas and WT gas are as similar as possible. The 'blue' and 'red' inlet lines were also designed to be as similar as possible, with the same fittings, components (with the exception of the diaphragm pumps, see Section 2.2.3.2), and similar tubing lengths between components, to ensure that the residence time of the air in each line was as similar as possible. Model A-10 (Wika Instruments Ltd.) pressure transmitters placed throughout the system ensure that pressures can be well matched (typically at a value between 1600 and 1700 mbar downstream of the sample pumps) between the red and blue inlet lines, and also help to diagnose problems, such as a blockage in the chiller trap, for example.

The pressure of the sample and WT air that passes through the analyser is balanced using a differential pressure transducer, known as a Baratron (MKS Instruments Inc., Baratron 223B; P11 in Fig. 2.1), which measures the pressure difference between the sample and WT air streams, and then adjusts the pressure of the sample side air to match the pressure of the WT air using a fast-response solenoid valve (MKS Instruments Inc., 248A; V8 in Fig. 2.1), via an MKS Instruments Inc. model 250E controller unit. These components are able to consistently maintain a pressure difference between the sample and reference sides of the shipboard measurement system of 0.00 ± 0.06 mbar for sustained periods of time (i.e. more than a week). A mass flow controller on the reference side of the system (MKS Instruments Inc., Type 1179A; MFC in Fig. 2.1) maintains the flow rate of the WT air at 100 mL min^{-1} , and also dictates the flow rate of the sample side of the system, via the 250E control system. A mass flow meter on the sample side of the system (McMillan Company Inc., model 50K; FL4 in Fig. 2.1) is used to diagnose the flow rate of the sample air, and to check that the sample and WT air flow rates are well matched. The needle valves (Brooks Instrument Co., model 8504; V9 and V10 in Fig. 2.1) downstream of the Li-6252 analyser help to ensure that the flows and pressures between the sample and reference sides are indeed well matched, by individually setting the restriction on

each side of the system, which will account for any differences in tubing length or other restrictions that might otherwise result in a flow rate discrepancy between the two sides of the system, even when the pressures are well-matched. Flow meters (Honeywell International Inc. AWM3000 Series; FL1, FL2 and FL3 in Fig. 2.1) and needle valves (Swagelok Company S Series metering valves) were also installed on the three purging lines, to prevent flow and pressure disruptions when either switching between the red and blue inlet lines, or between sample air and calibration cylinder air.

As mentioned in Section 2.2.2, the sample and WT air is switched between each Oxzilla II fuel cell using a four-way valve (consisting of two three-way miniature Numatics Inc., TM Series solenoid valves placed on a common manifold; V11 in Fig. 2.1). Originally, this valve had been placed inside the Oxzilla II housing, to reduce the length of tubing between V11 and the Oxzilla II cells, however, it was difficult to leak check the valve in this location, so I later mounted it on the front of the Oxzilla II housing (see Section 2.6). I inherited most of Unit 2 of the system from Phil Wilson, who assembled many of the components, fittings, and tubing during his Ph.D. project.

2.2.3.4. Temperature considerations and leaks

As well as strict pressure and flow control throughout the measurement system, it is also important to consider the effects of temperature changes. As mentioned in Section 2.2.2, the Li-6252 CO₂ analyser is sensitive to changes in room temperature, even though the effects of temperature changes are significantly mitigated by the differential measurement procedure. This was, therefore, my motivation in wanting to install the measurement system in an air conditioned room on board the Cap San Lorenzo, which the ship's captain allowed me to do. The O₂ mole fraction of the air from the calibration and WT cylinders is also sensitive to room temperature changes, owing to possible thermal fractionation of O₂ and N₂ within the cylinders. For this reason, the cylinders are stored in a thermally-insulated 'Blue Box' enclosure, which is resting on wooden planks and offset from all neighbouring walls to ensure air flow around all 6 sides of the box, and therefore prevents any thermal gradients from developing. The cylinders are all stored horizontally, not vertically, to prevent gravitational fractionation of O₂ and N₂, since O₂ molecules have a greater mass than N₂ molecules and will gravitate to the bottom of the cylinders over the long-term. Temperature gradients, even in an air

conditioned room, are much more likely to build up in the vertical coordinate than horizontally, which is also a key motivation for orienting the cylinders horizontally.

It is also important to ensure that there are no leaks anywhere in the measurement system, as this can cause biases in the O₂ and CO₂ measurements. For example, a leak upstream of the diaphragm pumps will likely result in room air contamination of the air stream. Such leaks are relatively easy to detect with my system by looking for differences in the CO₂ and O₂ mole fractions between the red and blue line air measurements. A leak downstream of the diaphragm pumps, where the sample and cylinder air is at a higher than ambient pressure, usually have a negligible effect on the CO₂ measurements, but can have a significant effect on the O₂ measurements, depending on the orifice size. An orifice with a diameter smaller than the average distance between collisions for a gas molecule will cause fractionation of O₂ molecules relative to N₂ molecules (via Knudsen diffusion), and can cause significant enrichment of O₂ in the measurement system tubing from even very small leaks (any leak where approximately >0.001% of the sample air is lost) (Keeling et al., 1998).

Consequently, the measurement system was thoroughly leak checked by conducting extensive 'pressure leak tests', whereby sections of the system were pressurised to about 1700 mbar and then sealed. A leak rate was then calculated by estimating the internal volume of the section, and recording any drop in pressure. The acceptable leak rate threshold for the main system tubing is 100 $\mu\text{L min}^{-1}$, corresponding to a loss of $\sim 0.001\%$ of the sample air when flow is set to 100 mL min^{-1} . For tubing directly attached to calibration and WT cylinders, where the internal pressure can be as high as 300 bar, the acceptable leak rate threshold is more stringent: 1 $\mu\text{L min}^{-1}$, which for a full 20 L cylinder, corresponds to a loss of 0.001% of the total volume of the cylinder over an ~ 3 hour period. Once deployed on the ship, leak checks were routinely performed using Snoop liquid leak detector (Swagelok Company), and by careful assessment of the mole fraction sample air data from the blue and red inlet lines (since an offset between red and blue line typically indicates a leak).

One final consideration in the gas handling procedures of high-precision O₂ and CO₂ measurement systems is to avoid the use of 'tee' junctions, where the incoming flow is divided into two branches. Tee junctions are employed frequently in atmospheric gas handling systems, since they can enable two different analysers to sample the same air stream, and can also be used to reduce the flow rate in the

system prior to analysis, which helps to keep the residence time of the air in the measurement system low, particularly if the inlet lines are long. However, (Manning, 2001) found that tees cause O₂/N₂ fractionation, because more O₂ molecules preferentially flow through one branch of the tee than N₂ molecules, even when pressure changes (e.g. caused by diaphragm pump pulsations) and temperature changes in the air stream are eliminated. Therefore, when designing the shipboard O₂ and CO₂ measurement system, I completely avoided the use of tee junctions. This meant that the flow rate had to be kept relatively low (100 ml min⁻¹) throughout the whole gas handling system, which is why the residence time of the air in the measurement system is quite long (~4 minutes).

2.3 Calibration procedures

2.3.1 Calibration gas handling

As mentioned in Section 2.2.3.4, all calibration and WT cylinders are stored horizontally in a thermally-insulated 'Blue Box' enclosure to prevent thermal and gravitational fractionation of O₂ and N₂. In total, there are three WT cylinders, four calibration cylinders, one Target Tank (see Section 2.3.3), and one Zero Tank (see Section 2.3.3). To ensure that the measurement system has enough WT gas to last for a full ship cycle (~8 weeks), three 10 L carbon fibre hoop wrap composite cylinders (Luxfer Gas Cylinders Ltd., model BFC 124-136-002) are used, which can be filled with up to 300 bar of pressure, as opposed to the 20 L aluminium alloy cylinders that are used for the other cylinders (Luxfer Gas Cylinders Ltd., model P3056Z), which can only be filled to 200 bar of pressure. Although the 10 L WT cylinders have an outer shell of carbon fibre, the internal lining is aluminium alloy 7060, which had never previously been used in the high precision atmospheric O₂ community (all other Luxfer cylinders used by the community are aluminium alloy 6061). Although the alloy is slightly different, the fact that the wetted material of these cylinders is still aluminium gave me confidence that they would be suitable for my application. In addition, in the manner they are used on my system, I would not be sensitive to small temporal variations in the O₂ or CO₂ content of the WT cylinders (in contrast, it is essential that the calibration and Target Tank cylinders are very stable with respect to O₂ and CO₂ content).

The WT cylinders are fitted with Rotarex C115 Series cylinder head valves, which are also rated up to 300 bar of pressure. Nevoc ISO 5145 cylinder valve fittings (Rotarex) and $1/16$ " steam cleaned nickel tubing (type 'Nickel 200', inside diameter 0.040 inch; VICI Valco Instruments Co. Inc.) are used to connect the WT cylinders to three Gas Arc Group Ltd. 2-stage regulators (model Spec-Master), which are rated to 300 bar of pressure, and are mounted outside of the 'Blue Box'. The 20 L cylinders have Rotarex cylinder head valves (Ceodeux D200 Series), which are connected to Model 14 (Scott Specialty Gases, now owned by Air Liquide S. A., and referred to as Calgaz model 1001) 2-stage high purity compact regulators (also mounted outside the Blue Box) via CGA-580 cylinder valve fittings and $1/16$ " nickel tubing.

All of the 20 L cylinders, except for the Zero Tank, are connected to a 6-port multi-position Valco valve (VICI Valco Instruments Co. Inc., part number EMTSD6MWE; VA13 in Fig. 2.1), which is controlled by the measurement system software (see Section 2.5). The Zero Tank is deliberately not connected to the Valco valve, to conserve the lifetime of the Valco valve rotor, since the Zero Tank air is passed through the system much more frequently than any of the air from the other 20 L cylinders. Instead, the Zero Tank regulator is connected to the outlet tubing from the Valco valve via a 3-way miniature solenoid valve (411 Series ASCO Valve Inc.; V14 in Fig. 2.1). The three WT cylinders are connected to the reference side of the measurement system via two 3-way solenoid valves (Numatics Inc., TM Series; V15 and V16 in Fig. 2.1). Three Wika A-10 pressure transducers are installed, monitoring the WT cylinder pressures, so that the switching of V15 and V16 can be controlled by the software, and that once a WT becomes empty, the next full WT will automatically be selected (see Section 2.5). Two Swagelok Company 2 μ m FW filters are placed downstream of V14 and V16, to prevent particulate matter, either from inside the cylinders, or from the valves themselves (owing to the moving parts), from travelling downstream to the analysers. In addition, a relief valve (Circle Seal Controls Inc., 500 Series; V12 in Fig. 2.1) prevents excessive pressure from damaging the mass flow controller (MFC in Fig. 2.1) and other components downstream, should one of the WT regulators malfunction.

2.3.2. Analyser calibration procedures

Calibrating both the Li-6252 CO₂ analyser and the Oxzilla II O₂ analyser using high pressure cylinders of air with known CO₂ and O₂ mole fractions is an essential

component of making high precision atmospheric O₂ and CO₂ measurements. The calibration routines described in this chapter allow the accuracy of the measurements to be quantified, where the term ‘accuracy’ really refers to the compatibility of the measurements to the central calibration laboratory for each species. The repeatability and compatibility of the analysers can also be quantified by measuring a ‘Target Tank’ cylinder (see Section 2.3.3), which does not pass through the inlet lines or the three-stage drying system of the measurement system, and therefore is mainly representative of the analysers’ precision only. Determining the compatibility of atmospheric measurements is important when combining more than one data set from different field stations or laboratories, and for long-term time series, where it is important that the measurements made at the beginning of the time series are compatible to those made later on from the same measurement system.

The Li-6252 CO₂ analyser has a non-linear response to CO₂. The internal electronics of the analyser cancel out much, but not all of this non-linearity; hence, a quadratic fit ($y = Ax^2 + Bx + C$) is required in order to appropriately fit the analyser response function. In order to determine the A, B and C coefficients, at least three calibration cylinders are required, however, it is preferable to have at least four calibration cylinders, so that the coefficient of determination (R^2) can be calculated, which indicates the ‘goodness’ of the fit. In addition, with at least four calibration cylinders, the data set is much less likely to be compromised should one of the cylinders become unstable with respect to its O₂ and/or CO₂ mole fraction.

The Oxzilla II O₂ analyser has a very linear response (i.e. of form $y = Bx + C$); hence, only two calibration cylinders are required, although it is again preferable to have at least three, as explained above. The shipboard measurement system has been calibrated with both four and three cylinders at various periods throughout its operation; analyses with four cylinders reveal that the R^2 values for the CO₂ response function are typically at least 0.999999 or higher, which indicates an extremely good fit. For O₂, the R^2 values are lower, with a mean value of 0.9990 ± 0.0015 (calculated from all of the accepted calibration runs while the ship was on board the Cap San Lorenzo during the period Sep 2014 to Oct 2015), which reflects the fact that atmospheric O₂ is more challenging to measure than atmospheric CO₂, with correspondingly greater uncertainties.

The calibration cylinders are filled with dry air to about 200 bar of pressure in the CFF at UEA, and are assigned ‘declared CO₂ values’ by measuring them against a suite of eight CO₂ standards, known as ‘Primary Secondary Standards’, or PSSes

(Manning, 2005). These measurements were carried out in UEA's Carbon Related Atmospheric Measurement (CRAM) laboratory, using an Ultramat 6F NDIR CO₂ analyser (Siemens Corp.). The first suite of ship calibration standards (used for all data up until Jan2016) were calibrated on the Scripps Institution of Oceanography (SIO) CO₂ scale, because this was the only scale available to me at the time the cylinders were prepared. From January 2016 onwards, the ship system was calibrated on the USA National Oceanic and Atmospheric Administration (NOAA) CO₂ scale, using a second suite of ship calibration standards. NOAA is the WMO Central Calibration Laboratory (CCL) for CO₂, and maintains the global CO₂ calibration scale (with the latest version called the 'X2007' scale). The eight PSSes were purchased from NOAA, and have been calibrated against the CCL 'Primary Standards' at NOAA. A comparison of TT air measured using both the Scripps and NOAA CO₂ calibration scales in the laboratory at UEA revealed that the scale offsets are small (<0.1 ppm), although not negligible, for the typical range of atmospheric CO₂ values measured today, which is in general agreement with a recent study (see Keeling et al., 2016).

My cylinders are also assigned 'declared O₂ values' in the CRAM laboratory by measuring them on a vacuum ultraviolet O₂ analyser (VUV; Stephens et al., 2003) against a suite of six O₂ PSSes received from SIO, who maintain the global O₂ calibration scale via their own suite of O₂ Primary Standards. The shipboard calibration cylinders are known as 'Working Secondary Standards' (WSSes), and are linked to the NOAA and SIO primary standards via the UEA PSSes.

The shipboard measurement system is calibrated fully every 23 hours. This measurement interval is specifically chosen to be offset from the number of hours in a single day, so that the timing of the calibration will slowly migrate earlier within each day, and therefore the calibrations will not be aliased by the specific ambient room conditions that might occur at any specific time of day.

The A and B coefficients of the quadratic fit for CO₂, and the B coefficient of the linear fit for O₂, may drift over time. Drifts in a fitting coefficient can have at least three possible explanations: firstly, that there has been a drift in the analyser sensitivity, or 'span' (that is, the sensitivity of the analyser's response to a given change in mole fraction); secondly, that there has been a drift in mole fraction in one or more of the calibration cylinders (i.e. the calibration scale has drifted); and thirdly, that a combination of span drift and calibration scale drift has occurred. With good calibration procedures, a drift in the analyser span will have no detrimental effects on the accuracy of the measurements, although a deterioration of the analyser's

sensitivity may mean that the measurement precision deteriorates. A drift in the calibration scale, however, has very severe implications on the accuracy of the measurements, depending on how large the drift is, and whether it can be corrected or not.

In order to determine the amount of drift in the calibration scale in ppm units, one must convert the units of the calibration coefficients, which are currently in ppm mV^{-2} (where mV denotes 'millivolt', which is the unit of the Li-6252 raw output) for A, and ppm mV^{-1} or ppmEq $\%^{-1}$ (where % is the unit of the Oxzilla II raw output and ppmEq denotes 'ppm equivalent O₂ units', which, in contrast to per meg units, is a measure of O₂ mole fraction) for the B coefficient of the CO₂ and O₂ fits, respectively. In order to separate calibration scale drift from analyser span drift, one would typically need information from additional long-term calibration standards, which are not used on my system. In an attempt to separate these two sources of drift without this information, and in order to quantify the drifts in meaningful units that are comparable to the WMO compatibility goals, I have converted the units of the coefficients into ppm for CO₂, and ppmEq for O₂, by multiplying the coefficients by a constant analyser response at an ambient mole fraction. To convert the A coefficient into ppm units, I have therefore multiplied by the square of the CO₂ analyser response. By multiplying by a constant analyser response, I am able to determine what the maximum possible drift in the calibration scale can be, if I assume that there has been no drift in the analyser span (or vice versa).

The calibration coefficient drifts in meaningful units are shown in Figure 2.8, and can be used to quantify what the maximum possible drift in the calibration scales has been, over the period of Sep 2014 to Sep 2015. The top panel of Fig 2.8 shows that the maximum CO₂ calibration scale drift from the A coefficient for CO₂ is about $-0.0002 \text{ ppm yr}^{-1}$, which is small enough to be insignificant. The maximum CO₂ calibration scale drift of the B coefficient for CO₂ is about 0.09 ppm yr^{-1} , however, Fig. 2.8 clearly shows that the majority of this change occurred between Nov 2014 and Feb 2015, when there were no data due to failure of a power supply in the electronics of the measurement system. It is very unlikely that the CO₂ calibration scale would drift substantially over a short period of time, and then remain relatively stable, which suggests that the step change shown in Fig. 2.8 is actually caused by a step change in the analyser span. When ignoring the 2014 data (blue regression line in middle panel of Fig. 2.8), the long-term change in the CO₂ B coefficient is about $-0.03 \text{ ppm yr}^{-1}$. Given that the lifetime of my WSS cylinders is about 18 months, this

indicates that the CO₂ calibration scale might potentially have drifted by a maximum of -0.045 ppm over the WSS lifetime (assuming no analyser response drift), which is very nearly significant, because this drift is only slightly smaller than the WMO compatibility goal for southern hemisphere CO₂. Therefore, ideally, it is important to retain enough gas within the WSSes to measure them against the CO₂ PSSes in the CRAM laboratory at the end of their use, so that any drift in the cylinders can be quantified. The B coefficient for O₂ indicates that there has been a maximum possible O₂ calibration scale drift of about 0.4 ppmEq yr⁻¹, or 2.4 per meg yr⁻¹, which is significant, because it is larger than the WMO compatibility goal for O₂; hence, ideally, it is also important to measure the calibration cylinders against the O₂ PSSes in the CRAM laboratory at the end of their lifetime, to quantify this potential drift in the O₂ calibration scale.

The C coefficient of both the CO₂ and O₂ calibration fits defines the WT CO₂ and O₂ mole fraction in ppm and ppmEq units respectively. It has been shown previously that WT O₂ mole fractions tend to decrease as the pressure inside the cylinder decreases, most likely owing to preferential desorption of N₂ relative to O₂ from the inside walls of the cylinders (Kozlova and Manning, 2009; Manning, 2001). CO₂ mole fraction, by contrast, has been shown to increase with decreasing cylinder pressure by some colleagues (e.g. Leuenberger et al., 2015), but, for cylinders oriented horizontally such as I have employed, this effect appears to disappear, and possibly even reverse. That is, for horizontal cylinders, CO₂ mole fraction possibly decreases slightly with decreasing pressure (Kozlova and Manning, 2009), but the effect, if real, is at least an order of magnitude less than the increase seen in vertically oriented cylinders. Figure 2.9 shows the WT CO₂ and O₂ mole fractions with time, for multiple WT cylinders on my system, as determined by the WSS calibrations that are run every 23 hours. There is no obvious consistent directional drift in the CO₂ mole fraction over the lifetime of the WTs, and in general, the changes in CO₂ mole fraction between WSS calibrations are small. The WT CO₂ mole fraction is in fact re-defined every 4 hours during the Zero Tank runs (see Section 2.3.3), which are not shown in Fig. 2.9; in general, the variability in CO₂ mole fraction inside the WTs during these 4 hour periods is not significant.

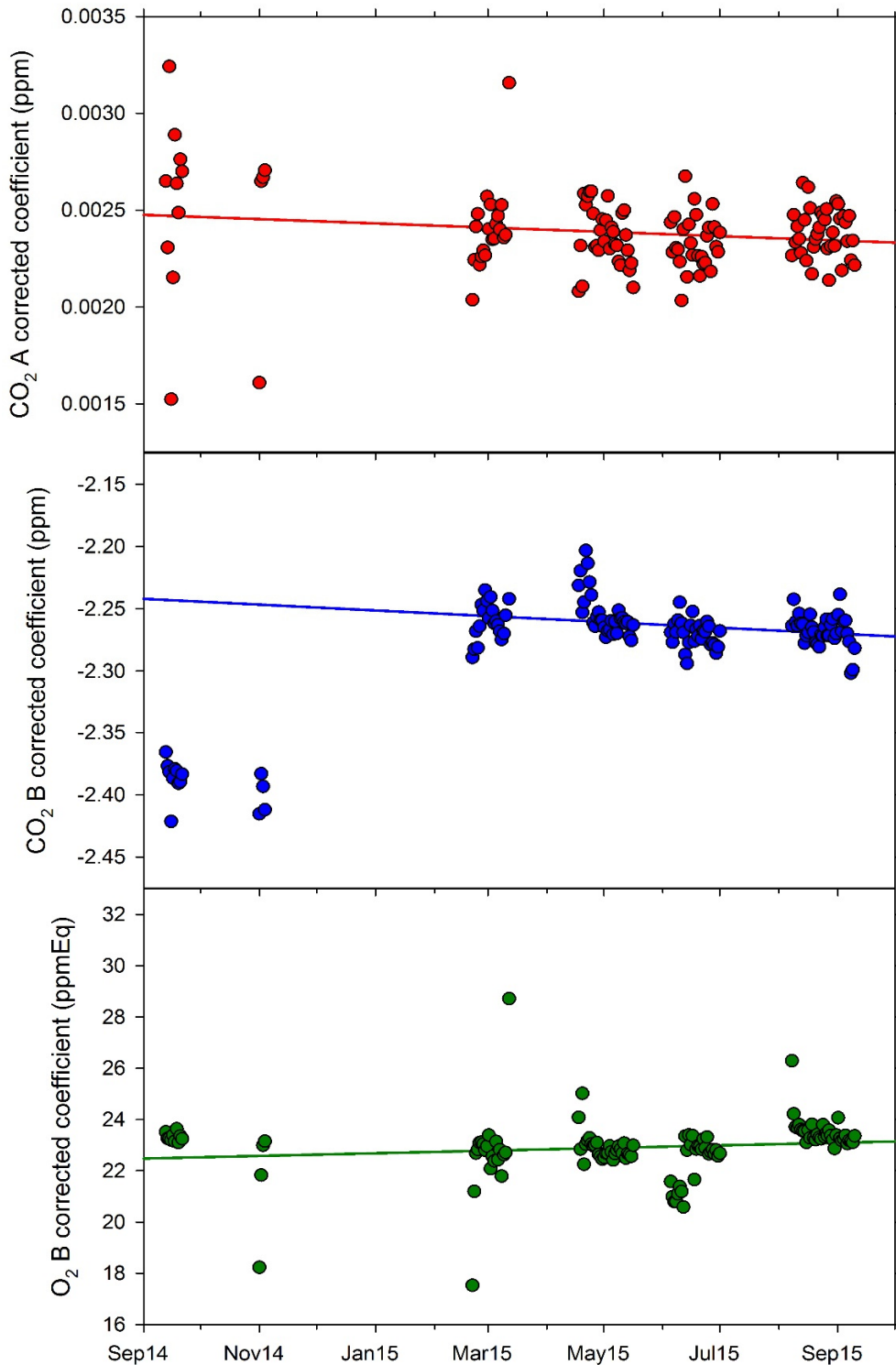


Figure 2.8. Drifts in the A and B coefficients of the quadratic CO₂ fit (top and middle panels, respectively), and drift in the B coefficient of the linear O₂ fit (bottom panel). Drifts represent the maximum possible drift in the calibration scales of CO₂ and O₂. These data were constructed using a -8.9 mV Δ CO₂ analyser response, equating to approximately 400 ppm, and using a 0.00444 % Δ O₂ analyser response, equating to approximately -125 ppmEq (-700 per meg). Linear regression fits have been added to the plots to highlight the direction of the drift. Gaps in the time series are when the measurement system stopped working and could not be restarted until the next time the Cap San Lorenzo visited the London port.

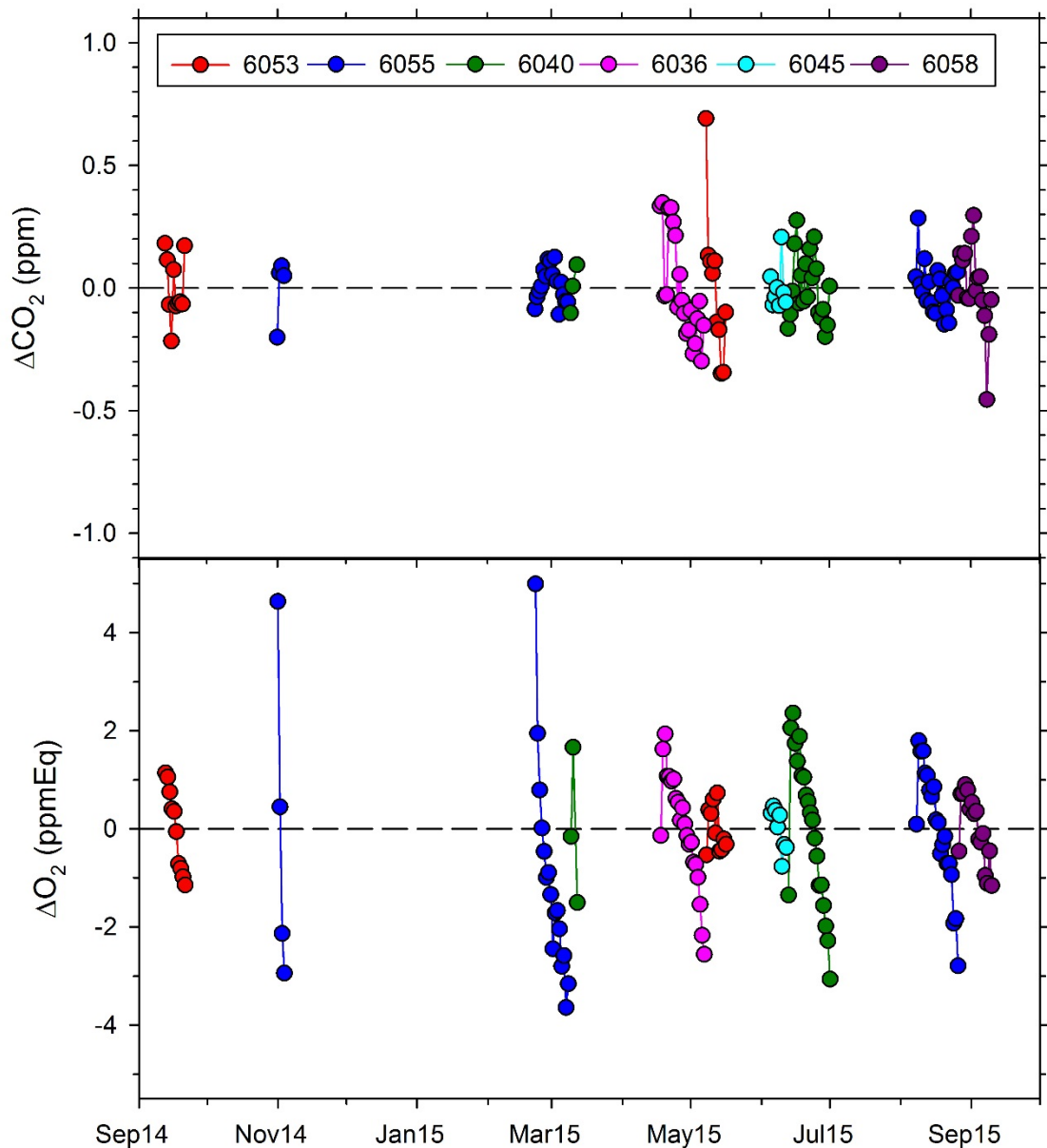


Figure 2.9. Stability of the CO₂ mole fraction (top panel) and O₂ mole fraction (bottom panel) in the WTs over time. Each point represents the WT CO₂ or O₂ mole fraction as defined during a WSS calibration, minus the average WT CO₂ or O₂ mole fraction for each WT. Different coloured symbols represent different WTs. Typically, the lifetime of the air in a WT cylinder is about 18 days, with a starting pressure of about 300 bar and a final pressure of about 5 bar. Gaps in the time series in this figure, and Figures 2.11 and 2.12 below, are caused by system faults, predominantly drying problems, which could only be fixed each time the Cap San Lorenzo visited the London port.

Fig. 2.9 shows that, in contrast to CO₂, there is a definite trend of O₂ mole fraction decreasing as the pressure inside the cylinders also decreases. These decreases in O₂ mole fraction can be up to 9 ppmEq, which is about 54 per meg, during the lifetime of the WT, and are of a comparable magnitude to the O₂ mole fraction depletion found in WT cylinders at the Zotino Tall Tower Observatory (Kozlova and Manning, 2009). This decrease in O₂ mole fraction is larger than that

found by (Manning, 2001), which is probably due to a combination factors: firstly, the cylinders were new, and were not very well 'conditioned' prior to use, which makes it more likely that surface reactions may occur; secondly, the cylinders were filled to 300 bar, instead of 140-200 bar, which is the typical range for O₂ and CO₂ measurement system WTs; and thirdly, the cylinders are small (10 L) compared to WT cylinders used on other measurement systems (typically 40-50 L), and so the cylinder pressure will decrease more quickly. In general, the difference in WT O₂ is small between WSS calibrations, however, sometimes a significant change in the measured WT O₂ can occur (e.g. ~1 ppmEq, which is about 6 per meg). The WT variability highlights the importance of carrying out a WSS calibration every 23 hours for the shipboard system, instead of every 47 hours, as is the procedure at some other continuous O₂ and CO₂ measurement sites (e.g. Wilson, 2013), to avoid significant WT O₂ mole fraction variability affecting the accuracy of the O₂ measurements, because the WT O₂ and CO₂ mole fractions are re-defined during a WSS calibration, and hence may cause a step-change in the O₂ and/or CO₂ measurements if the change in mole fraction is large between WSS calibrations.

In addition to the O₂ variability, it is also clear from Fig. 2.9 that the first WT O₂ measurement is quite often anomalously low or high, which results in a large jump in the declared O₂ mole fraction of the WT between the first and second WSS calibrations. To ensure that this does not have an effect on the accuracy of the O₂ data, I have flagged periods of data that were affected by these initial anomalous WT values, so that these data are not included in further analyses.

2.3.3. High pressure cylinder standards

All the cylinders mentioned in this chapter were prepared in-house at UEA in the CFF, with the help of Phil Wilson and Andrew Manning. All cylinders are filled to about 200 bar with dry (<1 ppm water vapour), natural air (with the exception of the WTs, which are filled to 300 bar). It is important that the cylinders contain dry air with <1 ppm water vapour to avoid water vapour dilution effects affecting the O₂ measurements (Stephens et al., 2007), and to maintain stable CO₂ and O₂ mole fractions within the cylinders. For example, Kozlova and Manning (2009) speculate that cylinders with just 5 ppm water vapour may have been responsible for relative poor O₂ stability in WT cylinders. It is also important that cylinders are filled with natural air containing argon and naturally occurring abundances of carbon isotopes

in CO₂, to avoid pressure broadening effects that occur in NDIR analyser cells, whereby the infrared beam absorption by a single molecule is affected by the absorption characteristics of the neighbouring molecules. Thus, differential CO₂ measurements made using a WT containing synthetic air (containing non-natural carbon isotope abundances in CO₂) would be biased compared to differential CO₂ measurements made using a WT containing natural air.

The shipboard WSSes and TTs were assigned declared O₂ and CO₂ values in the CRAM Laboratory on the SIO scale for O₂ and CO₂ for the 2013 WSS suite and 2014 TT (see Table 2.1), and on the WMO NOAA X2007 scale for CO₂ for the 2015 WSS suite, using a VUV analyser for O₂, and a Siemens Ultramat 6F NDIR analyser for CO₂, with multiple measurements made over a period of several weeks. The WSSes and TT prepared in 2013 were calibrated using Scripps O₂ and CO₂ scale values from 2006, and WSSes and TT prepared in 2015 onwards were calibrated using the same Scripps O₂ scale, and NOAA CO₂ X2007 scale values, which were last updated in October 2015.

Table 2.1 shows the resulting declared values for the shipboard WSSes and TTs. The WSS CO₂ and O₂ mole fractions bracket the ambient range for each species, accounting for long-term changes that will occur during the lifetime of the WSSes. All TT, ZT, and WT cylinders are prepared with approximately ambient CO₂ and O₂ values, which therefore fall within the WSS calibration ranges. One can also see from Table 2.1 that WSS4, filled in Sep 2013, was only used for a short period of time. This was because including this cylinder in the calibration routine resulted in a lower O₂ R² value than when calibrating with only the other three WSSes. The O₂ declared value of this WSS4 cylinder was quite similar to that of the WSS3 cylinder, hence a small inaccuracy in the declared O₂ value of WSS4, or a small drift in the O₂ mole fraction could easily reduce the R² value of the Oxzilla response fit. Unfortunately, it was not possible to re-measure this cylinder in the CRAM Laboratory, owing to a malfunction with the filling apparatus in the CFF, which meant that all air in this cylinder was consumed when used as a WT for another measurement system.

Table 2.1 Shipboard measurement system WSS and TT cylinders. ‘# Fills’ indicates the number of previous fills of the cylinders, and is an indication of how well ‘conditioned’ the cylinder is. Note that D596276 was evacuated between Jan 2015 and Nov 2015, owing to the air inside getting ‘wet’. Evacuating a cylinder effectively removes all conditioning from the cylinder, and re-starts the ‘# Fills’ counter. The upper values in the ‘Dec. O₂’ and ‘Dec. CO₂’ columns refer to the CRAM Laboratory declared values when the cylinders were prepared, while the bottom values refer to the declared values at the end of the cylinder lifetimes. Due to a technical issue with UEA’s cylinder filling system, it was not possible to prepare a 4th WSS in time for January 2016.

Cyl name	Cyl ID	Date prep	Period of use	H ₂ O (ppm)	# Fills	Dec. O ₂ (per meg)	Dec. CO ₂ (ppm)
WSS1	D88534	Jul 2013	Sep 2013- Jan 2016	0.8	4	-744.60 -	416.846 -
WSS2	D88535	Jul 2013	Sep 2013- Jan 2016	0.9	6	-515.38 -	439.491 -
WSS3	D88536	Jul 2013	Sep 2013- Jan 2016	0.6	7	-607.59 -	397.258 -
WSS4	D88532	Jul 2013	Sep 2013 only	0.8	7	-632.848 -	389.305 -
TT	D596276	Jul 2013	Sep 2013- Sep 2014	-	3	-621.565 -	402.818 -
TT	D596278	Aug 2014	Sep 2014- Oct 2015	0.9	2	- -581.474	- 395.992
WSS1	D88532	Dec 2015	Jan 2016- present	0.8	8	-489.478 -	382.105 -
WSS2	D88530	Dec 2015	Jan 2016- Feb 2018	1.0	3	-610.280 -	426.133 -
WSS3	D596277	Dec 2015	Jan 2016- Feb 2018	0.8	3	-748.028 -	398.260 -
TT	D596276	Nov 2015	Nov 2015- Jul 2016	0.8	3	-868.069 -	403.283 -

2.3.4. The role of the Zero Tank and Target Tank

As mentioned in Section 2.3.2, the C coefficient of the Li-6252 analyser response quadratic fit is re-assigned every 4 hours by analysis of a ‘Zero Tank’ (ZT), to correct for temperature related drift, which affects the baseline of the analyser calibration (see Figure 2.10). The term ‘Zero Tank’ refers to the zero coefficient of the calibration curve, which is re-defined every time the ZT is measured. The theory behind the ZT corrections to the C coefficient of the CO₂ calibration are explained in detail in (Wilson, 2013), and are briefly described below:

1. The initial value of the C coefficient is determined during a WSS calibration.

2. Immediately following the completion of the WSS calibration, the ZT CO₂ mole fraction is measured. It is assumed that no system variability or drift in scale or baseline has occurred between the WSS calibration and this first measurement of the ZT.
3. The ZT CO₂ mole fraction is then re-measured every 4 hours until the next WSS calibration occurs. For each successive ZT measurement, any difference in the CO₂ mole fraction between a given measurement and the previous measurement is used to correct the initial value of the C coefficient, which was determined by the WSS calibration.
4. Sample air CO₂ measurements made between the time of the first and second ZT measurements will be calibrated using the initial C coefficient that was determined during the WSS calibration. Sample air CO₂ measurements made between the time of the second and third ZT measurements will be calibrated using a C coefficient that has been adjusted by an amount equivalent to the difference in CO₂ mole fraction between the second and first ZT measurements, and so on for successive ZT measurements.
5. Therefore drift in the C coefficient is corrected at 4 hourly intervals by assessing differences in successive measurements of the ZT CO₂ mole fraction, until the next WSS calibration occurs (23 hours later), and the initial value of the C coefficient is redefined.

Although the purpose of the ZT is to correct for baseline variability in the CO₂ analyser response, the CO₂ and O₂ analysers are placed in series, and as such, the O₂ mole fraction of the ZT is measured as well (typically, ZT O₂ mole fraction is also in the ambient range). No corrections are applied to the Oxzilla response function coefficients from these O₂ measurements of the ZT, although the data can be used in a similar way to Target Tank measurements (see this section, below); hence, the ZT is stored horizontally inside the Blue Box with all the other cylinders, which would not be necessary if only the CO₂ ZT measurements were used.

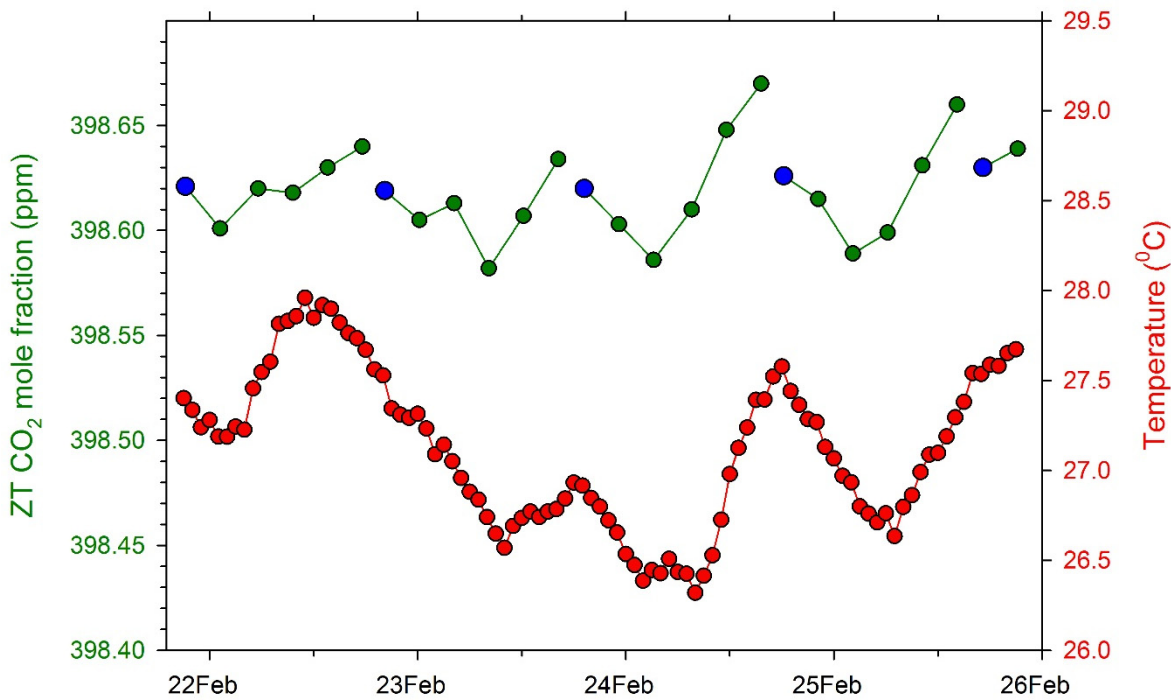


Figure 2.10. Short-term drift in the ZT CO₂ mole fraction, from the Cap San Lorenzo system for 4 days in Feb 2015. Blue symbols indicate ZT CO₂ measurements that immediately follow a WSS calibration, and green symbols indicate the subsequent ZT CO₂ measurements between WSS calibrations. Red symbols show the ambient temperature measured in the room. Each ZT measurement shown is the mean of 11 one-minute averages of CO₂ and O₂.

Figure 2.10 shows that the variability in the CO₂ analyser baseline is significant, as the measured ZT CO₂ mole fraction can vary by more than 0.5 ppm in the time between successive WSS calibrations. This demonstrates the importance of my calibration protocol to redefine the baseline every 4 hours. The drift in the CO₂ analyser baseline correlates very well with changes in room temperature, as indicated by changes in the measured ZT CO₂ mole fraction.

Figure 2.11 shows the stability of the ZT O₂ and CO₂ mole fractions over time during the measurement system's deployment on board the Cap San Lorenzo. The O₂ mole fraction of ZT cylinder with ID number 'D169300' seems to have decreased slightly over its lifetime, but this does not have any bearing on the O₂ measurements, because the O₂ mole fraction of the ZT is not used to calibrate the Oxzilla II in any way. There is no significant drift in the CO₂ mole fraction of either of the ZTs, and no change in the 'noise' (short-term variability on the order of hours to days) of the CO₂ measurements between the two cylinders. This implies that the step change in the B coefficient of the CO₂ calibration fit, shown in Fig. 2.8, is indeed due to a step change in the CO₂ analyser's span response, and was not caused by a change in the CO₂ calibration scale of the WSSes, since there was no corresponding change in the ZT CO₂

mole fraction. For O₂, however, the O₂ ‘noise’ is greater for ZT ID ‘D169300’ than for ‘D064564’; this reduction in noise is most likely a feature of the cylinders themselves, rather than related to an improvement in the analytical precision of the measurement system, although it is also possible that a previously undetected leak was fixed when the ZT was changed over in June 2015.

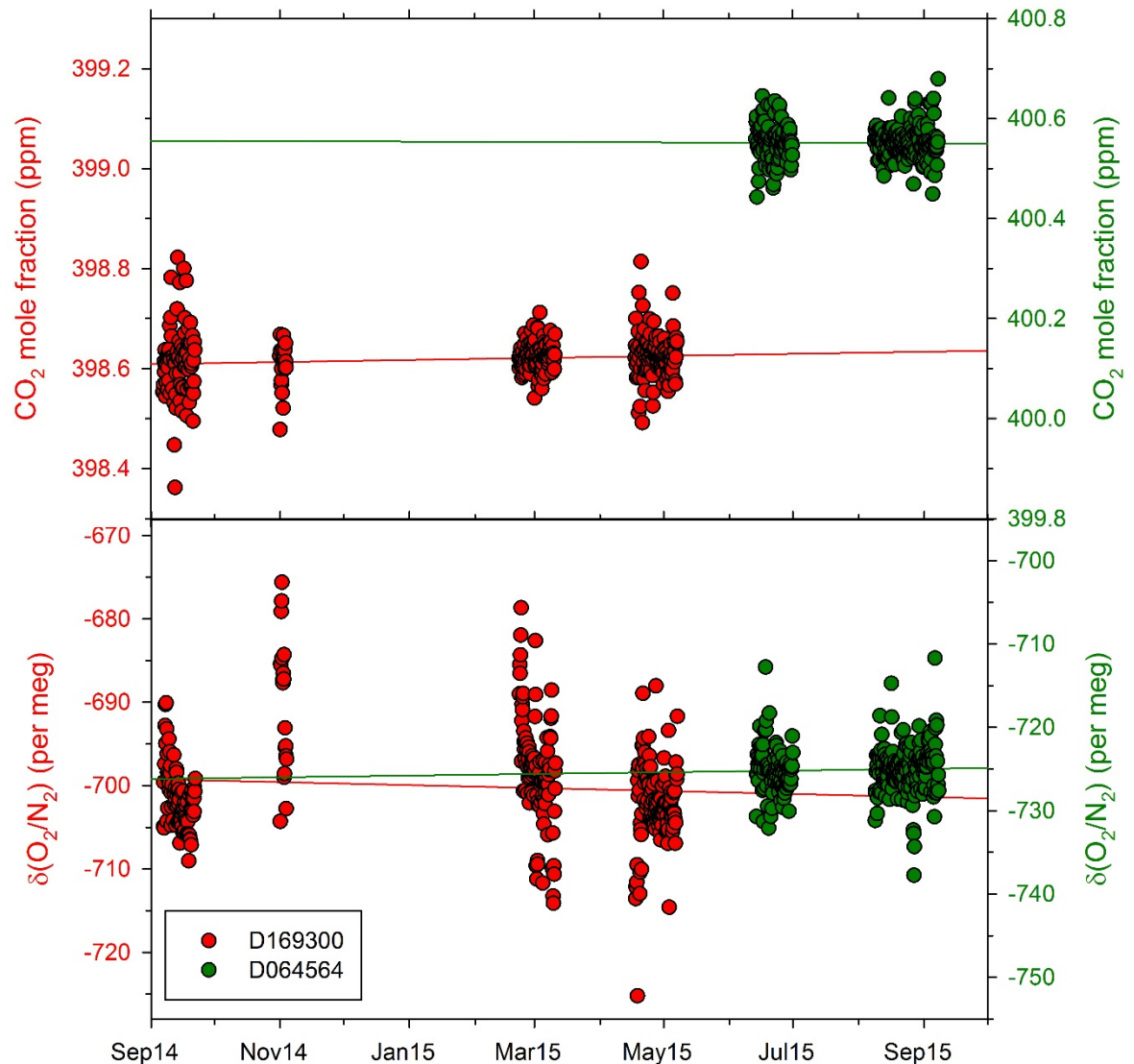


Figure 2.11. Stability of ZT CO₂ and O₂ during deployment on board the Cap San Lorenzo between Sep 2014 and Sep 2015. Red and green symbols denote the CO₂ and O₂ mole fractions of ZTs D169300 and D064564 respectively. The red and green lines are linear regressions to the data, and indicate the direction of the long-term drift.

Unlike the ZT, the Target Tank (TT) is not used to calibrate either of the analysers in any way. Rather, it is used as a quality control measure to check the ‘compatibility’ of the measurements relative to the calibration scale maintained in the laboratory at UEA, where compatibility is the closest measure to accuracy available (and is defined as the acceptable level of agreement required between two different field stations or laboratories when measuring the same air sample (Laurila, 2007)). In

addition, the TT measurements can provide an indication of the repeatability of the measurements, which is defined as: “the closeness of agreement between results of measurements of the same measure carried out under changed conditions of measurement”, (Laurila, 2007). On board the Cap San Lorenzo, the TT was measured for CO₂ and O₂ once every 10 hours.

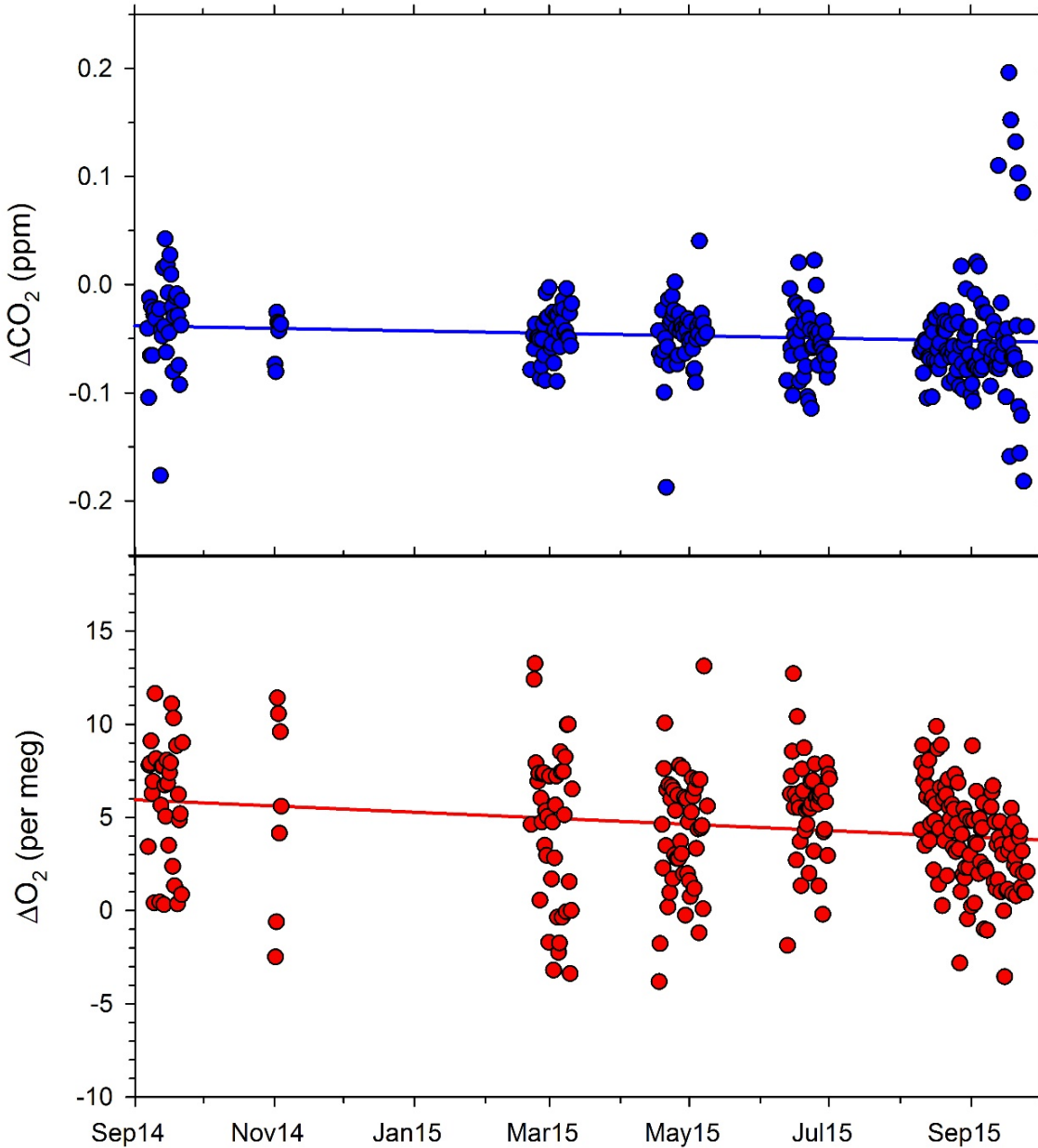


Figure 2.12. CO₂ (top panel) and O₂ (bottom panel) measurements of the TT cylinder on the Cap San Lorenzo. Data are shown as differences in mole fraction from the declared TT values. TT measurements that were made when the measurement system was experiencing known technical difficulties have been excluded. Each TT measurement shown is the mean of 13 consecutive one-minute averages of O₂ and CO₂ measurements.

Figure 2.12 shows the TT O₂ and CO₂ measurements from on board the Cap San Lorenzo, plotted as differences from the CRAM Laboratory ‘declared values’. Both the O₂ and CO₂ results show slight downwards drift of about 1.1 per meg yr⁻¹ and 0.02

ppm yr⁻¹ respectively, but, as with the ZT CO₂ measurements, there is no evidence of a step change in the CO₂ calibration scale. The measurement system compatibility is determined by calculating the mean offset between the TT CO₂ and O₂ measurements and the declared CO₂ and O₂ values of the TT. The measurement system repeatability is determined from TT O₂ and CO₂ measurements by calculating the mean ($\pm 1\sigma$ standard deviation) of the $\pm 1\sigma$ standard deviations from TT measurements, where a TT measurement is comprised of 13 one-minute averages of O₂ and CO₂. Both the compatibility and repeatability results for the Cap San Lorenzo deployment period are shown in Tables 2.2 and 2.3, in Section 2.4, as well as the repeatability and compatibility results from the JC090 cruise (Chapter 3), and from when the measurement system was running in the Wolfson Laboratory at UEA (Chapter 5).

2.4. Repeatability and compatibility of the measurement system

Tables 2.2 and 2.3 show respectively, the repeatability and compatibility of the shipboard measurement system at various times throughout its operation. Note that, at the time of writing, the shipboard measurement system is still deployed on the Cap San Lorenzo; hence, the ‘period of deployment’ refers to the time period over which TT data have been analysed. It should also be noted that the alternating switching between sample air and WT air through the two Oxzilla fuel cells had a periodicity of 60 seconds during the JC090 cruise, and 30 seconds at UEA and on the Cap San Lorenzo (see also Section 2.6). A single TT measurement from the JC090 cruise therefore refers to the mean (and $\pm 1\sigma$ standard deviation) of 7 two-minute averages of O₂ and CO₂, while a single TT measurement from UEA or from the Cap San Lorenzo refers to the mean (and $\pm 1\sigma$ standard deviation) of 13 one-minute averages of O₂ and CO₂. As an example when interpreting the data in Table 2.2, for the JC090 cruise, the TT measurements were run on a 10-hour frequency, so the data summarise 31 TT measurements, which is a total period of 310 hours, or about 13 days. Every 10 hours, the TT measurement reported is the mean of 13 one-minute values; so the O₂ value in the table of ± 5.9 per meg is the mean $\pm 1\sigma$ standard deviation from all 31 TT measurements, and the O₂ value of ± 2.9 per meg is the $\pm 1\sigma$ standard deviation of this mean, representing how the TT measurement standard deviation has varied about its mean of ± 5.9 per meg over the 13 days.

Table 2.2. Repeatability of O₂ and CO₂ analysers of shipboard measurement system, determined from TT analyses. Repeatability is calculated as the mean of the $\pm 1\sigma$ standard deviations from all the TT runs (where a run consists of either 7 two-minute averages or 13 one-minute averages, as mentioned above), and hence is denoted as the mean of these $\pm 1\sigma$ standard deviations, reported to $\pm 1\sigma$ standard deviation, thus demonstrating how the repeatability of the O₂ and CO₂ measurements varies over time.

Description	Period of deployment	TT O₂ (per meg)	TT CO₂ (ppm)	No. of TT runs
JC090 cruise	Sep 2013	$\pm 5.94 \pm 2.89$	$\pm 0.008 \pm 0.003$	31
Wolfson Laboratory, UEA	Jul-Aug 2014	$\pm 2.72 \pm 0.70$	$\pm 0.008 \pm 0.004$	80
Wolfson Laboratory, UEA (JT through drying)*	23Apr 2014	$\pm 6.50 \pm 0.76$	$\pm 0.006 \pm 0.001$	20
Cap San Lorenzo	Sep 2014 – Sep 2015	$\pm 3.47 \pm 2.19$	$\pm 0.010 \pm 0.003$	224

* See main text.

As shown in Fig. 2.1, the TT does not pass through the inlet sample air lines, diaphragm pumps, or drying traps of the measurement system. Therefore, analyses of repeatability from TT measurements are representative of the precision of the analysers and gas handling design between the TT and the analysers only, and not the whole measurement system. In order to better understand the analytical precision of the whole measurement system, a 'Junk Tank' (JT) was connected to the measurement system just after F5 on each of the inlet lines in turn, so that the JT air would pass through the diaphragm pump (which had air flowing through but was not turned on) and three stage drying system, before passing through the analysers (see Table 2.2, third row); thus, only the impact of the AAI and inlet tubing were excluded from this analytical repeatability estimate. JT repeatability was calculated as the mean of the $\pm 1\sigma$ standard deviations from 20 consecutive sections of 13 minutes of data, so as to be comparable to the other TT analyses.

As shown in Table 2.2, surprisingly, the CO₂ repeatability slightly improves when the JT air was passed through the majority of the gas handling system, which indicates there is no detrimental impact on the CO₂ precision caused by the wetted materials of the diaphragm pump, or by the 3-stage drying system. For O₂, the mean

of the 13-minute $\pm 1\sigma$ standard deviations at first appears to be significantly worse when the JT air was passed through the diaphragm pump and drying system, while the longer-term variability (i.e. the $\pm 1\sigma$ standard deviation of the mean) compares favourably to the other TT measurements. However, the measurement system was still in a period of intensive testing and performance improvements during April 2014, and the O_2 repeatability during this month was only $\pm 7.0 \pm 1.7$ per meg from 6 TT measurements, which suggests that there is no detrimental effect on the O_2 precision caused by the diaphragm pump or the 3-stage drying system. Ideally, however, this JT test should be repeated when the measurement system is performing at its optimum, as reflected by the last row of Table 2.2.

Table 2.3 shows the compatibility of the O_2 and CO_2 measurements of the shipboard system to the CRAM Laboratory calibration scales, which are traceable to the WMO NOAA CO_2 scale and the Scripps O_2 scale. The WMO compatibility goals for CO_2 and O_2 respectively, are ± 0.1 ppm (northern hemisphere; ± 0.05 ppm in the southern hemisphere) and ± 2 per meg respectively (Tans and Zellweger, 2013). One can see from Table 2.3 that for CO_2 , the shipboard measurement system has performed within the WMO southern hemisphere compatibility goal throughout all periods of its operation. In addition, the average CO_2 offsets reported are all insignificant at the $\pm 1\sigma$ standard deviation level (that is, the offsets are smaller than the $\pm 1\sigma$ standard deviation). For O_2 , the compatibility during the JC090 cruise is well within the 'extended' WMO compatibility goal for O_2 of ± 10 per meg (Tans and Zellweger, 2013), but is not within the ± 2 per meg WMO compatibility goal; however, given current analytical capabilities within the atmospheric O_2 community, this goal is currently considered aspirational, rather than a routinely achievable target. What is perhaps most concerning is the positive offset of my O_2 measurements compared to the UEA CRAM Laboratory declared values, which is significant at the $\pm 1\sigma$ standard deviation level (for the JC090 cruise and on the Cap San Lorenzo).

These offsets require further investigation, to be carried out in the CRAM Laboratory. Overall, however, the O_2 compatibility results shown in Table 2.3 are comparable to the best such measurements reported in the literature for O_2 fuel cell measurement systems. Finally, it is important to remember that I have quantified the compatibility of the ship system measurements to the UEA PSS CO_2 and O_2 scales, not to the NOAA and SIO scales directly, and therefore, for my data to be used in conjunction with datasets that are calibrated relative to other laboratories, I would

need to quantify the UEA calibration scale compatibility to those of the other laboratories.

Table 2.3. Compatibility of O₂ and CO₂ measurements, determined from TT analyses. Compatibility is calculated as the mean difference from the UEA CRAM Laboratory ‘declared value’ of the TT. Note that there is no compatibility entry for the Wolfson Lab period when JT air was passed through the drying system, as unfortunately, it was not possible to measure the JT against the UEA calibration scales. The upper values in the ‘No. of TT runs’ column refer to the CRAM Laboratory declared values when the cylinders were prepared, while the bottom values refer to the declared values at the end of the cylinder lifetimes.

Description	Period of deployment	TT O₂ (per meg)	TT CO₂ (ppm)	No. of TT runs
JC090 cruise	Sep 2013	6.81±3.59	0.005±0.054	31
Wolfson Laboratory, UEA	Jul 2014-Aug 2014	2.61±5.23	- 0.009±0.038	80
Cap San Lorenzo	Sep 2014-Sep 2015	3.98±2.88	- 0.045±0.058	224

2.5 Data acquisition and system control software

All diagnostic (i.e. pressure, flow and temperature data) and analyser data are recorded by the measurement system computer (Shuttle XH61V Intel System, Ambros Direct UK Ltd.), via an electronics box (custom built by Dave Blomfield, UEA), which also supplies power to all of the electrical components in Fig. 2.1, except for the analysers and the Valco valve, which are powered separately. All of the power supplied to the measurement system passes through a PowerGem Pro (British Power Conversion Company) 1000 W uninterruptible power supply (UPS) that converts the Cap San Lorenzo power frequency of 60 Hz to 50 Hz frequency, which is the required frequency for the ship measurement system components. The electronics box contains four USB DAQ (Universal Serial Bus Data Acquisition) devices, three Measurement Computing Minilabs (model 1008) and one Labjack Corporation (model U12), which collect the diagnostic data from the instrumentation and pass it to the computer via a Quatech Inc. USB serial adapter.

In order for the shipboard measurement system to be fully automated, without the need for human intervention for up to eight weeks, custom software was written in C# by Alex Etchells, UEA Research Computing Services (see Figure 2.13 for a software screen capture). The shipboard software is called ‘Nemo’ in order to

differentiate it from other similar software within the CRAM research group. Nemo enables all aspects of the measurement system to be automated and displays much of the data in real time. Nemo's automation functionality includes: customisable protocols for switching valves at pre-determined intervals (and enabling the user to over-ride these protocols); changing to the next WT cylinder when the current WT pressure indicates it is almost empty; setting the flow rate of the measurement system; determining whether the measurement system is in 'auto-run' mode, where sample air data are measured and recorded, or 'resting-state' mode, where only diagnostic data are collected and calibrations are suspended; performing calibration sequences at pre-determined (and customisable) intervals (including purging calibration and TT cylinders for pre-determined intervals prior to passing cylinder air through the analysers, and flushing the Li-6252 cell for a pre-determined interval, prior to recording the cylinder air); determining whether calibrations meet certain criteria for quality control thresholds, and can therefore be used, or whether data needs to be flagged; the frequency of automatically backing-up data files; the frequency of blue and red sample air line switching; reminders when routine maintenance tasks need to be performed; and calculating sample air data in calibrated ppm (CO₂) and per meg (O₂) units, using results from the most recent calibration sequences.

Several modifications were made to the Nemo software at my request, in order to improve some areas of its functionality. Some of these modifications were general improvements, whilst others were specific to the Cap San Lorenzo environment where, not only does the measurements system have to cope with unattended operation for eight weeks, but additionally, I cannot log into the system by remote control. Firstly, we included a sweepout time for the blue/red sample air line switching, which is settable by the user. This is to ensure that the tubing and fittings upstream of V1 are properly flushed out before the sample air data are recorded, and significantly reduces the amount of manual data flagging that is required. We also developed an automated line switching disable feature, so that if the pressure downstream of the diaphragm pump on either the blue or red line becomes too low (threshold settable by the user), then the line switching will be disabled, and V1 will be configured so that only the line with good pressure will be used; this change potentially prevents the loss of half of all data, should a pump fail early in the ship's eight week cycle. Additionally, we enabled the software system to collect sample air data while the WSS cylinders are purged, so that gaps in the sample data owing to

calibration sequences are reduced, and any changes in the sample air O₂ or CO₂ mole fraction following a WSS calibration are easier to diagnose (a step-change in sample air data during a WSS calibration most likely indicates a change in one of the calibration coefficients, not a change in atmospheric O₂ and/or CO₂, whereas a gradual change suggests a real change in atmospheric O₂ and/or CO₂).

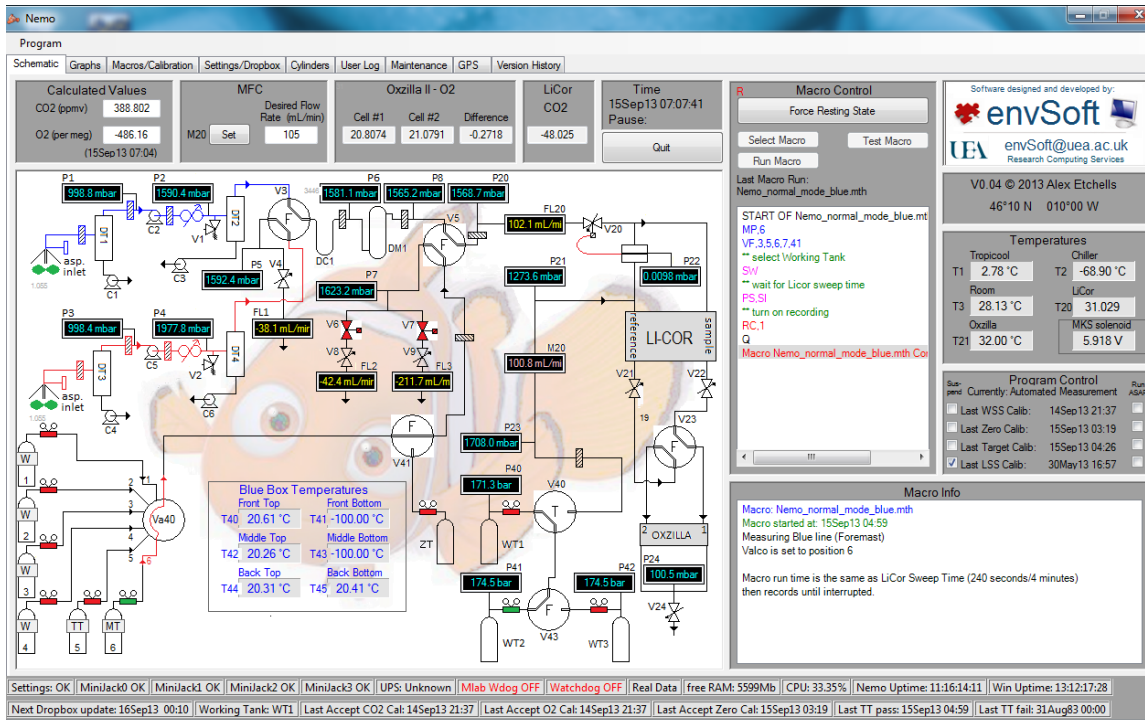


Figure 2.13. Schematic tab of the Nemo software. The ‘Schematic’ tab allows the user to over-ride the default valve settings by clicking on the valve symbols on the gas handling diagram, displays the measurement system pressures, temperatures and flow rates, allows the user to set the desired system flow rate, displays the current calibrated O₂ and CO₂ mole fractions, displays whether the software is in ‘auto-run’ or ‘resting-state’ mode, and displays the status of the macro control, which determines the exact sequence for how the calibration cylinders and TT cylinder are purged and measured. Note that for internal CRAM research group reasons, the numbered designators for the valves, pressure transducers and flow meters on this schematic are not consistent with the numbering used in Fig. 2.1.

Another key software modification, was that if the software automatically entered ‘resting-state’ mode for any reason (e.g. from a loss of sample air flow), then it would attempt to put itself back into ‘auto-run’ mode once every 24 hours. Enabling Nemo to automatically re-start ‘auto-run’ mode following from a short-term issue that may have caused ‘resting-state’ mode to be triggered (e.g. caused by a temporary blockage in the tubing) could potentially enable up to eight weeks of data to be collected that might otherwise have been lost if the software remained in ‘resting-state’ mode until the next London port maintenance visit.

2.6 Improvements implemented

Several improvements were made to the shipboard measurement system during the design process, including some changes to the Nemo software (see previous section), and some ship-specific alterations, such as using a three stage drying system, and utilising a smaller chiller and a $\text{Mg}(\text{ClO}_4)_2$ trap (discussed in section 2.2.3.2 previously). The main analytical improvement that I implemented was a change in the frequency of V11 switching, that is, the frequency of alternating sample air and WT air between the two Oxzilla fuel cells.

The V11 switching frequency for Oxzilla fuel cell O_2 measurement systems has typically been set between 60 and 120 seconds (Patecki and Manning, 2007; Popa, 2008; Stephens et al., 2007; Wilson, 2013). However, Allan Deviation analyses of the shipboard system ΔO_2 , with V11 switching disabled, indicated that a shorter averaging time would improve the short-term O_2 precision, owing to increased exclusion of O_2 variability caused by drift in the O_2 signal. The Allan Deviation plots (example shown in Fig. 2.14; see Appendix B for R programming language script) indicated that the optimum averaging time is about 14 seconds (corresponding to ~ 0.3 ppmEq). Since each $\Delta\Delta\text{O}_2$ value consists of three V11 switches, it is not possible to obtain the optimum precision from the fuel cells, because the response time of the fuel cells is up to 15 seconds (for a 90% response). However, as Fig. 2.14 demonstrates, any reduction in the frequency of V11 switching should translate into an improvement in short-term O_2 measurement precision. The pink dot in Fig. 2.14 shows the Allan deviation at 180 sec (equivalent to ~ 1.1 ppmEq), corresponding to a 1-minute V11 switching scheme, whereas the blue dot shows the Allan deviation at 90 sec (equivalent to ~ 0.6 ppmEq), corresponding to a 30-sec V11 switching scheme.

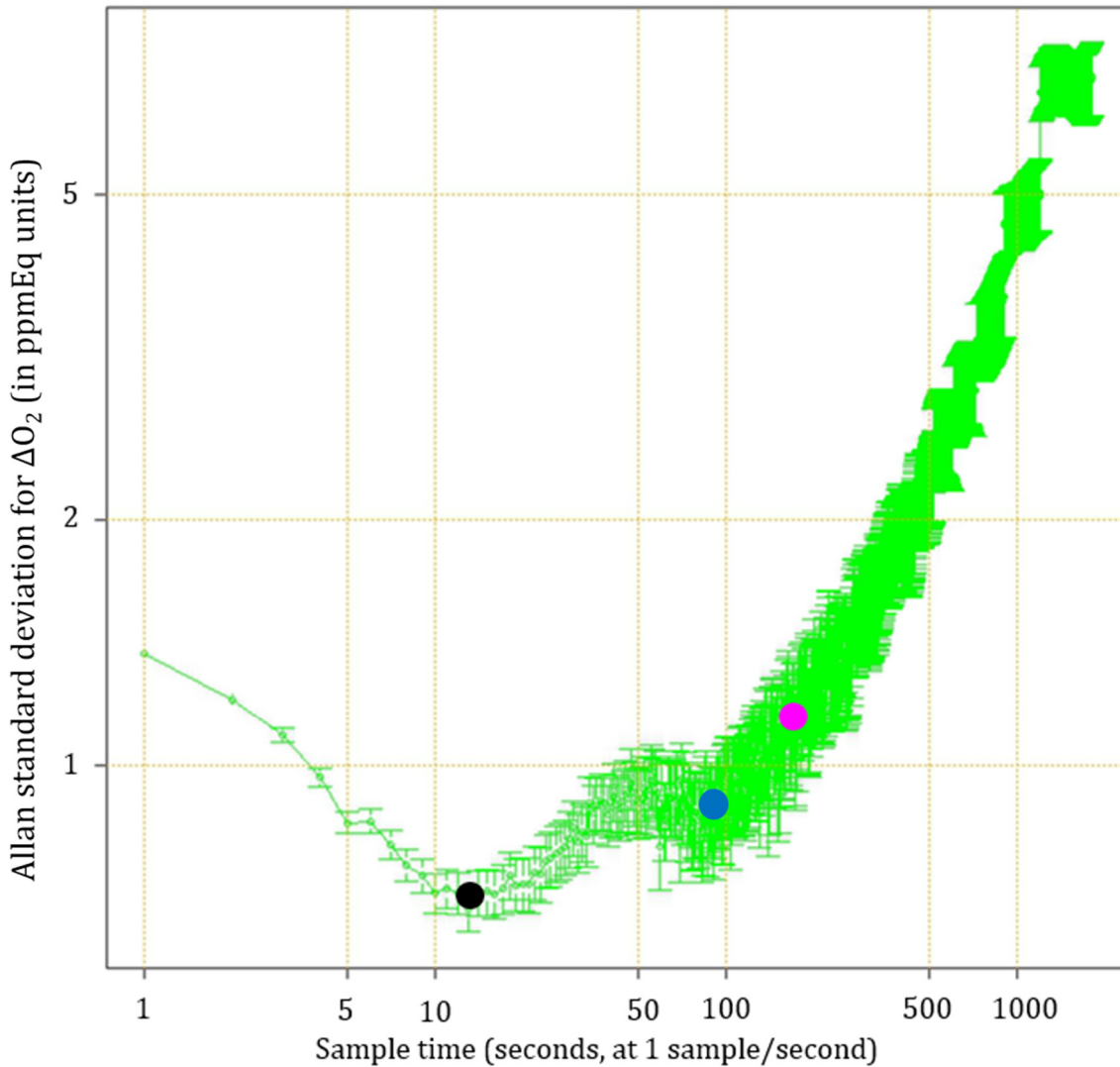


Figure 2.14. Allan deviation plot showing the optimum averaging period for the Oxzilla of about 14 seconds (black dot). This optimum averaging time represents the optimum trade-off between improved precision from averaging the signal noise and reduced precision owing to the inclusion of longer-term drifts in the differential O_2 signal. The Allan deviation for ΔO_2 with a ‘standard’ switching period of 1 minute is indicated by the pink dot (i.e. a jog length of 180 seconds), and the Allan deviation for ΔO_2 with a switching period of 30 seconds is indicated by the blue dot (i.e. a jog length of 90 seconds).

Table 2.4 shows the improvements in short-term O_2 precision gained by reducing the V11 switching frequency from 60 seconds to 30 seconds. The fuel cell sweepout time was also reduced from 30 seconds to 15 seconds, so that the latter 15 seconds of data from each V11 switching period are used to calculate the $\Delta\Delta O_2$ values of the jogs. It was important to ensure that the accuracy of the O_2 measurement was not compromised when reducing the sweepout time from 30 seconds to 15 seconds. In order to mitigate any potential accuracy compromise, I minimised the residence time of air in the tubing between V11 and the fuel cells, by installing the switching valve as close as possible to the fuel cells and using $1/16''$ external diameter tubing

(0.04" internal diameter) instead of the typically used 1/8" external diameter tubing. I found no change in O₂ accuracy as a result of reducing the sweep-out time to 15 seconds, however, reducing the sweep-out time to 10 seconds, did result in a bias in the O₂ mole fraction values.

Table 2.4. Improvements in short-term precision from reduced V11 switching frequency. Values are means of the $\pm 1\sigma$ standard deviations of the TT and ZT runs, reported with $\pm 1\sigma$ standard deviation, and are in per meg units. The improvement for TT and ZT measurements correspond to a 40% and 60% reduction, respectively.

V11 Switching time/sweepout time	60 /30 sec	30 /15 sec	Number of TT/ZT runs
TT	$\pm 4.6 \pm 0.4$	$\pm 2.8 \pm 1.0$	3
ZT	$\pm 5.7 \pm 3.5$	$\pm 2.3 \pm 0.4$	11

2.7 Experimental testing

The shipboard measurement system was tested extensively in the laboratory at UEA prior to deployment on board the Cap San Lorenzo. This testing included ensuring that two key pieces of equipment, that had not previously been used in high precision O₂ and CO₂ measurement systems (to my knowledge), were suitable for their purpose, and that they would not bias the O₂ measurements, or jeopardise the precision of the measurement system.

Firstly, following the failure of a KNF Neuberger KNF N05-ATI diaphragm pump during the JC090 research cruise (see Chapter 3), a new Air Dimensions Inc. J-Series Dia-Vac pump was tested for O₂ and CO₂ artefacts, prior to being installed on the blue inlet sample air line. Figure 2.15 shows two histograms of 1-minute frequency O₂ measurements from the same high pressure cylinder, which was passed through both a working KNF Neuberger pump (left histogram) and the Air Dimensions pump (right histogram), over a period of 207 minutes for each pump. The mean O₂ mole fractions measured by the Oxzilla II for the KNF Neuberger and Air Dimensions pumps were -614.3 ± 4.7 per meg and -613.3 ± 4.7 per meg, respectively, which are not significantly different from one another, and indicate that the Air Dimensions pump does not introduce any significant O₂ or CO₂ artefacts, given that the KNF Neuberger pump is known to be suitable for use in high-precision O₂ and CO₂ measurement systems (Manning, 2001).

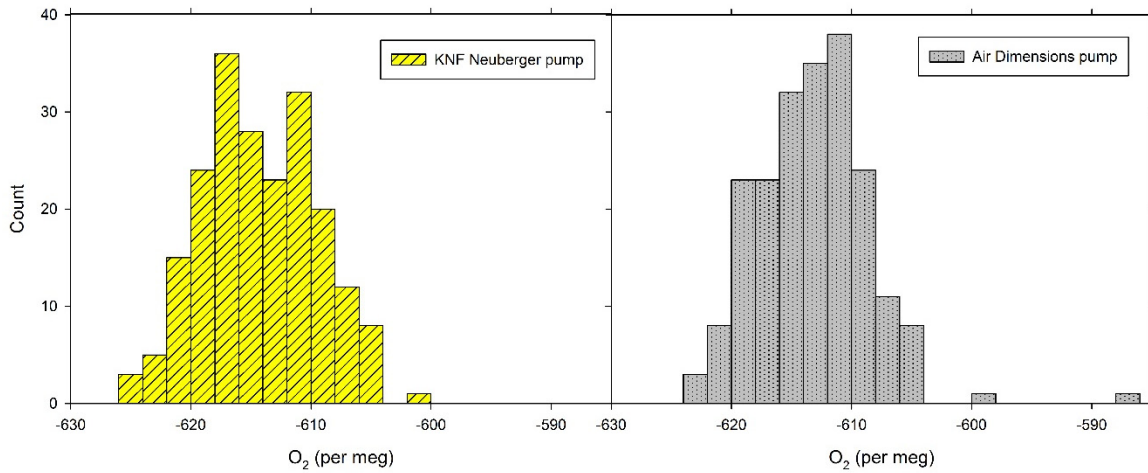


Figure 2.15. Histograms of 1-minute O_2 mole fraction when cylinder air was passed through a KNF Neuberger pump (left plot) and an Air Dimensions pump (right plot).

Secondly, a new Gas Arc two-stage high-pressure cylinder regulator was also tested for stability and O_2 and CO_2 artefacts, since the GO LG1-Series single-stage regulators that were used on the JC090 research cruise for the WTs were prone to drift in the delivery pressure set-point, and required manual daily re-setting (see Chapter 3). The reason why I was not using the ‘tried and tested’ Scott Specialty Gases model 14 regulators on the WT cylinders is because these regulators are rated to only 200 bar, whereas my WT cylinders are filled to 300 bar of pressure. In contrast to the single-stage GO regulator, the Gas Arc two-stage regulator was found to deliver a stable pressure within about 10 mbar for weeks at a time. The possibility of O_2 and CO_2 artefacts was examined by performing a series of TT measurements using both a Scott model 14 regulator and a Gas Arc regulator. The mean TT O_2 mole fraction was -616.0 ± 5.2 per meg for the Scott regulator, and -616.9 ± 4.4 per meg for the Gas Arc regulator, where the TT measurement routine was carried out three times per regulator, resulting in a total of 21 O_2 measurements for each regulator. This difference in the O_2 TT measurements is not significant, and indicates that the Gas Arc regulator does not introduce O_2 artefacts into the measurement system (within the measurement uncertainty).

Testing the shipboard O_2 and CO_2 measurement system in the UEA laboratory also afforded me with an opportunity to test the length of time required for a high-pressure O_2 calibration cylinder to be laid down horizontally before an accurate O_2 measurement can be made of the bulk O_2 content of the cylinder. As mentioned in section 2.1, high-precision atmospheric O_2 measurements are reported as $\delta(O_2/N_2)$ ratios, because O_2 mole fractions are sensitive to mole fraction changes in trace gases. But atmospheric O_2 can fractionate relative to N_2 within a high pressure cylinder due

to thermal differences between the top and bottom of the cylinder, and also due to gravity (since O_2 is a heavier molecule than N_2). This gravitational and thermal fractionation within calibration and WT cylinders means that a cylinder should lie horizontally when being measured, but also that a cylinder that has been stored upright will need to lie horizontally for a certain period of time to allow for the O_2 and N_2 within the cylinder to fully mix prior to being measured. To my knowledge, no previous worker has published results from experiments investigating the time period needed, and possible variability for different sizes of cylinders. Fig. 2.16 shows the O_2 mole fraction of two cylinders (20 L and 50 L volumes) as a function of the length of time since each cylinder was laid horizontally.

For the 50 L cylinder, there is a very significant change in the O_2 mole fraction of >200 per meg during the 40 hours after it is laid horizontally. For the 20 L cylinder, however, the change in O_2 is only about 20 per meg within the same time period. This is perhaps not unexpected, since a 50 L cylinder is much taller than a 20 L cylinder (149 cm body length compared to 93 cm body length), and will therefore experience a much greater amount of both thermal and gravitational fractionation. Interestingly, however, there does not appear to be much difference in the time taken for the O_2 mole fraction to stabilise between the two cylinders, even though the 50 L cylinder experiences a much larger change in O_2 than the 20 L cylinder. The direction of O_2 change in both cylinders after being laid horizontally is consistent with thermal and gravitational fractionation, since the air is sampled from the 'top' end of the cylinder, which will be the end that is enriched in N_2 relative to O_2 (lighter N_2 molecules will be more concentrated at the top owing to gravity, and the top is typically warmer than the bottom owing to vertical temperature gradients in the room, and N_2 tends to accumulate preferentially to O_2 in warmer regions), causing the O_2 measurements to be low initially, and then to rise once the O_2 and N_2 molecules within the cylinder become well mixed.

From Fig. 2.16, I have estimated that all cylinders should be laid horizontally for at least 40 hours prior to being used, although further testing using cylinders of different O_2 mole fractions, and cylinders that have been stored vertically for different periods of time is still required in order to be more certain about this time estimate. There are several ways in which this time could be significantly reduced in order to allow cylinders to be measured much sooner, without having to wait for almost two days prior to measurement. For example, using cylinder valves that contain dip tubes, so that the air is sampled from the middle of the cylinder, rather than the 'top' end of

the cylinder (Ralph Keeling, Scripps Institution of Oceanography, personal communication, 2014), would likely reduce the time required for the cylinder to be laid horizontally. Also, rolling cylinders, or placing ball bearings inside cylinders and rocking them, are both ways of significantly increasing the mixing of the air inside a cylinder, and would likely reduce the time required before measurement after a cylinder had been laid horizontally (Ralph Keeling, Scripps Institution of Oceanography, personal communication, 2014).

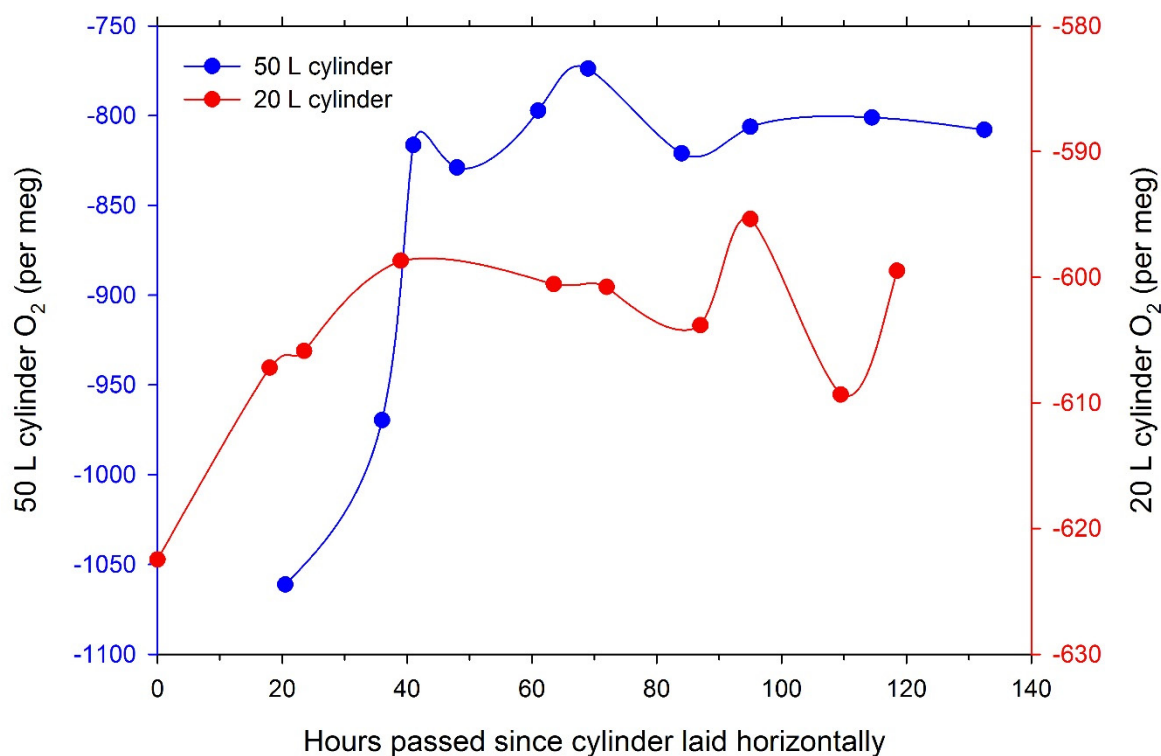


Figure 2.16. O₂ mole fraction of a 50 L cylinder (blue, left y-axis) and a 20 L cylinder (red, right y-axis) as a function of the number of hours since the cylinder was laid horizontally.

2.8 Future improvements

Although the shipboard O₂ and CO₂ measurement system performs well, and has already undergone several analytical improvements, as described in the previous sections of this chapter, there are some further improvements that could be made. Firstly, there are still a few small ‘dead volumes’ present in the gas handling system, most notably on the sample side of the Baratron differential pressure gauge (P11 in Fig. 2.1; 1.3 mL dead volume), which ideally should be eliminated in order to prevent underestimation of the analyser span (B coefficient), resulting from incomplete

flushing of the dead volumes. Adding a dip tube to the sample side of the Baratron would eliminate this dead volume issue.

Secondly, the TT would ideally be passed through exactly the same tubing as the sample air, so that the precision and accuracy determined from TT analyses reflect that of the whole measurement system (including the AAs, inlet tubing, sample pumps and drying system), rather than just the latter part of the measurement system (i.e. Unit 2 in Fig. 2.1). In reality, it is not practical to have TT air passed through the measurement system from the AAs onwards, but with some additional tubing, valves, and software control, it would be quite easily possible to enable TT air to pass through the sample pump and drying system from just before the first Tropicool trap passes (DT1/DT3 in Fig. 2.1) onwards. Such an improvement would enable potential offsets in O_2 and/or CO_2 caused by the sample pumps and drying system to be identified, by alternating between TT measurements that do and do not pass through this part of the measurement system. Furthermore, these are two parts of the system most vulnerable to problems arising, the sample pumps because they include moving parts which degrade over time (diaphragms and valve plates require replacement about annually), and the drying system also because of moving parts (e.g. peristaltic pumps) and because of frequent disturbance in this part of the system caused by human replacement of drying traps.

Thirdly, as mentioned in the previous section, the calibration and WT cylinders used for the shipboard measurement system would benefit from having dip tubes fitted to the cylinder valves, so that air is sampled from the middle of the cylinders, instead of from one end. This would particularly benefit the shipboard system, since the Cap San Lorenzo only makes berth in the UK for a period of about 12 hours, which is not long enough to allow the O_2 and N_2 molecules within the cylinders to mix properly once the cylinders are laid horizontally. Hence, the first 24 hours of data after the ship has left the UK usually requires flagging, if it is deemed that there has been significant O_2 drift in the cylinders between the first WSS calibration and subsequent calibrations.

Lastly, from a measurement system reliability and maintenance perspective, the greatest challenge for uninterrupted measurement on board the Cap San Lorenzo has been having the drying system function successfully throughout the 8 week period, resulting in the largest loss of data. Although the drying system was fully tested and deemed more than sufficient in the laboratory at UEA, the air in the tropics is much more humid than the air in Norwich, UK; hence, the second stage cryogenic

drying trap (chiller trap; DC in Fig. 2.1) usually blocks with ice after only 4-5 weeks, instead of the anticipated 8 weeks. This problem is most likely caused by the upstream Tropicool traps being overloaded, resulting in excess water breakthrough, which then shortens the lifetime of the chiller trap. Attempts to improve the performance of the Tropicool traps, by increasing the pumping action of the peristaltic pumps and re-optimising some of the plumbing configuration, have only been partially successful. What I suspect is needed, are larger volume Tropicool traps, increasing the residence time of the sample air in the traps, and thus obtaining greater efficiency of water removal.

Currently, the only way to enable the drying system to function for a full 8 weeks is to ask a ship crew member to change the chiller trap after 4 weeks with a freshly prepared, dry trap. Although this is generally very effective, the measurements are then dependent upon the goodwill of the ship's personnel, who volunteer to help and are not obliged to do so. Thus, a modified drying system design is required, which can function fully for 8 weeks completely independently from human intervention.

2.9 Summary

In this chapter, I have described the instrumentation and methodology that I have used for making shipboard continuous, high-precision measurements of atmospheric O_2 and CO_2 , including the gas handling, sample gas drying, data acquisition and calibration procedures. In addition, I have evaluated the performance of the shipboard measurement system in terms of measurement repeatability and compatibility, which demonstrate that the shipboard O_2 and CO_2 measurement system performs very well. Although the O_2 measurements do not meet the WMO compatibility goal, this goal is currently not routinely achievable within the atmospheric O_2 community, and the shipboard measurement system is performing at the limit of what is currently achievable for a field station. An analysis of variability in the O_2 and CO_2 calibration coefficients indicate that the O_2 and CO_2 calibration scales may be drifting by up to 2.4 per meg yr^{-1} and -0.045 ppm yr^{-1} , respectively, although this drift could also be caused by drift in the O_2 and CO_2 analyser responses. It has not yet been possible to re-measure the WSS cylinders in the CRAM laboratory, however, such measurements will allow me to quantify any calibration scale drifts in the near future, and possibly also correct for such drifts if they are found to be significant.

My main contribution to improving the measurement system design is the discovery that faster sample air – reference gas switching times results in improved short-term O₂ precision. Specifically, reducing this switching time from once a minute as typically used by other colleagues (e.g. Popa et al., 2010; Stephens et al., 2007; Thompson et al., 2007) to once every 30 seconds, improved the short-term precision for my measurement system (of the order of 2-3 per meg improvement in $\pm 1\sigma$ standard deviations). I have also described results from testing equipment that, to my knowledge, has not been used in high-precision O₂ and CO₂ measurement systems previously, and found both the pump and the cylinder regulator to be suitable for use in O₂ measurement systems. Although it has been known for some time that high-pressure cylinders need to be laid horizontally prior to being measured or used with O₂ measurement systems (Keeling, 1988), I have been able to quantify the minimum time required for cylinders to be in a horizontal position before being put into use, although my results are preliminary, and require further investigation. Finally, I have outlined how the measurement system could be improved in the future, both in terms of the performance of the O₂ and CO₂ measurements, and also the reliability of the measurement system.

It is worth bearing in mind, that even though this chapter contains many specific details, there are many other minor subtleties to making high-precision O₂ measurements that are not written down here, or indeed anywhere, and that are passed along by word of mouth. To write down all of these minor, but important, considerations would make rather long and tedious reading material; hence, I have focussed on what I consider to be the most important aspects of making high-precision O₂ measurements. Whilst individually very minor, collectively, these subtleties can make the difference between atmospheric O₂ measurements with precision of less than ± 10 per meg (on 1-2 minute time scales), and those with precision an order of magnitude (or more) greater than this. As mentioned in the opening paragraph of this chapter, making atmospheric measurements of O₂ to the required precision is much harder than measuring most other atmospheric gases, such as CO₂, however, such measurements are possible, and can provide much deeper insights into carbon cycle processes than those gained from CO₂ measurements alone.

References

- Bender, M., Tans, P. P., Ellis, J. T., Orchardo, J., and Habfast, K.: A high-precision isotope ratio mass-spectrometry method for measuring the O₂/N₂ ratio of air, *Geochimica Et Cosmochimica Acta*, 58, 4751-4758, 1994.
- Blaine, T. W., Keeling, R. F., and Paplawsky, W. J.: An improved inlet for precisely measuring the atmospheric Ar/N₂ ratio, *Atmospheric Chemistry and Physics*, 6, 1181-1184, 2006.
- Brailsford, G. W., (Ed.): Report of the Sixteenth WMO/IAEA Meeting on Carbon Dioxide, Other Greenhouse Gases, and Related Measurement Techniques (GGMT-2011), Jena, Germany, World Meteorological Organization Global Atmosphere Watch Report Series No. 206, WMO TD No. xxxx, available at <http://www.wmo.int/pages/prog/arep/gaw/gaw-reports.html> pp., 2012.
- Coplen, T. B.: Guidelines and recommended terms for expression of stable-isotope-ratio and gas-ratio measurement results. , *Rapid Communications in Mass Spectrometry*, 25, 2538-2560, 2011.
- Keeling, R. F.: Development of an interferometric oxygen analyzer for precise measurement of the atmospheric O₂ mole fraction, Ph.D. thesis, Harvard University, 1988.
- Keeling, R. F., Guenther, P. R., Walker, S. J., and Moss, D. J.: Scripps Reference Gas Calibration System for Carbon Dioxide-in-Nitrogen and Carbon Dioxide-in-Air Standards: Revision of 2012, Scripps Institution of Oceanography, 2016.
- Keeling, R. F., Manning, A. C., McEvoy, E. M., and Shertz, S. R.: Methods for measuring changes in atmospheric O₂ concentration and their application in southern hemisphere air, *Journal of Geophysical Research-Atmospheres*, 103, 3381-3397, 1998.
- Keeling, R. F., Najjar, R. P., Bender, M., and Tans, P. P.: What atmospheric oxygen measurements can tell us about the global carbon cycle, *Global Biogeochemical Cycles*, 7, 37-67, 1993.
- Kozlova, E. A. and Manning, A. C.: Methodology and calibration for continuous measurements of biogeochemical trace gas and O₂ concentrations from a 300-m tall tower in central Siberia, *Atmospheric Measurement Techniques*, 2, 205-220, 2009.
- Kozlova, E. A., Manning, A. C., Kisilyakhov, Y., Seifert, T., and Heimann, M.: Seasonal, synoptic, and diurnal-scale variability of biogeochemical trace gases and O₂ from a 300m tall tower in central Siberia, *Global Biogeochemical Cycles*, 22, 2008.
- Langenfelds, R. L.: Studies of the global carbon cycle using atmospheric oxygen and associated tracers, Ph.D. thesis, University of Tasmania, 2002.
- Laurila, T.: 14th WMO/IAEA Meeting of Experts on Carbon Dioxide, Other Greenhouse Gases and Related Tracers Measurement Techniques, 2007.
- Leuenberger, M. C., Schibig, M. F., and Nyfeler, P.: Gas adsorption and desorption effects on cylinders and their importance for long-term gas records, *Atmospheric Measurement Techniques*, 8, 5289-5299, 2015.
- LI-COR Inc: LI-6252 CO₂ Analyzer Operating and Service Manual, Lincoln, Nebraska, U.S.A., 1996.
- Manning, A. C.: A calibration and intercomparison scheme for continuous, multi-species measurements from a network of tall towers in Europe, World Meteorological Organization, Toronto Global Atmosphere Watch Report Series No. 161, WMO TD No. 1275, available at <http://www.wmo.int/pages/prog/arep/gaw/gaw-reports.html>, 2005.

- Manning, A. C.: Temporal variability of atmospheric oxygen from both continuous measurements and a flask sampling network: Tools for studying the global carbon cycle, Ph.D. thesis, Scripps Institution of Oceanography, University of California, 2001.
- Manning, A. C. and Keeling, R. F.: Global oceanic and land biotic carbon sinks from the scripps atmospheric oxygen flask sampling network, *Tellus, Series B: Chemical and Physical Meteorology*, 58, 95-116, 2006.
- Maxtec: New, motion stable weak acid electrolyte oxygen sensor MAX-250 series, Salt Lake City, Utah, U.S.A.
- Patecki, M. and Manning, A. C.: First results from shipboard atmospheric O₂ and CO₂ measurements over the North Atlantic Ocean, New York, 2007.
- Popa, M. E.: Continuous tall tower multispecies measurements in Europe for quantifying and understanding land-atmosphere carbon exchange, Ph.D. thesis, Friedrich-Schiller-Universität Jena, Germany, 2008.
- Popa, M. E., Gloor, M., Manning, A. C., Jordan, A., Schultz, U., Haensel, F., Seifert, T., and Heimann, M.: Measurements of greenhouse gases and related tracers at Bialystok tall tower station in Poland, *Atmospheric Measurement Techniques*, 3, 407-427, 2010.
- Stephens, B. B., Bakwin, P. S., Tans, P. P., Teclaw, R. M., and Baumann, D. D.: Application of a differential fuel-cell analyzer for measuring atmospheric oxygen variations, *Journal of Atmospheric and Oceanic Technology*, 24, 82-94, 2007.
- Stephens, B. B., Keeling, R. F., and Paplawsky, W. J.: Shipboard measurements of atmospheric oxygen using a vacuum-ultraviolet absorption technique, *Tellus Series B-Chemical and Physical Meteorology*, 55, 857-878, 2003.
- Tans, P. and Zellweger, C.: 17th WMO/IAEA Meeting on Carbon Dioxide, Other Greenhouse Gases and Related Tracers Measurement Techniques (GGMT-2013), Beijing, China, 2013.
- Thompson, R. L., Manning, A. C., Lowe, D. C., and Weatherburn, D. C.: A ship-based methodology for high precision atmospheric oxygen measurements and its application in the Southern Ocean region, *Tellus Series B-Chemical and Physical Meteorology*, 59, 643-653, 2007.
- Tohjima, Y.: Method for measuring changes in the atmospheric O₂/N₂ ratio by a gas chromatograph equipped with a thermal conductivity detector, *Journal of Geophysical Research-Atmospheres*, 105, 14575-14584, 2000.
- Tohjima, Y., Machida, T., Watai, T., Akama, I., Amari, T., and Moriwaki, Y.: Preparation of gravimetric standards for measurements of atmospheric oxygen and re-evaluation of atmospheric oxygen concentration, *Journal of Geophysical Research-Atmospheres*, 110, 2005.
- Wilson, P. A.: Insight into the Carbon Cycle from Continuous Measurements of Oxygen and Carbon Dioxide at Weybourne Atmospheric Observatory, UK, Ph.D. thesis, University of East Anglia, Norwich, UK, 2013.

Chapter 3

Measurements of atmospheric O₂ and CO₂ in the North Atlantic Ocean on board the RRS James Cook

3.1 Introduction

3.1.1 Scientific background and chapter outline

Currently, the global ocean is the largest long-term sink for anthropogenic CO₂, and yet the spatial and temporal variability of the oceanic CO₂ sink is poorly understood (Landschutzer et al., 2014; Sabine et al., 2004). Although the partial pressure of seawater and atmospheric CO₂ in the North Atlantic have been relatively well sampled compared to other oceanic regions using a network of volunteer observing ships (Watson et al., 2009), significant temporal and spatial variability in calculated air-sea CO₂ fluxes has led to discrepancies in assessments of the long-term trend of the CO₂ sink in this region (Park and Wanninkhof, 2012; Watson et al., 2009). High-precision atmospheric measurements of O₂ and CO₂ can be used to partition the land and ocean carbon sinks (Keeling and Manning, 2014; Manning and Keeling, 2006), and to provide an independent constraint on long-term changes to the oceanic CO₂ sink, which is independent of uncertainties associated with gas transfer velocities. Using continuous atmospheric O₂ and CO₂ measurements in this way requires a network of long-term measurement stations distributed over the Earth's surface, including in oceanic regions. High-precision, continuous atmospheric O₂ and CO₂ measurements are particularly sparse in oceanic regions, partly due to the fact that being able to measure atmospheric O₂ and CO₂ precisely is in itself quite challenging, and partly due to the logistical complexities and added costs associated with deploying an atmospheric O₂ and CO₂ measurement system on a ship, compared to deployment on land.

To date, almost all of the continuous atmospheric O₂ and CO₂ measurements made over the ocean have been from research vessels, which tend to have limited deployment periods of only a few weeks or months. The first research cruise to make continuous atmospheric measurements of O₂ and CO₂ was in April – May 1998, in the equatorial Pacific (Stephens et al., 2003). A second cruise in October 1998 followed, from Antarctica to Chile across the Drake Passage (Stephens et al., 2003). Two more research cruises in the western Pacific sector of the Southern Ocean made continuous atmospheric O₂ and CO₂ measurements in February 2003 and April 2004 (Thompson et al., 2008; Thompson et al., 2007), as well as a cruise from Canada to Iceland in August–September 2006 (Patecki and Manning, 2007).

The longest continuous atmospheric O₂ and CO₂ dataset from a research vessel is that of the Laurence M. Gould (a USA National Science Foundation icebreaker), which has been travelling semi-continuously between Chile and Antarctica across the Drake Passage since June 2012, with measurements maintained by Britton Stephens (National Center for Atmospheric Sciences, USA). In addition to research vessels, continuous atmospheric O₂ and CO₂ measurements were also made from the F3 oil platform in the North Sea, between 2008-2011 (van der Laan-Luijkx et al., 2010), and there are ongoing atmospheric O₂ and CO₂ measurements in the western Pacific Ocean from commercial container ships (see Chapter 4 for more details; Tohjima et al., 2005; Tohjima et al., 2015).

In this chapter, I present my atmospheric O₂ and CO₂ data measured on board the RRS (Royal Research Ship) James Cook, during September 2013. The data presented here thus represent only the second existing record of continuous shipboard atmospheric O₂ and CO₂ measurements over the Atlantic Ocean. The remainder of Section 3.1 explains the motivation for making atmospheric O₂ and CO₂ measurements on board the RRS James Cook, and describes the location of the research cruise. Section 3.2 describes differences in the measurement system design compared to the final design described in Chapter 2, as well as technical setbacks that were encountered during the cruise, and complementary data sets that were used in the data analyses. Section 3.3 explains the data flagging procedure and Section 3.4 presents and discusses the results and data analyses. Finally, Section 3.5 summarises the findings of this chapter and presents the overall conclusions.

3.1.2 Motivation for research cruise

The atmospheric O₂ and CO₂ measurement system described in Chapter 2 of this thesis was tested at sea on board the RRS James Cook in August and September 2013, as part of the 090 UK NERC (Natural Environment Research Council) funded cruise (from here on referred to as the JC090 cruise). The motivation for testing the measurement system at sea on a research vessel prior to its final deployment on a container ship was to ensure that the equipment was reliable in a marine environment. Once installed on board the container ship, the atmospheric O₂ and CO₂ measurement system would need to operate almost entirely automatically, and be able to run independent of human intervention. In addition, once deployed at sea, the only opportunities to carry out maintenance or repairs to the equipment would be

when the ship made berth in the UK, which would occur once every eight weeks, and only for a period of about 12 hours per visit.

3.1.3 Location of the cruise

The JC090 cruise was the final phase of fieldwork of the ‘Ocean Surface Mixing, Ocean Sub-mesoscale Interaction Study’ (OSMOSIS), led by Alberto Naveira Garabato (University of Southampton, UK). The purpose of the cruise was to recover several moorings and gliders at the Porcupine Abyssal Plain (PAP) site in the North Atlantic, conduct biogeochemical and hydrographic measurements for calibrating the mooring and glider measurements, and also obtain measurements of upper ocean microstructure and air-sea CO₂ exchange. As shown in Figure 3.1, the ship departed Vigo, Portugal on 31Aug2013 at 17:00 GMT, and sailed northwest to the PAP site, before returning to Santander, Spain, at 11:30 GMT on 16Sep2013.

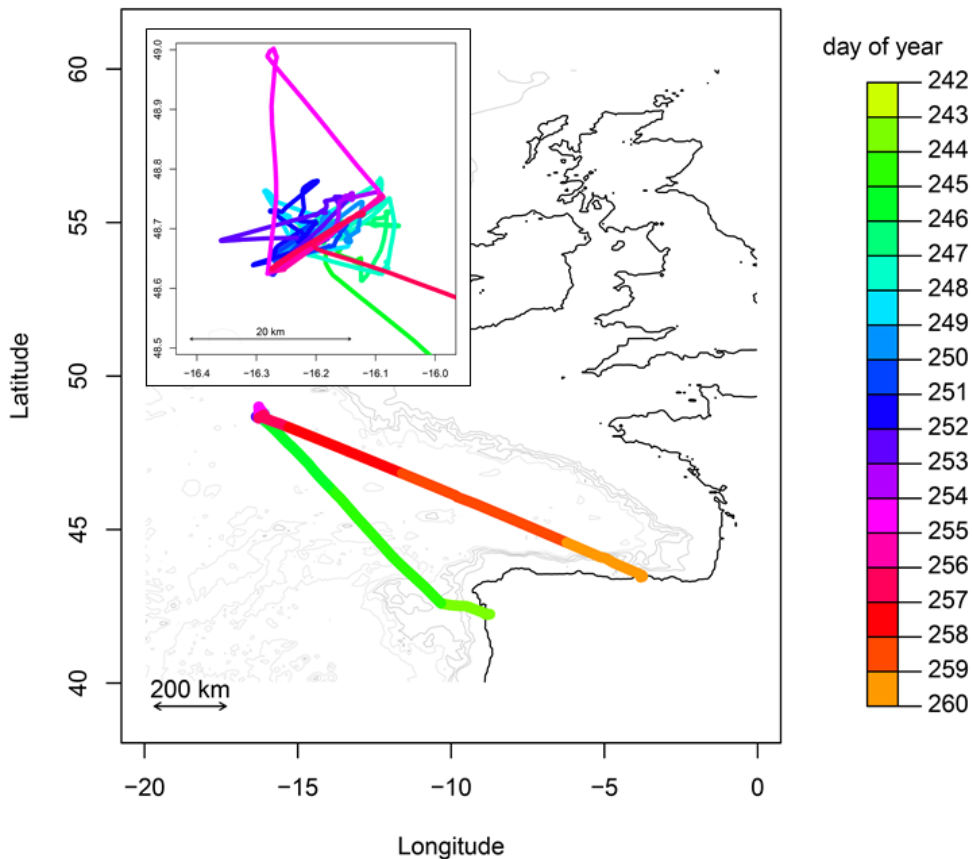


Figure 3.1. Bathymetric map showing the route of the RRS James Cook during the research cruise, from Vigo, Portugal, to the PAP site, and returning to Santander, Spain. Colours correspond to ordinal dates (where day 242 is 30Aug2013). The inset shows a zoomed version of the ship’s route in and around the PAP site.

3.2 Measurement system description, technical setbacks and complementary data

3.2.1 Description of O₂ and CO₂ measurement system

The O₂ and CO₂ measurement system was installed in the Meteorological Laboratory (Met Lab), located on the Boat Deck of the ship (see Figure 3.2). Air was pumped into the Met Lab via two aspirated air inlets (AAIs) (see Chapter 2, Section 2.2.3.1 for full description) connected to ½” outside diameter (OD) Synflex 1300 tubing. One AAI was mounted on the ship’s foremast, and the other on the front, right-hand corner of the bridge roof, also known as the Monkey Island (as shown in Fig. 3.2). The AAIs were deliberately installed in two different locations, to investigate whether data collected by the AAI located close to the ship’s exhaust stack (i.e. the Monkey Island AAI) would be more polluted by the exhaust fumes than data collected by the more distant AAI (on the foremast). Air was sampled from both AAIs, switching between the two intake lines every 30 minutes. The length of tubing from the foremast AAI to the measurement system was approximately 25m, and the length of tubing from the Monkey Island AAI to the measurement system was approximately 65m.

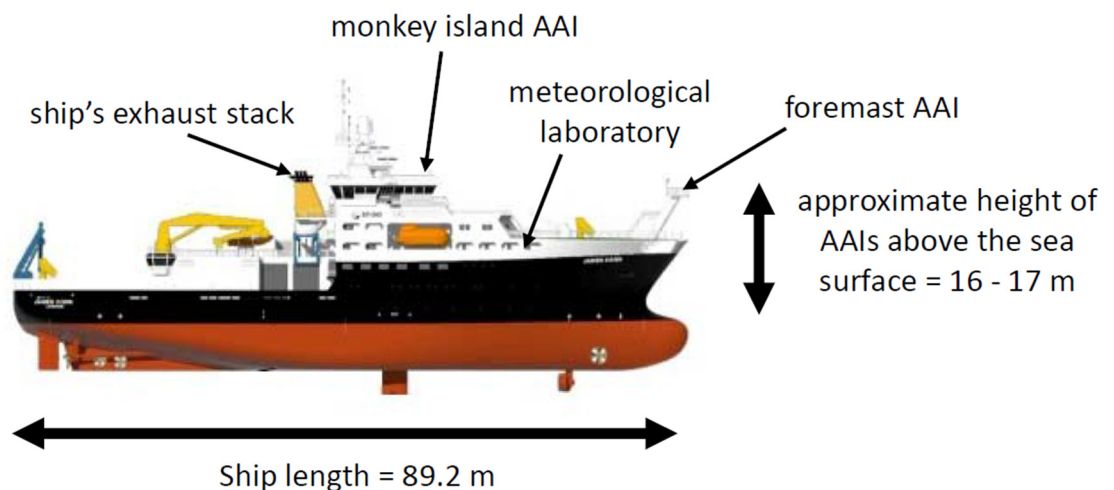


Figure 3.2. Schematic of the RRS James Cook, showing the locations of the meteorological lab and ship’s exhaust stack, and the position of the AAIs (image adapted from <http://noc.ac.uk/research-at-sea/ships/rrs-james-cook>).

The O₂ and CO₂ measurement system design and layout for the duration of the JC090 cruise was almost identical to the final design and layout described in detail in

Chapter 2 of this thesis. Some elements of the system design were modified between the JC090 cruise and the final installation on board the container ship, owing to technical issues that arose when the measurement system was tested at sea for the first time. These technical issues are described below, as are the subsequent modifications to the measurement system.

3.2.2 Technical issues that arose during the JC090 cruise

During the cruise, the measurement system included two Neuberger Inc., KNF N05-ATI pumps, instead of an Air Dimensions Inc., J-Series Dia-Vac pump and a Neuberger KNF N05-ATI pump, as stated in Chapter 2, Section 2.2.3.2. This difference is owing to a failure of one of the Neuberger pumps during the JC090 cruise (which are no longer available to purchase from the manufacturer), resulting from an accumulation of water in the pump head. To my knowledge, a J-Series Air Dimensions pump has not been used before in an O₂ and CO₂ measurement system, hence, I tested the pump for O₂ artefacts before it was incorporated permanently into the system design (see Chapter 2, Section 2.7). The pumps were also re-located from the bottom to the top of the drying rack to prevent future water accumulation in the pump heads.

Another difference between the JC090 and container ship measurement system setups is that during the JC090 cruise, ½" OD Synflex 1300 tubing was used to draw the air from the AAls to the measurement system in the lab, rather than ¼" OD Synflex 1300 tubing, as described in Chapter 2, Section 2.2.3.1. The wider diameter tubing was chosen for the JC090 cruise installation, because of concerns that the length of the inlet lines would result in a large pressure drop if ¼" tubing was used. Pressure measurements just downstream of the Synflex 1300 tubing made during the cruise revealed, however, that there was no detectable pressure drop.

I subsequently carried out a pressure drop calculation, and found that Synflex 1300 tubing with ½" OD, 65m length (corresponding to the length of the longer inlet line), and a flow rate of 100 ml/min, would theoretically result in a pressure drop of only 0.09 mbar. In reality, the inlet line pressure drop during the JC090 cruise was probably slightly larger than this theoretical value, owing to fittings in the lines, such as filters. Re-calculating this theoretical pressure drop with 200m of ¼" OD Synflex 1300 tubing (a maximum estimate of the length of tubing that would potentially be required for installation on the container ship), and the same flow rate of 100 ml/min, produced a pressure drop of only 6.95 mbar. Hence, I decided that for the

final installation on the container ship, ¼" OD Synflex 1300 tubing should be used, instead of ½" OD, since the pressure drop would be small and the residence time of the air in the tubing would be substantially reduced by using the thinner tubing. A residence time calculation showed that for 200m of ½" OD Synflex 1300 tubing and a flow rate of 100 ml/min, air would take 2 hours and 26 minutes to travel from the AAI to the measurement system, compared to only 29 minutes using ¼" OD Synflex 1300 tubing; since a residence time of more than 2 hours is extremely long, it was therefore very preferable to use the ¼" OD Synflex 1300 tubing for the final installation. For a full description of the pressure drop equations I used in these calculations, refer to Appendix A.

During the JC090 cruise, the working tank delivery pressure was controlled via three single stage GO LG1-Series regulators, rather than the Gas-Arc Group Ltd. Spec Master multi-stage regulators mentioned in Chapter 2, Section 2.3.1. Unfortunately, the GO regulators proved to be unreliable, as the delivery pressure kept drifting upwards and had to be reduced at least daily throughout the cruise. Hence, I replaced the GO regulators with Gas-Arc regulators after the cruise, which are suitable for use with the high pressure of the working tank cylinders (up to 300 bar), but are also stable over long periods of time. Since, to my knowledge, the Gas-Arc regulators have not been used before in an O₂ and CO₂ measurement system, they were tested for O₂ artefacts (see Chapter 2, Section 2.7) before being incorporated permanently into the measurement system.

In addition to the main system changes mentioned above, there were several smaller changes made to the electronic components to make them more ship-worthy, such as replacing the AAI blowers and electrical connectors with waterproof counterparts, and ensuring that all the crucial electrical cables and connectors were secured so that they would not become loose in transit or as a result of the ship's motion.

Finally, the experience of the JC090 cruise highlighted two other important technical issues. Firstly, the importance of switching between two air inlet sampling lines became apparent to me, when a CO₂ mole fraction offset of approximately 1-2 ppm developed between the Monkey Island and foremast lines, owing to a leak in the Monkey Island inlet line. If the Monkey Island inlet line had been the sole air sample inlet, it is likely that this leak would have gone unnoticed, and the bias in CO₂ data would not have been detected. Since there was no line switching sweepout capability in the software at the time of the JC090 cruise (see Chapter 2, Section 2.5 for more

details regarding the software), 5 minutes of the O₂ and CO₂ data were discarded following every switch of V1 (the inlet line switching valve), to ensure there were no artefacts introduced into the dataset as a result of the line switching.

Secondly, the Oxzilla II individual fuel cell data from the SEC file (see Appendices C and D for descriptions of Nemo software file outputs) reveal relatively large variations (of up to 0.002%; un-calibrated analyser response units) superimposed on the measurement signal (see Figure 3.3). These large variations occurred throughout the duration of the cruise with a frequency of approximately 5-6 wavelengths per minute, and affected both fuel cells similarly. There are no such variations present in any of the SEC data from testing the measurement system in the laboratory at UEA (University of East Anglia, UK); however, since the Oxzilla II is very sensitive to small changes in atmospheric pressure, the large variations in the cruise data are likely to be the result of small decreases and increases in atmospheric pressure as the ship moves up and down, respectively (Britton Stephens, personal communication, 2013).

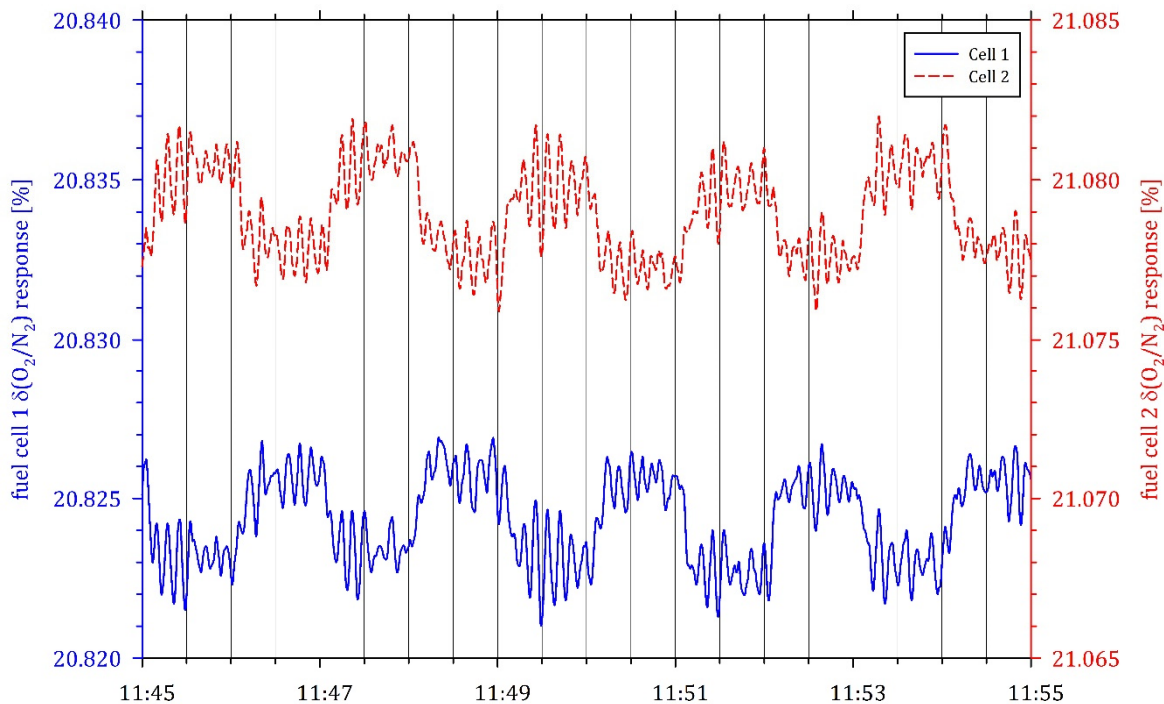


Figure 3.3. Un-calibrated Oxzilla II fuel cell data during the JC090 cruise, showing the large variations caused by the ship's motion superimposed on the 1-minute switching of the sample and working tank. Data are from the SEC file, recorded on 10Sep2013. Vertical grid lines are shown at 30 second intervals.

I tested this theory in the laboratory at UEA after the JC090 cruise by slowly moving the Oxzilla II vertically up and down to imitate the vertical motion of the ship, and was able to produce very similar variations in the fuel cell responses. Since both

fuel cells are affected similarly, the large variations in the ship SEC data cancel out when the fuel cell difference (ΔO_2) is calculated, and thus is not noticeably detrimental to the precision of the JC090 O_2 measurements.

3.2.3 Complementary data used in analyses

In addition to the atmospheric O_2 and CO_2 measurements made by my system, there were many other oceanographic and meteorological measurements made during the JC090 cruise that are very complementary to my measurements, and have facilitated more in-depth analyses of my atmospheric data, in particular with respect to the analysis of short-term events.

The James Cook meteorological data, provided by Martin Bridger (NERC), have been extremely useful for identifying CO_2 data that are polluted by the ship's exhaust, and for determining whether variations in the atmospheric O_2 and CO_2 data are due to changes in atmospheric transport, or due to local fluxes.

The James Cook underway system data (including seawater temperature, salinity, and fluorescence), provided by Alex Forryan (National Oceanography Centre, Southampton, UK), have also been very useful for examining whether variations in the atmospheric O_2 and CO_2 data reflect changes in the biochemical and physical properties of the surface seawater in the immediate locality of the ship. These data were measured at approximately 5.5 m depth below the sea surface.

Continuous data of the partial pressure of CO_2 in seawater and air were provided by Vassilis Kitidis from PML (Plymouth Marine Laboratory, UK). I have used these data to investigate biases in air-sea CO_2 fluxes that arise from inaccuracies in atmospheric CO_2 measurements. The PML CO_2 measurement system comprised of a vented-showerhead equilibrator to extract the CO_2 gas from the seawater and an infrared analyser to measure CO_2 mole fractions (LI-840, LI-COR Inc.), and is described in (Hardman-Mountford et al., 2008).

Lastly, the partial pressure of O_2 in seawater was measured from nine depth profiles, using a SeaBird SBE43 optode sensor mounted onto a CTD (conductivity, temperature and depth profiler), the data for which were made available by Alex Forryan. I have used these dissolved O_2 data to investigate air-sea exchange of O_2 , and to determine whether variations observed in my atmospheric O_2 data could be caused by local biogeochemical or physical processes, such as biological activity and ocean upwelling.

3.3 Data flagging

3.3.1 Preliminary results

The entire data set of 2-minute O_2 and CO_2 averages from the JC090 cruise is shown in Figure 3.4, prior to any post-software processing. Fig. 3.4 also shows the APO data, which are calculated from the O_2 and CO_2 data, whereby $APO = O_2 + (-1.1 \times CO_2)$. Although the ship departed Vigo on 31Aug2013, it took approximately a week to finish assembling and testing the equipment; hence, reliable measurements did not begin until 06Sep2013. The repeatability and compatibility of the O_2 and CO_2 measurements made during the JC090 cruise are discussed in Chapter 2, Section 2.4.

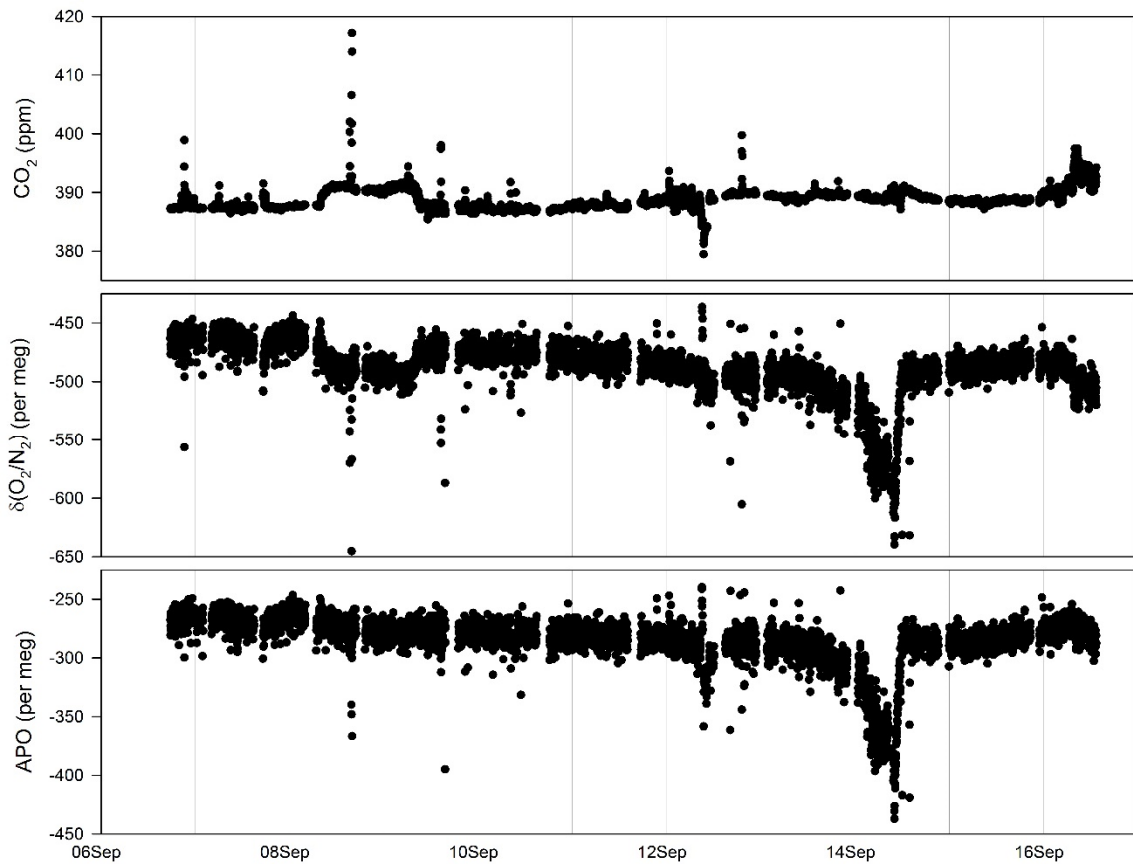


Figure 3.4. CO_2 , $\delta(O_2/N_2)$ and APO data from the JC090 cruise (2-minute frequency). The y-axes have been scaled to be visually comparable on a mole per mole basis (since 1 ppm $CO_2 \sim 5$ per meg $\delta(O_2/N_2)$). Gaps in the data correspond to periods when calibration cylinders were being analysed.

Fig. 3.4 immediately reveals several features in the data, including: an event of elevated CO_2 and reduced O_2 , but no change in APO on the 08-09Sep2013; a short negative excursion in CO_2 and APO, but no change in O_2 on 12Sep2013; and a negative O_2 and APO excursion, with no corresponding signal in CO_2 on 13-14Sep2013. There

are also numerous short-term positive and negative spikes apparent in the CO₂ and O₂ data, respectively. In order to assess whether these excursions represent real changes in the atmospheric O₂, CO₂ and APO, or whether they are the result of local pollution and/or technical problems with the measurement system (e.g. calibration issues), the measurement system diagnostic data were analysed.

3.3.2 Flagging of O₂, CO₂ and APO data, based on analysis of diagnostic parameters

There are several potential sources of error in the O₂ and CO₂ measurement system that could result in erroneous data, some of which would go unnoticed if it were not for the extensive range of diagnostic data that is also collected (such as measurement system flow rates and pressures). These sources of error include poor calibration parameters (i.e. inaccurate values of the O₂ and CO₂ slope and intercept, and non-linearity in the CO₂ slope), leaks, flow disruptions, temperature and pressure changes, general malfunctions of the measurement system parts, and human errors when manually over-riding the system controls. There were several periods during the JC090 cruise when measurement system problems resulted in erroneous data, which have been flagged as 'bad' and are not included in the following analyses of the data set. In total, 13.9% of the data were excluded from further analyses of the dataset. Note that the data presented in Chapters 4 and 5 of this thesis have also been flagged using the measurement system diagnostic data, in order to exclude 'bad' data from subsequent analyses.

3.3.3 Flagging O₂, CO₂ and APO data contaminated by the ship's exhaust fumes

Fig. 3.4 shows that there are numerous positive spikes in the CO₂ data set, and often corresponding negative spikes in the O₂ data set. These anti-correlated short-term spikes in the CO₂ and O₂ data are most likely caused by contamination from the ship's exhaust, and were therefore removed prior to any further analyses of the data. The pollution spikes were identified via a two-phase automated flagging routine, written in the R programming language. The first phase involves fitting a baseline to the CO₂ data, using the 'rftbaseline' function from the 'IDPmisc' R package, and calculating the $\pm 1\sigma$ standard deviations of the residuals from the baseline (SD_{res}). Any residuals that were > 2 times larger than SD_{res} were flagged as polluted data.

Additionally, any CO₂ residuals that were > 1.5 times larger than SD_{res}, and also adjacent to a data point that had already been flagged, were also flagged. The second phase flagged the corresponding O₂ and APO data (i.e. the O₂ and APO data at the same time stamps as the flagged CO₂ data).

The collective O₂, CO₂ and APO data that were flagged in this manner are referred to as ‘statistically flagged’, and indicate data that are polluted. The source of this pollution generally appears to be the ship’s exhaust fumes, although not all of the data that correspond to periods when the relative wind direction was from the ship’s stack (relative wind direction of ~200°-240°, depending on the AAI) are polluted. Further investigation reveals that some of the ‘statistically flagged’ data coincide with periods when the relative wind direction was from 180°-260° and also when the relative wind speed was less than 5 m s⁻¹. Hence, these data are referred to as ‘meteorologically flagged’.

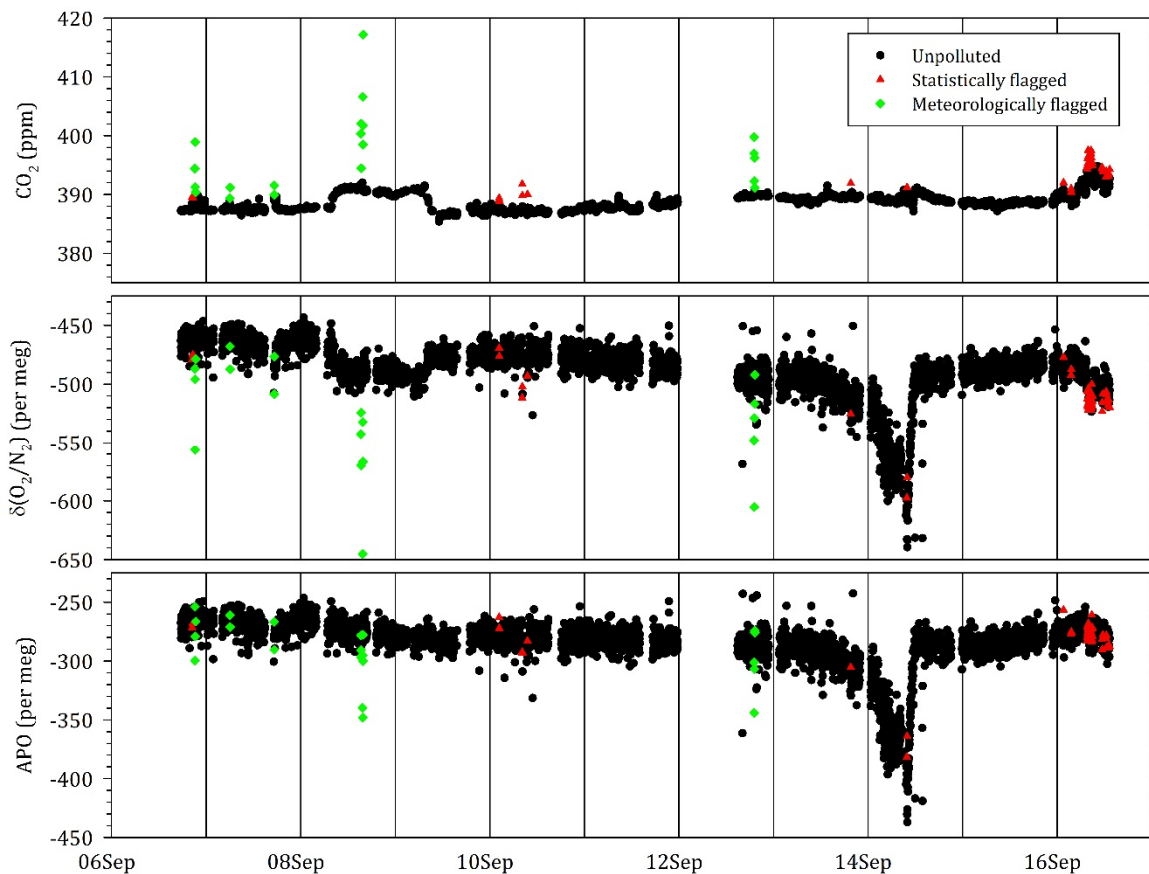


Figure 3.5. Unpolluted (black circles), statistically flagged (red triangles) and meteorologically flagged (green diamonds) CO₂, $\delta(O_2/N_2)$, and APO data. The CO₂, $\delta(O_2/N_2)$ and APO y-axes have been scaled to be visually comparable to each other on a mole per mole basis.

Figure 3.5 shows the O₂ and CO₂ data, with the statistically and meteorologically flagged pollution spikes. The majority of the pollution spikes are meteorologically flagged, except for at the end of the cruise. This is because the

pollution on 16Sep2013 is caused by proximity to the coast of Spain, and is not from the ship's exhaust. The mean $O_2:CO_2$ ratio of the pollution spikes is -1.38 (see Figure 3.6), which gives high confidence that these data are polluted, and not representative of terrestrial biosphere processes, since the oxidative ratios of fuel oil range from -1.39 to -1.44 (Keeling, 1988). In total, only 1.7% of the O_2 , CO_2 and APO data were identified as statistically or meteorologically polluted and were removed from further analyses of the dataset.

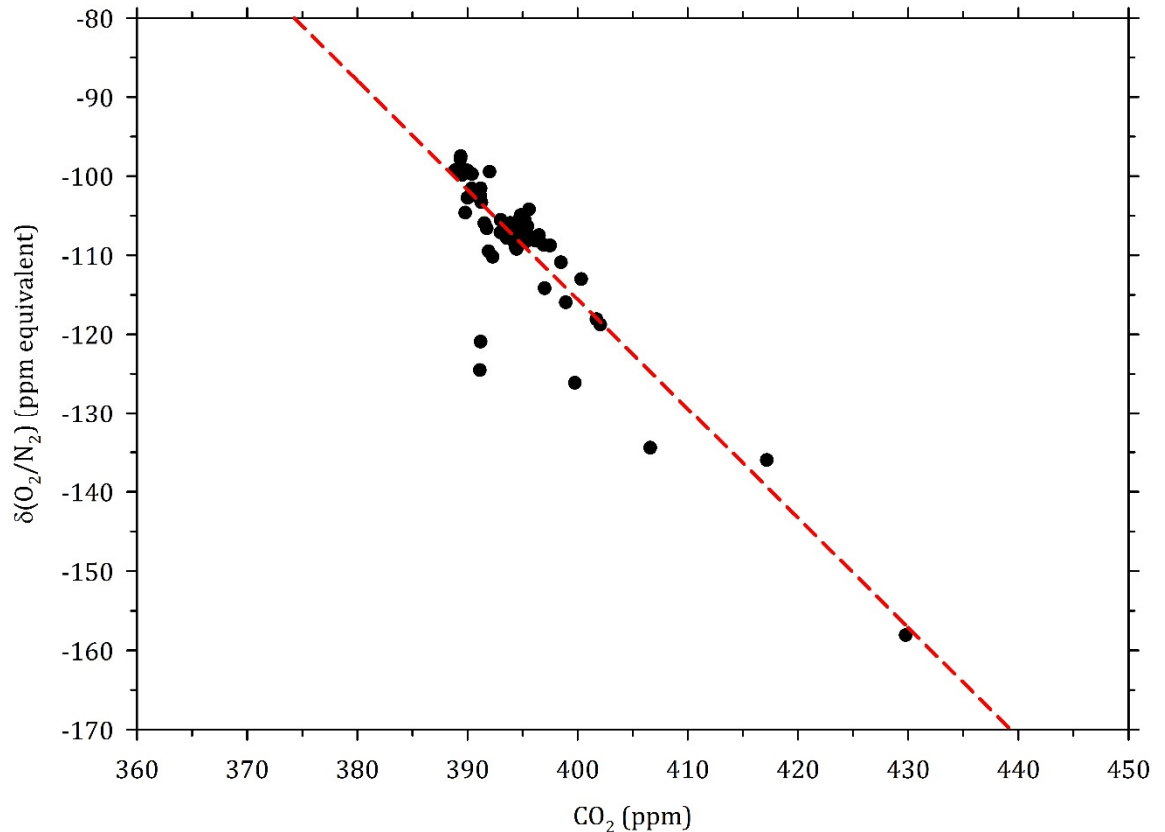


Figure 3.6. $O_2:CO_2$ ratio plot of the statistically and meteorologically flagged pollution spike data. $\delta(O_2/N_2)$ is given in ppm equivalent units (i.e. $\delta(O_2/N_2)$ ppm equivalent units = $\delta(O_2/N_2)$ per meg/4.77) to be comparable to CO_2 and enable correct calculation of the regression slope. The red dashed line indicates the major axis regression line, which has a slope of -1.38. The regression was weighted according to the difference in measurement uncertainty associated with the $\delta(O_2/N_2)$ and CO_2 data.

No difference was found between the occurrence of the pollution spikes when air was sampled from the red line (Monkey Island) compared to the blue line (foremast). In addition, there were some periods of polluted data that spanned a switch from one line to the other, which indicates that air sampled from each AAI was similarly affected by the ship's exhaust fumes, even though the red line AAI was located much closer to the ship's stack than the blue line AAI.

3.4 Results and Data Analysis

3.4.1 Comparison of CO₂ mole fractions with those measured by PML, and consequences for CO₂ flux estimates

As mentioned in Section 3.2.3, an atmospheric and dissolved seawater CO₂ partial pressure measurement system (hence referred to as a pCO₂ system), maintained by PML, was also operational during the JC090 cruise. Atmospheric CO₂ mole fractions were sampled from an inlet on the foremast, close to the foremast inlet of the UEA atmospheric O₂ and CO₂ measurement system. Figure 3.7 shows hourly averages of both the PML and UEA atmospheric CO₂ mole fractions. The PML pCO₂ system is much less precise than the CO₂ measurements made by the UEA O₂ and CO₂ measurement system, since a precision of only ± 1 ppm is required in order to calculate sufficiently accurate air-sea CO₂ fluxes, whereas a precision of $< \pm 0.1$ ppm is required in order to meet the WMO (World Meteorological Organization) compatibility goal for CO₂ measurements in the northern hemisphere (Tans and Zellweger, 2013). This difference in precision is most likely the reason why there is more detail visible in the UEA atmospheric CO₂ data, and more noise visible in the PML atmospheric CO₂ data.

Fig. 3.7 also shows that the PML data are on average lower than the UEA data by ~ 1.5 ppm. Owing to the extensive calibration procedures employed by the UEA O₂ and CO₂ system, I have high confidence in the accuracy of the atmospheric CO₂ data from the UEA measurement system; even though the UEA CO₂ measurements were calibrated on the Scripps CO₂ scale during the JC090 cruise and the PML pCO₂ measurements were calibrated on the NOAA CO₂ scale, CO₂ cylinder measurements made on both scales at UEA reveal that at ~ 390 ppm, the scale differences are small (< 0.1 ppm) compared the mean difference found between the PML and UEA atmospheric CO₂ data. In contrast, the PML pCO₂ measurement system was calibrated only once prior to the JC090 cruise, and not at all during the cruise. In addition, prior to the JC090 cruise, the PML pCO₂ system had a history of technical issues and poor performance (Dan Comben, National Oceanography Centre, Southampton, UK; personal communication, 2013). Therefore, it is likely that the CO₂ data measured by my system are more accurate than those measured by the PML system, although this is a tentative conclusion that would need to be confirmed by re-defining the UEA

measurement system calibration cylinders against primary standards in the lab to ensure that the CO₂ mole fractions of the cylinders have not drifted over time.

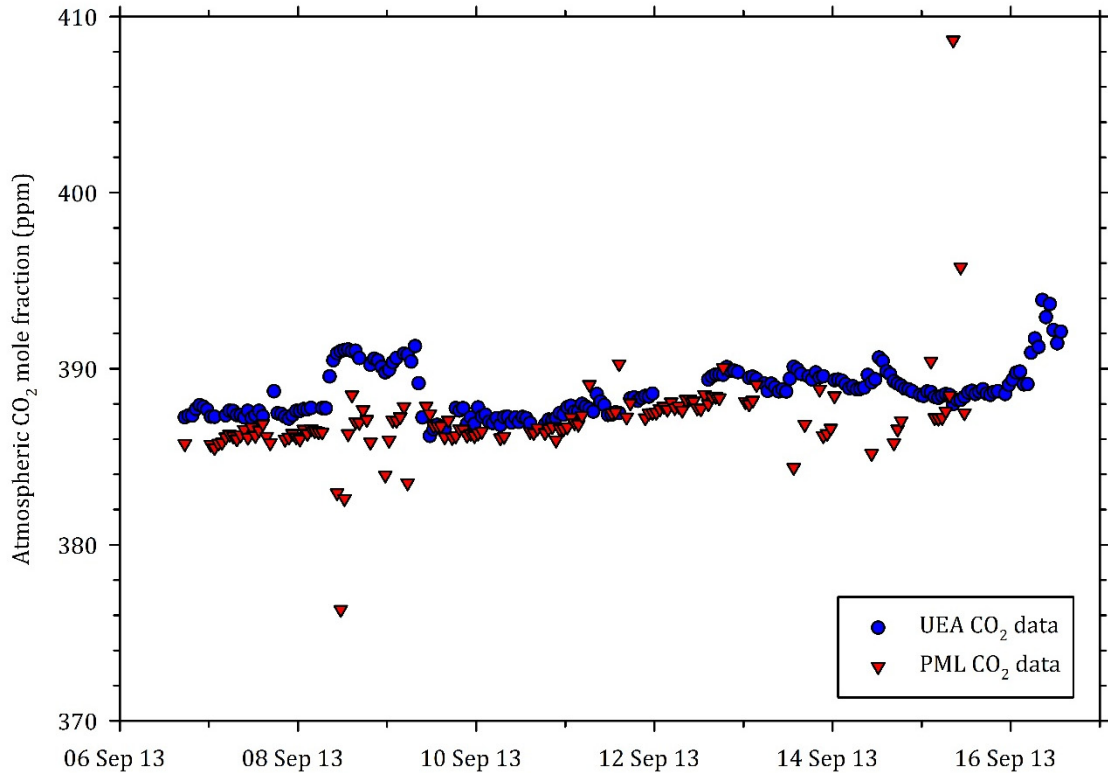


Figure 3.7. Atmospheric CO₂ data from the UEA O₂ and CO₂ measurement system (blue circles) and the PML pCO₂ measurement system (red triangles) during the JC090 cruise.

It is interesting to consider the implications of a ~1.5 ppm atmospheric CO₂ mole fraction offset on the calculation of the air-sea CO₂ flux. I calculated a time series of the air-sea CO₂ flux using the UEA atmospheric CO₂ mole fraction data and the PML seawater pCO₂ data, and compared this flux time series to that calculated by Vassilis Kitidis using the PML atmospheric and seawater pCO₂ data. First, I converted the UEA atmospheric CO₂ mole fractions into atmospheric CO₂ partial pressures, using Equation 3.1:

$$pCO_2(\text{air}) = vCO_2(\text{air}) \times (P_b - P_w) \quad (\text{Eq. 3.1})$$

where $vCO_2(\text{air})$ is the UEA atmospheric CO₂ mole fraction, P_b is the barometric pressure at the sea surface in atmospheres, and P_w is the equilibrium water vapour pressure in atmospheres calculated using the equation from (Weiss and Price, 1980). I then calculated the air-sea CO₂ flux in mol m⁻² yr⁻¹ using Equation 3.2:

$$\text{Flux} = k_0 \cdot k_{CO_2} \cdot \Delta pCO_2 \quad (\text{Eq. 3.2})$$

where k_0 is the solubility of CO_2 in seawater calculated from the temperature and salinity dependent equation of (Weiss, 1974), k_{CO_2} is the CO_2 gas transfer piston velocity calculated from wind speed using the equation of (Wanninkhof, 1992), and $\Delta p\text{CO}_2$ is the difference between the partial pressure of the atmospheric CO_2 (from Eq. 3.1) and the partial pressure of the seawater CO_2 .

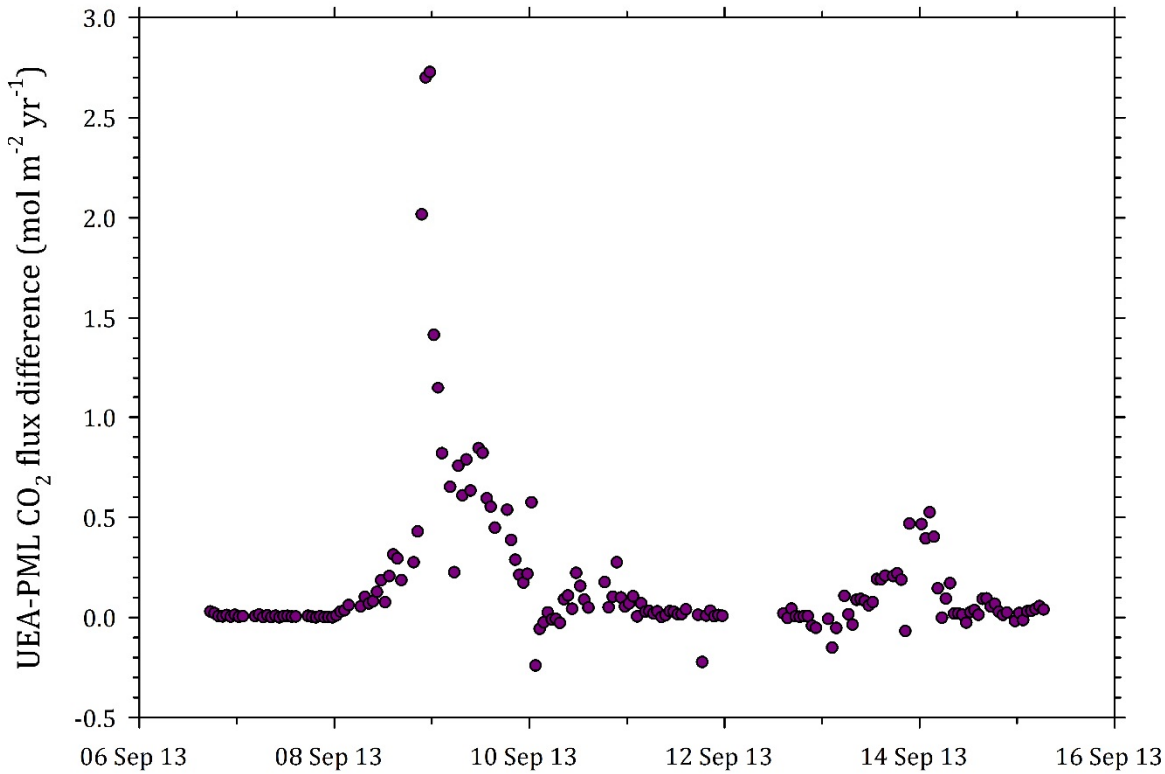


Figure 3.8. Difference between air-sea CO_2 flux calculated using UEA and PML atmospheric CO_2 mole fractions from the JC090 cruise. Positive values indicate that the UEA flux from the atmosphere into the ocean is greater than the PML flux. The overall mean CO_2 flux difference is $0.1731 \text{ mol m}^{-2} \text{ yr}^{-1}$.

Figure 3.8 shows the UEA-PML difference in air-sea CO_2 flux, and demonstrates that the higher atmospheric CO_2 values measured by the UEA system generally result in higher air-to-sea fluxes of CO_2 compared to those calculated using the PML atmospheric measurements. This is expected, since the partial pressure of CO_2 in the seawater is lower than that measured in the atmosphere on both systems; therefore, there is a greater difference between the air and seawater CO_2 partial pressures for the UEA atmospheric measurements than for the PML atmospheric measurements, resulting in a greater flux. The greatest differences also coincide with the CO_2 event on 09-10 Sep 2013, which is clearly visible in the UEA atmospheric CO_2 data, but hard to distinguish in the PML atmospheric CO_2 data. The mean difference between the PML and UEA air-sea CO_2 fluxes is $0.1731 \text{ mol CO}_2 \text{ m}^{-2} \text{ yr}^{-1}$, which is equivalent to $2.058 \text{ gC m}^{-2} \text{ yr}^{-1}$, or $0.1716 \text{ gC m}^{-2} \text{ month}^{-1}$. Given that the mean air-sea

CO₂ flux in the North Atlantic in winter is in the region of 2 grams C m⁻² month⁻¹ (Takahashi et al., 2009) and the mean air-sea CO₂ flux for the JC090 cruise was 3.394 gC m⁻² month⁻¹, the mean difference in air-sea flux calculated using the UEA versus PML atmospheric CO₂ data (a difference of only ~1.5 ppm) represents a flux bias of about 9% and 5%, respectively. This highlights the importance of using accurate atmospheric (and oceanic) measurements of CO₂ when calculating air-sea fluxes, and indicates that high-precision atmospheric CO₂ measurements could help to eliminate biases in air-sea fluxes, particularly when datasets from multiple ships are combined. Improvements in the accuracy of atmospheric CO₂ measurements from the oceanographic community might lead to atmospheric CO₂ data from pCO₂ measurement systems being included in the global atmospheric network, which would benefit the atmospheric community, by enabling separation of the two major northern hemisphere terrestrial carbon sinks (in North America/Canada and Asia).

3.4.2. Baseline data

The baseline of the shipboard CO₂ data in Figure 3.9 (i.e. excluding the short-term events) is approximately 387.5 ppm on 07Sep2013, rising to about 389.25 ppm on 16Sep2013, which is ~1.5 ppm lower than the continuously measured CO₂ baseline from Weybourne, located on the north Norfolk coast (Fig. 3.9, top panel, pink line). This is most likely because the shipboard data were collected at a lower latitude than Weybourne, and the seasonal cycle amplitude in CO₂ is attenuated at lower latitudes. The shipboard CO₂ baseline does, however, compare well with flask sampled CO₂ measurements from Mace Head, Ireland (not shown), which often receives air from the North Atlantic region, whereas the air arriving at Weybourne tends to originate either from the North Sea (and sometimes the Arctic), or from the south of the UK (including London) and Europe. Alternatively, a CO₂ calibration scale offset between the shipboard and Weybourne measurement systems could also contribute to the difference in CO₂ baseline concentration; however, it is unlikely that a calibration offset as large as 1.5 ppm would arise from cylinders prepared in the same laboratory at UEA, and therefore the difference in CO₂ baseline between the two datasets is most likely largely caused by differences in the air mass origins arriving at the two measurement locations.

The increase in the shipboard baseline CO₂ mole fraction corresponds with the northern hemisphere seasonal cycle of CO₂; the CO₂ baseline increases in September

as respiration dominates over photosynthesis, resulting in net CO₂ release from the land biosphere. There is a corresponding decrease in O₂, from approximately -462.5 per meg on 07Sep2013, to about -484.5 per meg on 16Sep2013. The shipboard O₂ baseline compares well to the Weybourne O₂ baseline (Fig. 3.9, second panel, pink line). It is expected that an increase in atmospheric CO₂ of 1.75 ppm due to land biospheric processes would cause atmospheric O₂ to decrease by 9.24 per meg, because the mean O₂:CO₂ ratio of biospheric processes is -1.1 (and 1 ppm CO₂ ~ 4.77 per meg O₂). The measured decrease in atmospheric O₂ is larger in magnitude than this expected decrease in atmospheric O₂, because the seasonal change in atmospheric O₂ is not only caused by a net drawdown of O₂ into the land biosphere (owing to the dominance of respiration over photosynthesis), but also from three oceanic seasonal processes, which have similar phasing as the land biosphere seasonal processes.

The first of these oceanic processes is the air-sea flux of O₂ corresponding to the seasonal change in ocean temperature. In summer, the temperature of the upper ocean warms, resulting in a net flux of O₂ from the seawater to the atmosphere, and vice versa in winter, owing to the temperature-dependence of the solubility of O₂ in seawater. Since the atmospheric O₂ data are measured as $\delta(\text{O}_2/\text{N}_2)$ ratios, the temperature-dependence of the solubility of N₂ in seawater reduces the effect on the atmospheric O₂ data by about 44% (Keeling and Shertz, 1992). The second process arises due to the dominance of phytoplankton photosynthesis over respiration in the euphotic zone, which occurs during the spring and summer, causing a net flux of O₂ from the ocean to the atmosphere. Conversely, in winter, the dominance of respiration in the euphotic zone, combined with vertical transport of deeper, O₂-depleted waters from below the euphotic zone (resulting from greater wind-driven circulation) causes a net flux of O₂ from the atmosphere to the ocean (Keeling and Shertz, 1992). Thirdly, the effect of increased ventilation of deep ocean waters owing to autumn and winter storms also decreases atmospheric O₂ (whilst increased stratification in the summer reduces the ventilation of deep ocean waters), since deep waters are old and depleted in O₂ (from respiration at depth), which causes a flux of O₂ from the atmosphere to the ocean.

The effects of these three processes on the seasonal cycle of atmospheric O₂ can be seen in the changing baseline of the APO data, which decreases more gradually than the atmospheric O₂ baseline, from approximately -266.5 per meg on 07Sep2013 to about -279 per meg on 16Sep2013. APO is conservative with respect to land

biosphere processes; hence, the seasonal variation in APO is reduced compared to atmospheric O₂, because the APO baseline changes are due to oceanic processes only, since there is little discernible seasonality in northern hemisphere fossil fuel emissions. As for O₂, the shipboard APO baseline compares well to the Weybourne APO baseline. The difference between the decrease in O₂ and the decrease in APO over the period of the cruise is 9.5 per meg. This value represents the atmospheric O₂ drawdown caused by land biosphere seasonal processes, and is very similar to the expected value of 9.24 per meg mentioned above, which is inferred from the measured increase in CO₂ baseline.

3.4.3 Short-term events: correlations with meteorological parameters

Fig. 3.9 shows hourly averages of the O₂, CO₂, and APO data with the flagged data based on diagnostic parameters and pollution spikes removed, as well as the temperature and humidity meteorological data from the JC090 cruise. One major difference between Fig 3.4 and Fig. 3.9 is that there are now only two events apparent in the data shown in Fig 3.9: the event on 12Sep2013 characterised by a short negative excursion in CO₂ and APO, but no change in O₂, has been removed from the data set, as this feature was in fact owing to a malfunction with one of the diaphragm pumps (described in 3.2.2). The event on 08-09Sep2013, characterised by elevated CO₂ and a corresponding decrease in O₂ with no change in APO (from here on referred to as ‘event 1’), also coincides with a period of elevated air temperature and humidity. In contrast, the event on 13-14Sep2013, characterised by a negative excursion in O₂ and APO with no change in CO₂ (from here on referred to as ‘event 2’), does not correlate with a change in air temperature or humidity. Analysis of the ship’s absolute wind speed and wind direction data shows that event 1 also coincides with a steady wind speed of about 17.5 m s⁻¹ and a westerly direction (see Figure 3.10; red triangles). Event 2, however, does not correspond to a particular wind speed or direction (see Fig. 3.10; green diamonds).

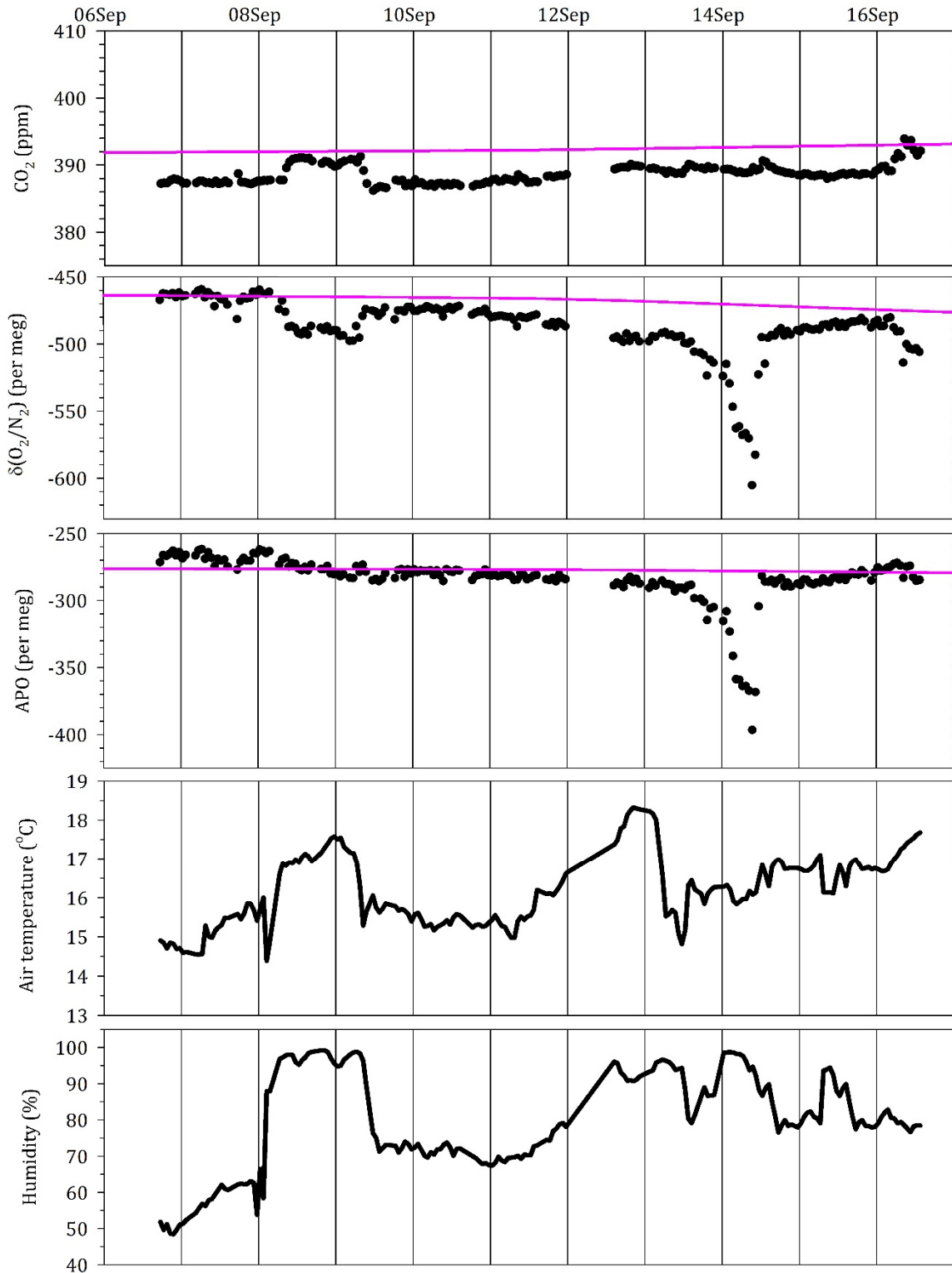


Figure 3.9. Hourly-averaged CO₂, δ(O₂/N₂), and APO data, plotted alongside temperature and humidity data from the RRS James Cook meteorological instruments. The CO₂ y-axis has been scaled so that the data are visually comparable to the δ(O₂/N₂) and APO data. The pink lines on the CO₂, δ(O₂/N₂) and APO plots show the background mole fractions for Weybourne, UK, calculated using the 'rfbaseline' function from the 'IDPmisc' R package.

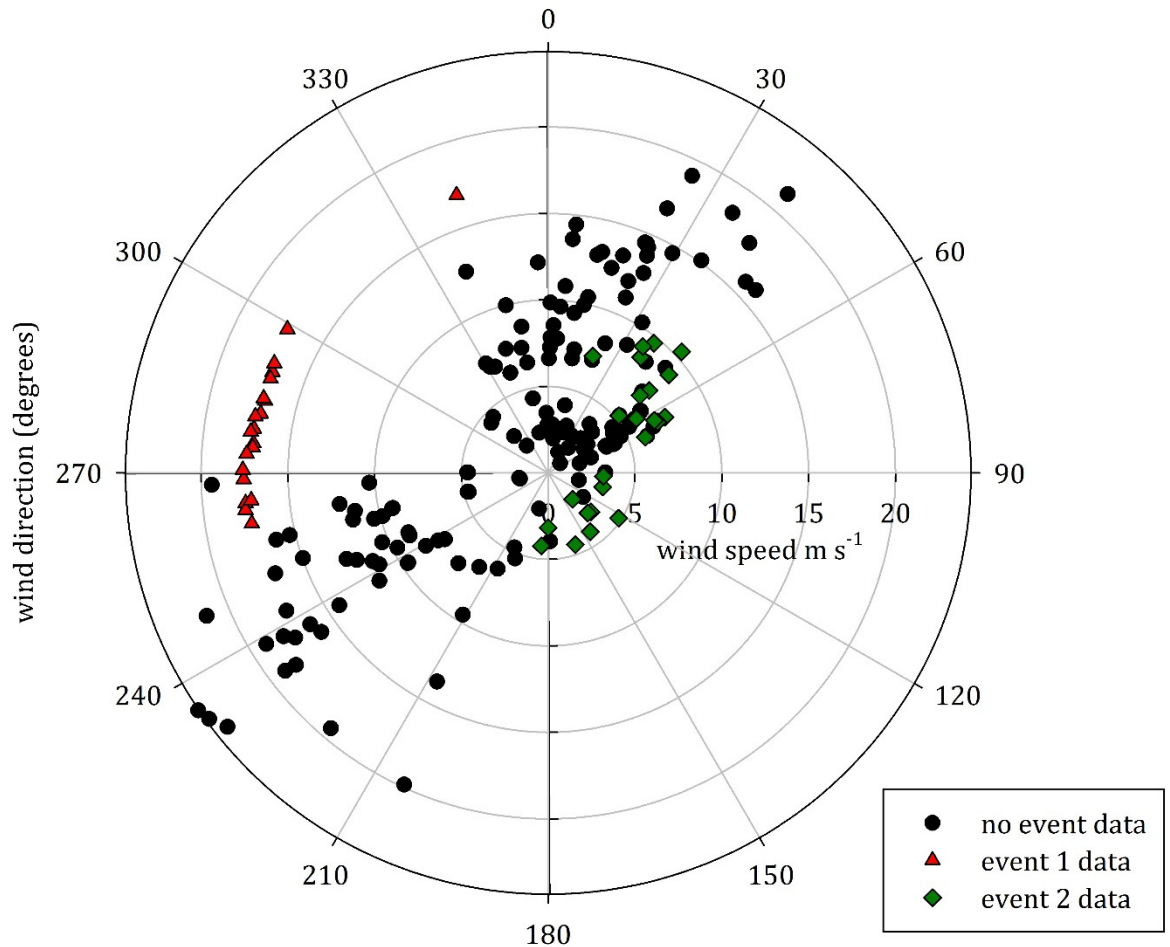


Figure 3.10. Wind rose showing wind speed and wind direction for event 1 data (red triangles), event 2 data (green diamonds), and all other data ('no event data'; black circles).

The correlation matrix plots shown in Figure 3.11 also indicate that event 1 (top plot) is strongly correlated/anti-correlated with several meteorological parameters, particularly air temperature, humidity and wind bearing, while event 2 (bottom plot) is not strongly correlated to any of the meteorological parameters. Figs. 3.9 to 3.11 therefore indicate that event 1 is likely to be caused by a change in atmospheric transport, bringing air to the ship from a more southerly latitude. This agrees with the change in CO_2 and O_2 at this time: the seasonal minimum in CO_2 and maximum in O_2 in the atmosphere occurs during late summer/early autumn (i.e. around the time of the JC090 cruise), and therefore air from a lower latitude would be expected to be higher in CO_2 and lower in O_2 , because the seasonal cycle is attenuated at lower latitudes. Meanwhile, event 2 is more likely to be caused by an oceanic O_2 sink, as indicated by the large negative APO excursion, since APO is conservative with respect to land biosphere fluxes. APO is also affected by fossil fuel combustion,

however, there is no corresponding positive CO₂ excursion, which one would expect if event 2 were caused by fossil fuel pollution.

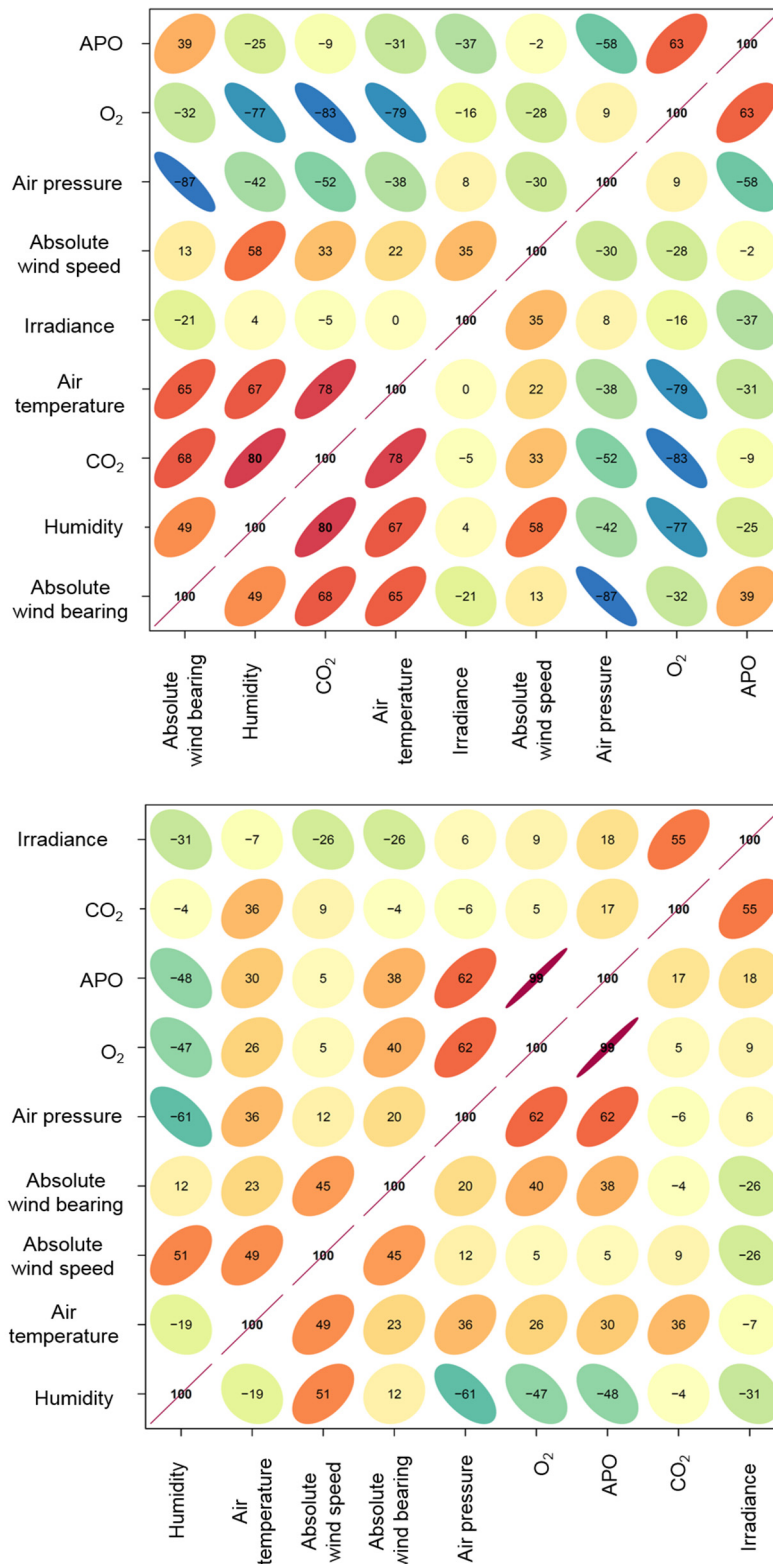


Figure 3.11. Correlation matrices for event 1 (top plot) and event 2 (bottom plot), created using the ‘corPlot’ function from the ‘openair’ package in R (Carslaw and Ropkins, 2012). Numbers indicate the correlation coefficients values from simple linear regressions of the variables. Strong positive correlations are shaded red, and strong negative correlations are shaded blue. The ellipsoids are more round in shape for weak correlations, and more elliptical in shape for strong correlations.

3.4.4 Short-term events: NAME footprints

Figures 3.12 to 3.16 show the distribution and concentration of the air particles arriving at the ship, known as an atmospheric ‘footprint’, and were generated by Zoë Fleming (National Centre for Atmospheric Science, UK) using the UK Met Office Numerical Atmospheric-dispersion Modelling Environment (NAME) model (Jones et al., 2007). The model was run backwards in time for 5 days, and only air particles in the region of 0 – 100 m above sea level are shown. The NAME footprints indicate that before event 1, the majority of air particles that were arriving at the ship were from the North Atlantic region (approximately 50°-55°N), with some influence from southern Greenland (as far as 70°N; see Fig. 3.12). During event 1, the air particles originate from the east (approximately 45°-50°N) with some contribution from lower latitudes in the North Atlantic (as far south as 30°N; see Fig. 3.13). This agrees with the air temperature and humidity data, which indicate that the air was warmer and more humid during event 1. After event 1, the air particles again originate from the North Atlantic, with some influence from Eastern Canada (see Fig. 3.14). During event 2, the origin of the air particles is local to the ship (within approximately 1°-2° latitude and longitude; see Fig. 3.15), and from the southwest (from about 45°N). After event 2, the air particles originate from the North Atlantic, from about 50°-58°N (see Fig. 3.16).

The NAME footprints therefore also indicate that event 1 is most likely caused by a shift in air mass origin from the temperate North Atlantic towards the warmer tropical North Atlantic region, and event 2 is most likely caused by an oceanic drawdown of atmospheric O₂ occurring predominantly locally to the region of the JC090 cruise in the north east Atlantic (at approximately 50°N).

5 day (0–100m) back trajectory of cruise release at: 201309070100

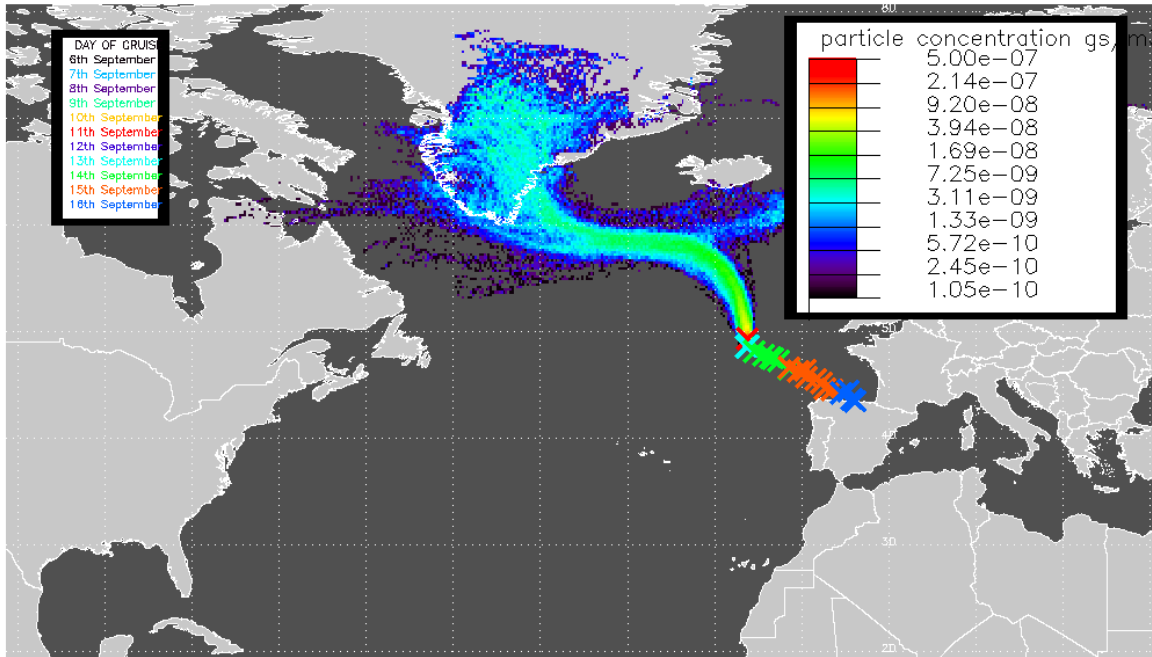


Figure 3.12. NAME footprint showing the origin of the air particles that were measured from the ship before event 1. At this time, NAME shows that the majority of the air particles originated from the northwest. Time-integrated particle concentrations are in units of gs m^{-3} .

5 day (0–100m) back trajectory of cruise release at: 201309082100

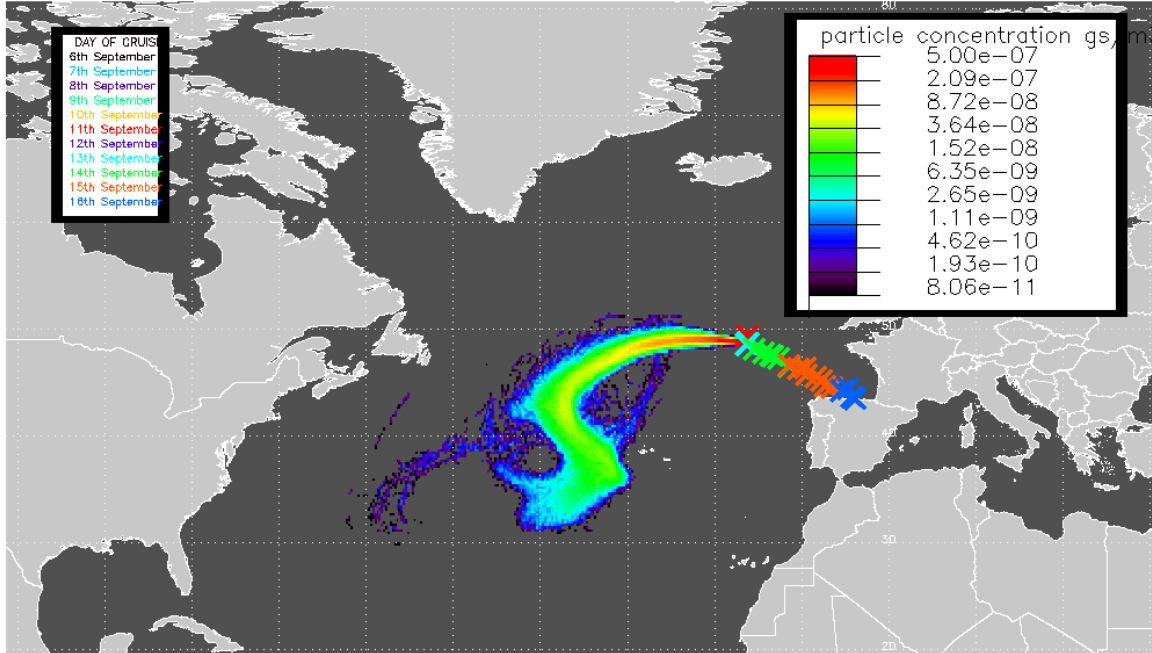


Figure 3.13. NAME footprint showing the origin of the air particles that were measured from the ship during event 1. At this time, NAME shows that the majority of air particles originated from the west and southwest. Time-integrated particle concentrations are in units of gs m^{-3} .

5 day (0–100m) back trajectory of cruise release at: 201309110200

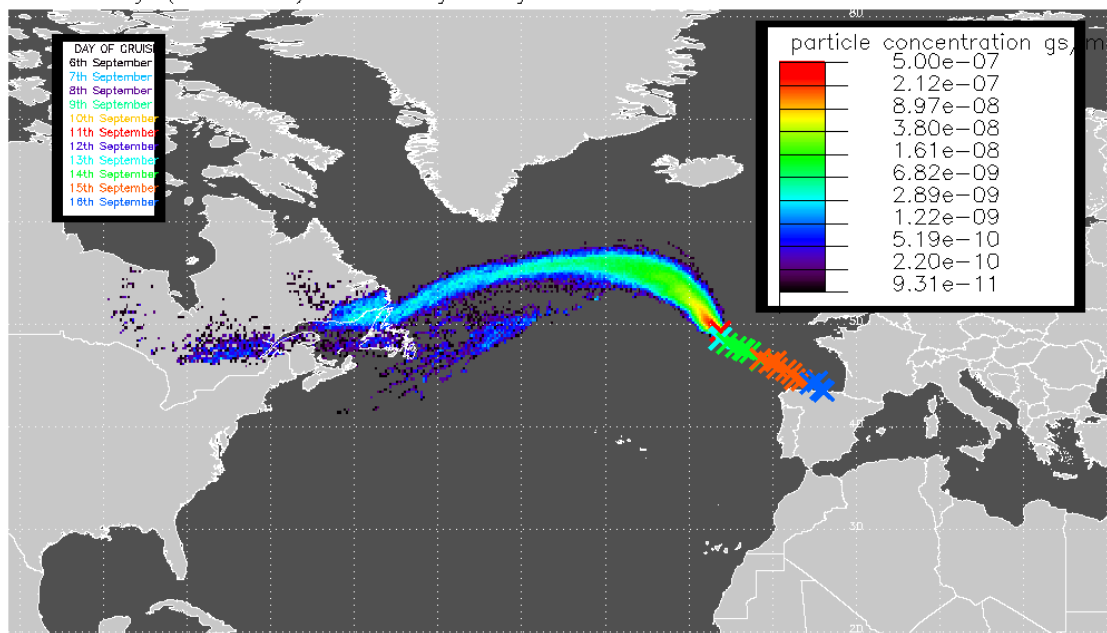


Figure 3.14. NAME footprint showing the origin of the air particles that were measured from the ship after event 1, and before event 2. At this time, NAME shows that the majority of the air particles originate from the northwest. Time-integrated particle concentrations are in units of gs m^{-3} .

5 day (0–100m) back trajectory of cruise release at: 201309140100

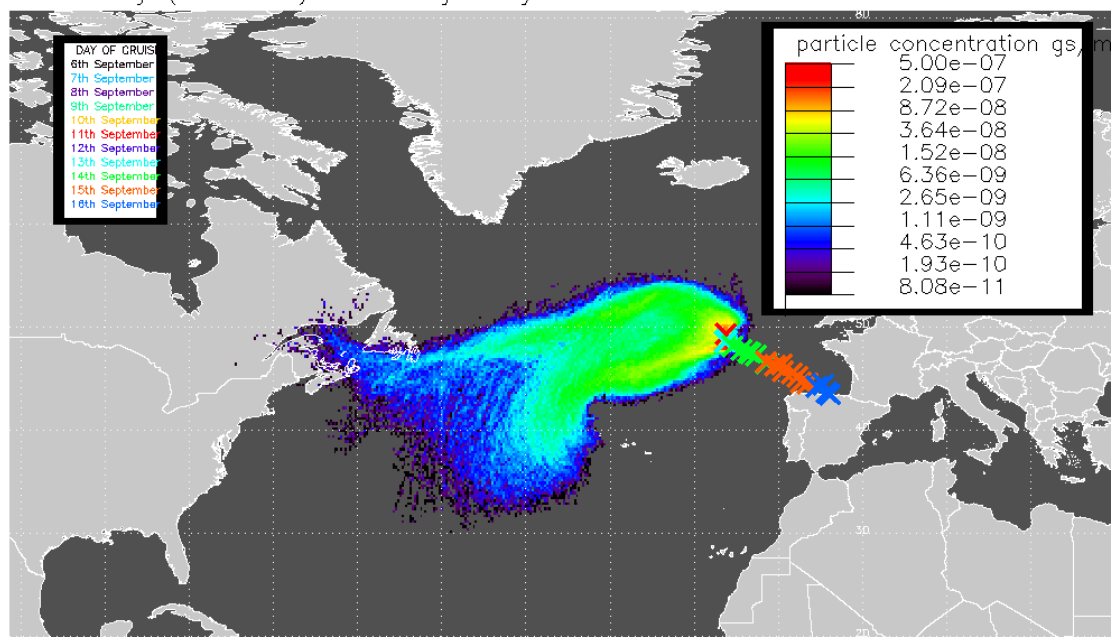


Figure 3.15. NAME footprint showing the origin of the air particles that were measured from the ship during event 2. This figure shows that the air particles were either very local at this time, or from the southwest. Time-integrated particle concentrations are in units of gs m^{-3} .

5 day (0–100m) back trajectory of cruise release at: 201309150500

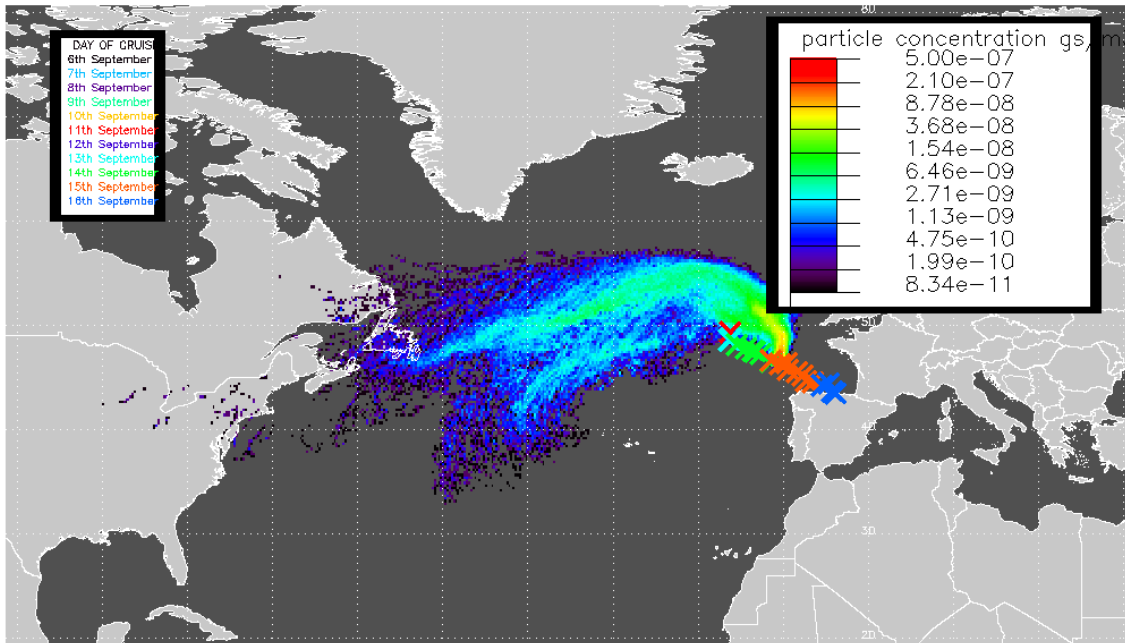


Figure 3.16. NAME footprint showing the origin of the air particles measured from the ship after event 2. NAME shows that most of the air particles originated from the north/northwest and west during this time. Time-integrated particle concentrations are in units of g s m^{-3} .

3.4.5 Short-term events: oxidative ratios

As mentioned previously, calculating the oxidative ratio from concurrent measurements of O_2 and CO_2 data can provide useful information about the source of the air mass arriving at the ship. For the JC090 cruise data, I have split the hourly-averaged data shown in Fig. 3.9 into background air (i.e. data that are not part of an ‘event’, and that represent the well-mixed atmosphere at the location of the cruise), event 1 data, and event 2 data, and I have calculated the $\text{O}_2:\text{CO}_2$ ratio for each group, as shown in Figure 3.17. As described in (van der Laan et al., 2014), I have only included the positive and negative slopes of events 1 and 2 respectively when calculating $\text{O}_2:\text{CO}_2$, since the event termination slopes are more likely to be associated with unstable or turbulent boundary conditions; hence, a small proportion of the data were not included as either event data or background data. The $\text{O}_2:\text{CO}_2$ ratio for the background data is -1.14, and the $\text{O}_2:\text{CO}_2$ ratio for the event 1 data is -1.19. These values are very similar to each other, and also similar to the global average biospheric value of -1.1. This is expected, because the O_2 and CO_2 values of the well-mixed atmosphere in the northern hemisphere are dominated by fluxes from the land biosphere. The fact that event 1 data has a very similar $\text{O}_2:\text{CO}_2$ ratio to that of

background air provides supporting evidence that event 1 represents air arriving from a lower latitude, and not from an oceanic process.

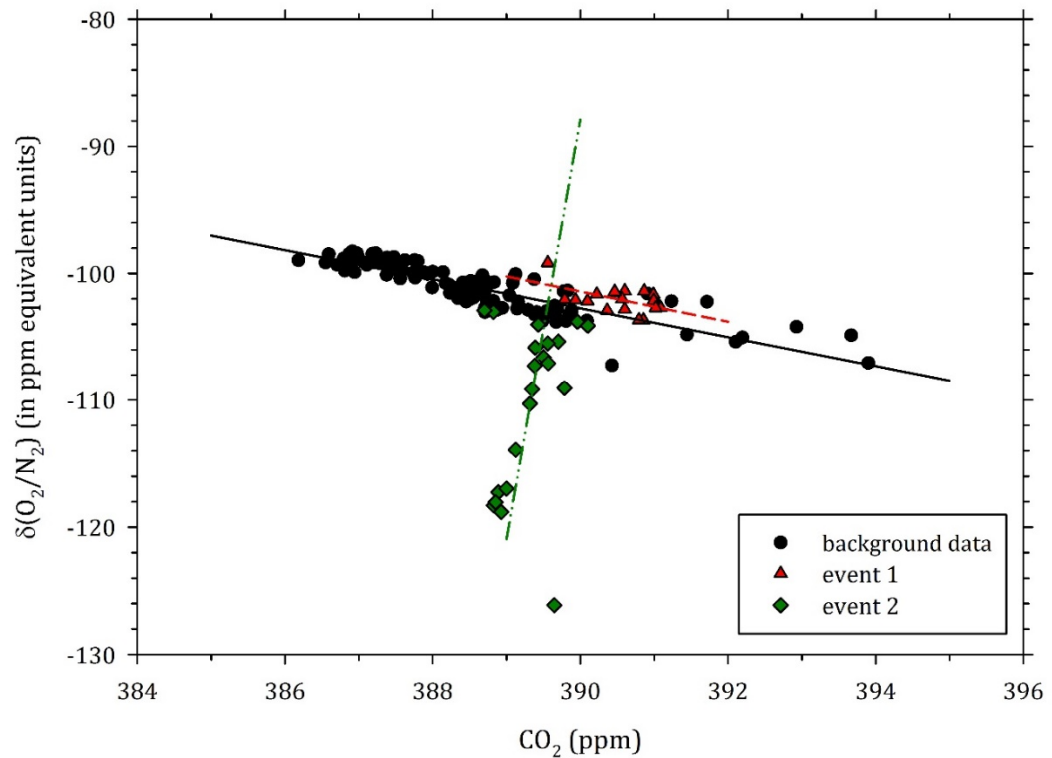


Figure 3.17. $O_2:CO_2$ ratio plot of background (i.e. non-event) data (black circles), event 1 data (red triangles), and event 2 data (green diamonds). As before, $\delta(O_2/N_2)$ is given in ppm equivalent units to be comparable to CO_2 and enable correct calculation of the regression slopes. The three lines indicates the major axis regression lines for background (black solid), event 1 (red dashed) and event 2 (green dashed-dotted) data. The regressions were weighted according to the difference in measurement uncertainty associated with the $\delta(O_2/N_2)$ and CO_2 data.

In contrast, event 2 has a very different $O_2:CO_2$ ratio of 33.03. This $O_2:CO_2$ ratio means that during event 2 there are 33.03 moles of O_2 being consumed for every mole of CO_2 being consumed; such a ratio is indicative of an oceanic process, since both land biosphere and fossil fuel processes are strongly anti-correlated for O_2 and CO_2 , whereas for event 2, O_2 and CO_2 are correlated.

3.4.6 Short-term events: correlations with the JC090 underway data

The data analysis in sections 3.4.2-3.4.4 indicates that event 2 is more likely to be caused by a drawdown of O_2 by the ocean than a change in atmospheric transport. On short timescales (e.g. hours to days) air-sea gas exchange of O_2 can occur from two main oceanic processes: phytoplankton blooms, which cause production of O_2 in the euphotic zone and emission of O_2 from the ocean to the atmosphere; and upwelling of deep, O_2 -depleted waters, which causes an O_2 flux from the atmosphere to the ocean

(Bender and Battle, 1999). Event 2 in the JC090 data is therefore most likely to be caused by the latter: an upwelling event.

Figure 3.18 shows the sea surface temperature, salinity and chlorophyll fluorescence data measured by the James Cook underway system, alongside the atmospheric O_2 , CO_2 and APO data. As expected, there is no discernible correlation between any of the three underway system parameters and the atmospheric data for event 1.

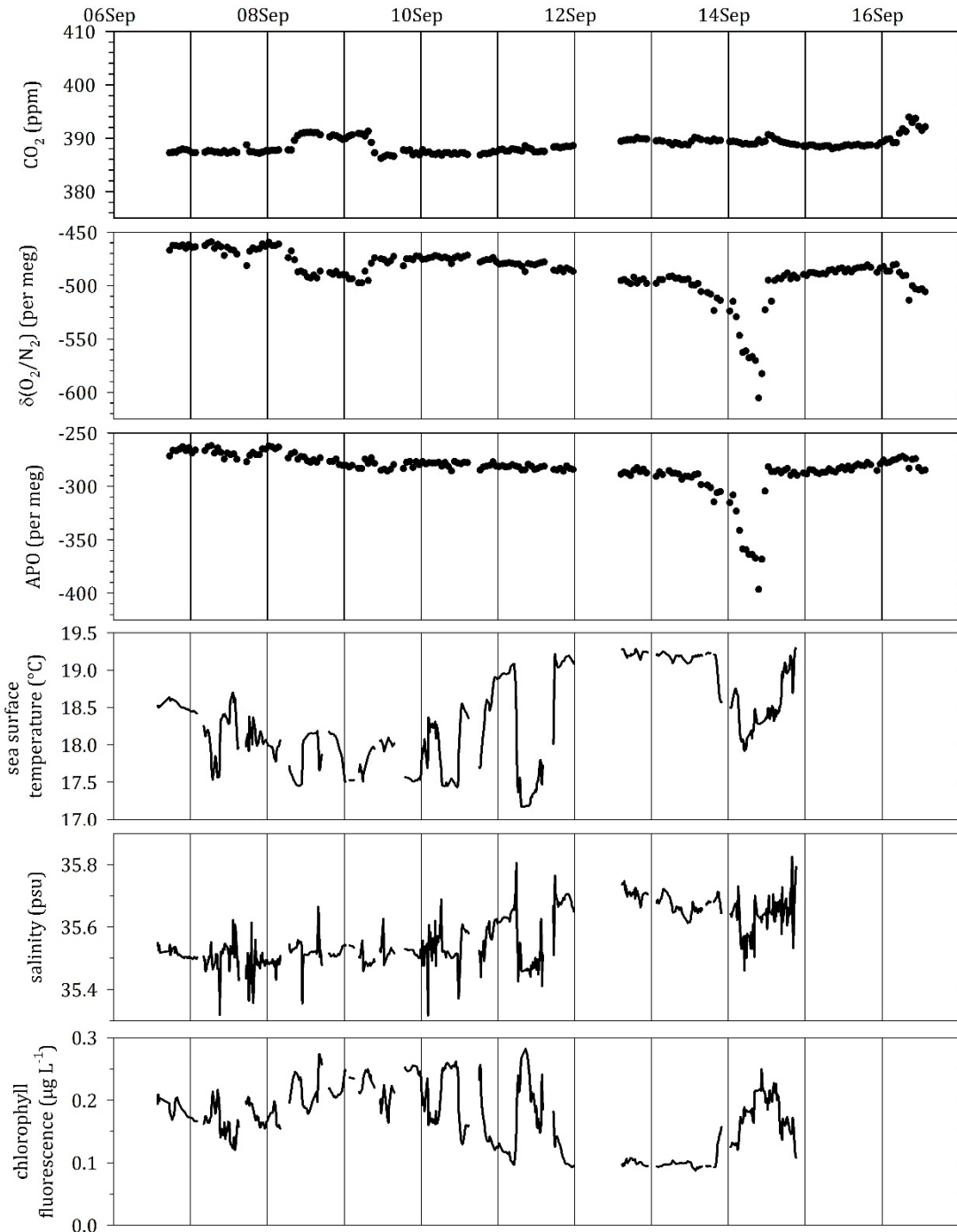


Figure 3.18. The top three panels show hourly averages of atmospheric CO_2 , $\delta(O_2/N_2)$ and APO, respectively. The bottom three panels show sea surface temperature, salinity and chlorophyll fluorescence data, respectively, measured by the James Cook underway system.

On first glance, event 2, seems to coincide with a period of slightly reduced sea surface temperature and slightly increased chlorophyll; on closer inspection, these data are very similar to the underway data between 06-11 Sep 2013, and it is the period just before the occurrence of event 2 that is unusual, with elevated sea surface temperatures, slightly elevated salinity, and reduced chlorophyll. This period of elevated temperature and salinity in the James Cook underway data is more indicative of a warm mesoscale eddy in the ocean, which would not be associated with the uptake of atmospheric O₂. An upwelling event, which is expected to be associated with the uptake of atmospheric O₂, would be characterised by colder sea surface temperatures and elevated primary productivity, owing to the entrainment of nutrients from deeper water into the euphotic zone. It therefore seems likely that event 2 was not caused by oceanic uptake of O₂ occurring in the immediate vicinity of the James Cook. Although Fig. 3.15 indicates that the air particles arriving at the ship during event 2 were of relatively local origin, this still includes an area of several tens of square kilometres, whereas the James Cook underway system can only measure the water that is directly beneath the ship.

3.4.7 Short-term events: evidence of eddies from satellite-derived altimetry and sea surface temperature data

There are several conditions in the North Atlantic under which upwelling can occur in the ocean. These include Ekman transport, whereby northerly winds travelling parallel to East Africa induce transport of water away from the coast, resulting in upwelling (e.g. McClain and Firestone, 1993); upwelling caused by processes at the shelf edge, such as along-slope shelf-edge currents, dense water cascading off the shelf, and the interaction of internal tides with the shelf-edge (Huthnance et al., 2009); and upwelling associated with cyclonic, cold-core eddies (Arhan et al., 2011).

Satellite derived sea surface chlorophyll and temperature data from the Aqua MODIS (moderate-resolution imaging spectroradiometer) satellite (<http://oceancolor.gsfc.nasa.gov/cgi/l3>) show evidence of Ekman upwelling off the coast of Portugal (not shown); however, the James Cook was too distant from the coast on 13Sep2013 for this to be the cause of event 2, and the NAME footprints during event 2 (shown in Fig. 3.15) show that the air originated from the west, not the east. The James Cook was relatively close to the European shelf edge during the

cruise, but the Aqua MODIS satellite chlorophyll and sea surface temperature data around the time of event 2 do not show any evidence of upwelling at the shelf edge.

Although mesoscale ocean eddies are now known to be ubiquitous in the ocean (Castelao, 2014), they are more prevalent in regions where strong ocean currents form, such as the Kuroshio current in the western North Pacific, the Agulhas current near South Africa that extends into the southern Indian Ocean, and the Gulf Stream in the western North Atlantic (as shown in Figure 3.19). Figure 3.20 shows the sea surface height anomalies for 13Sep2013, as well as the location of the James Cook. As indicated by the blue areas in Fig. 3.20, there are several cold-core cyclonic eddies in the vicinity of the James Cook on this day; most notably, an elongated eddy slightly to the east of the ship's position, which only exists during the period of event 2, before being dissipated. Figure 3.21 shows the sea surface temperature (SST) at this time, with the contours of the sea surface height anomalies from Fig. 3.20 overlaid. It should be noted that the SST in Fig. 3.21 is represented as a composite of 7 days of data, centred around 13Sep2013, since there are several gaps in the data at this time, owing to thick cloud cover. Cold-core cyclonic eddies are associated with lower sea surface temperatures of up to 2 °C (Castelao, 2014), although, owing to the lack of data, it is difficult to discern any such feature in Fig. 3.21. Thus, although there is evidence to support the occurrence of cold-core eddies in the vicinity of the JC090 cruise, it is not possible to determine specifically which eddy could be responsible for the O₂/APO excursion of event 2, or indeed, whether a cold-core eddy is the true cause of the excursion. It is important to remember that evidence of this eddy is solely based on a single gridded satellite data product, which has been interpolated from individual satellite swath data.

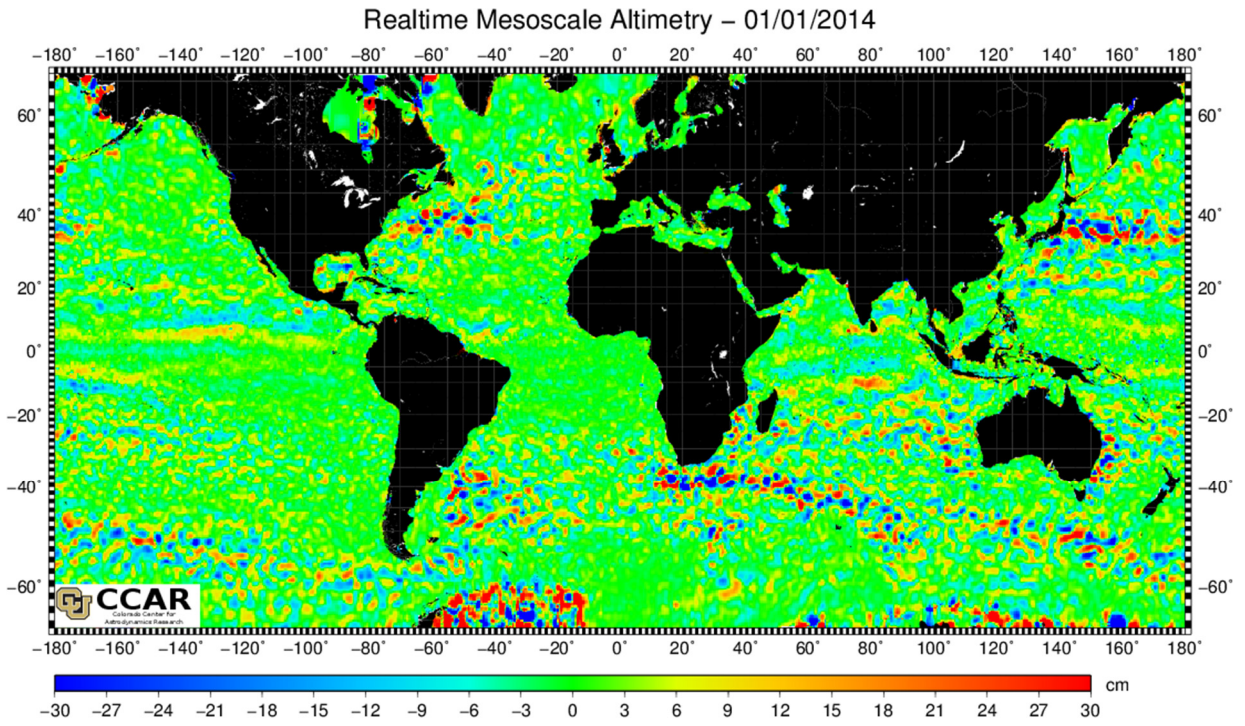


Figure 3.19. Gridded Sea Surface Height anomalies on 01Jan2014, produced from merged Jason-2/OSTM (Ocean Surface Topography Mission) and Cryosat-2 satellite data products (from: http://eddy.colorado.edu/ccar/ssh/nrt_global_grid_viewer). Blue areas are depressions in the mean sea surface height, which indicate cold core eddies, and red areas are elevations in the mean sea surface, which indicate warm core eddies.

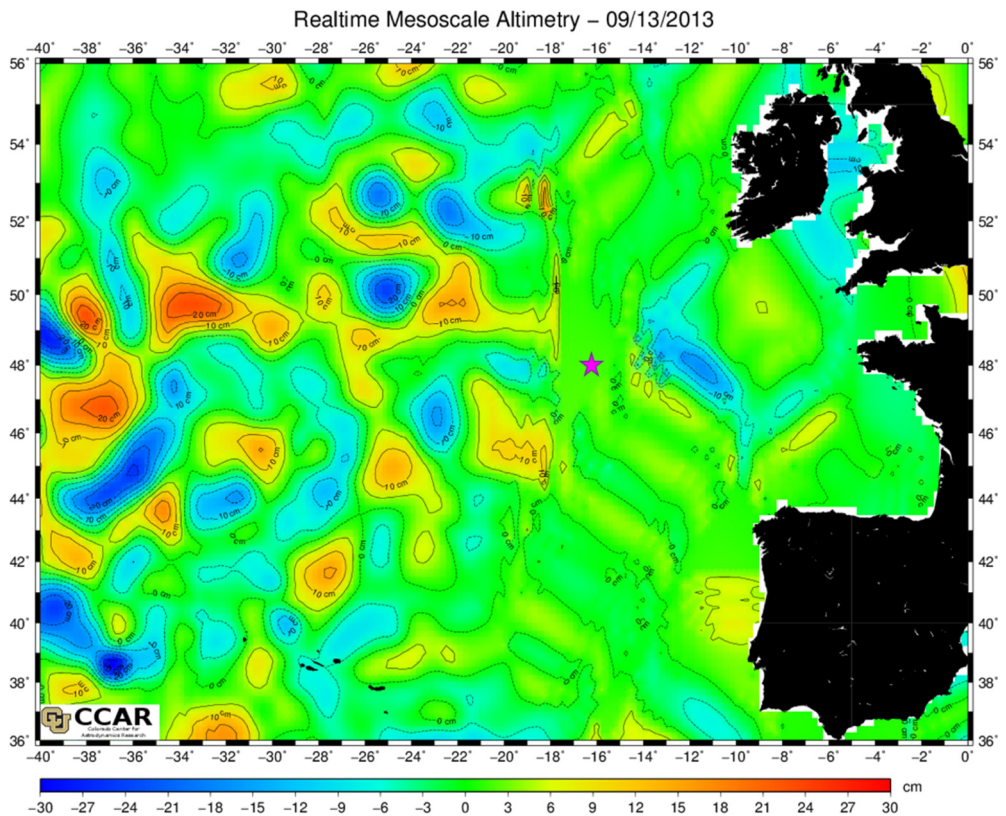


Figure 3.20. Gridded Sea Surface Height anomalies on 13Sep2013 (from: http://eddy.colorado.edu/ccar/ssh/nrt_global_grid_viewer). The pink star indicates the position of the James Cook on this day.

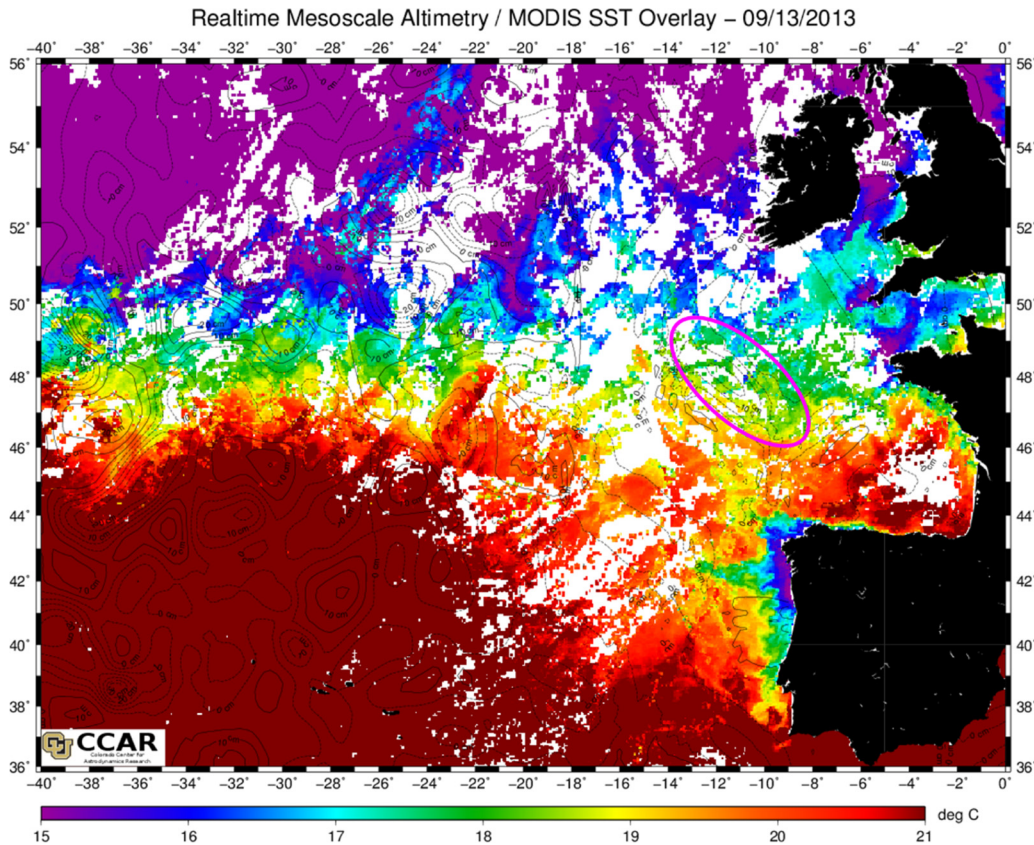


Figure 3.21. A 7-day composite of SST from the MODIS aqua satellite (4 km resolution), centred around 13Sep2013 (from: http://eddy.colorado.edu/ccar/ssh/nrt_global_grid_viewer). The dashed lines indicate the contours of the sea surface height anomalies on 13Sep2013, as shown in figure 3.20. The pink ellipsoid indicates the location of the cyclonic cold-core eddy located to the east of the James Cook on the 13Sep2013. The SST colour scale has been limited to the range of 15 – 21 °C in order to visually emphasise temperature variations in the region of the cold-core eddy.

3.4.8 Short-term events: O₂ flux estimate associated with a typical cold-core cyclonic eddy

It is important to consider whether a change in dissolved oceanic O₂ of the order of magnitude that is typically associated with cold-core eddies is sufficient to cause the magnitude of change in atmospheric O₂/APO seen in event 2, and hence, whether a cold-core eddy is a plausible cause for the event 2 O₂/APO excursion. The (Jacob, 1999) ‘Puff’ model (Equation 3.3) can be used to calculate the flux of a gas into a moving column of air (in mol m⁻² yr⁻¹), and has been used previously to calculate air-sea fluxes of O₂ (Lueker, 2004; Thompson et al., 2007; Yamagishi et al., 2008):

$$Flux = \frac{\Delta C \cdot h}{t[1 - \exp(-L/ut)]} \quad (\text{Eq. 3.3})$$

where ΔC is the change in atmospheric concentration of the gas within the column (in mol m^{-3}), h is the atmospheric vertical mixing height (in metres), also known as boundary layer height, t is an e -folding lifetime representing atmospheric mixing within the column (in years), L is the wind fetch (in metres), and u is the wind speed (in m yr^{-1}). Using Fig. 3.18, a value of $-9.3 \times 10^{-4} \text{ mol m}^{-3}$ of O_2 (i.e. -100 per meg) is used for ΔC (the negative sign denoting a decrease in atmospheric O_2). h is estimated to be 480 m from Global Data Assimilation System (GDAS) boundary layer height model output (see: <http://www.ncdc.noaa.gov/data-access/model-data/model-datasets/global-data-assimilation-system-gdas>), L is estimated to be $6 \times 10^5 \text{ m}$ (i.e. 600 km) based on the distribution of the majority of air particles from the NAME footprint in Fig. 3.15, and a value of $3.78 \times 10^8 \text{ m yr}^{-1}$ (i.e. 12 m s^{-1}) is used for u , based on the average wind speed measured by the James Cook meteorological instruments during event 2. t is estimated to be $2.74 \times 10^{-3} \text{ yr}$ (i.e. 24 hours), based on the mean duration of events 1 and 2. The flux of O_2 calculated using these values is $-371 \text{ mol m}^{-2} \text{ yr}^{-1}$, where the negative sign represents a flux of O_2 from the atmosphere to the ocean.

In order to determine whether an O_2 flux of $-371 \text{ mol m}^{-2} \text{ yr}^{-1}$ is a reasonable estimate for cold-core upwelling at this location and time, the surface ocean dissolved O_2 concentration required to cause such a flux can be calculated, and then compared to the dissolved O_2 profiles from the James Cook CTD casts. I have used Equation 3.4 from (Garcia and Keeling, 2001) to calculate the O_2 flux from a dissolved oxygen anomaly:

$$\text{Flux} = \rho \cdot k_{\text{O}_2} \cdot \Delta[\text{O}_2] \quad (\text{Eq. 3.4})$$

where ρ is the density of the seawater, in g cm^{-3} , k_{O_2} is the gas transfer velocity for O_2 , in m yr^{-1} , and $\Delta[\text{O}_2]$ is the oxygen anomaly in mol m^{-3} . k_{O_2} is calculated using Equation 3.5, from (Wanninkhof, 1992):

$$k_{\text{O}_2} = 0.39u^2 \left(\frac{Sc_{\text{O}_2}}{660} \right)^{-\frac{1}{2}} \quad (\text{Eq. 3.5})$$

where u is the wind speed in m yr^{-1} and Sc_{O_2} is the Schmidt number for O_2 . For Sc_{O_2} , I used Equation 3.6 from (Wanninkhof, 1992):

$$Sc_{O_2} = 1953.4 - 128T + 3.9918T^2 - 0.05009T^3 \quad (\text{Eq. 3.6})$$

where T is sea surface temperature in °C. In order to calculate the dissolved O_2 anomaly, $\Delta[O_2]$, from Eq. 3.2 I used Equation 3.7, from (Garcia and Keeling, 2001):

$$\Delta[O_2] = [O_2] - [O_2]^* + \delta_{skin} \quad (\text{Eq. 3.7})$$

where $[O_2]$ is the measured dissolved O_2 concentration of the sea water, $[O_2]^*$ is the O_2 solubility, and δ_{skin} is the skin temperature correction. Since δ_{skin} is typically very small (about $\pm 0.001 \text{ mol m}^{-3}$), I have not applied this correction in any of my calculations. $[O_2]^*$ is calculated using Equation 3.8 from (Garcia and Gordon, 1992):

$$\ln[O_2]^* = A_0 + A_1T_s + A_2T_s^2 + A_3T_s^2 + A_3T_s^3 + A_4T_s^4 + A_5T_s^5 + S(B_0 + B_1T_s + B_2T_s^2 + B_3T_s^3) + C_0S^2 \quad (\text{Eq. 3.8})$$

where S is salinity in per mil, and A_0 to A_5 , B_0 to B_3 and C_0 are constants from (Garcia and Gordon, 1992). T_s is given by Equation 3.9, also from (Garcia and Gordon, 1992):

$$T_s = \ln[(298.15 - t)(273.15 + t)^{-1}] \quad (\text{Eq. 3.9})$$

where t is the seawater temperature in °C. Now that all the terms of Eq. 3.4 are either known or can be calculated, one can substitute Eq. 3.7 into Eq. 3.4 and re-arrange to make $[O_2]$ the subject, as shown in Equation 3.10:

$$[O_2] = \frac{Flux}{\rho \cdot k_{O_2}} + [O_2]^* \quad (\text{Eq. 3.10})$$

The input values for calculating the terms in Eqs. 3.4-3.10 are as follows: ρ is defined as 1.025 g cm^{-3} (mean density of seawater), a value of $3.78 \times 10^8 \text{ m yr}^{-1}$ (i.e. 12 m s^{-1}) is used for u , based on the average wind speed measured by the James Cook meteorological instruments during event 2, both T and t are 18.5 °C , which is the average surface seawater temperature measured from the James Cook underway system during event 2, and S is 35.6 per mil, which is the average surface seawater salinity measured from the underway system during event 2. Thus, the value of

dissolved O₂ that is required in order to induce a flux of 371 mol m⁻² y⁻¹ from the atmosphere into the ocean is 0.1607 mol m⁻³, or 160.7 μ mol L⁻¹.

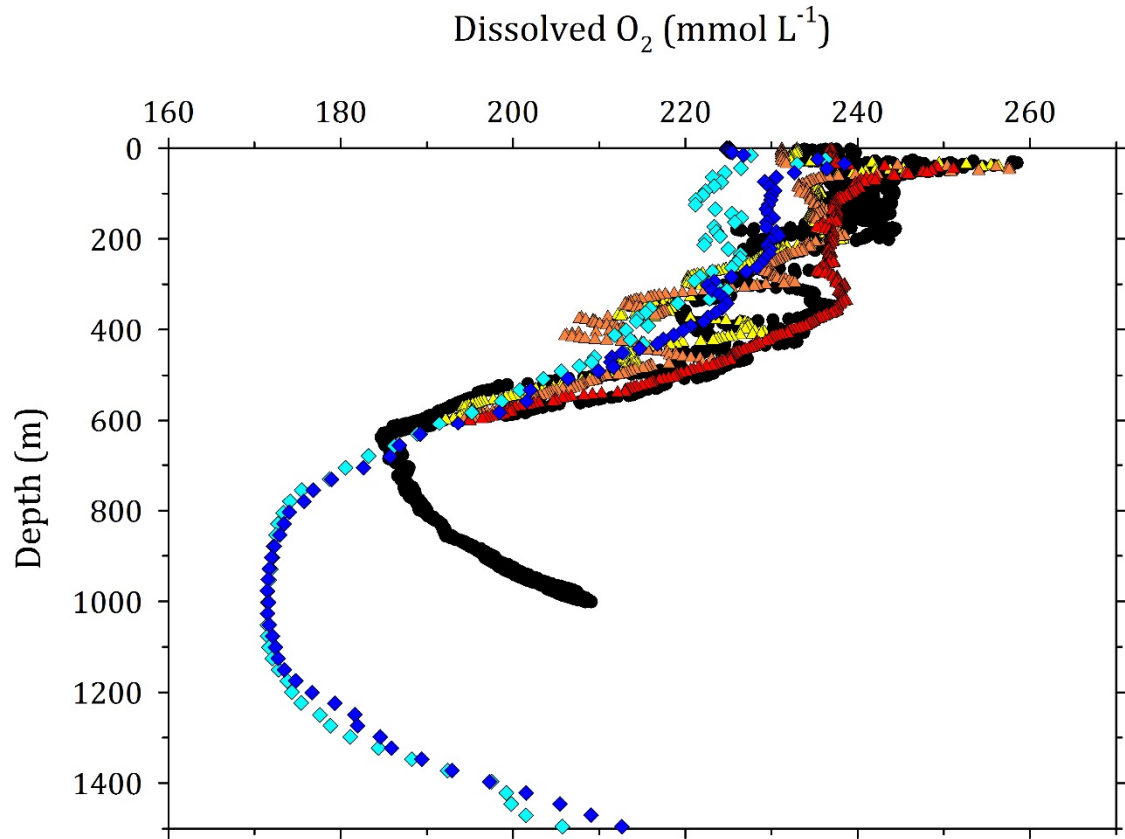


Figure 3.22. CTD cast dissolved O₂ from the JC090 cruise (black circles). The CTD casts just before, during, and after event 2 are indicated by the yellow, orange and red triangles respectively. The pale blue and dark blue diamonds show dissolved O₂ from an Argo float located southwest of the James Cook (at 44.5°N, 8.3°E), measured on 01Sep2013 and 11Sep2013, respectively.

Figure 3.22 shows the dissolved O₂ profiles from the James Cook CTD casts, including those immediately before, during and immediately after event 2. As with the James Cook underway data shown in Fig. 3.18, there is no evidence of upwelling (i.e. low dissolved O₂ concentrations at the sea surface) in these profiles, and therefore event 2 is unlikely caused by an ocean event that is in the immediate vicinity of the ship. The profiles of dissolved O₂ show that, at the sea surface, the O₂ concentration is approximately 240 μ mol L⁻¹, increasing to about 265 μ mol L⁻¹ in the thermocline, due to O₂ production from primary productivity, before declining to a minimum of approximately 188 μ mol L⁻¹ at about 620 m depth. It should be noted that the O₂ depth profiles around the time of event 2 were not deep enough to reach the O₂ minima at this time. The Argo float dissolved O₂ data from Fig. 3.22 show that if upwelling were the cause of event 2, the expected dissolved O₂ concentration at the

sea surface might be as low as 170-185 $\mu\text{ mol L}^{-1}$, which is only slightly higher than the value calculated using Eq. 3.10.

It is important to consider the sources of uncertainty and bias in Eqs. 3.3-3.10, to ensure that the calculated dissolved O_2 value does not agree well to the measured values simply by coincidence. The sources of uncertainty in Eqs. 3.4-3.10 are all relatively small, since most of the variables are from measurements, and the temperature and salinity ranges of the measurements are well within the ideal ranges for which Eqs. 3.6, 3.8 and 3.9 are suitable. It should be noted that the (Wanninkhof, 1992) equations (Eqs. 3.5 and 3.6) have been shown to not be representative of all oceanic conditions, since they do not take into account additional processes, such as bubble entrainment, that affect the air-sea exchange of gases (Liang et al., 2013). The (Jacob, 1999) 'Puff' model in Eq. 3.3 contains several terms that are poorly constrained. These terms are: the vertical mixing height, the e -folding time, and the wind fetch.

Table 3.1. Sensitivity of O_2 fluxes calculated using the (Jacob, 1999) 'Puff' model to variations in vertical mixing height, e -folding time, and wind fetch. Note that the O_2 flux values are in $\text{mol m}^{-2} \text{ yr}^{-1}$, and negative flux values denote air-to-sea fluxes.

Variable name	Range of variable values	Range of O_2 flux values
Vertical mixing height	200 – 600 m	-154.4 to -463.6
e -folding time	8 – 48 hours	-593.4 to -324.3
Wind fetch	200 – 2000 km	-928.8 to -190.6

Table 3.1 shows the effect on the O_2 flux when each of these three poorly defined terms is varied, one at a time. The change in atmospheric O_2 mole fraction and wind speed are kept constant, using the values stated previously. The large range of O_2 flux values in Table 3.1 demonstrates that the (Jacob, 1999) 'Puff' model is very sensitive to all three of the variables in the table. Since there are no direct measurements of any of these three variables, Eq. 3.1 can only provide a rough approximation of the O_2 flux that is expected to have caused a -100 per meg change in atmospheric O_2/APO . It becomes clear that it is possible to manipulate the 'Puff' model to produce a flux that, will in turn, produce a dissolved O_2 concentration matching that of the dissolved O_2 minima from the James Cook CTD casts exactly, simply by reducing the vertical mixing height from 480 m to 340 m, or by increasing the wind fetch from 600 km to 1000 km.

Another consideration is whether a cold-core eddy would actually result in the upwelling of deeper, O₂-depleted water all the way to the sea surface, or whether the surface-dissolved O₂ concentration would remain relatively unchanged. Data from (Arhan et al., 2011), who measured the vertical distribution of dissolved O₂ in both a warm and a cold-core eddy off the coast of South Africa, found the latter case to be true, where evidence of strong upwelling was observed in the temperature, salinity, and dissolved O₂ data, and yet this upwelling did not reach the surface, instead peaking at about 300 m depth. Therefore, while it is possible that the O₂ excursion of event 2 was caused by a cold-core eddy, there is no conclusive evidence to confirm whether this is indeed the case.

3.4.9 Short-term events: modelling short-term variability in APO using NAME and NEMO-PlankTOM

The JC090 O₂ and APO data show a clear negative excursion about 100 per meg in magnitude on 13-14Sep2013, which I have called 'event 2'. There is no indication in the measurement system diagnostic data that this event is caused by a technical problem with the measurement system, and yet I have also not been able to obtain any conclusive evidence explaining the origin of this O₂ event. Using a very simple box model and the dissolved O₂ concentrations from the James Cook CTD casts, I have been able to determine that theoretically, the O₂/APO excursion could be caused by the upwelling of sub-thermocline waters that are depleted in dissolved O₂. This hypothesis assumes that it is possible for these sub-thermocline waters to come into contact with the atmosphere in the region of the PAP mooring site, which is not an area known for strong upwelling. The CTD dissolved O₂ data reveal that there was no strong upwelling occurring in the immediate vicinity of the James Cook at the time of the atmospheric O₂/APO excursion, and therefore if the excursion is indeed real, it must have originated elsewhere, and has been transported to the ship. Since there are very few existing measurements in the North Atlantic with which to calculate air-sea O₂ fluxes, it is useful to look at model air-sea O₂ flux data to investigate whether such fluxes might actually exist in the region of the PAP site, and whether these modelled O₂ air-sea fluxes can replicate the event 2 atmospheric APO excursion at the ship's location, when combined with an atmospheric transport model.

In order to model APO, I have used 3-hourly, 5-day integrated backwards run NAME footprints (with 0.25° latitudinal and longitudinal resolution) from the RRS

James Cook location (footprints courtesy of Zoë Fleming) to ‘sample’ the O_2 and N_2 air-sea flux fields (since atmospheric O_2 measurements are reported as $\delta(O_2/N_2)$ ratios) from the Plankton Types Ocean Model (PlankTOM; version 5.3) embedded within the Nucleus for European Modelling of the Ocean (NEMO; version 2.3) framework (Buitenhuis et al., 2013), for each grid box. The weighted contribution of the O_2 and N_2 fluxes to APO are calculated at each NAME footprint time stamp, based on the proportion of air particles in the grid box, as shown in Equation 3.11 below:

$$\Delta APO = \left[\left(\sum_{t_1 b_1}^{t_n b_n} \frac{O_2 \text{ flux}}{BLH} \times P \right) \times \frac{1000 \times 22.4}{0.20946} \right] - \left[\left(\sum_{t_1 b_1}^{t_n b_n} \frac{N_2 \text{ flux}}{BLH} \times P \right) \times \frac{1000 \times 22.4}{0.78084} \right]$$

(Eq. 3.11)

where O_2 flux is the NEMO-PlankTOM air-sea O_2 flux, BLH is the atmospheric boundary layer height, which was obtained from the Met Office Unified Model (on 3-hourly time intervals and a 0.3516° longitude by 0.2344° latitude grid), N_2 flux is the air-sea N_2 flux derived from the NEMO-PlankTOM air-sea heat flux (see Equation 3.12), t is the time interval of the NAME footprints, b_1 to b_n are the individual grid boxes of the NAME footprint, P is the number of particles per grid box divided by the total number of particles in the NAME footprint, 0.20946 and 0.78084 are the mole fractions of O_2 and N_2 in dry air, respectively, and 22.4 is the number of litres per mole of an ideal gas. The latter three numbers are used to convert the modelled APO into per meg units. Note that normally, one would also need to include modelled CO_2 air-sea fluxes and fossil fuel combustion CO_2 and O_2 fluxes in order to accurately model APO; however, since the JC090 dataset is short, and the ship was located in the open ocean, I have assumed that the effects of air-sea CO_2 fluxes and fossil fuel combustion CO_2 and O_2 fluxes will be negligible on the modelled APO.

The NEMO-PlankTOM model produces daily air-sea fluxes of heat, which were converted into daily air-sea N_2 fluxes using the following equation from (Keeling et al., 1993):

$$N_2 \text{ Flux} = \frac{-dC_{eq}}{dT} \times \frac{Q}{c_p}$$

(Eq. 3.12)

where dC_{eq}/dT is the temperature derivative of the N_2 solubility coefficient in $\text{mol m}^{-3} \text{K}^{-1}$, Q is the heat flux in $\text{J m}^{-2} \text{s}^{-1}$, and C_p is the heat capacity of seawater in $\text{J m}^{-3} \text{K}^{-1}$. All NEMO-PlankTOM fluxes have a longitudinal and latitudinal resolution of 2° , with the latitudinal resolution enhanced to 0.5° in polar and equatorial regions.

Figure 3.23 shows both the JC090 measured APO data (which have been detrended and deseasonalised) and the modelled APO data, using the NEMO-PlankTOM and NAME modelling framework described above. The modelling framework does not reproduce the large negative APO excursion seen in the measured APO data, most likely because there is no parameterisation of mesoscale eddies included within NEMO-PlankTOM (Andrews, 2014). Thus, if the measured APO excursion is indeed real, then the fact that it is not replicated in the modelled APO supports the hypothesis that the event could be caused by a cyclonic, cold-core eddy. There is also a small difference between the modelled and measured APO on 08-09Sep2013, when ‘event 1’ occurs (which was caused by long-range transport of air from a lower latitude). Although the modelled APO does not replicate the measured APO of event 2, the very short-term variability (timescales up to a day) in the modelled APO is very similar in magnitude to that of the measured APO, when the large APO event is excluded.

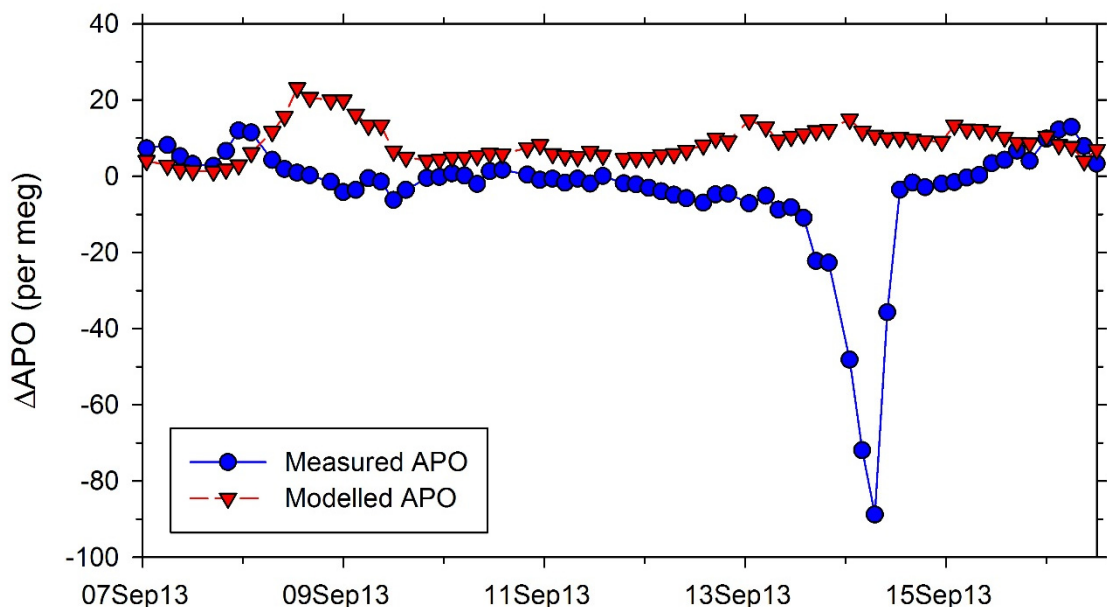


Figure 3.23. A comparison of the 3-hourly-averaged, detrended and deseasonalised measured ΔAPO (blue circles) and modelled ΔAPO (red triangles) for the JC090 cruise (where the Δ notation indicates that the APO values represent the difference from the APO baseline).

In the NEMO-PlankTOM and NAME modelling framework, the atmospheric footprint and BLH vary every 3 hours, and the O₂ and N₂ fluxes vary daily. By keeping two of the three variables (footprint, BLH, and fluxes) fixed and only allowing one to vary, it is possible to investigate the major contributor to the sub-daily variability shown in Fig. 3.23, which will indicate the dominant cause of such short-term small magnitude variations in the measured APO. Figure 3.24 shows the modelled APO from Fig. 3.23 alongside three versions of the modelled APO, each with two of the three variables fixed and only one variable changing. It is clear from Fig. 3.24 that it is the variation in the atmospheric footprint that dominates the variability in the modelled APO, with BLH and O₂ and N₂ flux variations only contributing slightly. What this actually indicates is that the greatest contributor to the sub-daily small magnitude variations in the modelled APO is the spatial variability in the O₂ and N₂ fluxes (as opposed to the temporal variability), since I did not include any atmospheric boundary conditions in the modelling framework to account for spatial variability (mostly latitudinal) in the APO baseline. The lack of atmospheric boundary conditions in the modelling framework most likely explains the event 1 disparity shown in Fig. 3.23.

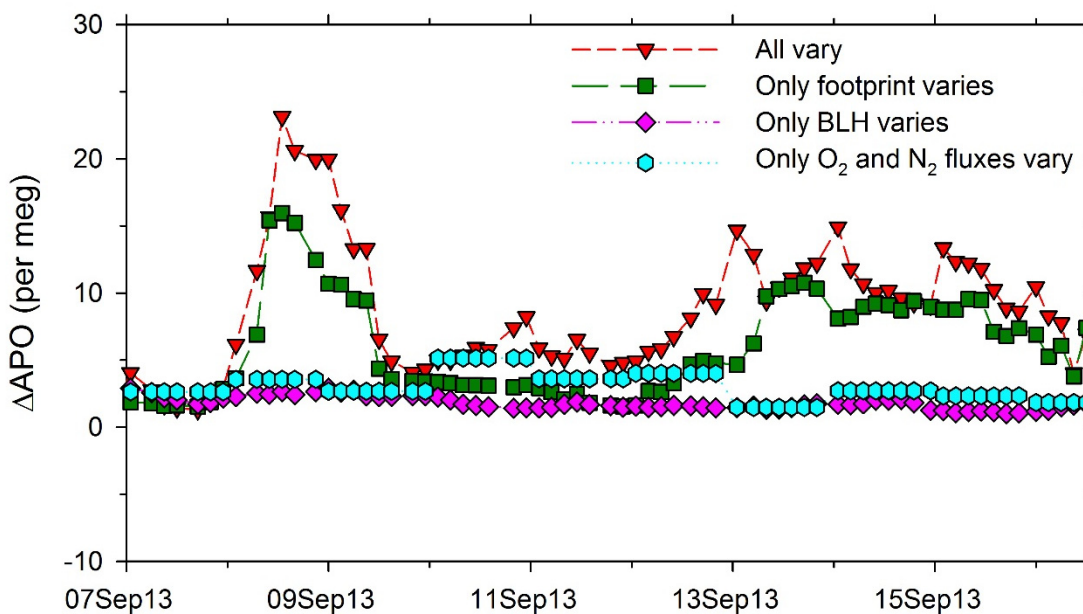


Figure 3.24. Modelled APO with all three variables changing as shown in Fig. 3.23 (red triangles), modelled APO with only the atmospheric footprint varying (green squares), modelled APO with only the BLH varying (pink diamonds), and modelled APO with only the O₂ and N₂ fluxes varying (cyan hexagons).

Although the APO modelling framework is useful for understanding short-term variability in the JC090 APO data, there are several assumptions and limitations inherent in the modelling framework that should be noted. Firstly, I have assumed

that air-sea O_2 and N_2 fluxes are equilibrated instantaneously, but in reality, the air-sea flux equilibration time is about 3 weeks (Blaine, 2005). This most likely means that the air-sea O_2 and N_2 fluxes (the latter of which were calculated from the NEMO-PlankTOM heat fluxes) have been overestimated in the modelling framework (Keeling et al., 1993). Secondly, I have used 5-day integrated NAME footprints in order to ‘sample’ the NEMO-PlankTOM flux fields, but I have not included a time lag to account for particles within the footprints that are close to the ship, and those that are far away from the ship (i.e. I have assumed that the air is transported to the ship instantaneously). Thirdly, the NEMO-PlankTOM air-sea fluxes have a daily resolution, but have been sampled every 3 hours, because the NAME footprints are 3-hourly, which causes daily step changes in the APO associated with the air-sea N_2 and O_2 fluxes at midnight (see Fig. 3.24, cyan symbols). As mentioned previously, I have not included the influences of air-sea CO_2 fluxes or fossil fuel derived CO_2 and O_2 fluxes on the modelled APO. This is because air-sea CO_2 fluxes have a negligible influence on APO on short timescales, and fossil fuel CO_2 and O_2 fluxes will only affect APO on short timescales when the ship is close to land, and therefore close to fossil fuel emission sources, and not in the mid-North Atlantic Ocean. Although these limitations may affect the modelled APO shown in Figs. 3.23 and 3.24, they are not expected to be significant, and the APO modelled framework presented here is expected to provide a simplistic, but reasonable estimate of the real world processes that affect APO on short timescales over the ocean.

3.5 Summary and conclusions

In this chapter, I have presented shipboard atmospheric O_2 , CO_2 and APO data from a short cruise on the RRS James Cook in the North Atlantic Ocean (JC090 cruise). After removing the data that were affected by technical issues, as well as those that were influenced by the ship’s own exhaust emissions, two atmospheric short-term ‘events’ were revealed. After investigating the air mass histories of these events using NAME, and analysing the James Cook meteorological and underway system data, I have concluded that the first event is caused by long-range transport of air from lower latitudes. This lower latitude air is associated with elevated CO_2 and decreased O_2 , as one would expect, given that the cruise occurred in September (close to the northern hemisphere summer seasonal minimum in CO_2 and maximum in O_2) and

that seasonal variability in both CO₂ and O₂ in the northern hemisphere is attenuated at lower latitudes.

A second short-term atmospheric event also occurred during the JC090 cruise, consisting of a very large (~100 per meg) negative excursion in O₂ (and also APO), with no significant change in CO₂. This second atmospheric event does not correspond to changes in either the meteorological data, or the underway system data in the immediate vicinity of the ship, and cannot be explained from changes in the NAME atmospheric footprints. The large change in O₂/APO with little change in CO₂ is indicative of an ocean upwelling event; however, satellite altimetry and sea-surface temperature data do not reveal any robust evidence of upwelling occurring either close to the James Cook, or within the NAME footprint, at the time that this event occurs. Using the Jacob (1999) 'Puff' model, I have determined that it is theoretically possible that a 100 per meg excursion in O₂/APO could be caused by an ocean upwelling event; however, the model is very simplistic, and can be easily manipulated in order to produce the correct result. It is also not possible to reproduce the large excursion in APO using a more sophisticated modelling framework, which samples O₂ and N₂ air-sea fluxes from the NEMO-PlankTOM model using NAME footprints: although much of the small magnitude, sub-daily variability can be reproduced in the modelling framework, this small magnitude variability is dominated by spatial variability in the air-sea O₂ and N₂ fluxes as the NAME footprints change with time. The fact that the modelling framework is unable to reproduce the large APO excursion, does not necessarily indicate that the event is not real, because the air-sea O₂ and N₂ fluxes produced by NEMO-PlankTOM do not include fluxes associated with mesoscale eddies, and the most plausible cause of the measured APO excursion is a mesoscale eddy.

It is possible that the large O₂/APO excursion of event 2 is not real, and has been caused by a technical problem with the measurement system that is not detectable in the diagnostic data. Making high-precision measurements of atmospheric O₂ is challenging, because there are many ways in which O₂ can fractionate relative to N₂. Unfortunately, the JC090 dataset is too short to determine whether the second event is caused by a technical problem, or represents a real world event, in which case, one would expect such O₂/APO excursions to re-occur relatively frequently. Only within the context of a much larger shipboard dataset is it possible to determine the validity of the JC090 event 2 O₂/APO excursion. Hence, in Chapter 4, I re-visit this discussion on the origin of event 2 in the context of a much larger

shipboard dataset collected on board the Cap San Lorenzo container ship, and also in the context of previous studies that have attributed short-term atmospheric O₂/APO events to air-sea fluxes.

References

- Andrews, O. D.: Fingerprints and Drivers of Recent Changes in Oceanic Oxygen: From Regional to Global Scales, PhD, School of Environmental Sciences, University of East Anglia, Norwich, UK, 2014.
- Arhan, M., Speich, S., Messenger, C., Dencausse, G., Fine, R., and Boye, M.: Anticyclonic and cyclonic eddies of subtropical origin in the subantarctic zone south of Africa, *Journal of Geophysical Research-Oceans*, 116, 2011.
- Bender, M. L. and Battle, M. O.: Carbon cycle studies based on the distribution of O₂ in air, *Tellus*, 51B, 165-169, 1999.
- Blaine, T. W.: Continuous Measurements of Atmospheric Ar/N₂ as a Tracer of Air-Sea Heat Flux: Models, Methods and Data., Ph.D. thesis, University of California, San Diego, California, USA, 2005.
- Buitenhuis, E. T., Hashioka, T., and Le Quere, C.: Combined constraints on global ocean primary production using observations and models, *Global Biogeochemical Cycles*, 27, 847-858, 2013.
- Carslaw, D. C. and Ropkins, K.: Openair — an R package for air quality data analysis., *Environmental Modelling & Software*, 27-28, 52-61, 2012.
- Castelao, R. M.: Mesoscale eddies in the South Atlantic Bight and the Gulf Stream Recirculation region: Vertical structure, *Journal of Geophysical Research-Oceans*, 119, 2048-2065, 2014.
- Garcia, H. E. and Gordon, L. I.: Oxygen solubility in seawater: better fitting equations, *Limnology and Oceanography*, 37, 1307-1312, 1992.
- Garcia, H. E. and Keeling, R. F.: On the global oxygen anomaly and air-sea flux, *Journal of Geophysical Research-Oceans*, 106, 31155-31166, 2001.
- Hardman-Mountford, N. J., Moore, G., Bakker, D. C. E., Watson, A. J., Schuster, U., Barciela, R., Hines, A., Moncoiffe, G., Brown, J., Dye, S., Blackford, J., Somerfield, P. J., Holt, J., Hydes, D. J., and Aiken, J.: An operational monitoring system to provide indicators of CO₂-related variables in the ocean, *Ices Journal of Marine Science*, 65, 1498-1503, 2008.
- Huthnance, J. M., Holt, J. T., and Wakelin, S. L.: Deep ocean exchange with west-European shelf seas, *Ocean Science*, 5, 621-634, 2009.
- Jacob, D. J.: Chapter 3: Simple models. In: *Introduction to Atmospheric Chemistry*, Princeton University Press, 1999.
- Jones, A. R., Thomson, D. J., Hort, M., and Devenish, B.: The U.K. Met Office's next-generation atmospheric dispersion model, NAME III In: *Air Pollution Modeling and its Application Borrego, C. and Norman, A. L. (Eds.), XVII (Proceedings of the 27th NATO/CCMS International Technical Meeting on Air Pollution Modelling and its Application)*, Springer, 2007.
- Keeling, C. D.: Measuring Correlations Between Atmospheric Oxygen and Carbon Dioxide Mole Fractions: A Preliminary Study in Urban Air, *Journal of Atmospheric Chemistry*, 7, 153-176, 1988.
- Keeling, R. F. and Manning, A. C.: 5.15 - Studies of Recent Changes in Atmospheric O₂ Content. In: *Treatise on Geochemistry (Second Edition)*, Holland, H. D. and Turekian, K. K. (Eds.), Elsevier, Oxford, 2014.

- Keeling, R. F., Najjar, R. P., Bender, M., and Tans, P. P.: What atmospheric oxygen measurements can tell us about the global carbon cycle, *Global Biogeochemical Cycles*, 7, 37-67, 1993.
- Keeling, R. F. and Shertz, S. R.: Seasonal and interannual variations in atmospheric oxygen and implications for the global carbon cycle, *Nature*, 358, 723-727, 1992.
- Landschutzer, P., Gruber, N., Bakker, D. C. E., and Schuster, U.: Recent variability of the global ocean carbon sink, *Glob. Biogeochem. Cycle*, 28, 927-949, 2014.
- Liang, J. H., Deutsch, C., McWilliams, J. C., Baschek, B., Sullivan, P. P., and Chiba, D.: Parameterizing bubble-mediated air-sea gas exchange and its effect on ocean ventilation, *Global Biogeochemical Cycles*, 27, 894-905, 2013.
- Lueker, T. J.: Coastal upwelling fluxes of O₂, N₂O, and CO₂ assessed from continuous atmospheric observations at Trinidad, California, *Biogeosciences*, 1, 101-111, 2004.
- Manning, A. C. and Keeling, R. F.: Global oceanic and land biotic carbon sinks from the Scripps atmospheric oxygen flask sampling network, *Tellus Series B-Chemical and Physical Meteorology*, 58, 95-116, 2006.
- McClain, C. R. and Firestone, J.: An Investigation of Ekman Upwelling in the North Atlantic, *Journal of Geophysical Research*, 98, 327-399, 1993.
- Park, G. H. and Wanninkhof, R.: A large increase of the CO₂ sink in the western tropical North Atlantic from 2002 to 2009, *Journal of Geophysical Research-Oceans*, 117, 2012.
- Patecki, M. and Manning, A. C.: First results from shipboard atmospheric O₂ and CO₂ measurements over the North Atlantic Ocean, *Oceans 2007 - Europe*, Aberdeen, 1-6, 2007.
- Sabine, C. L., Feely, R. A., Gruber, N., Key, R. M., Lee, K., Bullister, J. L., Wanninkhof, R., Wong, C. S., Wallace, D. W. R., Tilbrook, B., Millero, F. J., Peng, T. H., Kozyr, A., Ono, T., and Rios, A. F.: The oceanic sink for anthropogenic CO₂, *Science*, 305, 367-371, 2004.
- Stephens, B. B., Keeling, R. F., and Paplawsky, W. J.: Shipboard measurements of atmospheric oxygen using a vacuum-ultraviolet absorption technique, *Tellus Series B-Chemical and Physical Meteorology*, 55, 857-878, 2003.
- Takahashi, T., Sutherland, S. C., Wanninkhof, R., Sweeney, C., Feely, R. A., Chipman, D. W., Hales, B., Friederich, G., Chavez, F., Sabine, C., Watson, A., Bakker, D. C. E., Schuster, U., Metzl, N., Yoshikawa-Inoue, H., Ishii, M., Midorikawa, T., Nojiri, Y., Kortzinger, A., Steinhoff, T., Hoppema, M., Olafsson, J., Arnarson, T. S., Tilbrook, B., Johannessen, T., Olsen, A., Bellerby, R., Wong, C. S., Delille, B., Bates, N. R., and de Baar, H. J. W.: Climatological mean and decadal change in surface ocean pCO₂, and net sea-air CO₂ flux over the global oceans (vol 56, pg 554, 2009), *Deep-Sea Research Part I-Oceanographic Research Papers*, 56, 2075-2076, 2009.
- Tans, P. and Zellweger, C.: 17th WMO/IAEA Meeting on Carbon Dioxide, Other Greenhouse Gases and Related Tracers Measurement Techniques (GGMT-2013), Beijing, China, 2013.
- Thompson, R. L., Gloor, M., Manning, A. C., Lowe, D. C., Rodenbeck, C., and Le Quere, C.: Variability in atmospheric O₂ and CO₂ concentrations in the southern Pacific Ocean and their comparison with model estimates, *Journal of Geophysical Research-Biogeosciences*, 113, 2008.
- Thompson, R. L., Manning, A. C., Lowe, D. C., and Weatherburn, D. C.: A ship-based methodology for high precision atmospheric oxygen measurements and its application in the Southern Ocean region, *Tellus Series B-Chemical and Physical Meteorology*, 59, 643-653, 2007.

- Tohjima, Y., Mukai, H., Machida, T., Nojiri, Y., and Gloor, M.: First measurements of the latitudinal atmospheric O₂ and CO₂ distributions across the western Pacific, *Geophysical Research Letters*, 32, 2005.
- Tohjima, Y., Terao, Y., Mukai, H., Machida, T., Nojiri, Y., and Maksyutov, S.: ENSO-related variability in latitudinal distribution of annual mean atmospheric potential oxygen (APO) in the equatorial western Pacific, *Tellus B*, 67, 2015.
- van der Laan-Luijkx, I. T., Neubert, R. E. M., van der Laan, S., and Meijer, H. A. J.: Continuous measurements of atmospheric oxygen and carbon dioxide on a North Sea gas platform, *Atmospheric Measurement Techniques*, 3, 113-125, 2010.
- van der Laan, S., van der Laan-Luijkx, I. T., Zimmermann, L., Conen, F., and Leuenberger, M. C.: Net CO₂ surface emissions at Bern, Switzerland inferred from ambient observations of CO₂, $\delta(\text{O}_2/\text{N}_2)$, and ²²²Rn using a customized radon tracer inversion, *Journal of Geophysical Research: Atmospheres*, 119, 1580-1591, 2014.
- Wanninkhof, R.: Relationship between wind-speed and gas-exchange over the ocean, *Journal of Geophysical Research-Oceans*, 97, 7373-7382, 1992.
- Watson, A. J., Schuster, U., Bakker, D. C. E., Bates, N. R., Corbiere, A., Gonzalez-Davila, M., Friedrich, T., Hauck, J., Heinze, C., Johannessen, T., Kortzinger, A., Metzl, N., Olafsson, J., Olsen, A., Oschlies, A., Padin, X. A., Pfeil, B., Santana-Casiano, J. M., Steinhoff, T., Telszewski, M., Rios, A. F., Wallace, D. W. R., and Wanninkhof, R.: Tracking the Variable North Atlantic Sink for Atmospheric CO₂, *Science*, 326, 1391-1393, 2009.
- Weiss, R. F.: Carbon dioxide in water and seawater: the solubility of a non-ideal gas, *Marine Chemistry*, 2, 203-215, 1974.
- Weiss, R. F. and Price, B. A.: Nitrous oxide solubility in water and seawater, *Marine Chemistry*, 8, 347-359, 1980.
- Yamagishi, H., Tohjima, Y., Mukai, H., and Sasaoka, K.: Detection of regional scale sea-to-air oxygen emission related to spring bloom near Japan by using in-situ measurements of the atmospheric oxygen/nitrogen ratio, *Atmospheric Chemistry and Physics*, 8, 3325-3335, 2008.

Chapter 4

Latitudinal variability in atmospheric O₂, CO₂, and APO across the Atlantic Ocean

4.1. Introduction

As discussed in Chapter 1 of this thesis, concurrent measurements of atmospheric O₂ and CO₂ have much potential for furthering our understanding of ocean carbon cycle processes and ocean-atmosphere O₂ and CO₂ exchanges, and yet the global atmospheric O₂ measurement network is fairly sparse with large gaps, particularly in oceanic and developing regions. The motivation for the research presented in this chapter is to help to 'fill-in' one of these gaps, in the Atlantic Ocean region, by making continuous measurements of atmospheric O₂ and CO₂ from a commercial container ship travelling continuously from Europe to South America and back, thus covering a wide latitudinal range.

There are several other existing datasets of atmospheric O₂ and CO₂ measurements from oceanic regions, some of which are ongoing today. Those that have been/are from research vessels are described in the introduction of Chapter 3. To date, there have only been atmospheric O₂ and CO₂ datasets collected from three commercial container ship routes, in addition to the atmospheric O₂ and CO₂ data presented in this chapter. Table 4.1 shows the latitudinal and longitudinal ranges of these previous container ship O₂ and CO₂ datasets, as well as the time period of data collection, O₂ and CO₂ measurement techniques used, and whether the measurements were made continuously or from discrete flask samples.

The APO flask data of (Battle et al., 2006) (1st row of Table 4.1) were the first data to confirm the existence of the equatorial 'APO bulge' in the Pacific Ocean sector (see Section 4.4), which was predicted by the modelling studies of (Stephens et al., 1998) and (Gruber et al., 2001). The subsequent O₂ and CO₂ data from the western Pacific by Yasunori Tohjima and colleagues (rows 2 and 4 of Table 4.1) have been used to determine the effects of El Niño and La Niña events on the magnitude of the western Pacific Ocean equatorial APO bulge, and have also lead to the discovery of an APO minimum that exists in the North West Pacific at about 40°N (Tohjima et al., 2012; Tohjima et al., 2015). The flask and continuous O₂ and CO₂ measurements of Yasunori Tohjima and colleagues over the western Pacific Ocean are presently ongoing, and thus represent the longest record of shipboard atmospheric O₂ and CO₂ measurements to date.

Table 4.1. Previous O₂ and CO₂ measurements from commercial container ships. NDIR refers to non-dispersive infrared, and GC/TCD refers to gas chromatograph equipped with a thermal conductivity detector. Latitude and longitude ranges are approximate. The container ship O₂ and CO₂ flask measurements of Battle et al. (2006) were continued on board the ‘Ka’ imimoana’, a USA NOAA (National Oceanic and Atmospheric Administration) research vessel, which serviced a series of moorings between 8°N and 8°S in the Pacific, from 2001-2007. Cont/Flask refers to continuous or flask sample measurements.

Period	Latitude Range	Longitude Range	Cont/Flask	Measurement Technique	Publications
1996 - 2000	30°N to 30°S	175°E to 110°W	Flask	Interferomic/ Mass Spectrometric (O ₂) NDIR (CO ₂)	(Battle et al., 2006)
2001 - present	10°N to 55°N	140°E to 80°W	Flask	GC/TCD (O ₂) NDIR (CO ₂)	Tohjima et al. (2005, 2012, and 2015)
2001 - present	50°N to 40°S	130°E to 180°E	Flask	GC/TCD (O ₂) NDIR (CO ₂)	Tohjima et al. (2005, 2012, and 2015)
2007 - present	10°N to 55°N	140°E to 80°W	Cont	GC/TCD (O ₂) NDIR (CO ₂)	Yamagishi et al. (2012); Tohjima et al. (2015)
2007 - present	50°N to 40°S	130°E to 180°E	Cont	GC/TCD (O ₂) NDIR (CO ₂)	Yamagishi et al. (2012); Tohjima et al. (2015)

The previous datasets of shipboard atmospheric O₂ and CO₂ presented in Table 4.1 are all from the Pacific Ocean; hence, the data presented in this chapter represent the first ongoing shipboard measurements from the Atlantic Ocean, and can therefore help to provide new insights into atmospheric-ocean O₂ and CO₂ interactions in the Atlantic Ocean region on seasonal and annual time-scales. The advantage of making atmospheric O₂ and CO₂ measurements from a container ship is that, since the ship is continually following the same route, the data can be binned latitudinally, and can therefore provide time series information at multiple latitudes (with some data gaps). In other words, a single shipboard measurement system can act as multiple ‘virtual’ stationary measurement systems, providing similar seasonal and annual information. Utilising a moving platform that repeats the same route, such

as a container ship, is therefore a very efficient way of monitoring a relatively large area.

The disadvantage of making high-precision atmospheric measurements on board container ships, is that the equipment has to be capable of running independently of human intervention for long periods of time, since opportunities for maintenance and troubleshooting problems are usually limited to periods of a few hours once every 2-3 months. Additionally, container ships are known to change route every few years or so, with little or no notice given. Despite the logistical and technical difficulties, making use of a container ship as a 'voluntary observing ship' has enabled me to collect a unique dataset in a remote part of the world, which would not have been possible using research vessels.

The outline of this chapter is as follows: Section 4.1.1 describes the equipment setup on board the Cap San Lorenzo container ship, and the route that the ship takes when travelling between Europe and South America. In Section 4.2, I present the O₂, CO₂ and APO atmospheric data as meridional transects, analyse short-term variability in both the port and open ocean data, and discuss seasonal variability in the position of the ITCZ in the Atlantic sector. In Section 4.3, I have binned the atmospheric O₂, CO₂ and APO data into 5° latitudinal bands, and I present the seasonal variability in each species and discuss how the seasonal cycle changes with latitude. Lastly, in Section 4.4, I present the annual mean latitudinal distribution in O₂, CO₂ and APO over the Atlantic Ocean and compare the atmospheric data to model output, as well as shipboard APO data from the western Pacific Ocean. In Section 4.5, I summarise the results and conclusions of this chapter.

4.1.1. Installation of the shipboard atmospheric measurement system on board the Cap San Lorenzo

The Cap San Lorenzo is a commercial container ship operated by Hamburg Süd, which currently travels continuously between Hamburg, Germany (53.57°N, 10.00°E) and Buenos Aires, Argentina (34.60°S, 58.38°W), stopping in the UK at the 'London Gateway' port in Essex. As shown in Figure 4.1, the Cap San Lorenzo can carry up to 10,595 containers, and is over 330 m in length. The shipboard O₂ and CO₂ measurement system is located in the bridge stack on G deck, in the electronics server room, which is air conditioned. Air is sampled from the roof of the bridge, which is situated two floors above G deck (the inlet line length is ~25 m).

The ship is relatively new, and only came into service in April 2014. Consequently, the ship has a more ‘modern’ layout, whereby the engine and bridge are separated by about 150 m, to prevent excessive noise and vibrations from the engine disturbing the crew, who mainly reside in the bridge stack. This new layout is actually very beneficial to the shipboard O_2 and CO_2 measurement system, because data contamination from the ship’s exhaust stack is very rare, owing to the fact that the ship’s exhaust is far away from the sample air inlets.

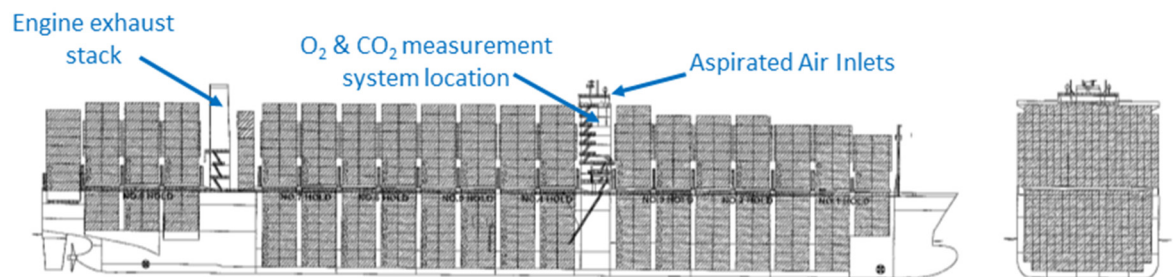


Figure 4.1. Schematic of the Cap San Lorenzo container ship, showing the location of the O_2 and CO_2 measurement system on G deck, the Aspirated Air Inlets, and the ship’s engine exhaust stack.

Figure 4.2 shows the route of the Cap San Lorenzo from Hamburg to Buenos Aires and back. The northwards and southwards routes are identical, with the exception that during the northwards voyage, the ship takes a detour at about $30^\circ N$ and stops at Tangier, Morocco, before continuing on to Europe. There is also remarkable similarity between the ship’s route on successive voyages (differences in route are negligible), which indicates that it is appropriate to construct time series from successive ship voyages. Likewise, it is also appropriate to treat the majority of the southwards and northwards routes as the same, since the ship mostly passes through the same positions when heading in both directions. The ship makes berth in port a total of 14 times in 12 different locations during a complete route from Europe to South America and back. In order, these stops are: London (UK), Hamburg (Germany), Antwerp (Belgium), Le Havre (France), Santos (Brazil), Paranaguá (Brazil), Buenos Aires (Argentina), Montevideo (Uruguay), Rio Grande (Brazil), Itapoá (Brazil), Paranaguá (Brazil), Santos (Brazil), Tangier (Morocco), and Rotterdam (the Netherlands).

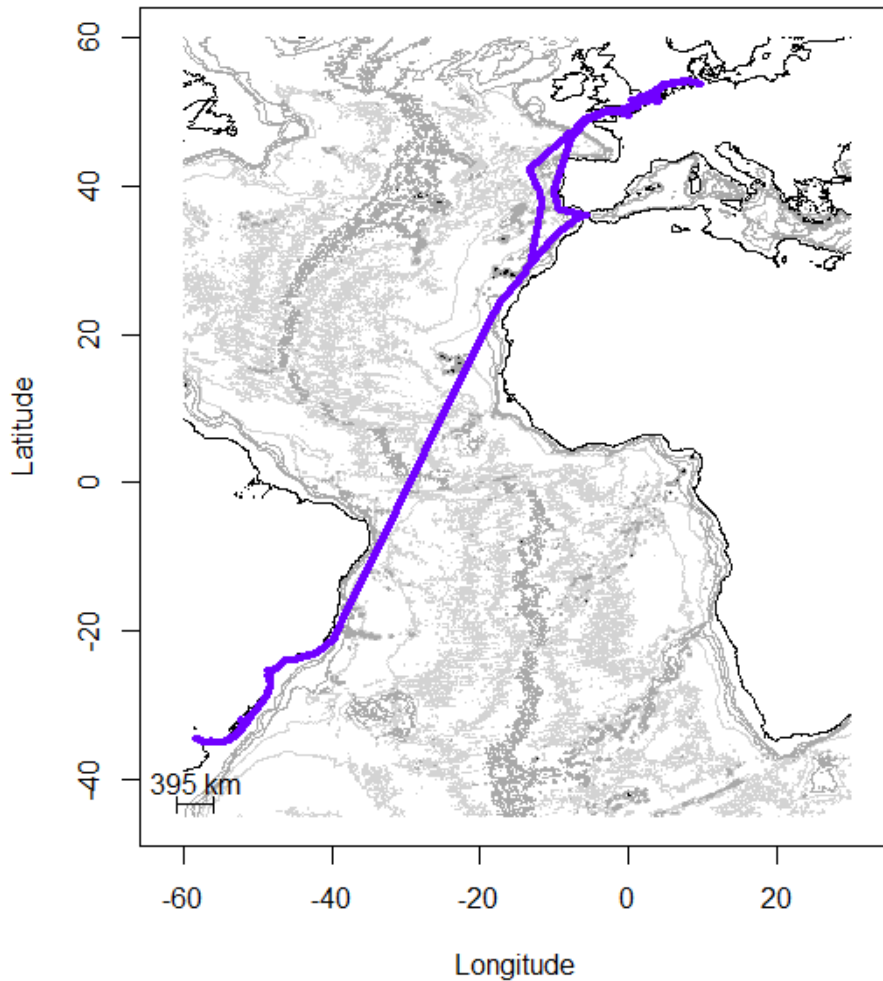


Figure 4.2. Route of the Cap San Lorenzo from Hamburg to Buenos Aires and back.

4.2. Meridional transects of atmospheric O_2 , CO_2 , and APO across the Atlantic Ocean

The Cap San Lorenzo takes exactly 8 weeks to travel from Hamburg, Germany, to Buenos Aires, Argentina, and back to Hamburg. Figure 4.3 shows the atmospheric O_2 , CO_2 and APO data from these meridional transects between September 2014 and January 2016. The plots demonstrate several features of the data. Firstly, there is a significant amount of data missing, due to technical issues with the measurement system drying traps, which were found to block more frequently than expected, because the air in the tropics is extremely humid. In particular, most of the meridional transects consist of the southwards data only, with little northwards data collected. Additionally, the failure of a power supply in the electronics of the measurement system meant that 16 weeks of data were lost from October 2014 to January 2015. The precision of the Nov-Dec2015 (southwards) and Jan2016

(northwards) O_2 and APO data was also compromised, due to the degradation of one of the Oxzilla II fuel cells.

Secondly, the data demonstrate that when the ship is in port, both in Europe and in South America, there is significant influence from the land, characterised by large, often diurnal variations in CO_2 and O_2 (with smaller fossil fuel related variations sometimes apparent in APO). At sea, however, the atmospheric variability in all three species is significantly reduced, with the main feature occurring close to the equator, at the Inter Tropical Convergence Zone (ITCZ), which migrates with latitude seasonally. This tropical atmospheric feature in the data usually consists of a step change in atmospheric mole fraction, caused by the seasonal differences between northern hemisphere and southern hemisphere air. For some of transects (e.g. Sep-Oct 2014), the change in mole fraction at the ITCZ is very sudden, whilst for other transects (e.g. Apr-May 2015), the change in mole fraction at the ITCZ is more gradual.

Both seasonal and long-term changes in O_2 , CO_2 and APO are apparent in the data. For example, CO_2 is higher (and O_2 is lower) in the northern hemisphere in Apr-May 2015 than in Jun-Jul 2015, which is expected, owing to the strong drawdown of CO_2 in the summer months by the land biosphere. APO is also lower in the mid-latitude northern hemisphere in Apr-May 2015 than in Jun-Jul 2015, most likely because as the oceans warm in the spring and summer, they emit O_2 to the atmosphere. CO_2 is also emitted to the atmosphere as the oceans warm, but this seasonal variability is not observed in atmospheric CO_2 data, because the air-sea equilibration time for CO_2 is relatively slow (~ 1 year) compared to atmospheric mixing times (~ 1 month), and because there are other CO_2 fluxes that counteract the release of CO_2 to the atmosphere induced by an increase in oceanic temperature (such as phytoplankton primary productivity; see Chapter 1, Section 1.2 for more details). Long-term changes in the atmospheric data are clear when one compares the atmospheric mole fraction of O_2 , CO_2 and APO for the same months in two successive years, such as Sep-Oct 2014 and Aug-Sep 2015, which show that CO_2 is increasing, while O_2 and APO are decreasing.

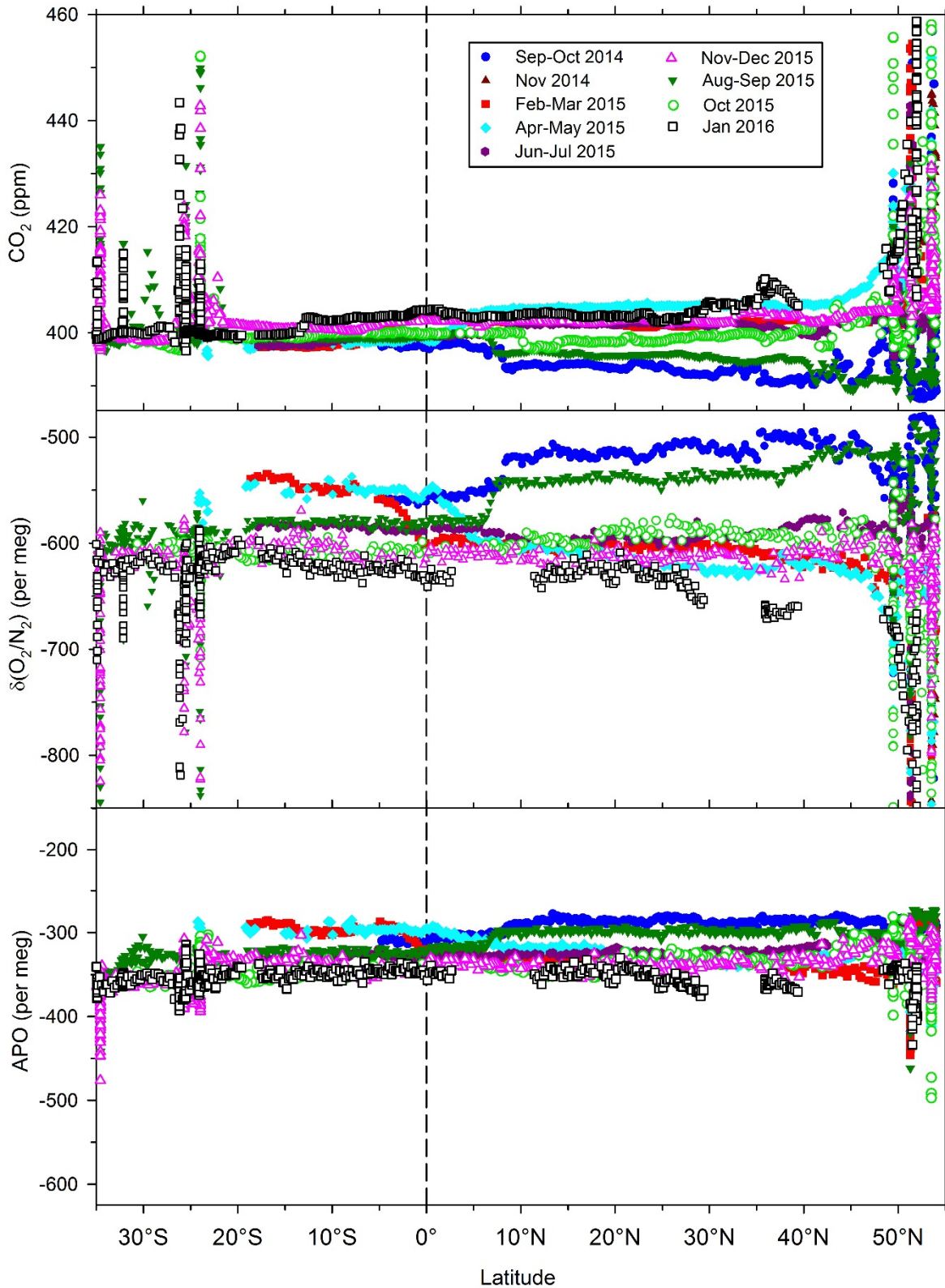


Figure 4.3. Meridional transects of hourly-averaged atmospheric CO_2 , $\delta(\text{O}_2/\text{N}_2)$, and APO across the Atlantic Ocean. The equator is represented by the dashed line. Different northwards and southwards crossings are represented by the symbols and colours in the figure legend. Y-axes have been scaled to be visually comparable on a mole per mole basis.

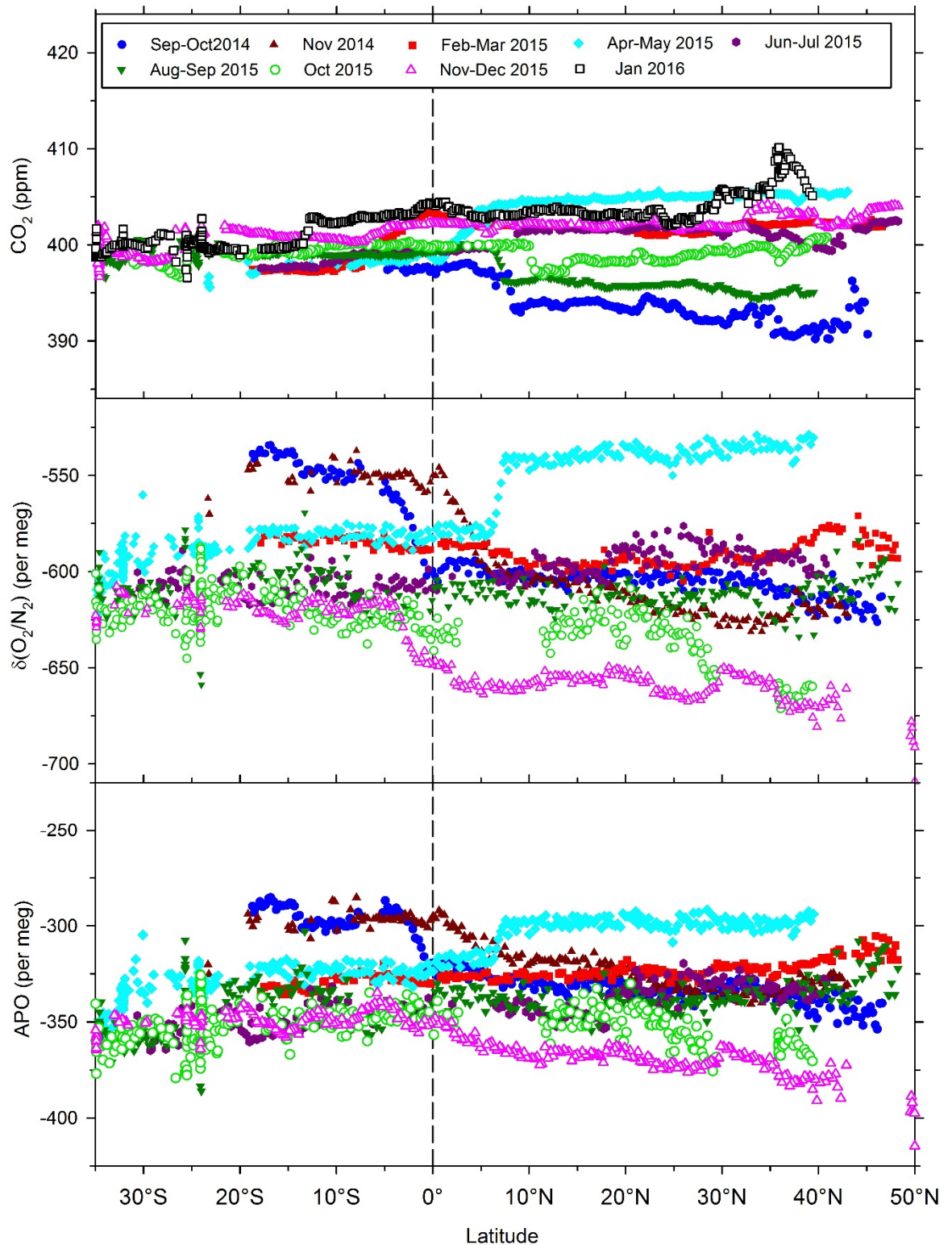


Figure 4.4. Meridional transects of hourly-averaged atmospheric CO_2 , $\delta(\text{O}_2/\text{N}_2)$ and APO across the Atlantic Ocean, with polluted ‘port air’ data excluded. Y-axes have been scaled to be visually comparable on a mole per mole basis.

Figure 4.4 shows the same meridional transects of O_2 , CO_2 and APO as those in Fig. 4.3, only this time with the polluted ‘port air’ data excluded, which makes it easier to discern the short-term variability over the open ocean. It is clear that there is still some land influence, even at sea, since there is more variability in CO_2 and O_2 than in

APO (which is invariant to land biosphere processes). This also explains why the ITCZ step changes in CO₂ and O₂ are more pronounced than those in APO, since these are driven by seasonal differences in CO₂ and O₂ between the two hemispheres that are dominated by land biosphere influences.

4.2.1 Short-term variability: equator and open ocean

There is some interesting short-term variability in the O₂, CO₂ and APO data, particularly around the equator, which is demonstrated more clearly in Figure 4.5. For example, in Apr-May 2015 there was a small positive excursion in CO₂ and corresponding negative excursions in O₂ and APO, just south of the equator, and after the ship had crossed the ITCZ. Similar excursions in O₂, CO₂ and APO also occurred at the equator in Feb-Mar 2015. There are two possible explanations for these excursions: either the excursions represent fluxes of O₂ and CO₂ between the ocean and the atmosphere, occurring in the vicinity of the equatorial upwelling region, or the excursions are caused by changes in atmospheric transport, bringing air to the ship from a different latitude, hemisphere, or even altitude.

There are in fact three reasons why the latter of these two explanations is the most likely, and that the excursions represent changes in atmospheric transport. Firstly, equatorial upwelling is not a seasonal phenomenon, and therefore, it seems strange that these excursions are only apparent in two of the eight meridional transects. Secondly, owing to the differences in the air-sea gas equilibration times for O₂ and CO₂, one would not expect to see oceanic-derived CO₂ and O₂ signals occurring at the same time, and with very similar magnitudes (on a mole per mole basis). Thirdly, in the case of the Apr-May 2015 transect, it is easy to see from Fig. 4.4 that the excursions could be due to a change in atmospheric transport, whereby after the ship crosses the ITCZ, northern hemisphere air is briefly transported south. Such changes between northern and southern hemisphere air have been observed before in time series of atmospheric CO₂ and O₂ data from equatorial regions (see Manning et al., 2003). Whilst this last reason can only be used to explain the equatorial excursions of the Apr-May 2015 transect, it is possible that the Feb-Mar 2015 equatorial excursions are caused by a similar southwards transport of air from a more northerly latitude, with the main difference being that in Feb-Mar 2015 the ITCZ was positioned in the southern hemisphere, not the northern hemisphere, so at the time of the excursions, the ship had not yet crossed the ITCZ.

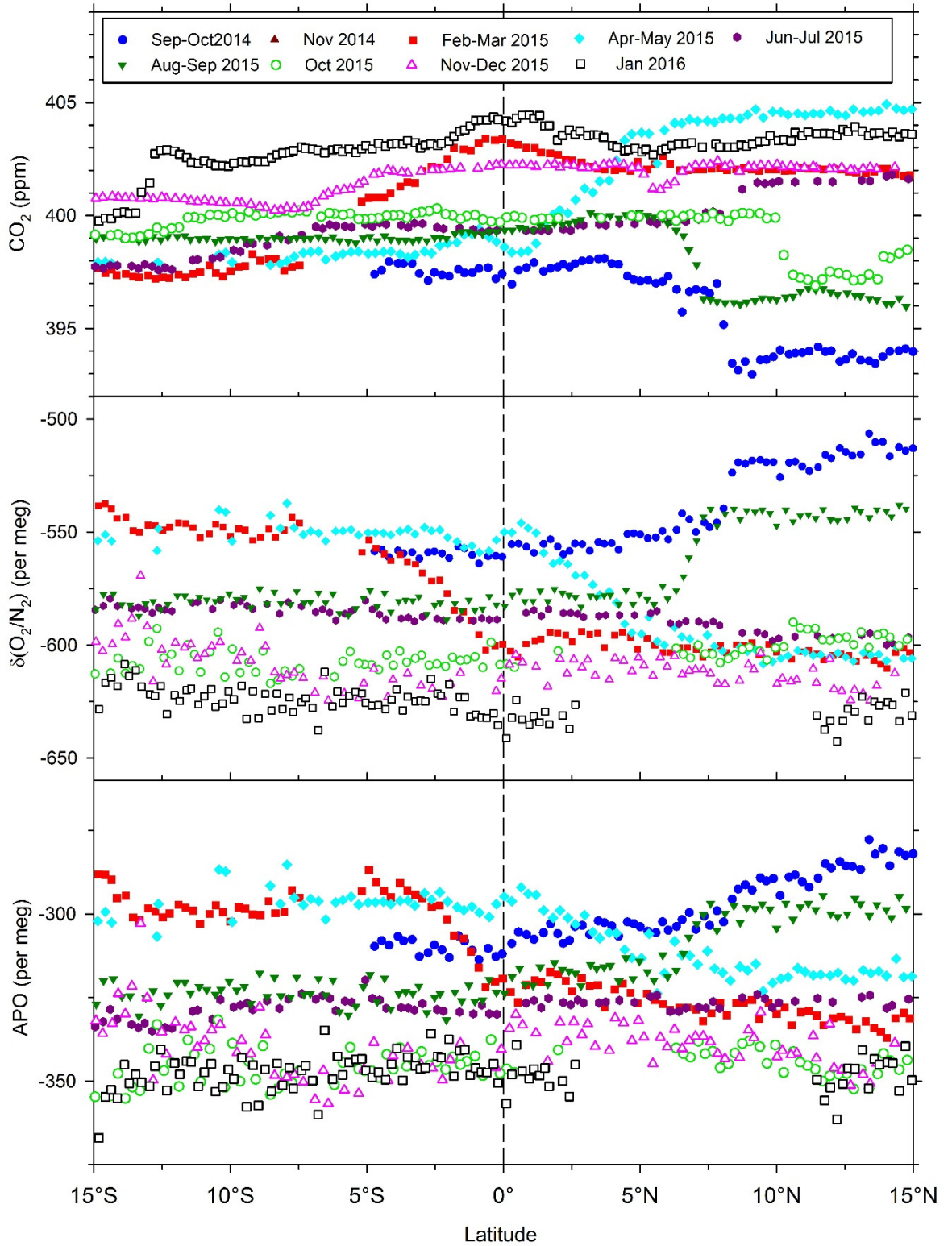


Figure 4.5. Atlantic equatorial variability in CO_2 (top panel), $\delta(\text{O}_2/\text{N}_2)$ (middle panel) and APO (bottom panel). Note that the y-axes have been scaled so that the APO and CO_2 axes are 1.5 times and 2 times zoomed, respectively, compared to the $\delta(\text{O}_2/\text{N}_2)$ axis on a mole per mole basis.

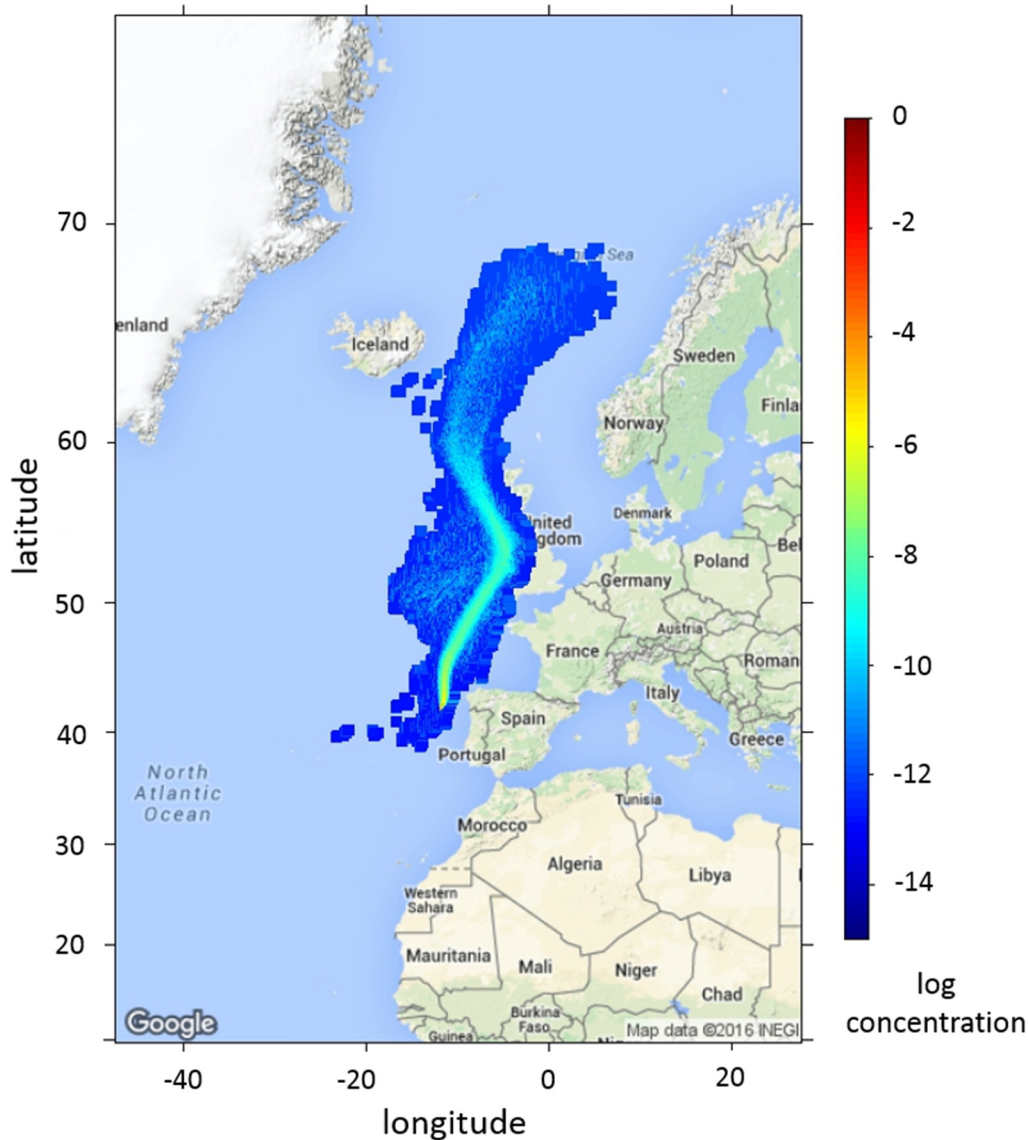


Figure 4.6. NAME footprint showing the air mass origin on 27Apr2015, as the Cap San Lorenzo was travelling south. The colour scale given is the log of the time integrated concentration of air particles gs m^{-3} .

Even though it seems likely that the equatorial excursions in O_2 , CO_2 and APO are caused by atmospheric transport changes, rather than air-sea fluxes, it is worth investigating this further, using an atmospheric transport model. Using the UK Met Office NAME (Numerical Atmospheric-dispersion Modelling Environment) model (Jones et al., 2007), I produced 3-day, backwards run atmospheric footprints consisting of 10,000 particles each, for various periods of short-term variability in atmospheric O_2 , CO_2 and APO. The NAME footprints show that much of the short-term variability in atmospheric O_2 , CO_2 and APO in the North Atlantic seems to be correlated with changes in air mass origin. For example, the brief negative excursion in CO_2 , and corresponding positive excursion in O_2 in April 2015 that occur at $\sim 37^\circ\text{N}$ (see Fig. 4.4) coincide with a change in air mass origin from the northwest (i.e. North

Atlantic open ocean) to the northeast, from over the UK and the Arctic (see Figure 4.6). Such a change in air mass origin is consistent with lower CO₂ and higher O₂, since the magnitude of seasonal variability in CO₂ and O₂ increases with latitude, and April is a period characterised by strong CO₂ uptake and O₂ release from the terrestrial biosphere in the northern hemisphere. Similarly, the variability in Sep-Oct2014 between 20°N and 40°N (see Fig. 4.4) is caused by a change in air mass origin (NAME footprints not shown) from the northwest (North Atlantic open ocean) to the southwest (equatorial Atlantic open ocean), and also from the northwest to the northeast (with some influence from northwest Africa).

The NAME footprints from the excursions close to the equator, show no evidence of the air mass origin switching back to the northern hemisphere, once the ship has passed the ITCZ on the southwards crossing in Apr-May2015. Similarly, there is no evidence of long-range transport of higher latitude northern hemisphere air for the Feb-Mar2015 equatorial excursions. This might be due to inaccuracies with the NAME transport model, which are more likely to occur at the equator, where the atmospheric transport is more complex. Alternatively, it is possible that between the equator and the ITCZ, in the doldrums where the winds are generally calm (particularly compared to the trade winds in the subtropical regions), that the atmospheric O₂, CO₂, and APO variability reflects local air from the equatorial region itself, rather than air from north or south of the equator, and that this might cause the equatorial excursions shown in Fig. 4.4 in Feb-Mar2015 and Apr-May2015. What is clear, is that it is very likely that these equatorial excursions in O₂, CO₂, and APO are caused by changes in atmospheric transport, and not caused by a temporary flux of each species between the ocean and atmosphere during the spring and early summer transects of 2015.

In addition to the short-term equatorial excursions shown in Fig. 4.4, there is also some variability in the shape of the ITCZ feature in the data, from a rather sharp step change (e.g. Sep2014, Jun-Jul2015, Aug-Sep2015, Oct2015 and Jan2016) to a more gradual slope (e.g. Feb-Mar2015, Apr-May2015, and Nov-Dec2015). This variability in the 'sharpness' of the ITCZ as the ship crosses from northern hemisphere to southern hemisphere air, and vice versa, can be explained from the NAME footprints, with sharp changes across the ITCZ corresponding with rapid changes in air mass origin from the northern hemisphere easterlies to the southern hemisphere easterlies, while more gradual changes across the ITCZ are characterised

by periods of mixed air origins from both hemispheres (the latter shown in Figure 4.7).

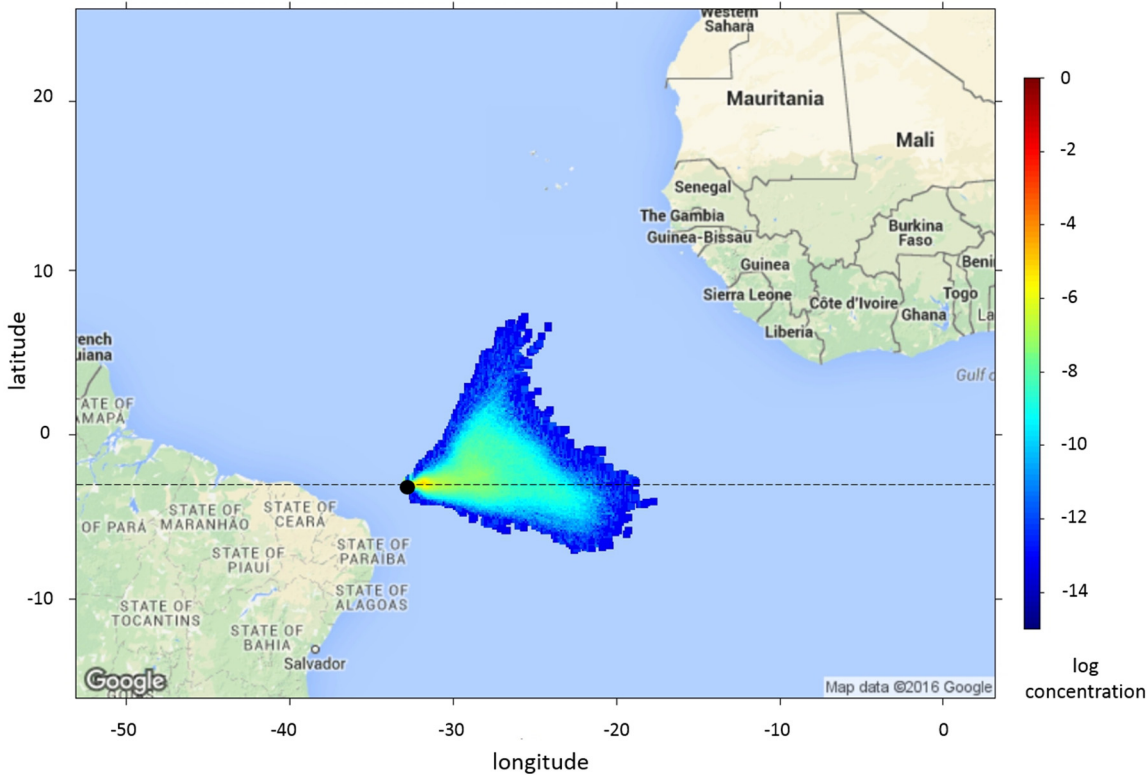


Figure 4.7. NAME footprint on 08Mar2015, showing the air mass origin as the Cap San Lorenzo crosses the ITCZ heading south. The colour scale given is the log of the time integrated concentration of air particles gs m^{-3} . The footprint demonstrates that the air originates from both the northern and southern hemispheres simultaneously while the ship crosses the ITCZ. The ship's location is indicated by the black circle, and the position of the ITCZ is shown by the horizontal dashed black line.

4.2.2 Short-term variability: The Channel and North Sea

Figure 4.8 shows two periods of atmospheric O_2 , CO_2 and APO data from when the Cap San Lorenzo was travelling between London, Hamburg, Antwerp and Le Havre; both periods of data also show short-term variability, but with some key differences to that displayed in the open ocean data. In general, the port data (defined as periods when the ship's speed was less than 5 mph) are characterised by elevated CO_2 and lower O_2 compared to the data when the ship is travelling through the Channel and the south North Sea. These anti-correlated O_2 and CO_2 variations represent terrestrial signals, most of which are photosynthesis and respiration of the land biosphere, but there is also some evidence of fossil fuel influence, which manifests as slight negative excursions in APO that correspond to positive excursions in CO_2 (see Chapter 5 for a detailed analysis of quantifying fossil fuel using APO).

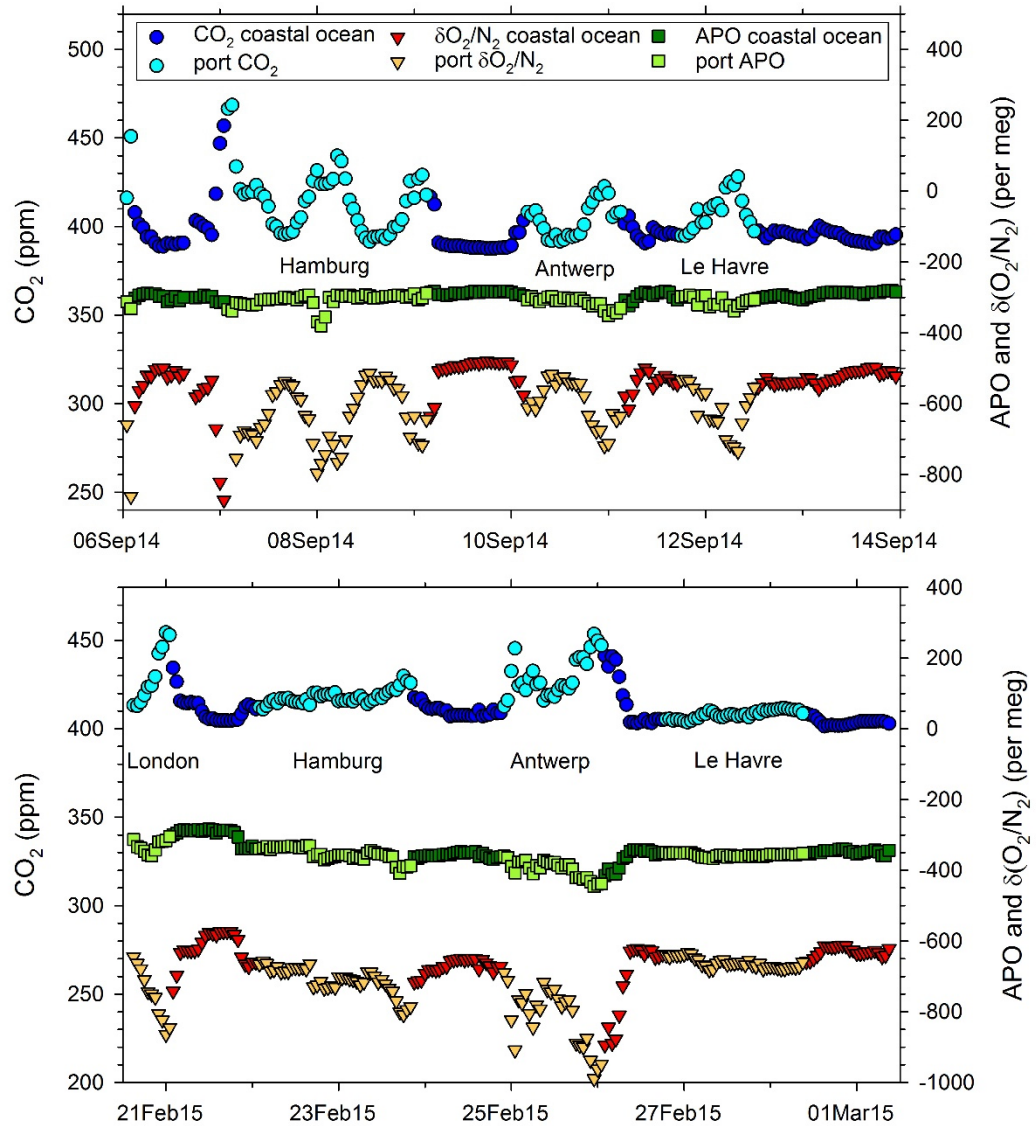


Figure 4.8. Hourly-averaged atmospheric CO₂ (circles), $\delta(\text{O}_2/\text{N}_2)$ (squares) and APO (triangles) from two periods (top panel from Sep2014; bottom panel from Feb2015) when the Cap San Lorenzo was travelling between ports in Europe. Data collected when the ship's speed was less than 5 mph are shown in turquoise, bright green and yellow for CO₂, $\delta(\text{O}_2/\text{N}_2)$, and APO, respectively. Both plots are annotated with the names of the ports in which the ship made berth. The y-axes have been scaled to be visually comparable on a mole per mole basis.

The CO₂ and O₂ excursions in Sep2014 are larger than those in Feb2015, because in September, the biosphere is still relatively active, whereas in February, many plants are dormant and do not photosynthesise, and their respiration rates are also substantially reduced. In fact, assuming that the APO:CO₂ fossil fuel emission ratio is approximately $-0.3 \text{ mol mol}^{-1}$, then the magnitude of the negative excursions in APO suggest that all of the CO₂ and O₂ variability in Feb2015, and up to half of the CO₂ and O₂ variability in Sep2014 is caused by fossil fuel burning. All of the port-related variability for both periods displays diurnal variability characteristic of

boundary layer height changes, whereby CO₂ is elevated and O₂ is reduced at night time due to a lower, more stable atmospheric boundary layer with reduced wind speeds and turbulence, which enhances the flux-related signals in the atmospheric time series data (also known as the rectifier effect).

4.2.3 Short-term variability: ocean upwelling and productivity events

The general lack of short-term variability in APO in all of the Cap San Lorenzo open ocean data is somewhat surprising, given that several publications have previously reported relatively large variations in APO from the ocean (either upwelling or primary productivity related events). For example, the papers of (Lueker et al., 2003) and (Lueker, 2004), (Thompson et al., 2007) and (Thompson et al., 2008), (van der Laan-Luijkx et al., 2010), and (Patecki and Manning, 2007), all present atmospheric variability in APO that has been attributed to fluxes in/out of the ocean. In addition, a very large APO event was observed during the JC090 cruise, which is presented in Chapter 3 of this thesis. It is therefore very surprising that there is no short-term APO variability greater than ~5 per meg observable in the Cap San Lorenzo open ocean data that can be explained or attributed to ocean-atmosphere exchange. Even in the European and South American coastal data, the only variations in APO are negative, and are associated with large positive excursions in CO₂, which only occur when the ship was approaching, leaving, or docked in port, and give strong indication of being caused by fossil fuel combustion.

There are three possible explanations: firstly, that it is simply a coincidence that no APO events have been observed by the shipboard measurement system on board the Cap San Lorenzo, although this is extremely unlikely, because the dataset is over a year in duration. Secondly, it is perhaps possible that since the inlets are at ~40 m above sea level on board the Cap San Lorenzo, whereas research vessel inlets are typically only ~25 m above sea level, and since the Cap San Lorenzo travels at speeds of up to 25 mph, then perhaps any ocean-atmosphere fluxes are attenuated by turbulent mixing processes in the atmosphere between the surface of the ocean and the measurement system aspirated air inlets. Although this second possibility is plausible, it does not seem to be likely, given that the magnitude of air-sea fluxes required in order to produce APO atmospheric excursions on the order of 50 – 100 per meg (see Chapter 3, Section 3.4.8) are of similar magnitude to forest fluxes (see Ishidoya et al., 2015) that are easily observable in atmospheric measurements from a

similar height. Thirdly, it is possible that some of the variability in APO, which has been ascribed to air-sea fluxes in the publications mentioned previously, has been misinterpreted and is in fact due to either technical issues, atmospheric transport, or fossil-fuel related variability in APO, rather than ocean-related variability.

For example, it is likely that the extremely large negative APO excursions measured by (van der Laan-Luijkx et al., 2010) are in fact caused by a technical problem with the measurement system (such as O₂/N₂ fractionation), given that the excursions are so large (up to ~450 per meg in magnitude), and to my knowledge, excursions of such magnitude have only ever been observed by the F3 platform measurement system. The Cap San Lorenzo passes close to the location of the F3 platform, and therefore likely samples very similar air, and yet there is no evidence of ocean-related APO events in the data. The short-term ocean-related variability presented in (Thompson et al., 2007), (Thompson et al., 2008) and (Patecki and Manning, 2007), of which all measurements were made from research vessels in the open ocean, is generally small compared to the precision of the O₂ measurements, and could easily be caused by a combination of technical issues (which seem likely, given that anti-correlation between O₂ and CO₂ is not always very strong) and changes in atmospheric transport.

Finally, the APO events of (Lueker et al., 2003) and (Lueker, 2004) do not seem to be affected by technical issues with the measurement system, but may have been misinterpreted as oceanic upwelling events, given that the APO negative excursions often coincide with large positive CO₂ excursions (of up to ~40 ppm), which are more indicative of fossil fuel related signals rather than oceanic upwelling events. In addition, natural soils are the largest contributor to the global N₂O budget (Ciais et al., 2013), and thus the positive N₂O excursions that are also attributed to ocean upwelling events by Lueker and colleagues could be explained by air masses that originate from the forested regions of northern California and Oregon. I have not been able to analyse the air mass history of these anti-correlated APO and N₂O events using NAME, since the Met Office Unified Model meteorological data is not available to me for the period 2000 – 2002, when the events occurred. It is possible, however, to generate atmospheric back trajectories for these events using the NOAA HYSPLIT (Hybrid Single Particle Lagrangian Integrated Trajectory) model (Stein et al., 2015). Figure 4.9 shows ensemble HYSPLIT back trajectories, which indicate the origin of the air masses for two periods of the data presented by Lueker and colleagues; a period reported to be an ocean upwelling event, and a period of very little short-term

variability in APO, CO₂ and N₂O. In addition to the two periods shown in Fig. 4.9, a total of 7 ‘ocean upwelling’ periods and 5 periods with little APO, N₂O and CO₂ short-term variability were investigated using HYSPLIT between June 2000 and October 2002. Out of these 12 periods, all 7 of the ‘ocean upwelling’ periods were found to originate from the land (all from the north or north east), and all 5 of the periods with little short-term variability were found to originate from the ocean (mostly from the northwest). While it is likely that off-shore winds will enhance the upwelling by pushing the water away from the coast, the positive excursions in CO₂ indicate that a large proportion of the air masses arriving at Trinidad Head, USA, during the event periods have been influenced by land processes.

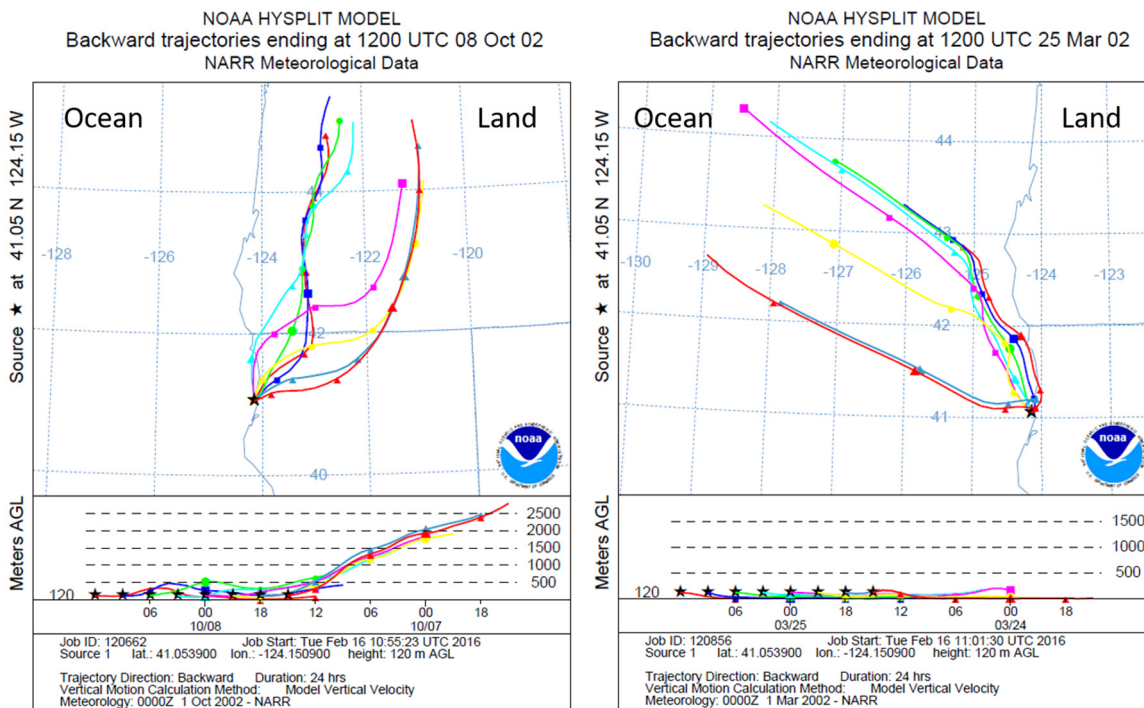


Figure 4.9. HYSPLIT ensemble back trajectories for 08 Oct 2002 (left plot) and 25 Mar 2002 (right plot), consisting of eight, 3-hourly trajectories 24 hours in length from Trinidad Head, California, USA. The left plot corresponds to a period exhibiting low APO, and elevated CO₂ and N₂O, which was previously reported by Lueker and colleagues as being an ocean upwelling event, and the right plot corresponds to a period of little short-term variability in either APO, CO₂ or N₂O, which is of oceanic origin.

Figure 4.10 shows the N₂O, CFC-12 and CFC-11 variability from the AGAGE (Advanced Global Atmospheric Gases Experiment) measurements at Trinidad Head for 2000, with the approximate timing of the (Lueker, 2004) ‘upwelling’ events shown by the orange boxes. It is clear that there is a strong correlation between the positive N₂O excursions, and positive excursions in both CFC-12 and CFC-11, which both are chloroflorocarbons of anthropogenic origin only. The AGAGE data therefore also support the hypothesis that the air arriving at Trinidad Head exhibits significant

influences from anthropogenic activities, which has been noted previously, by (Prinn et al., 2000), and also by (Li et al., 2005), who found that 533 pollution events are apparent in both the CFC-11 and CFC-12 AGAGE data for the year 2000.

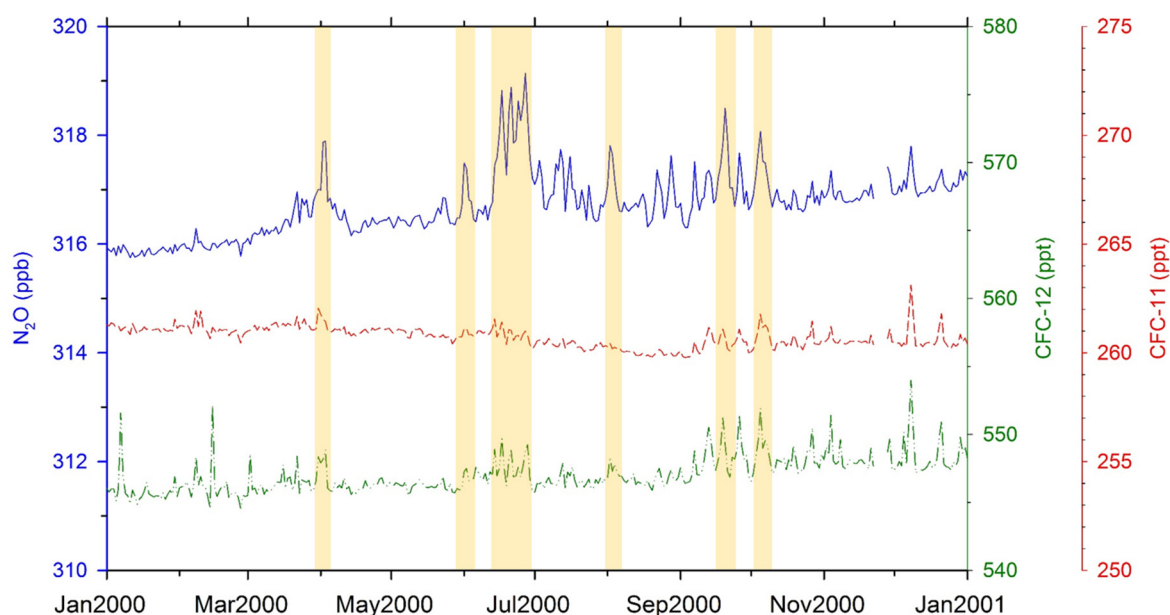


Figure 4.10. Short-term variability in N_2O (blue solid line), CFC-12 (green dashed-dotted line) and CFC-11 (red dashed line) from the AGAGE measurements at Trinidad Head. The orange shading indicates the approximate timing of the ‘upwelling’ events published in (Lueker, 2004).

It is therefore likely that the ‘ocean upwelling’ events reported by Lueker and colleagues are of land origin, and that the negative APO excursions represent influences from fossil fuel combustion, although it is also possible that the APO and N_2O signals are from a combination of fossil fuel and ocean influences. Thus, I propose that APO excursions caused by air-sea gas exchange are typically very small, because atmospheric mixing processes are relatively fast compared to the diffusion of O_2 across the air-sea interface, and therefore do not easily manifest in APO data. It therefore follows that the negative APO excursion observed during the JC090 cruise (and presented in Chapter 3) probably does not reflect a real atmospheric event, and was in fact likely caused by a technical measurement system issue, such as O_2/N_2 fractionation. I therefore recommend extreme caution when attributing short-term variations in atmospheric O_2 or APO data to ocean upwelling or primary productivity events, because unexplained APO variability is often an indication of a technical problem, and negative APO excursions can also be caused by fossil fuel emissions.

4.2.4 Variability in the position of the ITCZ

In addition to the variability in atmospheric O₂, CO₂ and APO shown in Figs. 4.4 and 4.5, variability in the position of the ITCZ is also clear from the data. The ITCZ is typically defined by either the convergence of the northeast and southeast trade winds, or by the location of the equatorial precipitation maximum (since the converging branches of the Hadley circulation cause uplift of warm, moist air, resulting in precipitation); a step change in CO₂ or O₂ is also a suitable proxy for the position of the ITCZ, since such a change represents a shift from air that is representative of the northern hemisphere to air that is representative of the southern hemisphere, or vice versa.

The ITCZ is known to seasonally migrate towards the hemisphere that is warming, and away from the hemisphere that is cooling, with corresponding cross-equatorial atmospheric and surface ocean energy fluxes from the warming hemisphere into the cooling hemisphere (Schneider et al., 2014). The magnitude of these cross-equatorial fluxes are strongly coupled to the position of the ITCZ, in that stronger cross-equatorial fluxes occur when the ITCZ moves poleward, and weaker fluxes occur when the ITCZ is close to the equator (Bischoff and Schneider, 2014). Figure 4.11 shows the seasonal migration in the Atlantic ITCZ position from the step changes in the shipboard atmospheric CO₂ and O₂ data. Also shown are ITCZ positions from step changes in atmospheric CO₂ and CH₄ data collected on board the RRS James Clark Ross (courtesy of Euan Nisbet and Rebecca Brownlow, Royal Holloway University of London; RHUL), and ITCZ positions inferred using monthly mean precipitation from NASA (National Aeronautics and Space Administration) Tropical Rainfall Measuring Mission (TRMM) satellite data, which has a spatial resolution of 0.5° by 0.5°. The TRMM and RHUL data provide a useful comparison to the ITCZ positions derived from the Cap San Lorenzo data, and provide insight into interannual variability of ITCZ migrations in the Atlantic.

The Cap San Lorenzo 2015 ITCZ position data show that the ITCZ exists mainly in the northern hemisphere, and only shifts to the southern hemisphere during the boreal winter. The latitudinal range for 2015 is from about 6°S to 10°N; this is a slightly larger range than one would expect in the Atlantic sector according to (Schneider et al., 2014), who state that the ITCZ migrates seasonally from 2°N to 10°N. This range is consistent with the 2014 – 2015 TRMM ITCZ position data, which varies from 7°S to 9°N. The TRMM 2014 data show a double maximum feature, which

is also apparent in the Cap San Lorenzo 2015 data, albeit earlier during the year. The Cap San Lorenzo and RHUL 2014 data points are also in agreement with the TRMM and Cap San Lorenzo 2015 data. The RHUL 2013 data point indicates that the ITCZ migrated as far as 14.5°N, which is further north than the ITCZ positions reported by (Lefèvre et al., 2013), who also used the TRMM data to analyse the position of the ITCZ from 1998–2011, as well as NASA Global Precipitation Climatology Project (GPCP) data from 1982–2010. The RHUL 2013 data point could therefore be inaccurate, or it may simply represent shorter than monthly variability, since the RHUL data are discrete measurements, not monthly averages.

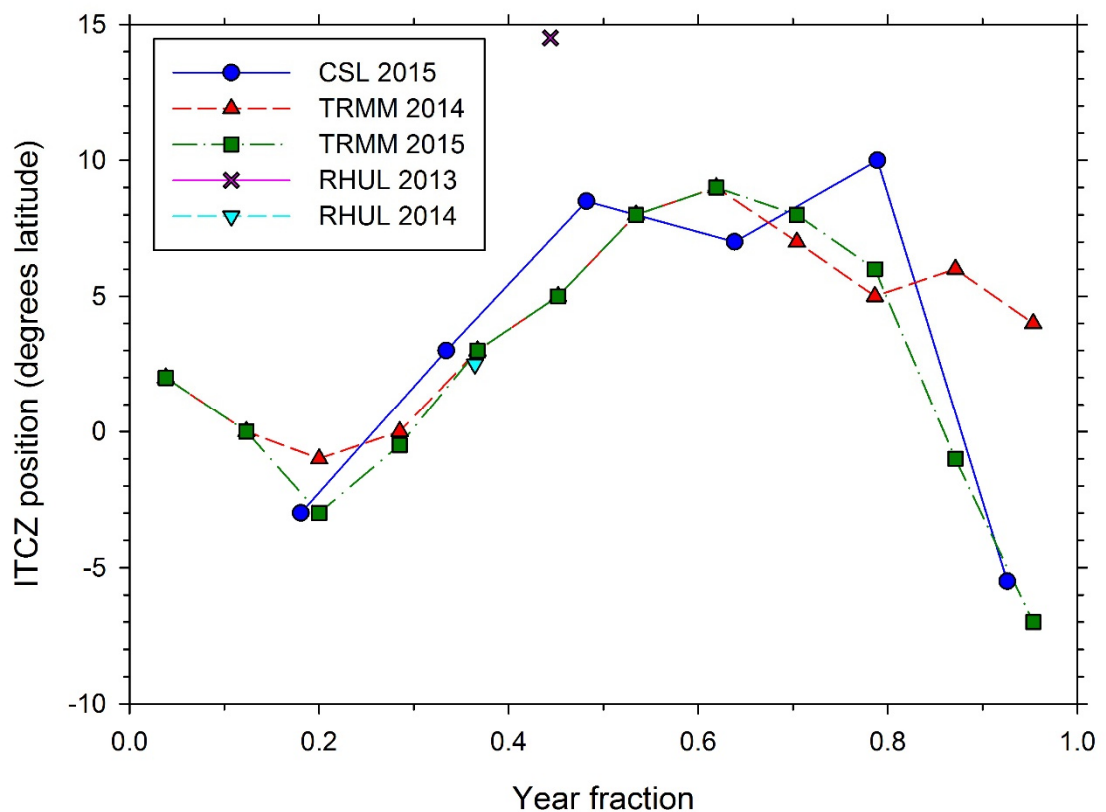


Figure 4.11. Seasonal migration in the position of the ITCZ in the Atlantic Ocean. Positions obtained from the atmospheric CO₂ and O₂ from the Cap San Lorenzo (CSL) are shown in blue, positions obtained from atmospheric CO₂ and CH₄ data by Royal Holloway University of London (RHUL) on board the RRS James Clark Ross are shown in pink and cyan for 2013 and 2014 respectively, and positions obtained from rainfall maxima using NASA's Tropical Rainfall Measuring Mission (TRMM) are shown in red and green for 2014 and 2015 respectively.

In general, using step changes in atmospheric O₂, CO₂ or CH₄ data appears to be an accurate proxy for the position of the ITCZ. The mean position of the ITCZ in the Atlantic is 4.0°N for 2014, using the TRMM rainfall data, and 3.3°N for 2015, using the Cap San Lorenzo atmospheric CO₂ and O₂ data. As mentioned previously, there is a strong connection between the position of the ITCZ, and the cross-equatorial

atmospheric and oceanic energy fluxes (Bischoff and Schneider, 2014). The mean values of the ITCZ position in the North Atlantic are in close agreement with the values presented in (Schneider et al., 2014), in which the authors calculate that the southward cross-equatorial atmospheric energy flux is 0.3 ± 0.2 PW, according to:

$$\delta \approx -\frac{1}{a} \frac{F}{S-L-O} \quad (\text{Eq. 4.1})$$

where δ is the latitude of the ITCZ, a is the Earth's radius, F is the atmospheric energy flux across the equator, S is the net downward shortwave radiation at the equator, L is the outgoing longwave radiation at the equator, and O is the ocean energy uptake at the equator due to storage or transport in the oceans.

The southwards cross-equatorial energy flux in the oceans induced by the energy imbalance between the northern and southern hemispheres is approximately equivalent to that in the atmosphere. The Atlantic Ocean meridional overturning circulation (AMOC), which transports energy northwards (and against the thermal gradient), dominates over the southwards equatorial cross energy flux, meaning that the net flow of energy in the oceans is in fact 0.5 PW northwards.

The position of the ITCZ has been found to change with both short-term climatic variations, such as El Niño/La Niña oscillations, and also long-term climatic changes, such as global warming or cooling (Bischoff and Schneider, 2014). For example, (Lefèvre et al., 2013) found that the ITCZ in the Atlantic shifted poleward during 2010, after the 2009 El Niño event. This shift in the ITCZ occurs because the tropical oceans warm during El Niño conditions; hence, there is a reduction in the uptake of energy by the surface equatorial oceans, causing the ITCZ to migrate towards the equator during El Niño events, and away from the equator during La Niña events (Bischoff and Schneider, 2014; Schneider et al., 2014). Therefore, I expect the position of the ITCZ in the Atlantic to shift equatorward during 2016, owing to the strong El Niño event of 2015/2016. This predicted equatorward shift is supported by the Cap San Lorenzo ITCZ position data from late 2015 and early 2016, which demonstrate that the ITCZ position is located further south than expected. On longer timescales, (Hwang et al., 2013) found that the ITCZ shifted south during the mid and latter half of the 20th century, owing to an increase in the atmospheric concentration of sulphate aerosols in the northern hemisphere (of anthropogenic origins), which

reduced the interhemispheric atmospheric temperature gradient. Thus, since the northern hemisphere is currently warming faster than the southern hemisphere owing to the prevalence of greenhouse gas emissions in the north (Friedman et al., 2013), I expect the ITCZ to gradually shift to a more poleward position, as the interhemispheric temperature gradient increases. Such a feature may become visible in satellite rainfall records, or in atmospheric measurements, should such time series be continued for a sufficient amount of time in order to detect any long-term trend amid seasonal and interannual variability.

4.3. Seasonality in atmospheric O₂, CO₂, and APO across the Atlantic Ocean at different latitudes.

In order to investigate seasonal variability in atmospheric O₂, CO₂ and APO over the Atlantic Ocean, I have binned the meridional data into nineteen 5° latitude bands, from 50°-55°N, to 40°-35°S. Data that are representative of terrestrial influences, such as the data collected when the ship is close to port, and those that have been identified as anomalous, or caused by atmospheric transport processes, have been excluded from the seasonal analysis. I then used a curve fitting program, known as 'HPspline', maintained by Ralph Keeling at Scripps Institution of Oceanography, USA (Scripps), to determine the seasonal variability in O₂, CO₂ and APO for each latitude band (see Figures 4.12, 4.13 and 4.14, respectively). Since the full dataset is only approximately one year in length, I artificially extended the datasets for each latitude band by a year at each end, using fixed long-term trends of -25 per meg yr⁻¹, 2.5 ppm yr⁻¹, and -13 per meg yr⁻¹ for O₂, CO₂ and APO, respectively, prior to curve fitting, so that the HPspline output would not be unduly biased by 'end effects' (i.e. anomalous curve fit results at the ends of the datasets). The long-term trend values used were based on those from (Wilson, 2013), which were calculated using ~3 years (January 2009 – April 2012) of atmospheric O₂, CO₂ and APO data from Weybourne Atmospheric Observatory, UK. Only the curve fit results from the real Cap San Lorenzo data, and not those from the artificially extended data, have been included in the seasonal analysis presented in this section. Since I have prescribed the long-term trend of the atmospheric O₂, CO₂ and APO data, the curve fit results can only be used to quantify the seasonal characteristics at each latitude (from the detrended data), and not the long-term trend, or growth rate of the

long-term trend, as it is not appropriate (or even possible) to accurately determine long-term trend characteristics from a single year of atmospheric measurements.

HPspline is a parametric curve fitting program, comprising of a harmonic function, a polynomial function and a stiff cubic spline (Pickers and Manning, 2015). Usually, 4 harmonics are used when applying HPspline to an atmospheric time series, so that interannual and more complex seasonal features (such as multiple seasonal maxima and minima) can be represented by the curve fits. I decided to use only two harmonics when applying HPspline to the latitudinally-binned Cap San Lorenzo data, in order to avoid HPspline erroneously attributing complex seasonal phenomena to one-time variations in the atmospheric data, since the latitudinally-binned time series are currently short (only ~1 year in duration).

Ideally, it is preferable to use more than one curve fitting program when analysing time series data, to ensure that the analysis results are not biased by the choice of curve fitting program employed (Pickers and Manning, 2015). Unfortunately, it was not possible to employ either of the other two curve fitting programs that I am familiar with, owing to the characteristics of the latitudinally-binned data. The curve fitting program 'CCGCRV' (NOAA's Carbon Cycle Group Curve fitting program; see Thoning et al., 1989) was unable to produce smooth curves, and significantly underestimated the magnitude of the seasonal cycle amplitude, owing to the sparsity of the data. I was also unable to use the curve fitting program 'STL' (Seasonal and Trend decomposition using LOESS; see Cleveland et al., 1990) because the currently available version of the STL is unable to recognise gaps in the data, and requires the data to be evenly spaced (Manning et al., 1990).

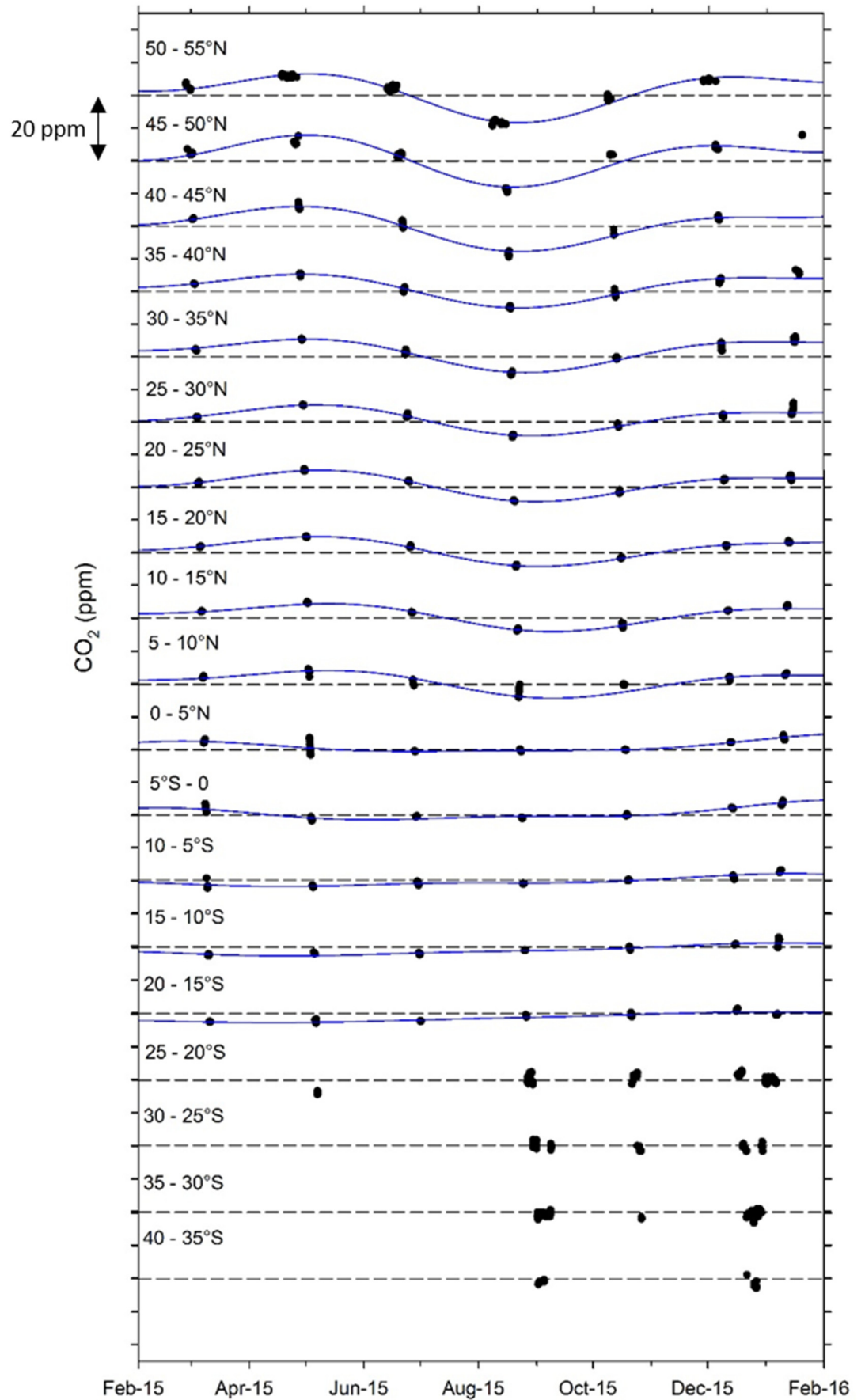


Figure 4.12. Atmospheric CO₂ from the Cap San Lorenzo, binned into 5° latitude bands (black symbols). The curve fits were produced using HPspline (solid blue lines). For each latitude band, 400 ppm is shown by the dashed black horizontal line.

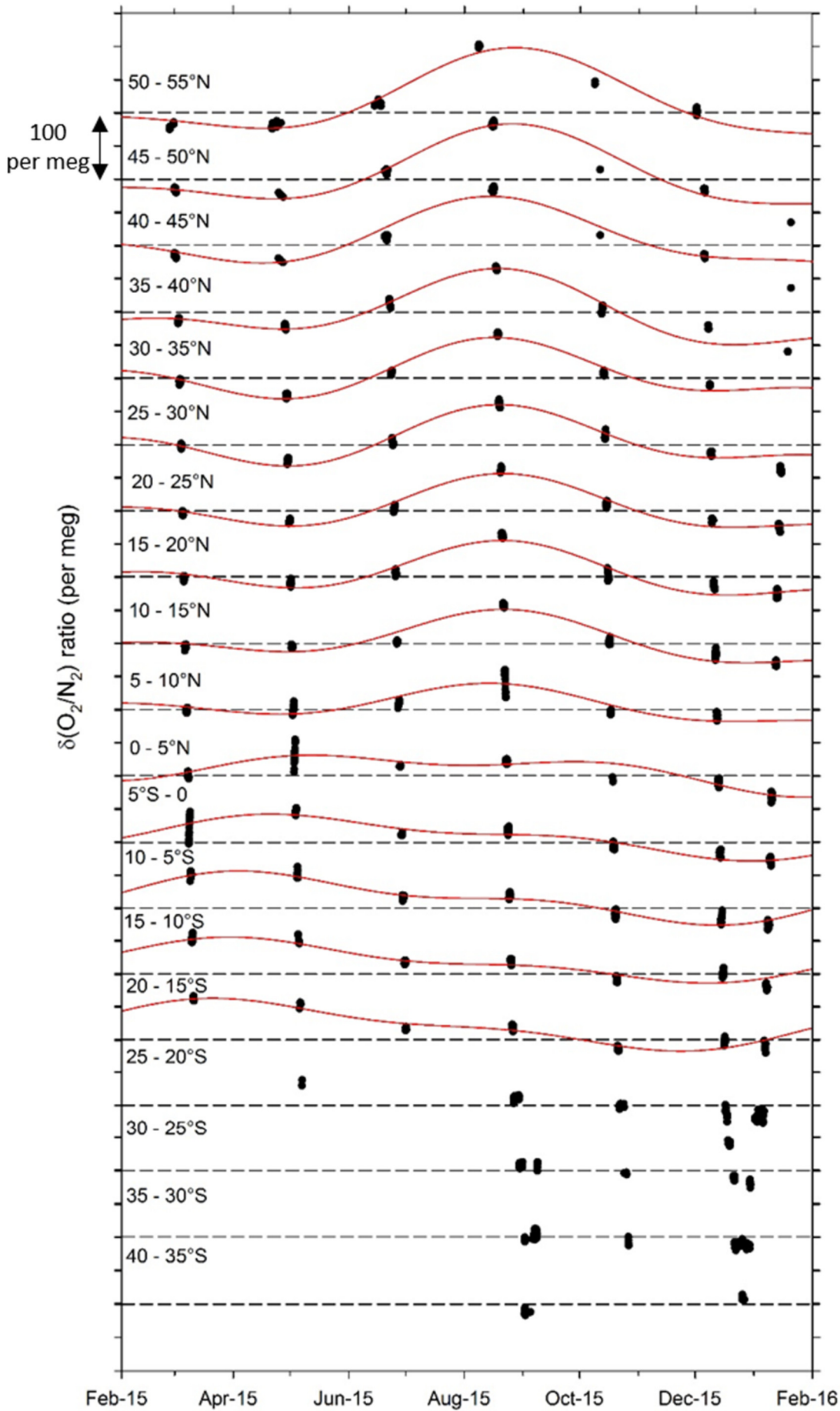


Figure 4.13. Atmospheric $\delta(\text{O}_2/\text{N}_2)$ from the Cap San Lorenzo, binned into 5° latitude bands (black symbols). The curve fits were produced using HPspline (solid red lines). For each latitude band, -600 per meg is shown by the dashed black horizontal line.

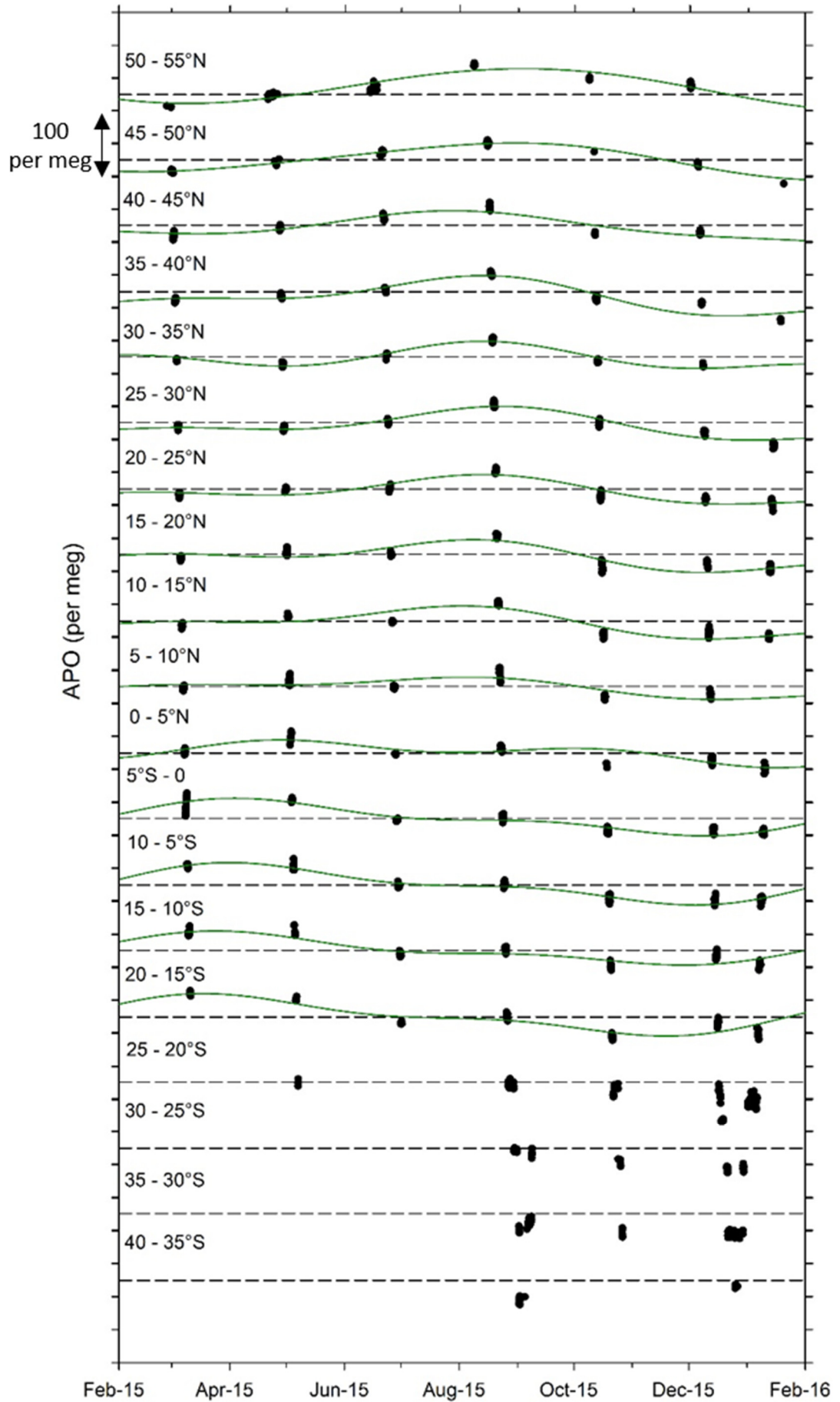


Figure 4.14. APO from the Cap San Lorenzo, binned into 5° latitude bands (black symbols). The curve fits were produced using HPspline (solid green lines). For each latitude band, -325 per meg is shown by the dashed black horizontal line.

The sensitivity of the HPspline curve fit results to the choice of input smoothing parameters was also tested, in order to determine the dependency of the curve fitting outputs on the smoothing algorithms employed in the fitting procedure. Changing the HPspline smoothing parameter setting (the 'stiffness' of the cubic spline) had negligible effects on the curve fit results. This is most likely due to the sparsity of the data once it is latitudinally-binned, relative to the length of the gaps between some of the data points. In order to determine the uncertainty of the seasonal characteristics determined by the HPspline curve fitting, ideally, one would either compare the differences between HPspline curve fits using a range of cubic spline stiffnesses, or one would compare the differences between outputs from several curve fitting programs; however, since neither of these options is currently possible for the latitudinally-binned Cap San Lorenzo data, then the residuals of the HPspline curve fits (i.e. the spread of the data points around the curve fits) can be used instead, to provide a measure of uncertainty of the curve fitting results, particularly at the seasonal inflexion points.

Figs. 4.12, 4.13 and 4.14 clearly show that O_2 , CO_2 and APO seasonality changes with latitude. Note that there is not yet enough data available to produce curve fits for the most southerly latitude bands (owing to technical issues with the measurement system that resulted in large data gaps in the first half of 2015). In the northern hemisphere, the CO_2 seasonal maximum occurs during May and the seasonal minimum occurs during September. This is expected, since the main driver of CO_2 seasonality is the terrestrial biosphere, which is a net source of CO_2 to the atmosphere during winter (because respiration dominates over photosynthesis), and a net sink of CO_2 from the atmosphere during summer (because photosynthesis dominates over respiration). It is also apparent in Fig. 4.12 that the seasonal maximum is much broader than the seasonal minimum, which is comparatively steeper, and shorter in duration. This is also expected, because the biosphere is very active during the spring and summer (both photosynthesis and respiration) due to the warmer temperatures (and increased light availability for photosynthesis), and inactive during the winter, where both photosynthesis and respiration rates are severely reduced due to the low temperatures (and low light availability for photosynthesis). This seasonal difference between summer and winter is more extreme at higher latitudes, and attenuated at lower latitudes; this feature also manifests in the atmospheric CO_2 curve fits in Fig. 4.12, which decrease in amplitude towards the equator.

From 5°N to 20°S, the phasing of the CO₂ seasonal cycle changes, and the maximum occurs during December-January, and the minimum occurs during May. This change in phasing represents the dominance of southern hemisphere air over northern hemisphere air, because the CO₂ seasonality is more in-phase with the terrestrial biosphere of the southern hemisphere, which is exactly 6 months out of phase with the northern hemisphere. While the low latitude southern hemisphere CO₂ minimum now occurs at the same time as the northern hemisphere CO₂ maximum, the low latitude southern hemisphere CO₂ maximum occurs 3-4 months after the northern hemisphere CO₂ minimum. This offset is most likely caused by the mixing of northern hemisphere and southern hemisphere air, so although the overall shape of the CO₂ seasonal cycle in the low latitude southern hemisphere is dominated by the southern hemisphere terrestrial biosphere, there is still a discernible influence from the northern hemisphere. This influence likely manifests so clearly because the terrestrial biosphere in the southern hemisphere is much smaller than that in the northern hemisphere, because there is much less land in the southern hemisphere compared to the northern hemisphere. This also explains why the CO₂ seasonal amplitudes of the southern hemisphere latitude bands are much smaller than those for the corresponding northern hemisphere latitude bands.

Fig. 4.13 shows the atmospheric O₂ seasonal variability and how it changes with latitude. In fact, the O₂ seasonal variability is exactly the opposite to the CO₂ seasonal variability in Fig. 4.12, with the only exception being that in the southern hemisphere, the O₂ seasonal maximum occurs from March – May, whereas the CO₂ seasonal minimum at the same latitudes always occurs in May. This anti-correlation between the seasonal variability of CO₂ and O₂ is expected, because the terrestrial processes of photosynthesis and respiration, which dominate the atmospheric CO₂ seasonal cycle, produce almost equal but opposite fluxes of O₂ between the terrestrial biosphere and the atmosphere (the global molar O₂:CO₂ exchange ratio for terrestrial photosynthesis and respiration is about -1.1, where the negative sign denotes that the O₂ and CO₂ fluxes are anti-correlated).

Unlike the seasonal cycle of atmospheric CO₂, which largely represents terrestrial biospheric processes, the seasonal cycle of atmospheric O₂ represents both terrestrial biospheric and oceanic processes, owing to the fact that the air-sea equilibration time for O₂ is much faster than for CO₂. This is demonstrated in Fig. 4.13 by the O₂ seasonal amplitudes, which are larger on a mole per mole basis than the corresponding CO₂ seasonal amplitudes at the same latitudes. This is because oceanic

O₂ seasonal processes operate with a similar phasing to terrestrial O₂ seasonal processes, and therefore amplify the magnitude of the seasonal variability. In summer, when the terrestrial biosphere is a net source of O₂ to the atmosphere, the ocean is also a net source of O₂ to the atmosphere, due to three reinforcing oceanic processes. Firstly, there is production of O₂ in the surface waters due to the proliferation of phytoplankton blooms, which induces a flux of O₂ from the ocean to the atmosphere. Secondly, the surface ocean waters are warmed by the sun, which causes out-gassing of O₂ to the atmosphere, because the solubility of gases in seawater decreases as the temperature of the seawater increases. Thirdly, ocean waters are more stratified during the summer, due to increased solar input that warms the surface waters, and a decrease in storm frequency and severity, resulting in a decrease in wind-induced mixing. This increased stratification inhibits the upwelling of O₂-depleted deep waters, which cause a flux of O₂ into the ocean according to Henry's Law when they come into contact with the atmosphere. Conversely, these three oceanic processes also operate to reinforce the O₂ seasonality of the terrestrial biosphere in winter, when both the land and the ocean are a net sink of O₂ from the atmosphere.

The relative contribution of these three oceanic processes to the net global average oceanic O₂ seasonal flux is as follows: about 85% of the total oceanic flux is attributed to marine biological processes, and the remaining 15% is due to a combination of thermally-driven solubility changes and upwelling (Keeling et al., 1993; Keeling and Shertz, 1992). In reality, the thermally-driven O₂ flux is in fact 44% greater in magnitude (Keeling and Shertz, 1992), but since it is the $\delta(\text{O}_2/\text{N}_2)$ ratio that is reported, and all thermally-driven O₂ fluxes have corresponding thermally-driven N₂ fluxes, the thermal contribution to the seasonal cycle in reported atmospheric $\delta(\text{O}_2/\text{N}_2)$ ratios is significantly reduced. Ventilation O₂ fluxes do not have associated N₂ fluxes, because the O₂ deficit in the water is caused by microbial respiration and decomposition of organic matter as it sinks to the ocean floor; however, the ventilation contribution is relatively small compared to the thermal contribution, because it is less ubiquitous and occurs more regionally.

There are also three more subtle manifestations of the oceanic influence on O₂ seasonality apparent in Fig. 4.13, in addition to the greater seasonal amplitude mentioned above. Firstly, the slightly earlier timing of the O₂ seasonal maximum in the southern hemisphere compared to the CO₂ seasonal minimum in the northern hemisphere might be explained by a slightly faster response of atmospheric O₂ to

oceanic processes compared to terrestrial biospheric processes. Secondly, the shape of the O_2 seasonal cycle is more uniform between summer and winter compared to the CO_2 seasonal cycle, which is characterised by a broad maximum and short, steep minimum. This is most likely due to the influences of physical oceanic processes on atmospheric O_2 , which correlate strongly with seasonal changes in solar radiation and temperature, and/or differences in the timing of biological processes on land and in the ocean, which largely mitigate the asymmetry associated with the terrestrial influence on the atmospheric O_2 seasonal cycle. Thirdly, unlike CO_2 , the O_2 seasonal amplitudes in the low latitude southern hemisphere are of similar magnitudes to the O_2 seasonal amplitudes at the corresponding low latitudes in the northern hemisphere. This is also due to the influences of both terrestrial and oceanic processes on atmospheric O_2 seasonality. While there is more land in the northern hemisphere than the southern hemisphere, it follows that there is more ocean in the southern hemisphere than the northern hemisphere, and therefore the differences in O_2 seasonal amplitudes between low latitudes in the northern and southern hemispheres are much smaller than those for CO_2 .

The APO seasonality shown in Fig. 4.14 is quite similar to the atmospheric O_2 seasonality in Fig. 4.13, only with smaller amplitudes in the northern hemisphere. This is because APO is invariant with respect to terrestrial biospheric processes, therefore in the northern hemisphere, where land masses are more abundant, there is a large influence from the land on the O_2 seasonal cycle (contributing about 50% of the total seasonal amplitude), whereas the APO seasonal cycle reflects northern hemisphere oceanic processes only. In the southern hemisphere, where there is significantly less land, the APO and O_2 seasonal amplitudes are relatively similar in magnitude, because both are dominated by oceanic processes, and because the land influence on the O_2 seasonality in the southern hemisphere is relatively small. In terms of phasing, in both hemispheres, the timing of the APO seasonal maxima and minima are roughly the same as the O_2 seasonal maxima and minima, although there is more variability in the timing of the APO curve fit inflexion points compared to those for O_2 . This is most likely a function of the curve fitting programs, which sometimes struggle to accurately fit the APO seasonal cycle, owing to a combination of the sparsity of data points and the relatively small seasonal cycle amplitude.

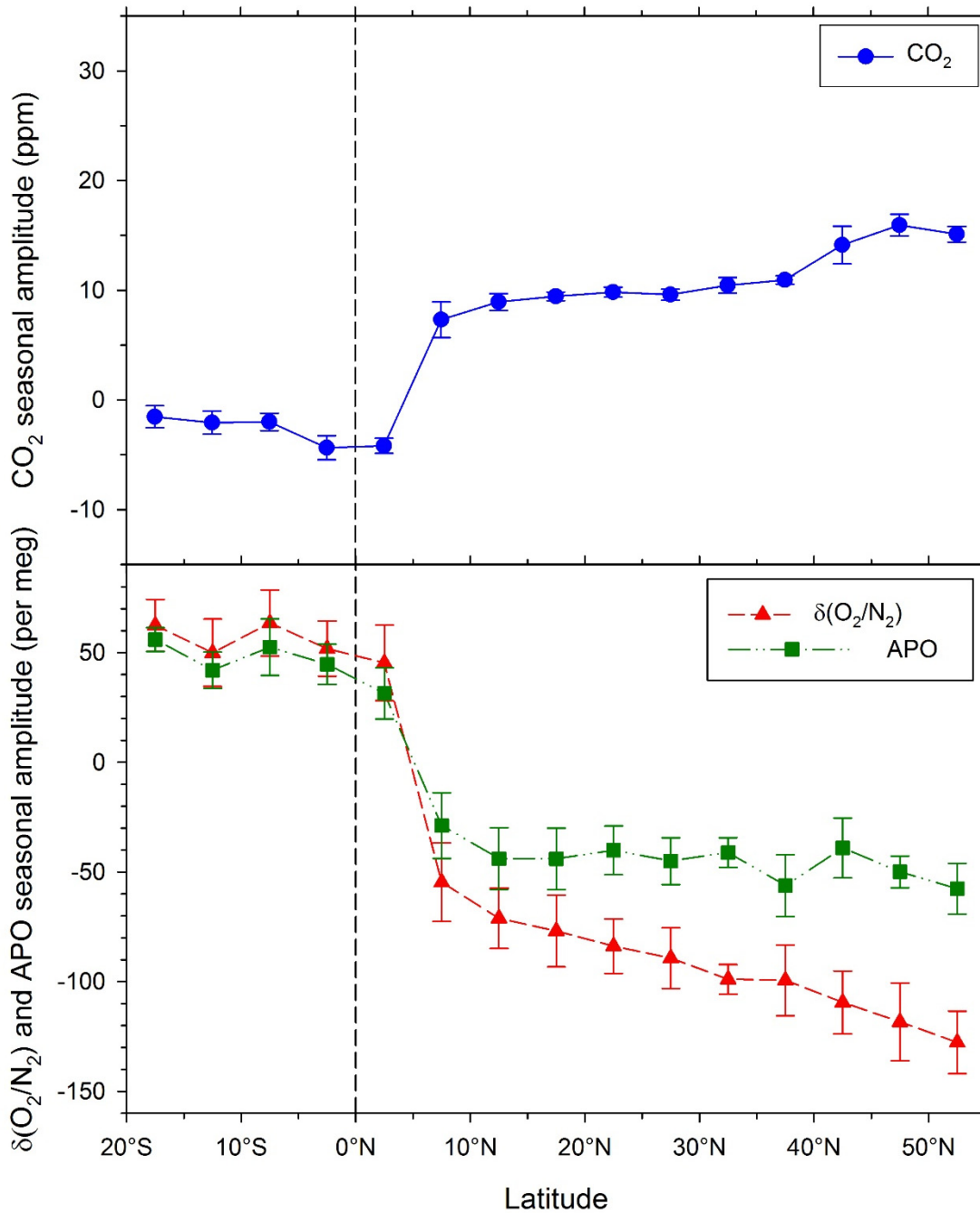


Figure 4.15. CO₂ (top panel; blue circles and solid lines), $\delta(\text{O}_2/\text{N}_2)$ (bottom panel; red triangles and dashed lines) and APO (bottom panel; green squares and dash-dotted lines) seasonal amplitude as a function of latitude. Error bars show the uncertainty in the seasonal amplitude for each species, which was determined from the mean magnitude of the HPspline curve fit residuals at the seasonal inflexion points. Y-axes have been scaled to be visually comparable on a mole per mole basis. The equator is indicated by the vertical black dashed line.

Figure 4.15 shows the changes in seasonal cycle amplitude as a function of latitude for O₂, CO₂ and APO. Seasonal cycle amplitudes were determined from the detrended HPspline curve fit data (i.e. with the long-term trend removed). Fig. 4.15 demonstrates that there is a distinct change in the sign of the seasonal cycle amplitude at about 5°N for all three species, which happens to coincide with the mean

position of the ITCZ in the Atlantic Ocean, and therefore the mean interface between northern hemisphere and southern hemisphere air. In all three species, this change in sign at the ITCZ is significantly larger than the seasonal amplitude uncertainty (indicated by the error bars in Fig. 4.15), and is therefore very unlikely to be caused by an artefact or bias in either the atmospheric data, latitudinal binning process, or HPspline curve fitting. As shown in Figs. 4.12 and 4.13, the atmospheric CO₂ and O₂ seasonal amplitude decreases with decreasing latitude in the northern hemisphere. For CO₂, the seasonal cycle amplitude in the southern hemisphere is significantly less than at corresponding latitudes in the northern hemisphere, while for O₂, the seasonal cycle amplitudes are similar in magnitude in both the northern and southern hemisphere low latitudes, but by 20°N and 20°S, the magnitude of the O₂ seasonal cycle in the northern hemisphere is significantly larger than that in the southern hemisphere. Conversely, for APO, there is no increase in seasonal cycle amplitude with increasing latitude, and northern and southern hemisphere seasonal cycle amplitudes are of similar magnitudes.

It is also possible to determine the relative contributions of the land and ocean to the seasonal cycle of O₂ in each hemisphere, by comparing the O₂ seasonal magnitude to the APO and CO₂ seasonal magnitudes. At ~50°N, the APO seasonal cycle magnitude is approximately 46% of the O₂ seasonal cycle amplitude, which indicates that about half of the O₂ seasonal cycle can be attributed to ocean processes, and half to land processes. The difference in magnitude between the APO and O₂ seasonal cycle amplitudes is about 70 per meg; this is equivalent to 14.6 ppm, and is very similar to the observed CO₂ seasonal cycle amplitude at ~50°N, which is caused by land processes only. At ~15°S. The APO seasonal cycle magnitude is approximately 82% of the O₂ seasonal cycle amplitude, suggesting that the majority of the O₂ seasonal cycle can be attributed to ocean processes, with only about 20% attributed to land processes. The difference in magnitude between the APO and O₂ seasonal cycle amplitudes at ~15°S is about 10 per meg, which is equivalent to 2.1 ppm. This value is very similar to the observed CO₂ seasonal cycle amplitude at this latitude, which reflects land processes only.

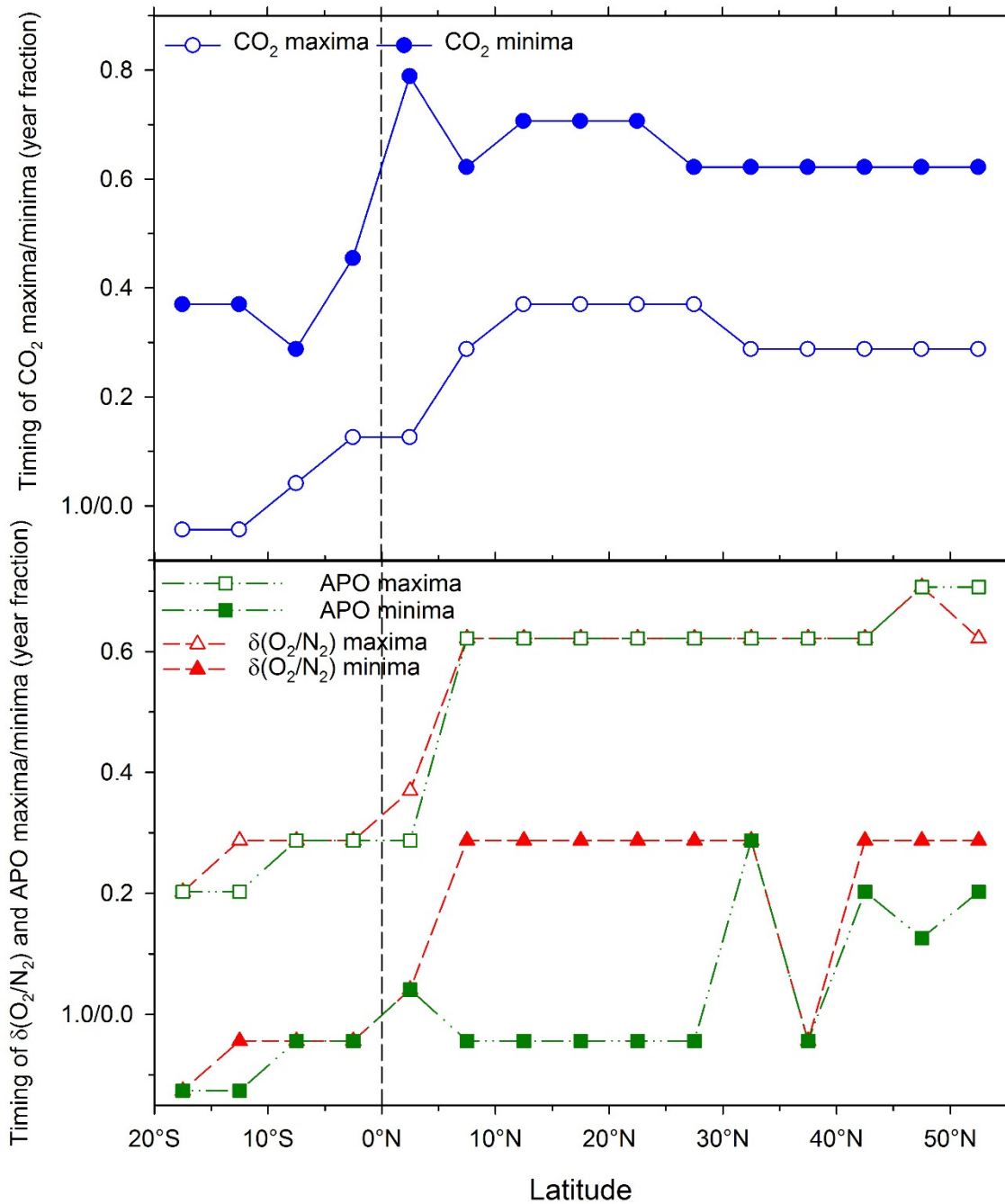


Figure 4.16. Timing of the seasonal maxima (open symbols) and minima (filled symbols) in atmospheric CO₂ (top panel; blue circles and solid lines), $\delta(\text{O}_2/\text{N}_2)$ (bottom panel; red triangles and dashed lines) and APO (bottom panel; green squares and dash-dotted lines) as a function of latitude, determined from the detrended HPspline curve fits. The equator is indicated by the vertical black dashed line.

The timing of the seasonal maxima and minima for O₂, CO₂ and APO at different latitudes is shown in Figure 4.16. There is a migration in the timing of the seasonal maxima and minima for each species at the transition between northern and southern hemisphere air, although this migration is not always as clear as the amplitude sign changes in Fig. 4.15. This is particularly true for the APO seasonal minima, for which the main shift in timing does not occur close to the equator or the

ITCZ. The timing of the seasonal cycle maxima and minima are also not always six months different from each other between the northern hemisphere and southern hemisphere. For example, for CO₂, the timing of the seasonal minima in the southern hemisphere coincides with the timing of the seasonal maxima in the northern hemisphere, but the timing of the seasonal maxima in the southern hemisphere does not shift to be as early in the year as the timing of the seasonal minima in the northern hemisphere. This same pattern is also observed in the timing changes of the O₂ seasonal maxima and minima between the northern and the southern hemisphere. The large variations in the timing of the O₂ and APO seasonal minima between 25-45°N could be caused by either real variability, or by an artefact of the data analysis and curve fitting procedures, and until more data become available, it is probably not possible to discern which is more likely.

Table 4.2 shows the O₂, CO₂ and APO seasonal cycle amplitudes from other high-precision CO₂ and O₂ measurement stations, and compares them to the Cap San Lorenzo O₂, CO₂ and APO seasonal cycle amplitudes from similar latitudes. Overall, the Cap San Lorenzo seasonal amplitude data compare well to the seasonal amplitude data from other measurement stations around the world. Where differences do occur, many of these can be explained by differences in the locations of the measurement sites. For example, the Cap San Lorenzo CO₂ and O₂ amplitudes are smaller than those from Sendai, Japan, and the Gobabeb, Namibia, whilst the Cap San Lorenzo APO amplitudes are larger. These differences are most likely attributable to the fact that the Sendai and Gobabeb data will be more strongly influenced by land processes compared to the Cap San Lorenzo data, which are collected from the open ocean at both latitudes. Other differences are likely to be caused by a combination of differences in the time period the seasonal amplitudes were calculated for, the method used to determine the 'baseline' or 'background' air (Fang et al., 2015), the curve fitting program or procedure used to detrend the time series data (Pickers and Manning, 2015), the atmospheric footprints of the individual measurement stations, and small offsets or biases owing to undetected or uncorrected technical problems.

Table 4.2. Comparison of Cap San Lorenzo O₂, CO₂ and APO seasonal cycle amplitudes with those from other O₂ and CO₂ measurement stations at similar latitudes. Data are either from the literature (please refer to the citations in Table 1.1) or are from personal communication with the measurement station personnel.

Station Name	Location	Time Period	CO₂ (ppm)	O₂ (per meg)	APO (per meg)
Weybourne, UK	52.95°N, 1.12°E	2009-2012	14.9±0.8	134.2±7.8	59.0±5.6
Mace Head, Ireland	53.33°N, 9.9°W	2014-2015	17.8±2.3	149.0±10.1	76.6±7.0
Lutjewad, The Netherlands	53.39°N, 6.35°E	2000-2009	12.0±0.6	114.0±8.0	64.0±6.0
Cap San Lorenzo	50°N to 55°N	2015-2016	15.1±0.7	127.8±14.3	57.7±11.6
Sendai, Japan	38°N, 140°E	1999-2012	13.9±2.5	128±22	52±10
Cap San Lorenzo	35°N to 40°N	2015-2016	10.9±0.4	99.4±16.2	56.2±14.0
Pacific Ocean ship	~15°N	2001-2004	~5	~50	~25
Cap San Lorenzo	10°N to 15°N	2015-2016	8.9±0.8	71.1±13.8	43.9±14.0
Gobabeb, Namibia	23.56°S, 15.05°E	2012-2014	2.4	61.0	49.7
Cap San Lorenzo	15°S to 20°S	2015-2016	1.5±1.0	62.4±11.8	55.9±5.4

4.4. Annual mean latitudinal distribution of atmospheric O₂, CO₂ and APO across the Atlantic Ocean: the missing equatorial APO bulge

Large scale features in APO data, such as the APO latitudinal gradient, can be used to examine ocean circulation and air-sea interactions in climate models. For example, Stephens et al. (1998) found that model-generated latitudinal gradients in annual mean APO over the Pacific Ocean significantly underestimated the observed

interhemispheric difference in APO from the Scripps Institution of Oceanography (SIO) flask sampling network, and suggested that the ocean models were underestimating the net southwards transport of the sum of O_2 and CO_2 in the oceans. A later study by Gruber et al. (2001) also found that modelled APO underestimated the observed APO interhemispheric gradient, particularly at southern hemisphere high latitude stations; however, these authors found that robustly constraining oceanic transport of O_2 and CO_2 was not possible, owing to large uncertainties in the modelled APO, stemming from a combination of the seasonal O_2 rectifier effect and a lack of APO observations. Both studies found a large equatorial APO ‘bulge’ (between 5-15 per meg in magnitude) in modelled APO over the Pacific Ocean, caused by O_2 and CO_2 solubility-driven outgassing from the equatorial Pacific Ocean. At the time, the existence of this equatorial APO bulge could not be confirmed, however, subsequent shipboard measurements presented in Battle et al. (2006), were used to verify the existence of the bulge, which was found to peak just south of the equator. More recently, the long O_2 and CO_2 dataset of Tohjima et al. (2015) over the western Pacific Ocean (see Figure 4.17) has been used to examine interannual variability in the magnitude of the Pacific equatorial APO bulge, which was found to be anti-correlated to the El Niño – Southern Oscillation (ENSO; the APO bulge is suppressed during El Niño conditions), and appears to be mostly caused by changes in atmospheric circulation associated with meridional shifts in the ITCZ (Intertropical Convergence Zone).

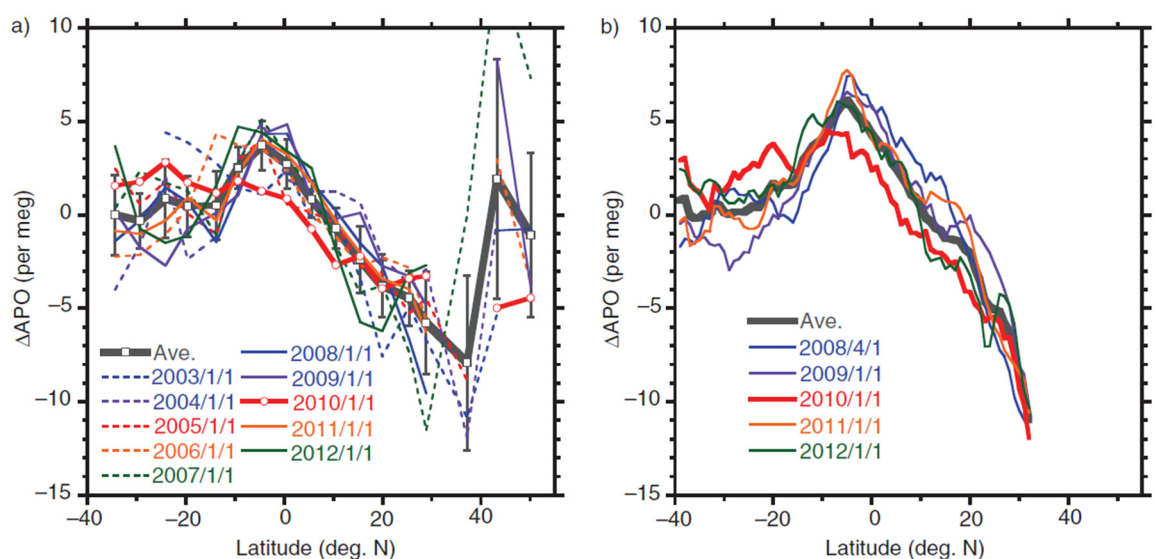


Figure 4.17. Annual mean latitudinal distribution in detrended APO flask (left panel) and continuous (right panel) data from cargo ships crossing the Pacific Ocean, from Tohjima et al. (2015). Different colours correspond to data from different years, as shown in the legend, and the thick dark grey lines indicate the mean from all the years.

It is now possible to test ocean models for latitudinal gradients in annual mean APO in the Atlantic Ocean sector, using the shipboard data from the Cap San Lorenzo presented in the previous section of this chapter. The latitudinal variability in annual mean O₂, CO₂ and APO is presented in Figure 4.18. The annual means were calculated using the detrended monthly mean HPspline curve fit output for each latitudinal bin. In order to determine whether the latitudinal variability, particularly around the equator, was statistically significant, the uncertainties of the annual means were calculated from the mean standard error of the data at each latitude, and are denoted in Fig. 4.18 by the error bars. The standard error was chosen as the metric of uncertainty instead of the standard deviation for several reasons. Firstly, the standard deviation represents the degree to which individual measurements within a sample differ from the sample mean, whereas the standard error represents the degree to which the sample mean is likely to be from the population mean. It is therefore more appropriate in this case to use the standard error, instead of the standard deviation, since I am trying to determine whether the difference between one mean and another might be significant within the context of the uncertainty of the data. Secondly, the annual means are calculated from the HPspline monthly output, and the uncertainty is determined from the clusters of residuals of the data to the curve fits. Since the number of residuals in each cluster differs throughout the year, it is more appropriate to use the annual mean standard error, which is comparable between different numbers of data points, rather than the annual mean standard deviation, which would require using the same number of data points in order to compare the clusters.

It should be noted that using the standard error of the data to calculate the uncertainty of the annual means produces smaller error bars in Fig. 4.18 than if the standard deviation is used (about 2.5-3 times smaller when using the standard error). In addition, there are several sources of uncertainty that are not included in the error bars of Fig. 4.18 because they cannot be quantified. For example, the uncertainty caused by large gaps in the dataset, the uncertainty associated with relying on a single year of measurements to calculate latitudinal variability in the annual mean, and the uncertainty associated with the latitudinal binning and curve fitting procedures are not included in the estimates denoted by the error bars of Fig. 4.18. Therefore, although some differences may appear to be statistically significant, it is important to remember these additional sources of uncertainty when interpreting the data.

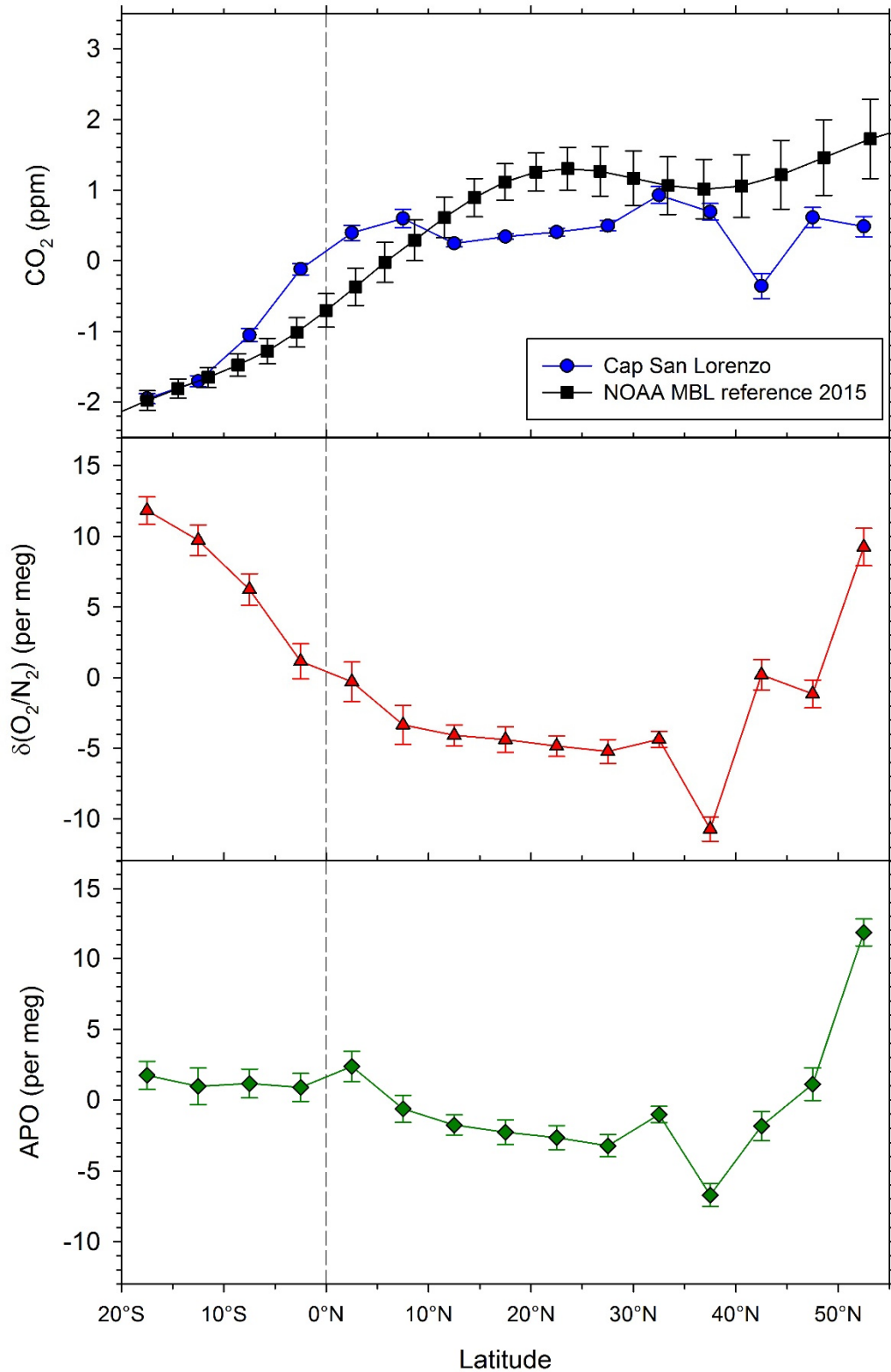


Figure 4.18. Latitudinally varying annual mean CO_2 (top panel; blue circles), $\delta(\text{O}_2/\text{N}_2)$ (middle panel; red triangles) and APO (bottom panel; green diamonds) from the Cap San Lorenzo. Also shown in the top panel is the meridional variation in global annual mean CO_2 from the NOAA Marine Boundary Layer (MBL) reference product for 2015 (black squares), which was estimated by adding 2 ppm yr^{-1} to the 2014 values, because the 2015 data are not currently available. Error bars represent the mean standard error of the measurements at each latitude (see main text for justification). The vertical dashed line in each panel represents the equator. Note that y-axes for each panel have been scaled to be visually comparable on a mole per mole basis.

Fig. 4.18 shows that annual mean CO₂ in the southern hemisphere is approximately 2 ppm lower than in the northern hemisphere, when comparing 20°S with 55°N. This is expected, owing to greater fossil fuel emissions in the northern hemisphere than the southern hemisphere. The NOAA Marine Boundary Layer (MBL) reference CO₂ data product in general agrees with the Cap San Lorenzo CO₂ data, although the NOAA data are much less variable, slightly higher in the northern hemisphere (by up to ~1 ppm), and display a more gradual cross-equatorial change in CO₂. Most of these differences likely arise because the NOAA MBL CO₂ data are a meridional global average that have been smoothed and interpolated from measurements in the NOAA global network, whereas the Cap San Lorenzo data represent the Atlantic Ocean sector only.

The latitudinal variability in annual mean O₂ from the Cap San Lorenzo is approximately the inverse of the CO₂ latitudinal annual mean variability, which is also largely caused by greater atmospheric O₂ uptake in the northern hemisphere from fossil fuel burning compared to the southern hemisphere. There is a significant negative excursion in annual mean O₂ between 35-40°N, with little corresponding change in the CO₂ annual mean, while the CO₂ annual mean experiences a slight negative excursion between 40-45°N. The annual mean O₂ also significantly increases between 50-55°N, to similar values as those at 15-20°S. It is difficult to determine whether these variations in the northern hemisphere are indeed real, or whether they are caused by curve fitting anomalies and data gaps, because I currently only have a single year of data from the Cap San Lorenzo. The real world processes that might be responsible for such variations in O₂ include a latitudinal minimum in fossil fuel emissions (negative excursion) and the seasonal O₂ rectifier effect (positive excursion and subsequent increase).

The bottom panel of Fig. 4.18 shows the latitudinal variability in annual mean APO. It is clear to see that between 30-55°N, the latitudinal variability in annual mean APO follows a similar pattern to that seen in annual mean O₂, and also that the annual mean APO in the southern hemisphere is slightly higher (2-3 per meg) than annual mean APO in the northern hemisphere, which is also most likely due to fossil fuel burning. It is also clear that there is hardly any bulge in APO at the equator compared to the Pacific shipboard data of (Tohjima et al., 2015) in Fig. 4.17. Although there is significant interannual variability in the Pacific shipboard data in Fig. 4.17, the 2003-2012 mean (thick grey lines in Fig. 4.17) shows an equatorial APO bulge of between 4-6 per meg in magnitude, which spans 20° of latitude, whereas the equatorial bulge

in the Cap San Lorenzo APO data is only about 1.5 per meg in magnitude, at most spans 10° of latitude, and is only apparent in a single data point in Fig. 4.18, occurring between 0° - 5° N. In addition, the magnitude of this small equatorial APO bulge in the Cap San Lorenzo data is not statistically significant when compared to the annual mean APO data between the equator and 20° S, based on the size of the error bars.

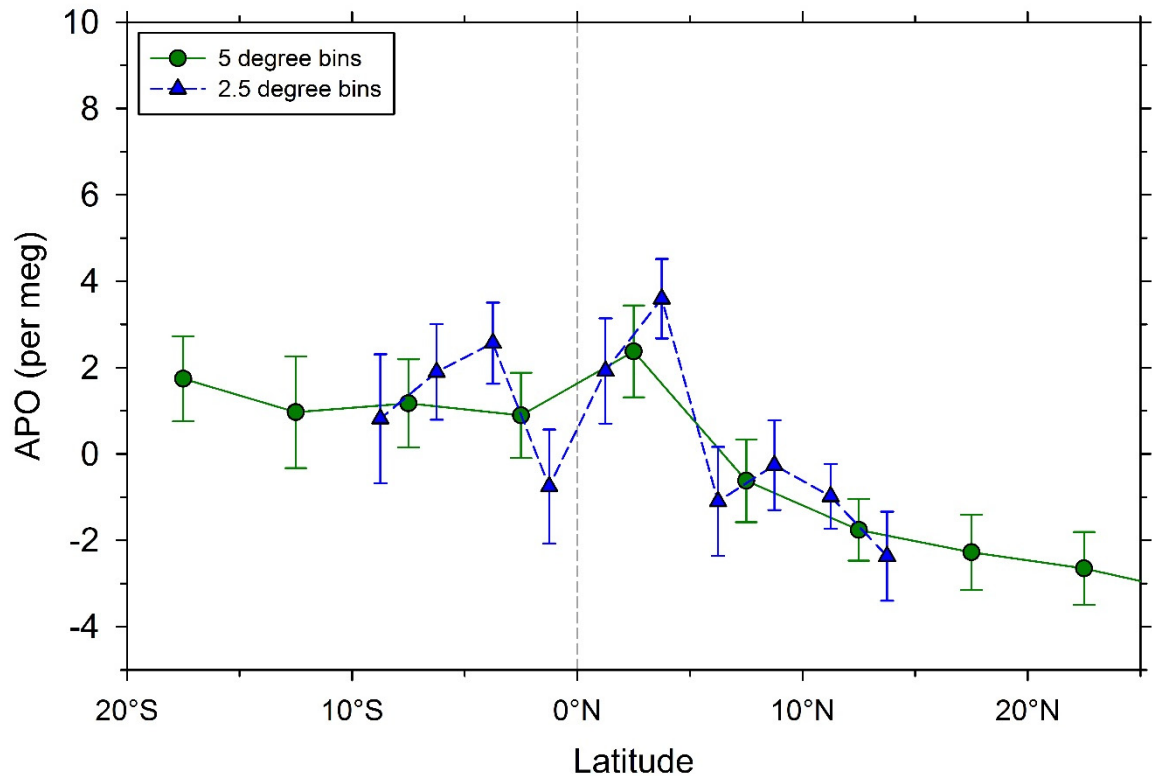


Figure 4.19. Latitudinal variability in annual mean APO calculated using 5° binned APO (green circles; same as in Fig. 4.17), and 2.5° binned APO (blue triangles). Error bars represent the mean standard error of the measurements at each latitude. The vertical dashed line represents the equator.

In order to investigate the significance of the Cap San Lorenzo equatorial APO bulge, I have re-calculated the annual mean APO across the equatorial region using 2.5° latitude bins, instead of 5° latitude bins, so that I can determine whether the bulge is indeed representative of the annual mean APO between 0° - 5° N. Figure 4.19 shows that when the 2.5° binning is used, there is a lot more variability in annual mean APO across the equator. With the exception of the 2.5° - 5° N data point, none of the 2.5° binned annual means are significantly different from the 5° binned annual means between the equator and 20° S, based on the size of the error bars. The 2.5° - 5° N data point is significantly different from the southern hemisphere 5° binned annual means; however, as before, the presence of an equatorial APO bulge during 2015 in the Atlantic is contingent upon a single data point. In addition, it is very unlikely that the double peak feature that becomes apparent in the 2.5° binned data

in Fig. 4.19 is caused by variability in equatorial O_2 out-gassing; therefore, this variability represents either variability in atmospheric transport (which might be causing bias in the annual means, owing to the large gaps in the dataset), or more likely, biases associated with the curve fitting or binning process (which are caused by the gaps in the dataset). Thus, the Cap San Lorenzo 2015 annual mean APO data indicate that there is no significant equatorial APO bulge in the Atlantic Ocean.

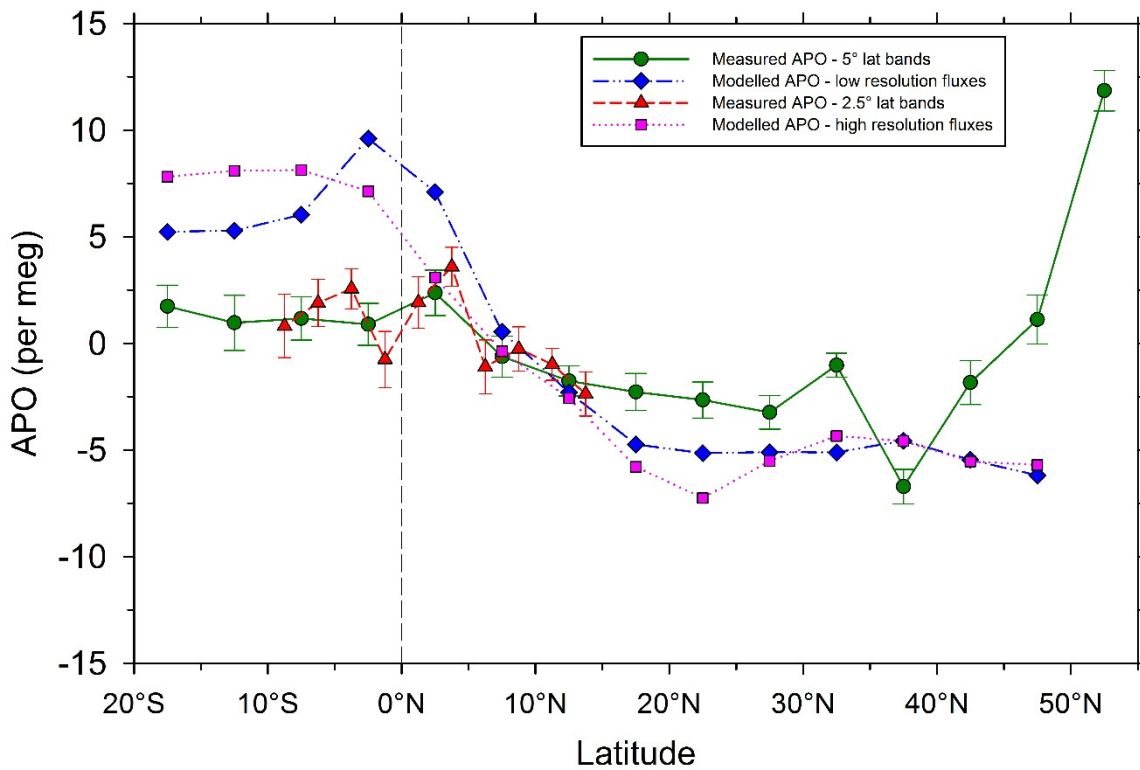


Figure 4.20. Annual mean latitudinal variability in APO from the Cap San Lorenzo measurements, binned into 5° latitude bands (green circles, solid lines) and 2.5° latitude bands (red triangles, dashed lines), as well as the annual mean variability in modelled APO using TM3 and low spatial resolution fluxes (blue diamonds, dotted and dashed lines) and high spatial resolution fluxes (pink squares, dotted lines). The vertical dashed line represents the equator.

Although the measured APO across the Atlantic Ocean reveals that there is no significant equatorial APO bulge present, this is not replicated in the modelled APO, as shown in Figure 4.20. The modelled APO, provided by Sara Mikaloff-Fletcher, is produced using the TM3 atmospheric tracer transport model (Heimann and Körner, 2003), which is driven offline using the National Centers for Environmental Prediction (NCEP) reanalysis wind fields (Kalnay et al., 1996). The input flux fields used are as follows: fossil fuel emissions are from the Carbon Dioxide Information Analysis Center (CDIAC), annual ocean O_2 and N_2 fluxes are from (Gruber et al., 2001) and (Gloor et al., 2001), respectively, ocean seasonal O_2 and N_2 variability is from the climatologies of (Garcia and Keeling, 2001), and ocean seasonal CO_2 variability is

from the climatology of (Takahashi et al., 2009). Two versions of the modelled APO were produced: one version using the inputs mentioned previously (referred to in Fig. 4.20 as 'low resolution', blue diamonds), and a new version, using an updated ocean model inversion method to estimate higher spatial resolution air-sea fluxes from a suite of ten ocean general circulation models (referred to in Fig. 4.20 as 'high resolution', pink squares).

Fig. 4.20 shows that both versions of the modelled APO exhibit a larger interhemispheric gradient in APO, caused by an over-estimation of the southern hemisphere APO compared to the observed annual means from the Cap San Lorenzo data. There is also a clear mismatch between the northern hemisphere modelled and measured APO annual means between 45° – 50° N, and neither versions of the modelled APO reproduce the observed APO variability between 25° - 45° N. The low resolution version of the modelled APO shows a distinct APO bulge close to the equator, whereas the high-resolution version does not produce any detectable bulge. The annual mean latitudinal APO variability of the high-resolution model run therefore matches the measured annual mean latitudinal variability in APO more closely than that from the low-resolution model run, suggesting that using the higher resolution air-sea fluxes yields improved model APO results at the equator, although there is still a significant mismatch between both versions of the modelled APO and the measured APO in terms of the inter-hemispheric APO gradient.

It is hard to properly diagnose the reason for the mismatch between the modelled APO and measured APO in Fig. 4.20 without further modelling analysis, since there are several possible options. For example, it may be that the over-estimated interhemispheric gradient in the modelled APO is caused by inaccuracies in the flux data products, and/or an over-estimation of the southward sum of CO_2 and O_2 transport in the Atlantic Ocean from the ocean models. The equatorial disparity between the modelled and measured APO could also be caused by over-estimated equatorial air-sea fluxes in the Atlantic Ocean sector, or by atmospheric transport errors, or both. It is also possible that the measured annual mean APO latitudinal distribution is very unusual in 2015 compared to previous years, perhaps owing to the strong development of El Niño conditions, which have been shown to suppress equatorial O_2 out-gassing in the western Pacific (Tohjima et al., 2015), and that this interannual variability is not represented in the air-sea fluxes used to produce the modelled APO.

In order to assess this question of interannual variability in the measured APO equatorial bulge in the Atlantic Ocean sector, I have looked at the interannual variability in air-sea O₂ fluxes from the NEMO-PlankTOM model (see Chapter 3, Section 3.4.9 for details) to try and assess whether the fluxes in 2015 were suppressed compared to those from previous years, because I only currently have a single year of measurements from the Cap San Lorenzo. Figure 4.21 shows the NEMO-PlankTOM monthly air-sea O₂ fluxes for 10° latitude bands through the Atlantic Ocean (longitudinal bounds are 61°W to 20°E), from 2012 to 2015. Note that positive values denote fluxes into the ocean, while negative values denote fluxes out of the ocean. While there is some interannual variability apparent in Fig. 4.21, this is mostly in the mid-latitude Atlantic, with less interannual variability apparent in the equatorial latitude bands (10°S to 10°N). This difference likely corresponds to the difference in the air-sea O₂ flux driving processes: (Friedrich et al., 2006) found that extratropical air-sea O₂ fluxes are mostly driven by surface heat fluxes, whereas tropical air-sea O₂ fluxes are driven by wind speed. It therefore seems unlikely that the equatorial out-gassing in 2015 was suppressed, based on the NEMO-PlankTOM fluxes.

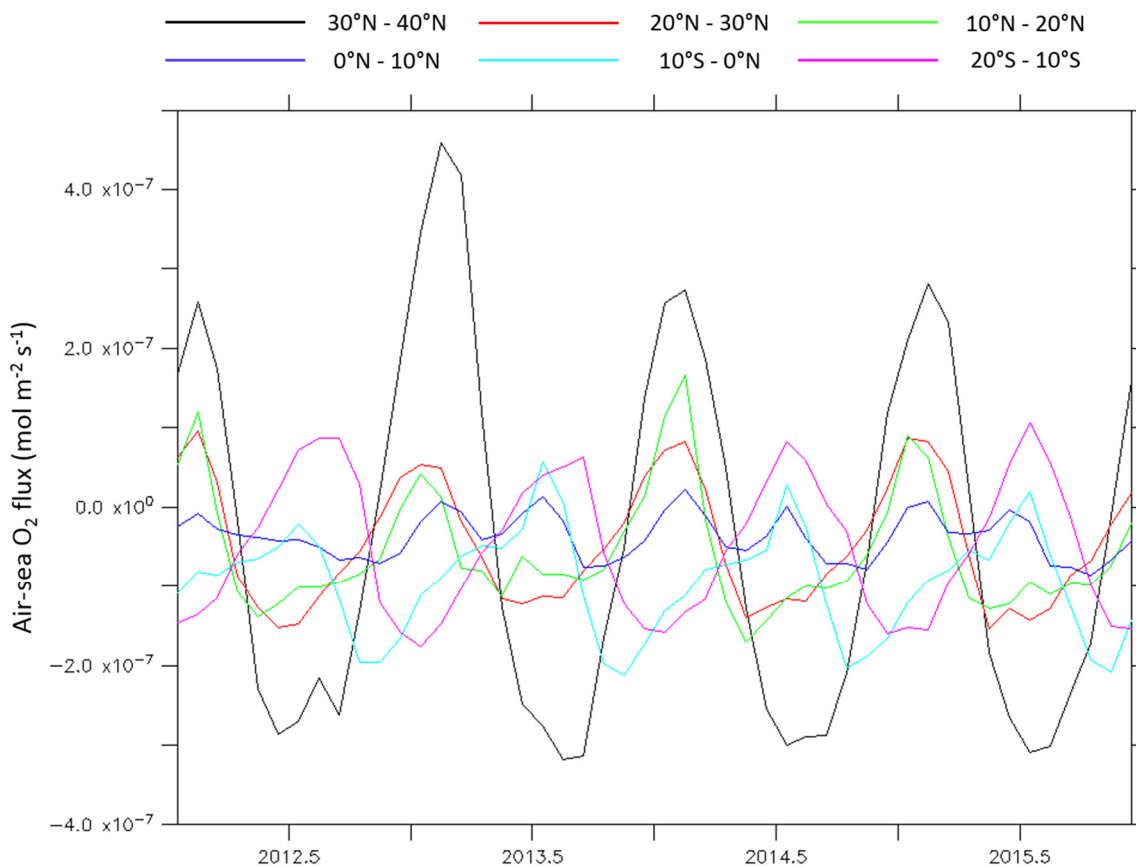


Figure 4.21. Atlantic Ocean Air-sea O₂ fluxes from the NEMO-PlankTOM model, binned into 10° latitude bands. The longitudinal range used in the latitudinal binning was 61°W to 20°E. Note that negative numbers indicate fluxes from the ocean to the atmosphere.

The NEMO-PlankTOM results do not rule out the possibility that 2015 was an unusual year, since it is also possible that a change in the regional atmospheric transport, such as an increase in the transport of northern hemisphere air into the equatorial Atlantic, could also cause a suppression of the equatorial APO bulge; this was found to be the case by (Tohjima et al., 2015) during the El Niño event of 2010, owing to a shift in the position of the ITCZ towards the equator. The influence of El Niño and La Niña events in the Atlantic Ocean is not expected to be as strong as those in the Pacific Ocean, and so one might expect that the interannual variability of annual mean APO through the Atlantic Ocean might be smaller than that found in the western Pacific Ocean.

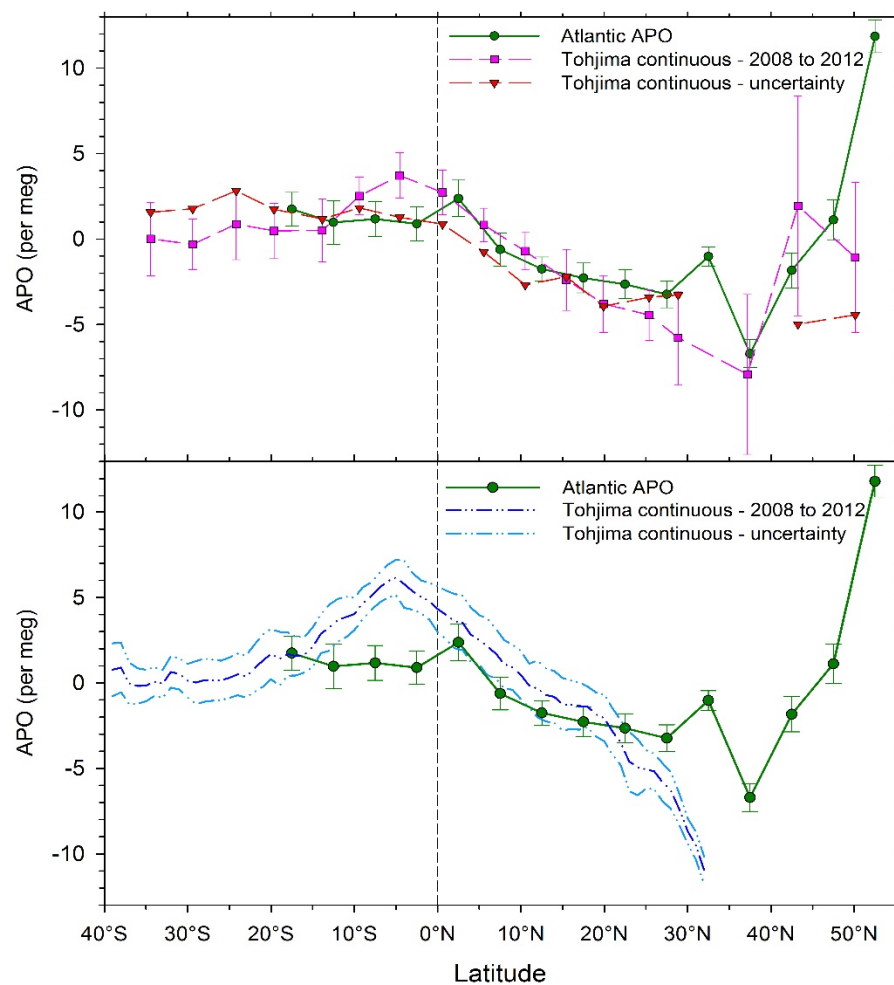


Figure 4.22. Comparison of annual mean latitudinal variability in Atlantic APO from the Cap San Lorenzo (green circles and solid lines; both panels) with annual mean latitudinal variability in western Pacific APO from 2003 – 2012 flask data (pink squares and dashed line; top panel), 2010 only flask data (red triangles and dashed lines; top panel), and 2008 – 2012 continuous data (dark blue dash-dotted lines on the bottom panel, with uncertainties indicated by the turquoise dash-dotted lines). All western Pacific data are courtesy of Yasunori Tohjima (National Institute of Environmental Studies, Japan) and are published in (Tohjima et al., 2015).

Figure 4.22 shows a comparison between the annual mean latitudinal variability in Atlantic APO from the Cap San Lorenzo data, with flask (top panel) and continuous (bottom panel) data from the shipboard measurements in the western Pacific, which are published in Tohjima et al. (2015). The comparison reveals that the interhemispheric gradient in APO in the Atlantic during 2015 is similar to the interhemispheric gradient from both the flask and the continuous data. As discussed previously, one can also see that there is a pronounced equatorial bulge in APO seen in the western Pacific flask and continuous data, which is not apparent in the Atlantic APO data. The top panel of Fig. 4.22 does show that during 2010, which was an El Niño year, the equatorial APO bulge in the western Pacific is not present, and that the 2010 western Pacific APO flask data agree quite well to the 2015 Atlantic APO data, during which strong El Niño conditions also developed. Thus, while it is not currently possible to determine how unusual the annual mean latitudinal distribution in Atlantic APO was during 2015, Fig. 4.22 suggests that the equatorial air-sea fluxes and atmospheric transport conditions in the Atlantic Ocean in 2015 are likely to be relatively similar to those in the western Pacific, during 2010.

Another feature that is apparent in both the western Pacific and Atlantic APO data in the top panel of Fig. 4.22 is a significant negative excursion in APO at 35°-40°N, followed by an increase in APO with increasing latitude. In the case of the western Pacific APO data, this sharp decrease and subsequent increase in APO has been attributed to an oceanic O₂ sink located in the northwest Pacific (at about 30° - 35° N), and the reinforcing effects of seasonal air-sea O₂ fluxes in the northern Pacific combining with a seasonal rectifier effect north of ~40°N, which act to enhance the measured APO in the northern hemisphere at mid to high latitudes (Tohjima et al., 2012). Figure 4.23, which shows the annual mean air-sea O₂ fluxes for 2015 from the NEMO-PlankTOM model, reveals that there is a similar O₂ sink located in the western Atlantic, just off the northeast USA and eastern Canadian coastlines. Hence, a similar combination of an oceanic O₂ sink, followed by covariation in air-sea O₂ fluxes and the seasonal rectifier effect could therefore be responsible for the Atlantic latitudinal distribution in annual mean APO that is apparent between 35°-55°N.

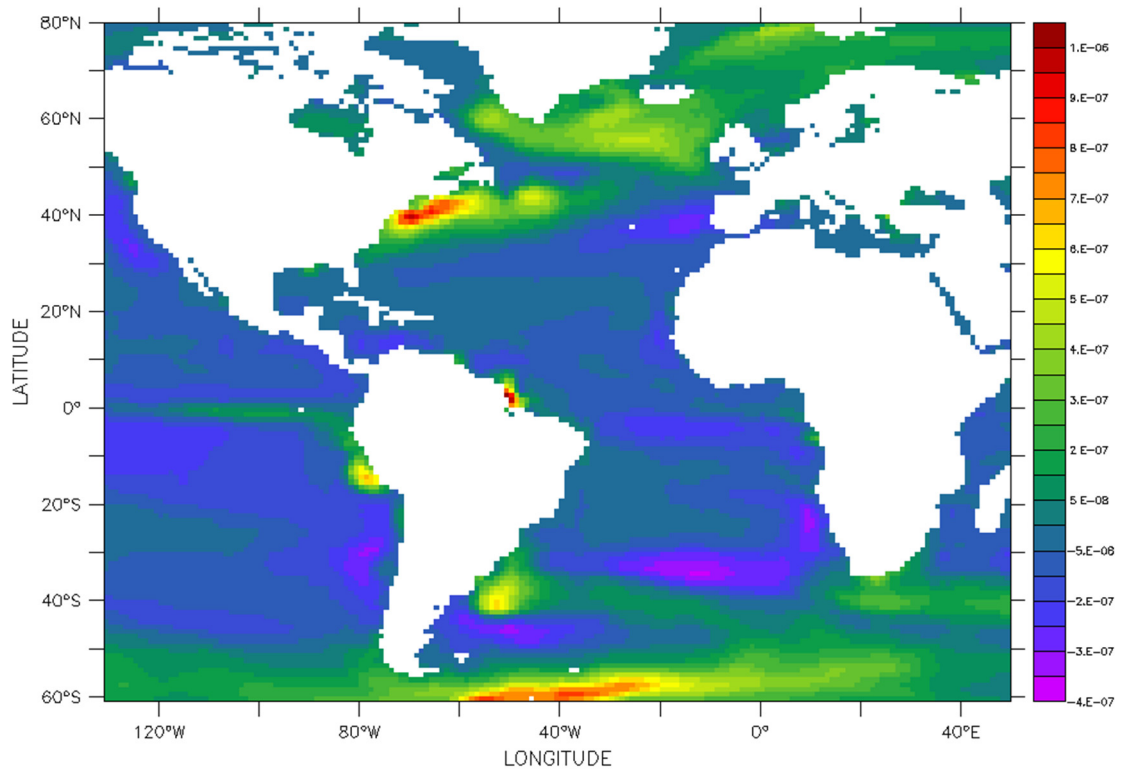


Figure 4.23. Annual mean air-sea O_2 flux for 2015 from the NEMO-PlankTOM model. Note that positive values indicate fluxes into the ocean (green to red shading), and negative values indicate fluxes out of the ocean (blue/purple shading). O_2 fluxes are shown in units of $\text{mol m}^{-2} \text{s}^{-1}$.

One feature that occurs in the Atlantic APO data, which is not apparent in the western Pacific APO data, is a small positive excursion in APO between 30° - 35°N . This positive excursion may be explained by the seasonal rectifier effect, but could also be caused by the sinking of high-altitude air over the mid-latitude North Atlantic, which would be characterised by higher APO values (because the air is older). Recently, (Jiang et al., 2015) found that summer-time sinking of high-altitude air over the mid-latitude South Atlantic Ocean caused a decrease in mid-tropospheric Atmospheric Infrared Sounder (AIRS) CO_2 data. To investigate whether the sinking of high-altitude air might also occur over the Northern Atlantic, I have looked at vertical pressure velocity data from National Centers for Environmental Prediction reanalysis 2 (NCEP2) (Kistler et al., 2001), which is shown in Figure 4.24. The NCEP2 data reveal that there is strong downwards transport of air at about 25° - 30°N over the Atlantic Ocean. Since high altitude air is comparatively ‘older’ than surface air, one would expect high altitude APO values to be slightly higher than surface values, given that over the long-term, APO is decreasing owing to fossil fuel combustion. Therefore, it is possible that the positive excursion in APO seen at about 30° - 35°N could be caused by sinking high-altitude air over the mid-latitude North Atlantic, although there is no

corresponding decrease in CO₂ at this latitude (see Fig. 4.18), which would also be expected, given that CO₂ is increasing in the atmosphere (also because of fossil fuel combustion). An alternative explanation, is that the positive APO excursion between 30°-35°N represents the period when the Cap San Lorenzo passes through the Northwest African coastal upwelling region, which has an annual net out-gassing O₂ flux (see Fig. 4.23), and is most likely caused by the dominance of primary productivity (O₂ out-gassing) over deep water upwelling (O₂ in-gassing), which is characteristic of coastal upwelling zones.

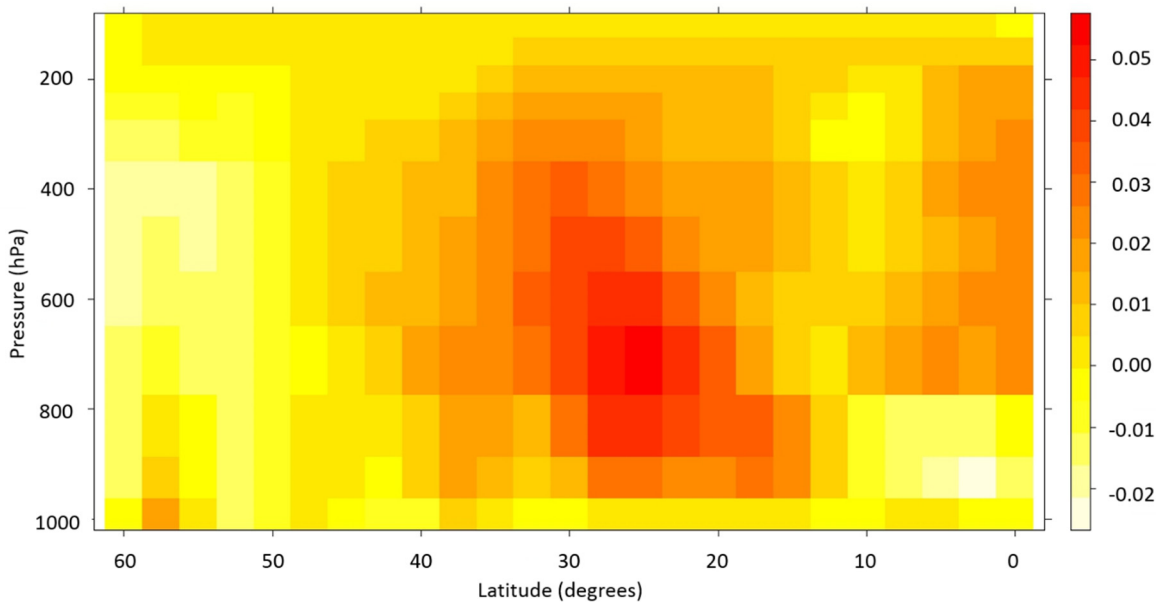


Figure 4.24. NCEP2 vertical pressure velocity data (in Pa s⁻¹) over the North Atlantic along a 22.5°E meridional transect. Note that positive values indicate downwards atmospheric transport, while negative values indicate upwards atmospheric transport.

4.5. Summary and Conclusions

In this chapter, I have presented atmospheric O₂, CO₂ and APO data from a shipboard measurement system that has been deployed on board the Cap San Lorenzo container ship since September 2014. The Cap San Lorenzo travels continuously from Europe to South America and back, covering a latitudinal range of about 55°N to 35°S through the Atlantic Ocean. The data presented in this chapter represent the first on-going atmospheric O₂ measurements across the Atlantic Ocean, and are able to provide insight into air-sea O₂ fluxes and atmospheric transport in the Atlantic sector.

The meridional transects of atmospheric O₂, CO₂ and APO exhibit step-changes as the ship crosses the ITCZ, as well as additional short-term variability near the

equator (shown in Fig. 4.5). While the step-changes are visible in all of the transects, the additional equatorial variability is only apparent in two of the eight transects, and is most likely caused by transient changes in atmospheric transport, which brings air from a different latitude, or even hemisphere, to the ship. Other short-term ‘events’ that occur in the extra-tropical regions also seem to be caused by atmospheric transport changes, as determined by examining NAME footprints. In general, the short-term variability in the meridional O₂, CO₂ and APO data is very small when the ship is in the open ocean, with maximum magnitudes of approximately 30 per meg (O₂), 5 ppm (CO₂), and 5 per meg (APO). The short-term variability in atmospheric O₂, CO₂ and APO when the ship is travelling between the ports in Europe and South America reveals large excursions in all species (see Fig. 4.3), which are due to terrestrial biosphere and fossil fuel influences from the land (Fig. 4.8).

The general lack of short-term variability in APO in the Cap San Lorenzo open ocean data is surprising, given the length of the dataset (~1 year), and the fact that several publications, some from relatively short research cruises (e.g. Patecki and Manning, 2007; Thompson et al., 2008), have reported relatively large variations in APO, attributing such variations to either ocean upwelling events (resulting in negative excursions in APO) or ocean productivity events (resulting in positive excursions in APO). I have examined some of these previously reported events in APO, in particular, those of (Lueker et al., 2003) and (Lueker, 2004), and have found that the APO ocean upwelling events identified at Trinidad Head, USA, correlate with air mass trajectories originating from the land, relatively large positive excursions in CO₂, and positive excursions in both CFC-11 and CFC-12. These data suggest that the events are at least partly, if not entirely, caused by land influences; therefore, the negative APO excursions that were previously identified as ocean upwelling events may actually represent fossil fuel combustion. In addition, the NEMO-PlankTOM annual mean O₂ fluxes (see Fig. 4.23) suggest that O₂ out-gassing from primary productivity dominates over O₂ in-gassing from upwelling at coastal upwelling locations, and yet there are fewer and smaller positive APO excursions in the Trinidad Head data that are indicative of coastal ocean primary productivity events than there are upwelling-related APO excursions.

Given the dearth of APO ocean events in the Cap San Lorenzo data, I have also come to the conclusion that the large negative APO excursion (~100 per meg in magnitude) in the JC090 cruise that I presented in Chapter 3 is most likely not a real event, and is probably caused by O₂/N₂ fractionation in the gas handling system. If the

large APO excursion from Chapter 3 is real, then it must be a very rare event, given that the Cap San Lorenzo passes through the same region as the JC090 cruise, and no APO variability larger than ~ 5 per meg is apparent in the open ocean Cap San Lorenzo data. I therefore propose that it is extremely difficult to detect short-term ocean-related events in APO data, because atmospheric mixing is relatively fast compared to the diffusion of O_2 across the air-sea interface, and that one should exercise extreme caution when attributing short-term variability in APO to specific/localised oceanic upwelling or productivity events, because short-term APO variability is often related to technical issues, and can also be caused by fossil fuel combustion.

To examine seasonal variability and annual mean latitudinal distribution in O_2 , CO_2 and APO across the Atlantic Ocean, I have binned the Cap San Lorenzo meridional data into 5° latitude bands. The seasonal variability for O_2 , CO_2 and APO is as expected: the CO_2 seasonal cycles reflect seasonal changes in the terrestrial biosphere, have a larger amplitude in the northern hemisphere than the southern hemisphere, seasonal cycle amplitudes in the northern hemisphere increase with latitude, phasing is opposite between the two hemispheres, and the seasonal maxima are broader than the minima; the O_2 seasonal cycles reflect both ocean and terrestrial biosphere seasonal changes, are anti-correlated to the seasonal variability in CO_2 , have a larger amplitude than the CO_2 seasonal cycle amplitudes at the same latitude, are more uniform in shape than the CO_2 seasonal cycles (i.e. maxima and minima are more equally balanced), have different phasing between the two hemispheres, and have amplitudes that increase with latitude in the northern hemisphere; the APO seasonal cycles reflect mostly oceanic seasonal changes, are relatively similar in both shape and phasing to the O_2 seasonal cycles, do not increase in amplitude with increasing latitude in the northern hemisphere (as the CO_2 and O_2 seasonal cycles do), and have smaller amplitudes in the northern hemisphere than the northern hemisphere O_2 seasonal cycle amplitudes.

Lastly, I have examined the annual mean APO latitudinal distribution over the Atlantic Ocean and compared my Atlantic results to those measured by Tohjima and colleagues in the western Pacific, and to modelled APO estimates. Unlike the western Pacific and modelled APO data, the Atlantic shipboard annual mean data do not exhibit a significant equatorial APO bulge. It is not currently possible to tell whether the missing APO bulge is a transient feature, caused by the strengthening El Niño conditions during 2015, because I only have a single year of shipboard

measurements, or a permanent feature over the Atlantic Ocean. Examining the interannual variability in NEMO-PlankTOM air-sea O₂ fluxes, suggests that there is little inter-annual variability in the tropics. Tohjima et al. (2015) found that interannual variability in atmospheric transport associated with a shift in the position of the ITCZ to a more southerly latitude during El Niño conditions was the main driver of interannual variability in the western Pacific equatorial APO bulge; however, by using step-changes in the Cap San Lorenzo O₂, CO₂ and APO data as a proxy for the position of the ITCZ in the Atlantic, I am able to determine that the ITCZ position during 2015 was not situated uncommonly far south compared to the 2014 ITCZ position (shown in Fig. 4.11). It therefore seems likely that a pronounced equatorial APO bulge is not a permanent feature in the Atlantic Ocean. As a result, the discrepancy between the Atlantic measured APO and the modelled APO in Fig. 4.20 suggests that either the ocean fluxes used in the TM3 model are too large in the tropical Atlantic, or that there is an error associated with the atmospheric transport in TM3 (such as Hadley cell circulation that is too weak, for example).

The Atlantic APO annual mean data also exhibit a negative APO excursion in the northern hemisphere followed by an increase in APO with latitude, and follows a very similar pattern to that exhibited in the western Pacific APO data. It is likely that the cause of this northern hemisphere variability is a strong oceanic O₂ sink in the western Atlantic (as shown by the NEMO-PlankTOM annual mean O₂ fluxes in Fig. 4.23), followed by the covariation of seasonal oceanic O₂ fluxes and a seasonal atmospheric rectifier effect, which act to reinforce each other, although further modelling of Atlantic APO (similar to that of Tohjima et al., 2012) is required in order to confirm this hypothesis.

To summarise, the shipboard O₂, CO₂ and APO data presented in this chapter provide new insights into air-sea O₂ fluxes in the Atlantic Ocean. The main limitations of the current dataset are two-fold: firstly, there are some gaps in the dataset, particularly in the southern hemisphere, owing to technical issues with the drying components of the measurement system, and secondly, the dataset is only a single year in duration. Thus, a longer dataset with fewer gaps will reveal more robust seasonal and annual mean analyses, and will also enable me to examine O₂, CO₂ and APO interannual variability across the Atlantic Ocean. Further modelling analyses will allow me to separate out thermal and biological O₂ and CO₂ flux components in the modelled APO to determine which processes are most responsible for the mismatch between the modelled and measured latitudinal mean APO. The potential for using

this Atlantic shipboard dataset in future research is great, particularly if the measurements are kept running for several years or more. In addition to interannual analyses of O₂, CO₂ and APO, the dataset can be used in atmospheric inverse modelling in order to learn more about ocean O₂ and CO₂ fluxes in the Atlantic, to constrain modelled estimates of heat and carbon transport in the Atlantic ocean sector, owing to the strong relationship between heat flux and O₂/N₂ gas solubility, as mentioned in (Keeling and Shertz, 1992), and to separate the land and carbon ocean sinks in the Atlantic Ocean sector, using the method of (Manning and Keeling, 2006).

References

- Battle, M., Fletcher, S. E. M., Bender, M. L., Keeling, R. F., Manning, A. C., Gruber, N., Tans, P. P., Hendricks, M. B., Ho, D. T., Simonds, C., Mika, R., and Paplawsky, B.: Atmospheric potential oxygen: New observations and their implications for some atmospheric and oceanic models, *Global Biogeochemical Cycles*, 20, 2006.
- Bischoff, T. and Schneider, T.: Energetic Constraints on the Position of the Intertropical Convergence Zone, *Journal of Climate*, 27, 4937-4951, 2014.
- Ciais, P., Sabine, C., Bala, G., Bopp, L., Brovkin, V., Canadell, J., Chhabra, A., DeFries, R., Galloway, J., Heimann, M., Jones, C., Le Quéré, C., Myneni, R. B., Piao, S., and Thornton, P.: Carbon and Other Biogeochemical Cycles In: *Climate Change 2013: The Physical Science Basis. Contribution of Working Group I to the Fifth Assessment Report of the Intergovernmental Panel on Climate Change*, Stocker, T. F., D. Qin, G.-K. Plattner, M. Tignor, S.K. Allen, J. Boschung, A. Nauels, Y. Xia, V. Bex and P.M. Midgley (Ed.), Cambridge University Press, Cambridge, United Kingdom and New York, NY, USA., 2013.
- Cleveland, R. B., Cleveland, W. S., McRae, J. E., and Terpenning, I.: STL: A seasonal-trend decomposition procedure based on Loess, *Journal of Official Statistics*, 6, 3-33, 1990.
- Fang, S. X., Tans, P. P., Steinbacher, M., Zhou, L. X., and Luan, T.: Comparison of the regional CO₂ mole fraction filtering approaches at a WMO/GAW regional station in China, *Atmospheric Measurement Techniques*, 8, 5301-5313, 2015.
- Friedman, A. R., Hwang, Y. T., Chiang, J. C. H., and Frierson, D. M. W.: Interhemispheric Temperature Asymmetry over the Twentieth Century and in Future Projections, *Journal of Climate*, 26, 5419-5433, 2013.
- Friedrich, T., Oschlies, A., and Eden, C.: Role of wind stress and heat fluxes in interannual-to-decadal variability of air-sea CO₂ and O₂ fluxes in the North Atlantic, *Geophysical Research Letters*, 33, 2006.
- Garcia, H. E. and Keeling, R. F.: On the global oxygen anomaly and air-sea flux, *Journal of Geophysical Research-Oceans*, 106, 31155-31166, 2001.
- Gloor, M., Gruber, N., Hughes, T. M. C., and Sarmiento, J. L.: Estimating net air-sea fluxes from ocean bulk data: Methodology and application to the heat cycle, *Global Biogeochemical Cycles*, 15, 767-782, 2001.
- Gruber, N., Gloor, M., Fan, S. M., and Sarmiento, J. L.: Air-sea flux of oxygen estimated from bulk data: Implications for the marine and atmospheric oxygen cycles, *Global Biogeochemical Cycles*, 15, 783-803, 2001.
- Heimann, M. and Körner, S.: *The Global Atmospheric Tracer Model TM3*, Max-Planck-Institut für Biogeochemistry, Jena, 2003.

- Hwang, Y. T., Frierson, D. M. W., and Kang, S. M.: Anthropogenic sulfate aerosol and the southward shift of tropical precipitation in the late 20th century, *Geophysical Research Letters*, 40, 2845-2850, 2013.
- Ishidoya, S., Murayama, S., Kondo, H., Saigusa, N., Kishimoto-Mo, A., and Yamamoto, S.: Observation of O₂:CO₂ exchange ratio for net turbulent fluxes and its application to forest carbon cycles, *Ecological Research*, 30, 225-234, 2015.
- Jiang, X., Olsen, E. T., Pagano, T. S., Su, H., and Yung, Y. L.: Modulation of Midtropospheric CO₂ by the South Atlantic Walker Circulation, *Journal of the Atmospheric Sciences*, 72, 2241-2247, 2015.
- Jones, A. R., Thomson, D. J., Hort, M., and Devenish, B.: The U.K. Met Office's next-generation atmospheric dispersion model, NAME III In: *Air Pollution Modeling and its Application Borrego, C. and Norman, A. L. (Eds.), XVII (Proceedings of the 27th NATO/CCMS International Technical Meeting on Air Pollution Modelling and its Application)*, Springer, 2007.
- Kalnay, E., Kanamitsu, M., Kistler, R., Collins, W., Deaven, D., Gandin, L., Iredell, M., Saha, S., White, G., Woollen, J., Zhu, Y., Chelliah, M., Ebisuzaki, W., Higgins, W., Janowiak, J., Mo, K. C., Ropelewski, C., Wang, J., Leetmaa, A., Reynolds, R., Jenne, R., and Joseph, D.: The NCEP/NCAR 40-year reanalysis project, *Bulletin of the American Meteorological Society*, 77, 437-471, 1996.
- Keeling, R. F., Najjar, R. P., Bender, M., and Tans, P. P.: What atmospheric oxygen measurements can tell us about the global carbon cycle, *Global Biogeochemical Cycles*, 7, 37-67, 1993.
- Keeling, R. F. and Shertz, S. R.: Seasonal and interannual variations in atmospheric oxygen and implications for the global carbon cycle, *Nature*, 358, 723-727, 1992.
- Kistler, R., Kalnay, E., Collins, W., Saha, S., White, G., Woollen, J., Chelliah, M., Ebisuzaki, W., Kanamitsu, M., Kousky, V., van den Dool, H., Jenne, R., and Fiorino, M.: The NCEP-NCAR 50-year reanalysis: Monthly means CD-ROM and documentation, *Bulletin of the American Meteorological Society*, 82, 247-267, 2001.
- Lefèvre, N., Caniaux, G., Janicot, S., and Gueye, A. K.: Increased CO₂ outgassing in February-May 2010 in the tropical Atlantic following the 2009 Pacific El Niño, *Journal of Geophysical Research-Oceans*, 118, 1645-1657, 2013.
- Li, J. L., Cunnold, D. M., Wang, H. J., Weiss, R. F., Miller, B. R., Harth, C., Salameh, P., and Harris, J. M.: Halocarbon emissions estimated from advanced global atmospheric gases experiment measured pollution events at Trinidad Head, California, *Journal of Geophysical Research-Atmospheres*, 110, 2005.
- Lueker, T. J.: Coastal upwelling fluxes of O₂, N₂O, and CO₂ assessed from continuous atmospheric observations at Trinidad, California, *Biogeosciences*, 1, 101-111, 2004.
- Lueker, T. J., Walker, S. J., Vollmer, M. K., Keeling, R. F., Nevison, C. D., Weiss, R. F., and Garcia, H. E.: Coastal upwelling air-sea fluxes revealed in atmospheric observations of O₂/N₂, CO₂ and N₂O, *Geophysical Research Letters*, 30, 2003.
- Manning, A. C. and Keeling, R. F.: Global oceanic and land biotic carbon sinks from the scripps atmospheric oxygen flask sampling network, *Tellus, Series B: Chemical and Physical Meteorology*, 58, 95-116, 2006.
- Manning, A. C., Keeling, R. F., Katz, L. E., Paplawsky, W. J., and McEvoy, E. M.: Interpreting the seasonal cycles of atmospheric oxygen and carbon dioxide concentrations at American Samoa Observatory, *Geophysical Research Letters*, 30, 2003.
- Manning, M. R., Lowe, D. C., Melhuish, W. H., Sparks, R. J., Wallace, G., Brenninkmeijer, C. A. M., and McGill, R. C.: The use of radiocarbon measurements in atmospheric studies, *Radiocarbon*, 32, 37-58, 1990.

- Patecki, M. and Manning, A. C.: First results from shipboard atmospheric O₂ and CO₂ measurements over the North Atlantic Ocean, New York, 2007.
- Pickers, P. A. and Manning, A. C.: Investigating bias in the application of curve fitting programs to atmospheric time series, *Atmospheric Measurement Techniques*, 8, 1469-1489, 2015.
- Prinn, R. G., Weiss, R. F., Fraser, P. J., Simmonds, P. G., Cunnold, D. M., Alyea, F. N., O'Doherty, S., Salameh, P., Miller, B. R., Huang, J., Wang, R. H. J., Hartley, D. E., Harth, C., Steele, L. P., Sturrock, G., Midgley, P. M., and McCulloch, A.: A history of chemically and radiatively important gases in air deduced from ALE/GAGE/AGAGE, *Journal of Geophysical Research-Atmospheres*, 105, 17751-17792, 2000.
- Schneider, T., Bischoff, T., and Haug, G. H.: Migrations and dynamics of the intertropical convergence zone, *Nature*, 315, 45-53, 2014.
- Stein, A. F., Draxler, R. R., Rolph, G. D., Stunder, B. J. B., Cohen, M. D., and Ngan, F.: NOAA'S HYSPLIT Atmospheric Transport and Dispersion Modeling System, *Bulletin of the American Meteorological Society*, 96, 2059-2077, 2015.
- Stephens, B. B., Keeling, R. F., Heimann, M., Six, K. D., Murnane, R., and Caldeira, K.: Testing global ocean carbon cycle models using measurements of atmospheric O₂ and CO₂ concentration, *Global Biogeochemical Cycles*, 12, 213-230, 1998.
- Takahashi, T., Sutherland, S. C., Wanninkhof, R., Sweeney, C., Feely, R. A., Chipman, D. W., Hales, B., Friederich, G., Chavez, F., Sabine, C., Watson, A., Bakker, D. C. E., Schuster, U., Metzl, N., Yoshikawa-Inoue, H., Ishii, M., Midorikawa, T., Nojiri, Y., Kortzinger, A., Steinhoff, T., Hoppema, M., Olafsson, J., Arnarson, T. S., Tilbrook, B., Johannessen, T., Olsen, A., Bellerby, R., Wong, C. S., Delille, B., Bates, N. R., and de Baar, H. J. W.: Climatological mean and decadal change in surface ocean pCO₂, and net sea-air CO₂ flux over the global oceans, *Deep-Sea Research Part II-Topical Studies in Oceanography*, 56, 554-577, 2009.
- Thompson, R. L., Gloor, M., Manning, A. C., Lowe, D. C., Rodenbeck, C., and Le Quere, C.: Variability in atmospheric O₂ and CO₂ concentrations in the southern Pacific Ocean and their comparison with model estimates, *Journal of Geophysical Research-Biogeosciences*, 113, 2008.
- Thompson, R. L., Manning, A. C., Lowe, D. C., and Weatherburn, D. C.: A ship-based methodology for high precision atmospheric oxygen measurements and its application in the Southern Ocean region, *Tellus Series B-Chemical and Physical Meteorology*, 59, 643-653, 2007.
- Thoning, K. W., Tans, P. P., and Komhyr, W. D.: Atmospheric carbon dioxide at Mauna Loa Observatory 2. Analysis of the NOAA GMCC data, 1974-1985, *Journal of Geophysical Research-Atmospheres*, 94, 8549-8565, 1989.
- Tohjima, Y., Minejima, C., Mukai, H., Machida, T., Yamagishi, H., and Nojiri, Y.: Analysis of seasonality and annual mean distribution of atmospheric potential oxygen (APO) in the Pacific region, *Global Biogeochemical Cycles*, 26, 2012.
- Tohjima, Y., Mukai, H., Machida, T., Nojiri, Y., and Gloor, M.: First measurements of the latitudinal atmospheric O₂ and CO₂ distributions across the western Pacific, *Geophysical Research Letters*, 32, 2005.
- Tohjima, Y., Terao, Y., Mukai, H., Machida, T., Nojiri, Y., and Maksyutov, S.: ENSO-related variability in latitudinal distribution of annual mean atmospheric potential oxygen (APO) in the equatorial western Pacific, *Tellus B*, 67, 2015.
- van der Laan-Luijkx, I. T., Neubert, R. E. M., van der Laan, S., and Meijer, H. A. J.: Continuous measurements of atmospheric oxygen and carbon dioxide on a North Sea gas platform, *Atmospheric Measurement Techniques*, 3, 113-125, 2010.

Wilson, P. A.: Insight into the Carbon Cycle from Continuous Measurements of Oxygen and Carbon Dioxide at Weybourne Atmospheric Observatory, UK, Ph.D. thesis, University of East Anglia, Norwich, UK, 2013.

Chapter 5

Quantifying fossil fuel CO₂ using APO: a novel approach

5.1 Introduction

Anthropogenic greenhouse gas emissions from fossil fuel burning are the dominant driver of current climate change. In order to mitigate adverse consequences of anthropogenic climate change, emissions of anthropogenic CO₂ and non-CO₂ long-lived greenhouse gases, such as methane (CH₄) and nitrous oxide (N₂O), require significant reduction, which has led to widespread national and international regulation of some anthropogenic greenhouse gas emissions in recent years (Weiss and Prinn, 2011). Although on a global scale, annual anthropogenic greenhouse gas emissions are relatively well known, there is significant uncertainty associated with regional and country-scale annual emissions, as well as the intra-annual variability of emissions (Peylin et al., 2011).

The source of uncertainty in anthropogenic greenhouse gas emissions largely stems from the so-called 'bottom-up' methodologies employed; typically, greenhouse gas emissions are calculated using a book-keeping or inventory approach, whereby emission factors are applied to particular economic activities, which are then scaled-up to regional and country-level spatial scales using land-use and economic databases, with uncertainties that are often either stated as 'unknown' or are quoted to unrealistically high precision (Nisbet and Weiss, 2010; Weiss and Prinn, 2011). Such bottom-up methods are vulnerable to large uncertainties and biases because they are based on emission factors associated with the raw materials used for various economic activities, rather than the actual emissions that are generated by such economic activities, which can be very variable, depending on the efficiency of individual processes and on the quality of the fuel, for example. As stated by (Nisbet and Weiss, 2010), relying on bottom-up methodologies for quantifying and subsequently mitigating anthropogenic greenhouse gas emissions is analogous to "dieting without weighing oneself", or in other words, relying on calorie counting alone.

Accurate and precise quantification of anthropogenic greenhouse gas emissions may be necessary in order to facilitate a legally binding international agreement on climate change, with truly effective emissions reductions. In addition, well-known anthropogenic greenhouse gas emissions are required in order to provide stability to the carbon emissions trading markets, which are currently worth about US\$350 billion per year globally (Kossov et al., 2015). There is also a strong need from the scientific community for accurate anthropogenic greenhouse gas quantification, owing to the fact that many greenhouse gases (such as CO₂ and CH₄) have anthropogenic and natural sources. Inverse modelling studies aiming to quantify natural greenhouse gas sources and sinks often assume that anthropogenic greenhouse gas emissions are accurate and precise, which can lead to significant biases in natural greenhouse

gas fluxes, particularly as the spatial and temporal resolution of atmospheric transport models increases (Gurney et al., 2005; Peylin et al., 2011).

Using atmospheric measurements and inverse modelling to verify anthropogenic greenhouse gas emissions, known as a ‘top-down’ approach, can provide an independent method for verifying anthropogenic greenhouse gas emissions. Recent improvements in atmospheric greenhouse gas measurement technologies, the expansion of measurement networks, and developments in inverse modelling techniques now enable country-scale top-down verification of some anthropogenic greenhouse gas emissions in developed regions, such as North America and Europe (e.g. Bergamaschi et al., 2005; Levin et al., 2011), with uncertainties that are at least comparable to realistic bottom up inventory estimates (Nisbet and Weiss, 2010; Weiss and Prinn, 2011).

Quantifying fossil fuel CO₂ emissions using atmospheric measurements requires the separation of natural (mainly biospheric) and anthropogenic (mainly fossil fuel) influences on atmospheric CO₂ mole fractions, in order to isolate the fossil fuel component of atmospheric CO₂ (ffCO₂). Inverse modelling can then be performed using atmospheric ffCO₂ data (in ppm) to verify fossil fuel CO₂ emissions. This top-down separation of biospheric and fossil fuel derived CO₂ and subsequent quantification of ffCO₂ is not trivial. The current methodology for quantifying ffCO₂ from atmospheric CO₂ measurements is to use discrete measurements of radiocarbon (¹⁴C) content in CO₂ (¹⁴CO₂): ¹⁴C has a half-life of about 5730 years, and therefore fossil fuel derived CO₂ contains no ¹⁴C (Manning et al., 1990; Turnbull et al., 2009; Zondervan and Meijer, 1996). Measurements of ¹⁴CO₂ are, expensive, however, and cannot be made continuously; hence, most ¹⁴CO₂ time series consist of a single measurement approximately once or twice every two weeks. ffCO₂ is calculated from ¹⁴CO₂ measurements as follows (Levin et al., 2003; Turnbull et al., 2009):

$$ffCO_2 = \frac{CO_2obs(\Delta_{obs} - \Delta_{bg})}{(\Delta_{ff} - \Delta_{bg})} \quad (\text{Eq. 5.1})$$

where CO_2obs denotes the atmospheric CO₂ mole fraction, and Δ_{obs} , Δ_{bg} and Δ_{ff} denote the ¹⁴C content of CO₂ (in permil units) of the observations, well-mixed atmospheric background, and fossil fuels (-1000 ‰, which is the value for zero ¹⁴C content), respectively. In addition to the terms shown in Equation 5.1, a small correction is also applied to ffCO₂ which accounts for other minor sources of ¹⁴C, including heterotrophic respiration and nuclear industry sources (Turnbull et al., 2009).

In order to obtain higher temporal resolution ffCO₂ quantification (i.e. daily or hourly, as opposed to weekly or fortnightly), continuous atmospheric measurements of carbon monoxide (CO) can be used according to Equation 5.2, because CO is co-emitted with CO₂ when fossil fuels are combusted (Gamnitzer et al., 2006; Turnbull et al., 2006; van der Laan et al., 2010).

$$ffCO_2 = \frac{CO_{obs} - CO_{bg}}{R_{CO:CO_2}} \quad (\text{Eq. 5.2})$$

where CO_{obs} and CO_{bg} are the CO mole fractions of the observations and of the well-mixed atmospheric background respectively, and $R_{CO:CO_2}$ is the CO:CO₂ combustion ratio for fossil fuel emissions, which varies both temporally and spatially according to changes in fuel type.

Although it is a lot cheaper to make continuous CO measurements than discrete ¹⁴CO₂ measurements, it is not possible to use CO alone as a reliable tracer for ffCO₂, owing to the large uncertainty and spatial and temporal variability associated with $R_{CO:CO_2}$ (Gamnitzer et al., 2006; Vogel et al., 2010). In addition, there is large uncertainty associated with non-fossil fuel related CO sources (e.g. biomass burning, soils, and atmospheric methane oxidation) and sinks (e.g. from hydroxyl radical reactions, and uptake by soils) (Gamnitzer et al., 2006). ffCO₂ from continuous CO measurements can, however, be calibrated by co-located ¹⁴CO₂ measurements, which can be used to determine accurate $R_{CO:CO_2}$ values (Vogel et al., 2010). Therefore, continuous CO measurements combined with discrete ¹⁴CO₂ measurements can be used to quantify ffCO₂ with high temporal resolution, but this method still assumes that any natural influences on CO are negligible.

There are several key limitations to using ¹⁴CO₂ and CO measurements in order to quantify ffCO₂. Firstly, $R_{CO:CO_2}$ is highly variable, and is known to vary on diurnal and sub-diurnal timescales. Thus, using ¹⁴CO₂ to calibrate ffCO₂ from CO measurements once per week or once per fortnight will only guarantee accurate ffCO₂ at the time of the ¹⁴CO₂ measurements. Secondly, it is not possible to distinguish between fossil fuel sources and bioenergy sources using atmospheric CO data; hence, calculating ffCO₂ using CO may result in erroneously allocating bioenergy-derived CO₂ as ffCO₂. Although bioenergy currently accounts for a small proportion of total anthropogenic fuel sources (approximately 10% of global primary energy supply; IEA, 2012b), it is predicted to become much more prevalent in the coming decades, which may render CO measurements redundant as a method for quantifying ffCO₂ in the future. Thirdly, it is not possible to accurately quantify ffCO₂ from ¹⁴CO₂ measurements in some

regions, owing to interference from certain nuclear power plant ^{14}C emissions (Graven and Gruber, 2011; Vogel et al., 2013). This is particularly a problem in the UK, where the prevailing south-westerly winds often prevent accurate ffCO_2 from $^{14}\text{CO}_2$ quantification, owing to the abundance of gas-cooled nuclear power plants in southern England. Thus, in the UK, the only top-down method for CO_2 emissions verification that is currently available involves performing atmospheric inversions using winter-time only total CO_2 atmospheric measurements (Alistair Manning, personal communication, 2015), which are very likely to be significantly influenced by winter-time biospheric respiration. For Paris, the current approach is to quantify ffCO_2 from down-wind gradients in CO_2 data, in combination with biogenic CO_2 fluxes from land surface models, although this method results in very drastic data flagging and posterior flux estimates that are heavily reliant on the prior inventory estimates (Breon et al., 2015; Staufer et al., 2016).

In addition to the nuclear power plant emissions issue, (Graven, 2015) suggests that the sensitivity of $^{14}\text{CO}_2$ to fossil fuel derived CO_2 is currently decreasing, owing to the global increase in anthropogenic CO_2 in the atmosphere, and that $^{14}\text{CO}_2$ measurement precision will need to improve by a factor of 2 over the next few decades, in order to maintain today's detection capability of $^{14}\text{CO}_2$ to ffCO_2 . The development of a new tracer to quantify ffCO_2 , which is more precise and more accurate than CO , and which can also be used independently from $^{14}\text{CO}_2$ measurements, would therefore be a highly valued tool for atmospheric verification of fossil fuel CO_2 inventory estimates; such a tool would be extremely useful today, in regions that are severely affected by gas-cooled nuclear power plant ^{14}C influences, and also in the coming decades, as the sensitivity of $^{14}\text{CO}_2$ measurements to ffCO_2 declines.

5.1.1 Outline of this chapter

In Section 5.2, I present atmospheric O_2 , CO_2 and APO data measured from the roof of the Environmental Sciences building at the University of East Anglia (UEA), during the summer of 2014. I then compare the short term variability in these data to two other measurement sites in Norfolk, UK: the Tacolneston tall tower (TAC) and Weybourne Atmospheric Observatory (WAO). In Section 5.3, I present a new methodology for calculating ffCO_2 from APO data, and compare the results to ffCO_2 calculated using CO and $^{14}\text{CO}_2$ measurements and to modelled ffCO_2 using bottom up inventory data. Lastly, in Section 5.4, I summarise the results from this chapter, and outline a new potential for urban atmospheric O_2 and CO_2 measurements.

5.2 Atmospheric O₂ and CO₂ measured from the Environmental Sciences building, University of East Anglia

Prior to final deployment on board the Cap San Lorenzo container ship, the atmospheric O₂ and CO₂ measurement system was tested in the CRAM Laboratory at UEA (52.62°N, 1.24°E; see Figure 5.1), and air was sampled from the roof of the Environmental Sciences building (~25 m above the ground) using aspirated air inlets, from 09Jul-03Sep 2014. The aspirated air inlets were mounted at the highest point of the environmental sciences building, and therefore were not obstructed by any other buildings, and were not close to any of the building vents. For technical details relating to the atmospheric O₂ and CO₂ measurement system, see Chapter 2.

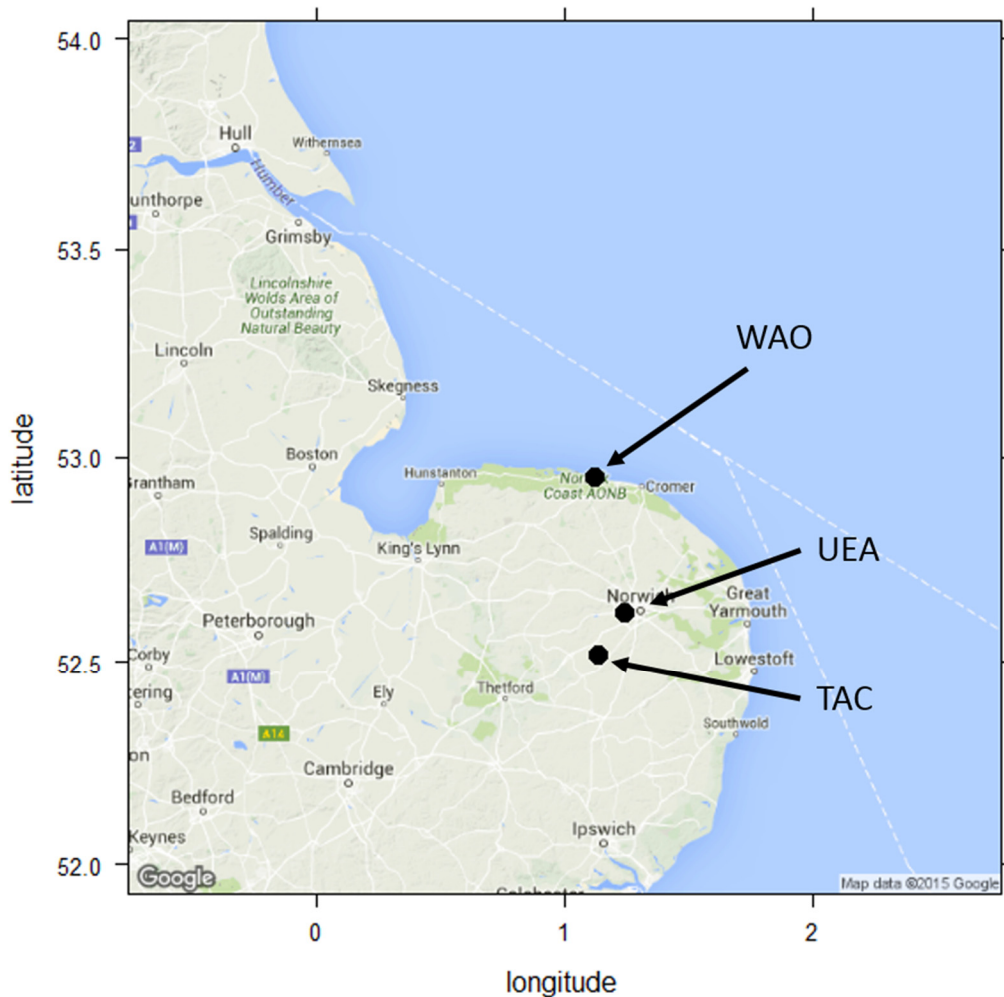


Figure 5.1. Map showing the location of the University of East Anglia (UEA), and also the Tacolneston tall tower (TAC) and Weybourne Atmospheric Observatory (WAO).

Figure 5.2 presents the UEA atmospheric O₂, CO₂, and APO data, as well as model-derived meteorological data (atmospheric temperature, relative humidity, atmospheric pressure, wind direction, and wind speed), which are from the USA National Oceanic and

Atmospheric Administration (NOAA) Global Data Assimilation System (GDAS) database. APO is calculated from the UEA atmospheric O₂ and CO₂ data using Equation 5.3:

$$APO = O_2 + \left(\frac{-1.1}{0.2095} \right) \times (350 - CO_2) \quad (\text{Eq. 5.3})$$

where O_2 and CO_2 are the atmospheric O₂ and CO₂ measurements in per meg and ppm units, respectively, -1.1 is the O₂:CO₂ ratio of global terrestrial biosphere-atmosphere exchange, 0.2095 is the mole fraction of O₂ molecules in dry air, and 350 is an arbitrary reference. Multiplying CO₂ by -1.1 and dividing by 0.2095 converts the CO₂ data from ppm to per meg units.

Large gaps in the atmospheric O₂, CO₂ and APO data are due to periods of experimental testing of the measurement system (for example, when checking the measurement system for leaks), which meant that it was not possible to sample outside air. Short gaps (1-3 hours) are mostly caused by WSS, ZT, and TT calibration routines being carried out (see Chapter 2, Section 2.3 for details). As shown in Figure 5.2, the CO₂ and O₂ data are strongly anti-correlated, owing to the dominance of terrestrial processes on the data. Strong diurnal variability is apparent in both species, with higher CO₂ and lower O₂ generally occurring at night-time. This diurnal variability is likely to be strongly influenced by the diurnal rectifier effect, whereby atmospheric CO₂ and O₂ is diluted during the day, owing to a well-mixed boundary layer, and relatively high boundary layer height, and both species are concentrated at night, when the boundary layer is stable and the boundary layer height is relatively low. In addition, owing to the time of year and relatively rural location, photosynthesis will likely be dominating the atmospheric CO₂ and O₂ signals during the day, causing a drawdown of CO₂ and release of O₂, whereas at night, respiration will be the dominant biospheric process, resulting in the release of CO₂ and uptake of O₂.

Thus, in the summer, diurnal variability in atmospheric CO₂ and O₂ is caused by two reinforcing effects: diurnal variability in atmospheric mixing, and diurnal variability in biospheric O₂ and CO₂ fluxes. In contrast with the atmospheric O₂ and CO₂ data from UEA, the APO data show very little variability, and in general, do not exhibit a strong diurnal pattern. This is because APO is invariant to land biospheric influences, and largely reflects only fossil fuel influences on short-time scales, and ocean influences on seasonal and long-term time scales.

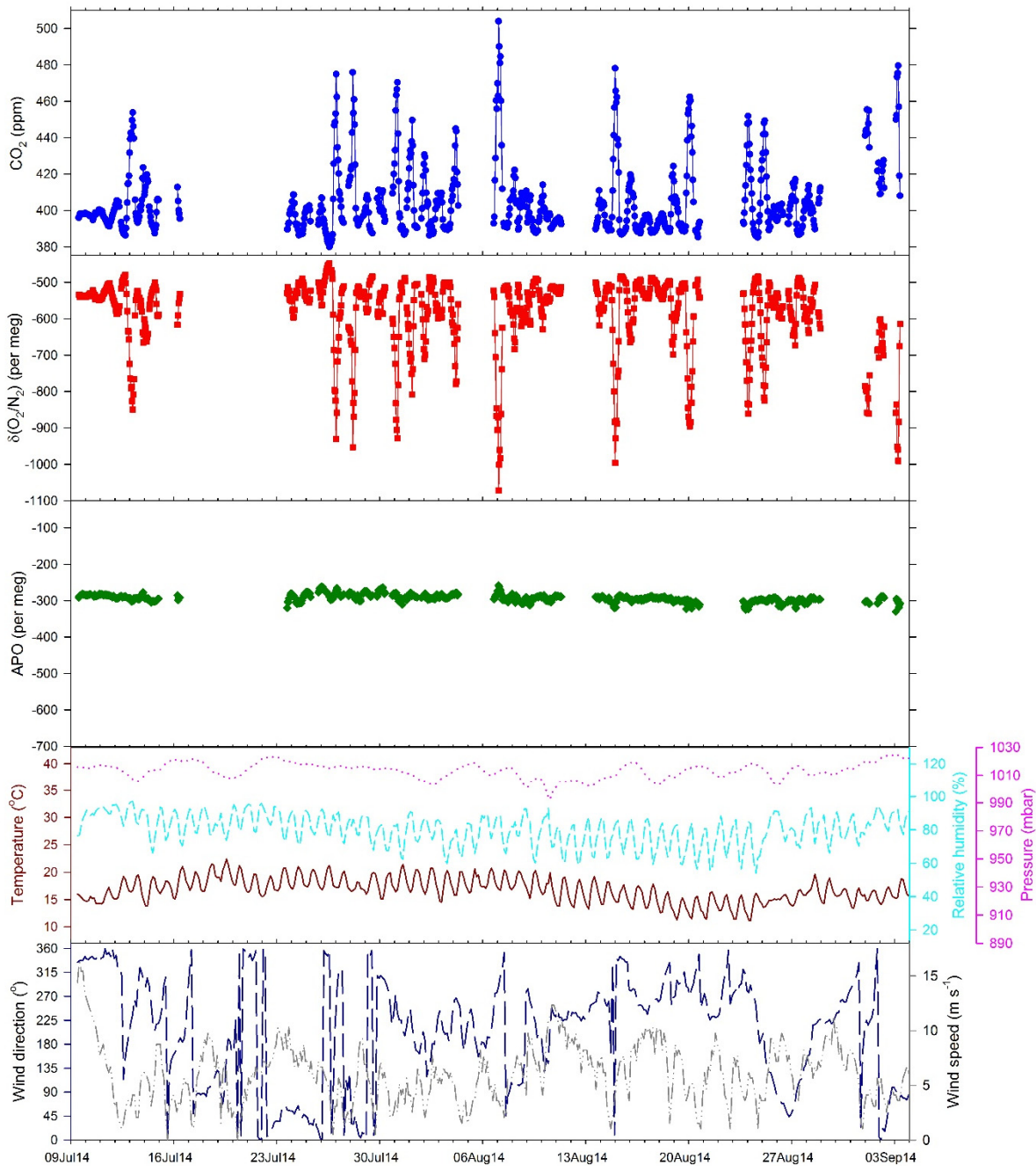


Figure 5.2. Hourly-averaged atmospheric CO_2 (top panel), $\delta(\text{O}_2/\text{N}_2)$ (2nd panel) and APO (3rd panel) measured from the roof of the Environmental Sciences building at UEA. Note that the y-axes for $\delta(\text{O}_2/\text{N}_2)$ and APO have been scaled to be visually comparable to the CO_2 y-axis on a mole per mole basis, and ‘bad’ data caused by technical problems have been excluded prior to averaging. Also shown are 3-hourly model-derived GDAS meteorological data (NOAA): atmospheric temperature (4th panel: dark red solid line), relative humidity (4th panel: cyan short-dashed line), atmospheric pressure (4th panel: pink dotted line), wind direction (bottom panel: dark navy long-dashed line), and wind speed (bottom panel: grey dashed/dotted line).

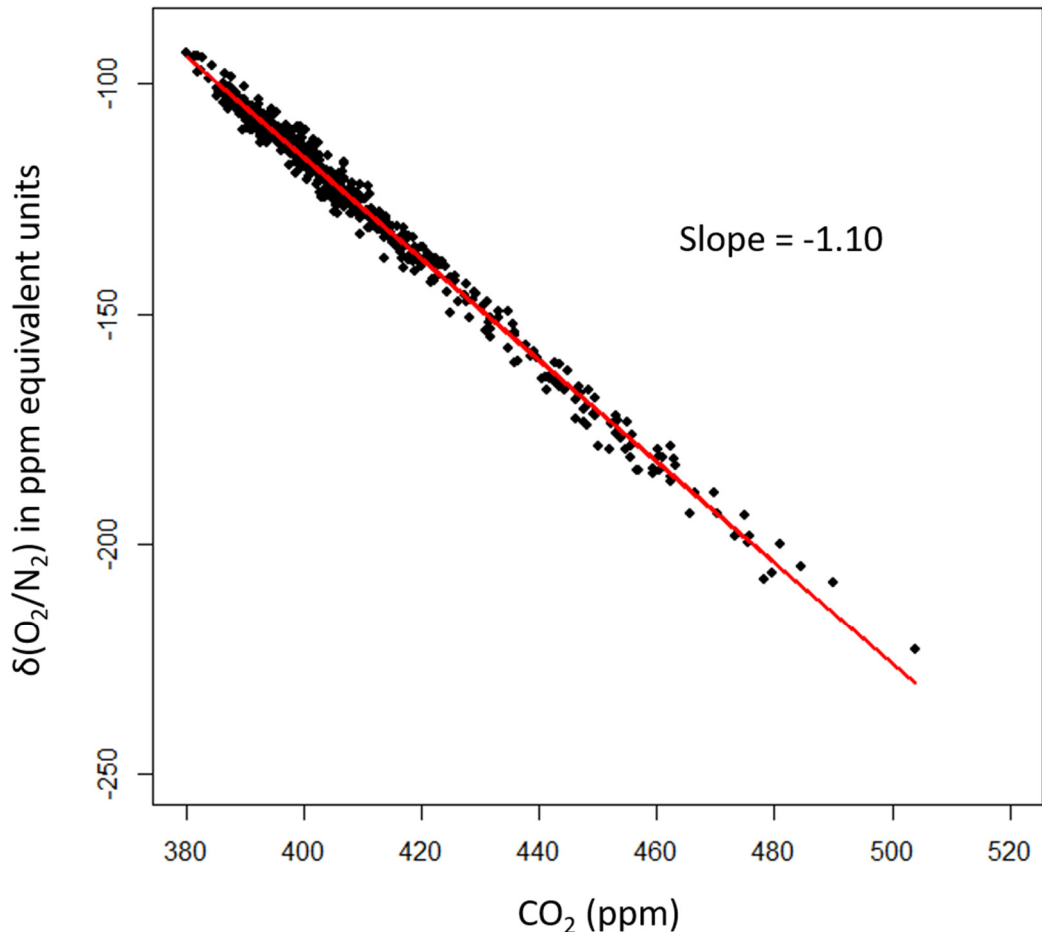


Figure 5.3. O₂:CO₂ ratio of hourly-averaged data measured at UEA during the summer of 2014. $\delta(\text{O}_2/\text{N}_2)$ is given in ppm equivalent units to be comparable to CO₂ on a mole per mole basis. The solid red line indicates the major axis regression line, which is weighted according to the difference in measurement precision (and therefore uncertainty) associated with the $\delta(\text{O}_2/\text{N}_2)$ and CO₂ data, and has a slope of -1.10. The negative value of the O₂:CO₂ ratio indicates that the two species are anti-correlated.

As mentioned above, the UEA CO₂ and O₂ variability shown in Fig. 5.2 is dominated by terrestrial processes, rather than fossil fuel burning. This is also demonstrated in Figure 5.3, which shows that the mean O₂:CO₂ molar ratio for the dataset is -1.10; a value that is indicative of terrestrial biosphere O₂ and CO₂ exchange (Severinghaus, 1995). There is a small amount of scatter around the major axis regression line shown in Fig. 5.3, which suggests that there is some temporal variability in the O₂:CO₂ ratio during this period.

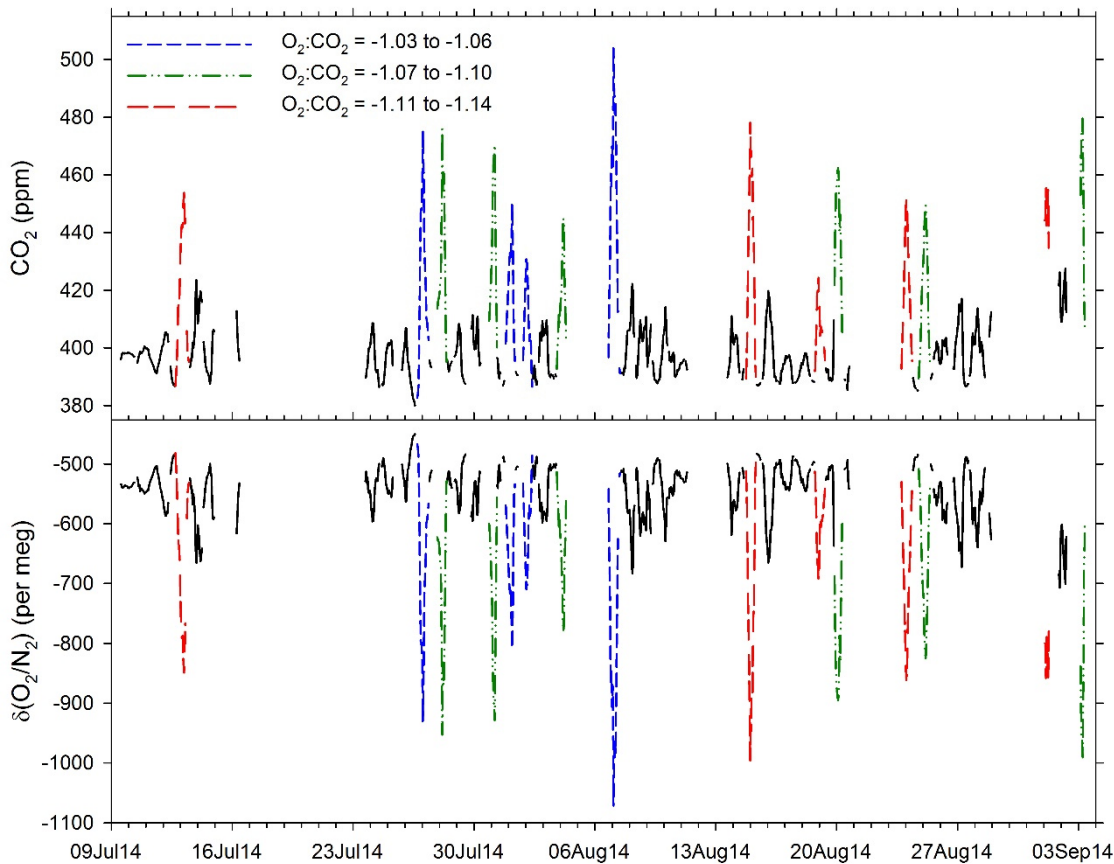


Figure 5.4. Hourly-averaged CO_2 (top panel) and $\delta(\text{O}_2/\text{N}_2)$ (bottom panel) with selected diurnal events coloured according to the $\text{O}_2:\text{CO}_2$ ratio (see legend in figure). The y-axes have been scaled so that the $\delta(\text{O}_2/\text{N}_2)$ and CO_2 panels are visually comparable on a mole per mole basis.

In order to investigate this $\text{O}_2:\text{CO}_2$ temporal variability, I calculated the $\text{O}_2:\text{CO}_2$ ratio for some of the largest (in magnitude) individual diurnal O_2 and CO_2 events, and then categorised these events into three groups, according to the $\text{O}_2:\text{CO}_2$ ratio values. Figure 5.4 shows that there is no correlation between the magnitude and the $\text{O}_2:\text{CO}_2$ ratio of the diurnal events, which indicates that the largest events are not caused by a common source, and suggests that atmospheric transport effects may have a significant impact on the magnitude of the diurnal variability at UEA. The range of $\text{O}_2:\text{CO}_2$ ratios for the diurnal events is -1.03 to -1.14, which suggests that many of the events with more negative $\text{O}_2:\text{CO}_2$ ratios are caused by a combination of biospheric and fossil fuel CO_2 . Since the terrestrial biosphere is dominating the O_2 and CO_2 variability so strongly, it is difficult to identify which events are likely to be influenced by fossil fuel processes, and which are not. This difficulty is in part caused by uncertainty in the $\text{O}_2:\text{CO}_2$ ratio of the local terrestrial biosphere. Although on a global scale, terrestrial processes have an oxidative ratio of approximately -1.1, on a local scale, this value can be either lower or higher, depending on the local types of vegetation and soil. The data shown in Fig. 5.4 seem to indicate that in Norfolk, the $\text{O}_2:\text{CO}_2$ ratio of the local terrestrial

biosphere may be slightly higher (less negative) than -1.1, although an exact value cannot be determined from the atmospheric O₂ and CO₂ data alone without also having independent quantitative knowledge of the impact of fossil fuel combustion on the atmospheric CO₂ data, or conducting an elemental analysis of the O₂:CO₂ ratio of various soils and vegetation representative of the Norfolk region.

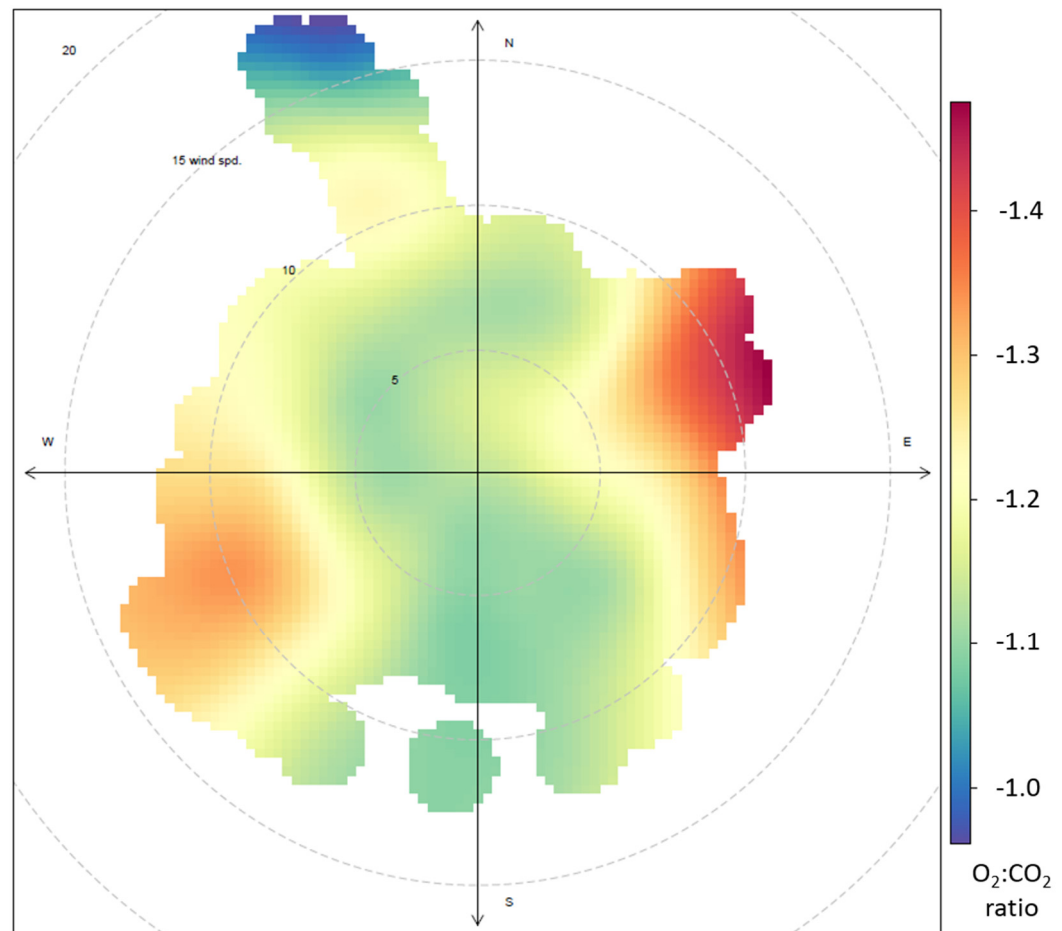


Figure 5.5. A polar plot of the variability in 2-minute O₂:CO₂ ratios with wind speed (m s⁻¹) and wind direction. Meteorological data are from the NOAA GDAS product. The polar plot was created in R using the ‘polarPlot’ function from the ‘Openair’ package (Carslaw and Ropkins, 2012).

By using the high-resolution, 2-minute O₂ and CO₂ data to calculate 2-minute O₂:CO₂ ratios, it is possible to create a polar plot, as shown in Figure 5.5, to examine the origin of oxidative ratios that are indicative of fossil fuel influences, and those that are indicative of biospheric influences. The lowest (most negative) O₂:CO₂ ratios (i.e. those that are indicative of fossil fuel combustion) originate from the east, which indicates that there is a strong fossil fuel influence from Norwich. There is also a noticeable fossil fuel oxidative ratio signal from the south-west, which is suggestive of fossil fuel influences from London, and possibly also from the nearby A47 and A11 major roads to the south-west. The UEA campus is over 1.2 km² in area, and is characterised by woodland, marshland, and open green areas. The campus is

surrounded by fields and farmland, with a few small villages to the north, south and west, and the suburbs of Norwich city to the east. The abundance of vegetation on the UEA campus and in the surrounding area likely explains why the $O_2:CO_2$ ratios are close to the expected value for terrestrial biosphere processes when the wind speed is low ($< 5 \text{ m s}^{-1}$), with the exception of winds that originate from the north-east, for which the $O_2:CO_2$ ratios are more negative. There is also a small amount of data that displays quite high (less negative) $O_2:CO_2$ ratios, which occurs when the wind speed is high ($> 15 \text{ m s}^{-1}$) and the wind direction is from the north-west. This data may be representative of oceanic influence, which can cause $O_2:CO_2$ ratios to be close to or less negative than -1.0, long-range transport of air from a higher latitude, or an undiagnosed technical problem with the measurement system.

It is useful to compare the atmospheric O_2 and CO_2 data from UEA to other nearby atmospheric measurements of each species, in order to gain greater understanding of the spatial variability of atmospheric O_2 and CO_2 . The Tacolneston tall tower (TAC) is situated about 12 km south-west of UEA (see Fig. 5.1), and is funded by the UK Government Department of Energy and Climate Change (DECC) to measure a range of atmospheric species, including CO_2 (from three heights: 54 m, 100 m, and 185 m) and CO (from a single height: 100 m). Weybourne Atmospheric Observatory (WAO) is situated about 35 km north of UEA on the north Norfolk coast (see Fig. 5.1). WAO is managed by the University of East Anglia and is also supported by NCAS (National Centre for Atmospheric Science), to make measurements of atmospheric greenhouse gases and related species, including atmospheric O_2 , CO_2 , and CO (all from $\sim 15 \text{ m}$ height).

Figure 5.6 compares atmospheric CO_2 at UEA and TAC, and atmospheric CO_2 and O_2 at UEA and WAO. In general, the three measurement locations exhibit very similar diurnal variability in CO_2 (and O_2 for UEA and WAO), with only a few rare exceptions, such as the differences in O_2 and CO_2 between WAO and UEA on 26-27 August. Although the diurnal pattern in the atmospheric CO_2 and O_2 is very similar between the measurement sites, the magnitude of the variability differs significantly. CO_2 measured at UEA is almost always higher at night-time than CO_2 measured at TAC and WAO. Similarly, night-time O_2 at UEA is almost always lower than O_2 measured at WAO. The most likely reason for these differences in magnitude between UEA and TAC is that the measurement height at UEA ($\sim 25 \text{ m}$) is much lower than all three of the measurement heights at TAC (lowest height of 54 m). CO_2 measurements that are made closer to the ground are usually higher in CO_2 mole fraction than those that are measured further up in the atmosphere, partly because CO_2 sources are mainly at ground level, and partly because the entrainment of 'background air' (lower CO_2 mole fractions) from above the boundary layer will affect CO_2 measurements made higher up more

than those made close to the ground. Thus, CO₂ measurements made from ~25 m height above the ground will largely reflect local influences on CO₂, whereas CO₂ measurements made at 185 m above the ground will reflect CO₂ influences from an entire region, covering at least several hundred square kilometres.

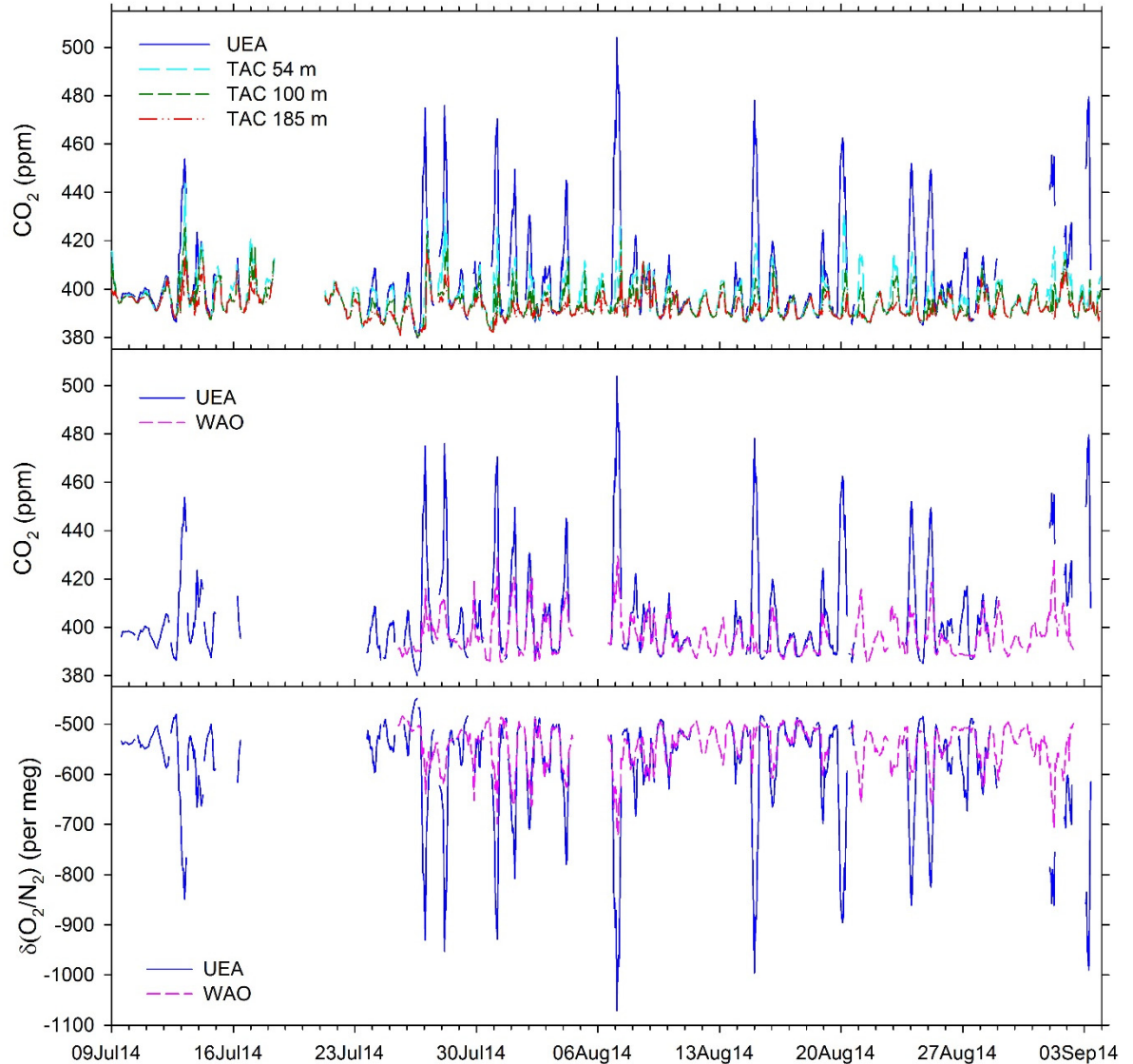


Figure 5.6. Comparison of atmospheric CO₂ at UEA and TAC (top panel), and comparison of atmospheric CO₂ and $\delta(\text{O}_2/\text{N}_2)$ at UEA and WAO (middle panel and bottom panel). Y-axes have been scaled so that the $\delta(\text{O}_2/\text{N}_2)$ and CO₂ panels are visually comparable on a mole per mole basis.

Somewhat contradictory to this explanation, is the fact that UEA consistently exhibits higher CO₂ than WAO at night, when the measurements at WAO are made ~10 m closer to the ground than those at UEA. The reason why O₂ and CO₂ variability at WAO is attenuated in magnitude compared to O₂ and CO₂ variability at UEA, is that WAO is situated on the coast, and so any terrestrial sources or sinks of O₂ and CO₂ will be diluted with coastal and open ocean air, which will usually exhibit O₂ and CO₂ mole fractions close to those of well-mixed 'background

air'. This also explains why, during the day-time, atmospheric CO₂ mole fractions are often lower at UEA than at WAO, and atmospheric O₂ mole fractions are often higher at UEA than WAO (e.g. 26 July), whereas the atmospheric CO₂ mole fraction at TAC does not ever drop significantly below the atmospheric CO₂ mole fraction at UEA. During the summer, the biospheric photosynthesis during the day time will take up CO₂ and produce O₂; this biospheric signal will manifest much more strongly at a rural, in-land measurement location, such as UEA, than at a coastal measurement site, such as WAO.

There are also some significant differences in the anthropogenic signals in atmospheric species between TAC, UEA and WAO. Figure 5.7 compares short-term variability in APO from UEA and CO from TAC (100 m height), as well as APO and CO from WAO. It is clear that there is often significant anti-correlation in the APO and CO short-term variability, which is likely attributable to the fact that both species are predominantly affected by anthropogenic sources. Although the UEA APO and TAC CO data are not co-located, it is assumed that they are situated close enough that the patterns of variability seen at each location will largely be similar. Hence, periods when the APO and CO data do not display anti-correlated signals may be due to the fact that the measurements are not co-located and are sampled from different heights above the ground, but also may be caused by the significant natural sources and sinks that exist for CO, such as soils and tropospheric photochemical reactions (Bergamaschi et al., 2000; Moxley and Cape, 1997), whereas the main natural influence on APO is from the oceans, which is not expected to have a significant effect on APO on short timescales (see Chapter 4, Section 4.2 for details).

The middle panel of Fig. 5.7 shows co-located APO and CO measured at WAO, from the same sampling height. As with the UEA and TAC data, there is substantial anti-correlation between the two species, as well as some periods where the variability is not anti-correlated. Based on visually inspection of Fig. 5.7 alone, there is a similar amount of anti-correlation between the WAO CO and APO data as there is between the UEA APO and TAC CO data, where the two species are not co-located. This finding suggests that periods of data that do not show anti-correlation between APO and CO may be dominated by differences in the CO and APO sources and sinks, and not by whether the measurements are co-located or not. The bottom panel of Fig. 5.7, showing wind direction measured at WAO, shows that the periods of strongest anti-correlation between WAO CO and APO mostly coincide with south-westerly wind directions (i.e. from the land), and periods showing little or no anti-correlation between CO and APO often coincide with northerly and easterly wind directions (i.e. from the sea), although the link between CO and APO correlation/anti-correlation and wind direction at WAO does not always hold true.

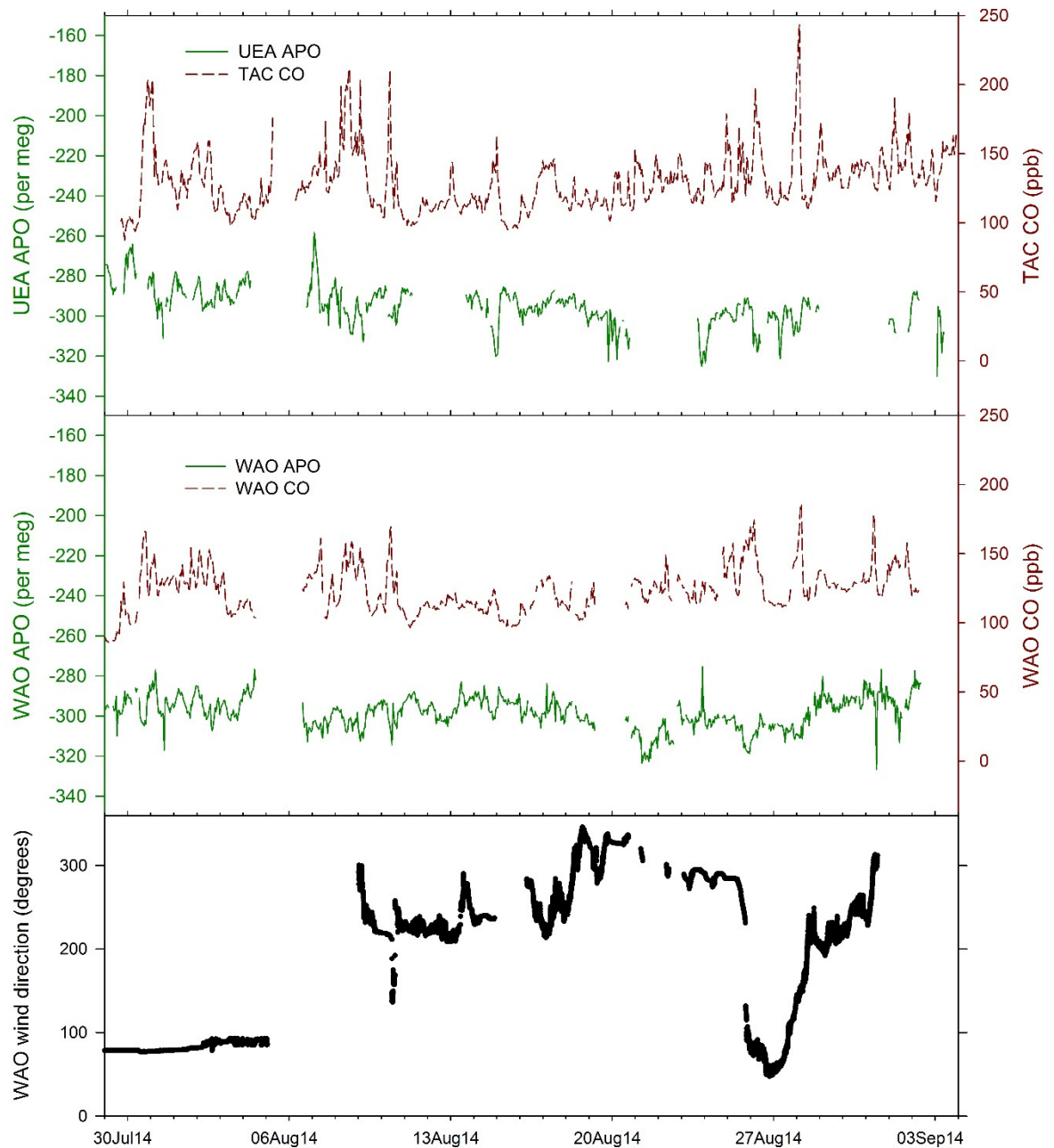


Figure 5.7. Comparison of hourly-averaged TAC CO and UEA APO data (top panel) and hourly-averaged WAO CO and APO data (middle panel), illustrating that a lot of the short-term variability in CO and APO is anti-correlated. Also shown is wind direction measured at WAO (bottom panel). The CO measurements at TAC are sampled from the 100 m tower inlet. It should be noted that the TAC CO data shown above are not the finalised, quality controlled data, due to an on-going calibration issue that is affecting the accuracy of the high CO values.

5.3 Fossil fuel CO₂ quantification using APO from sites in Norfolk, UK

5.3.1. Using 'fixed' fossil fuel emission ratios

In this section, I present a new methodology for quantifying ffCO₂ using APO data from UEA and WAO. As mentioned previously, there are several limitations associated with using CO as a tracer for quantifying ffCO₂, including large uncertainty in the natural sources and sinks,

large uncertainty in the CO:CO₂ emission ratios for fossil fuels, and the CO tracer method is unable to distinguish between CO₂ produced by renewable bioenergy sources and ffCO₂. In contrast, the only significant natural source/sink affecting APO is the ocean, which is not expected to have an impact on short timescales. In addition, any short-term oceanic influences on APO should be easy to identify, because oceanic air masses are characterised by invariant CO₂ (owing to the long-equilibration time of air-sea CO₂ fluxes compared to the rate of atmospheric mixing). APO is also associated with a much smaller range of possible O₂:CO₂ emission ratios for fossil fuels (from ~-1.2 to ~-1.95, but typically in the range of -1.3 to -1.4) compared to CO:CO₂ emission ratios (from <5 to >100, but typically in the range of 5 to 25), which translates into lower uncertainty in the denominator of Equation 5.4 (see below) compared to the denominator of Eq. 5.2.

Finally, although APO cannot distinguish between biodiesel and biogas emissions and their fossil fuel counterparts, owing to the fact that the oxidative ratios for biodiesel and biogas are very similar to those for liquid and gaseous fossil fuels, APO is able to distinguish between biomass burning emissions, which have an oxidative ratio of approximately -1.1, and fossil fuel emissions, which have oxidative ratios in the range of ~-1.2 to ~-1.95. This potentially enables APO to be used as a tracer of ffCO₂ in cities in developing countries, such as India, which still heavily rely on biomass burning as a major source of energy in domestic settings, and also in cities in developed countries that are frequently affected by local forest fires, such as in Victoria, Australia, and California, USA.

ffCO₂ can be calculated from APO data using Equation 5.4, which is analogous to Eq. 5.2 for calculating ffCO₂ from CO:

$$ffCO_2 = \frac{APO - APO_{bg}}{R_{APO:CO_2}} \quad (\text{Eq. 5.4})$$

where *APO* is the atmospheric value calculated from high-precision atmospheric O₂ and CO₂ data, *APO_{bg}* is the APO background, or baseline value, which is determined using a statistical baseline fitting method, and *R_{APO:CO₂}* is the APO:CO₂ combustion ratio for fossil fuel emissions.

I have used Eq. 5.4 to calculate ffCO₂ from APO data at UEA and WAO, and have compared the results to ffCO₂ from CO data at TAC and WAO, calculated using Eq. 5.2 (see Figure 5.8). Note that a small amount of APO data was excluded from the ffCO₂ calculation as it was not deemed to be related to fossil fuel variability (owing to little or no variability in CO₂), and is most likely caused by technical problems. There are two important unknown

parameters that must be determined in Eq. 5.2 and 5.4: the CO and APO baselines, and the CO:CO₂ and APO:CO₂ emission ratios. For now, I have used time-invariant values of 5 ppb ppm⁻¹ for the CO:CO₂ emission ratio at TAC and WAO (a typical value for traffic emissions), and -0.3 mol mol⁻¹ for the APO:CO₂ emission ratio at UEA and WAO (a typical value for liquid fossil fuel emissions, given that APO:CO₂ ratio = O₂:CO₂ ratio + 1.1). A more sophisticated method for calculating time-varying CO:CO₂ and APO:CO₂ emission ratios will be discussed and presented later in this section. It should be noted that the equation for calculating APO from O₂ and CO₂ measurements that I have used throughout this thesis is actually a simplification of the full APO equation given in (Stephens et al., 1998), which also takes into account the effects of CH₄ and CO oxidation on O₂, although these effects are negligible for most applications. I have not used the full APO equation in this chapter because CH₄ and CO emissions in Norfolk are relatively low, and I calculated that they would not significantly affect APO. For urban APO measurements, however, it may be advisable to use the full APO equation that is conservative with respect to CH₄ and CO oxidation in addition to terrestrial biosphere processes, because CH₄ and CO fluxes are much larger in urban environments.

Fig. 5.8 shows ffCO₂ calculated using CO and ¹⁴CO₂ from TAC and APO from UEA (top panel), as well as ffCO₂ calculated using CO and APO from WAO (bottom panel). Although the CO and APO data at TAC and UEA are not co-located, the ffCO₂ calculated using the two tracers appears very similar, with the main differences presenting as differences in the magnitude of the ffCO₂ peaks (e.g. 14-15 Aug), rather than differences in the patterns of ffCO₂ variability (e.g. 3 Aug). The ffCO₂ from ¹⁴CO₂ data at TAC were provided by Angelina Wenger, University of Bristol. Approximately 40% of the ffCO₂ from ¹⁴CO₂ data at TAC collected from Jul-Sep 2014 were deemed to be unreliable, either owing to negative ffCO₂ values, which are caused by strong nuclear power plant emissions cancelling out any ffCO₂ signal in ¹⁴CO₂, or because NAME model back trajectories indicated the air masses arriving at TAC had originated from the south-west, and ffCO₂ from ¹⁴CO₂ was therefore likely to be biased by nuclear power plant influences, even though the values were not negative. In general, the ffCO₂ from ¹⁴CO₂ agrees well with the ffCO₂ calculated from the CO and APO data, although, owing to data gaps, there are only two ¹⁴CO₂ data points that coincide with periods of APO data. All of the ¹⁴CO₂ data points also happen to coincide with periods of relatively low ffCO₂, because the ¹⁴CO₂ flask

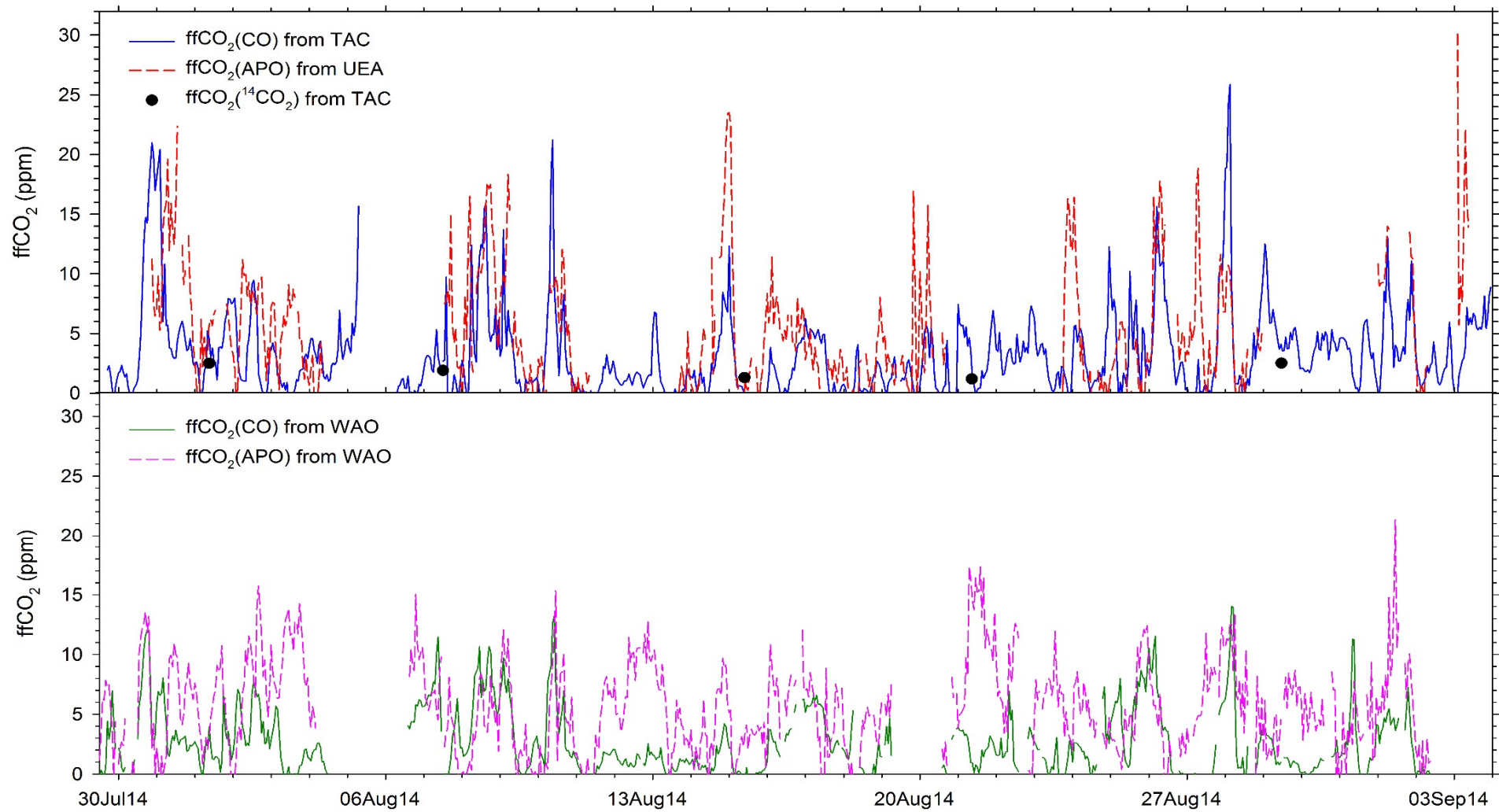


Figure 5.8. ffCO₂ from CO at TAC and APO at UEA (top panel) and ffCO₂ from CO and APO at WAO (bottom panel). Also shown is ffCO₂ from ¹⁴CO₂ at TAC (top panel, black dots).

samples are deliberately collected during ‘clean air’ conditions, to try and avoid nuclear power plant influences. When a difference in ffCO_2 between the $^{14}\text{CO}_2$ method and the other two methods does occur, and the ffCO_2 from $^{14}\text{CO}_2$ value is lower than the ffCO_2 from CO or APO (e.g. 29Aug), it is difficult to ascertain which ffCO_2 value is correct, because nuclear power plant influences will cause the ffCO_2 from $^{14}\text{CO}_2$ to be biased low, and it is therefore difficult to have confidence in the accuracy of the $^{14}\text{CO}_2$ data in such instances.

At WAO, the ffCO_2 agreement between the APO and CO tracers is similar to that at UEA and TAC, with periods when the ffCO_2 from the two tracers agree well (e.g. 7-11Aug), and other times when the ffCO_2 pattern of variability is very similar, but the magnitudes of the ffCO_2 signals differ (e.g. 31Jul-2Aug). Overall, the ffCO_2 observed at WAO is less than that observed at UEA and TAC, which is expected, given the dilution of terrestrial signals that occur at WAO, due to its coastal location, as well as the fact that WAO is located further from the main local ffCO_2 hotspots, such as Norwich, and the A11 and A47 main roads.

The CO and APO baselines have been calculated using the ‘ rfbaseline ’ function from the ‘IDPmisc’ package in R. ‘ rfbaseline ’ is a statistical method for calculating a baseline from atmospheric data based on robust local regression, and employs asymmetrical weighting to the residuals of the fit, in order to prevent the baseline from being biased by uni-directional pollution events, which is a common characteristic of many atmospheric species (Ruckstuhl et al., 2012). This asymmetrical weighting is important in the baseline fitting of both APO and CO, because all of the fossil fuel related variability in APO presents as negative excursions (because O_2 is consumed during fossil fuel combustion), while the fossil fuel related variability in CO presents as positive excursions (because CO is produced during fossil fuel combustion), as illustrated in Fig. 5.7.

5.3.2. Baseline and measurement uncertainty analysis

In order to determine the uncertainty of the ffCO_2 calculated using APO or CO, one must determine the uncertainty associated with the three components of Eqs. 5.2 and 5.4: the APO or CO measurement uncertainty, the uncertainty associated with the baseline fitting, and the uncertainty associated with the fossil fuel emission ratios ($R_{\text{CO:CO}_2}$ or $R_{\text{APO:CO}_2}$). The baseline uncertainty can be quantified by assessing the variability in the ffCO_2 when different baselines are used. In Fig. 5.8, I used APO and CO baselines of moderate flexibility to calculate ffCO_2 . In Figure 5.9, I present ffCO_2 for both APO and CO at UEA and TAC using the baselines employed for Fig. 5.8, as well as very flexible baselines, where a lot more of the short-term variability in

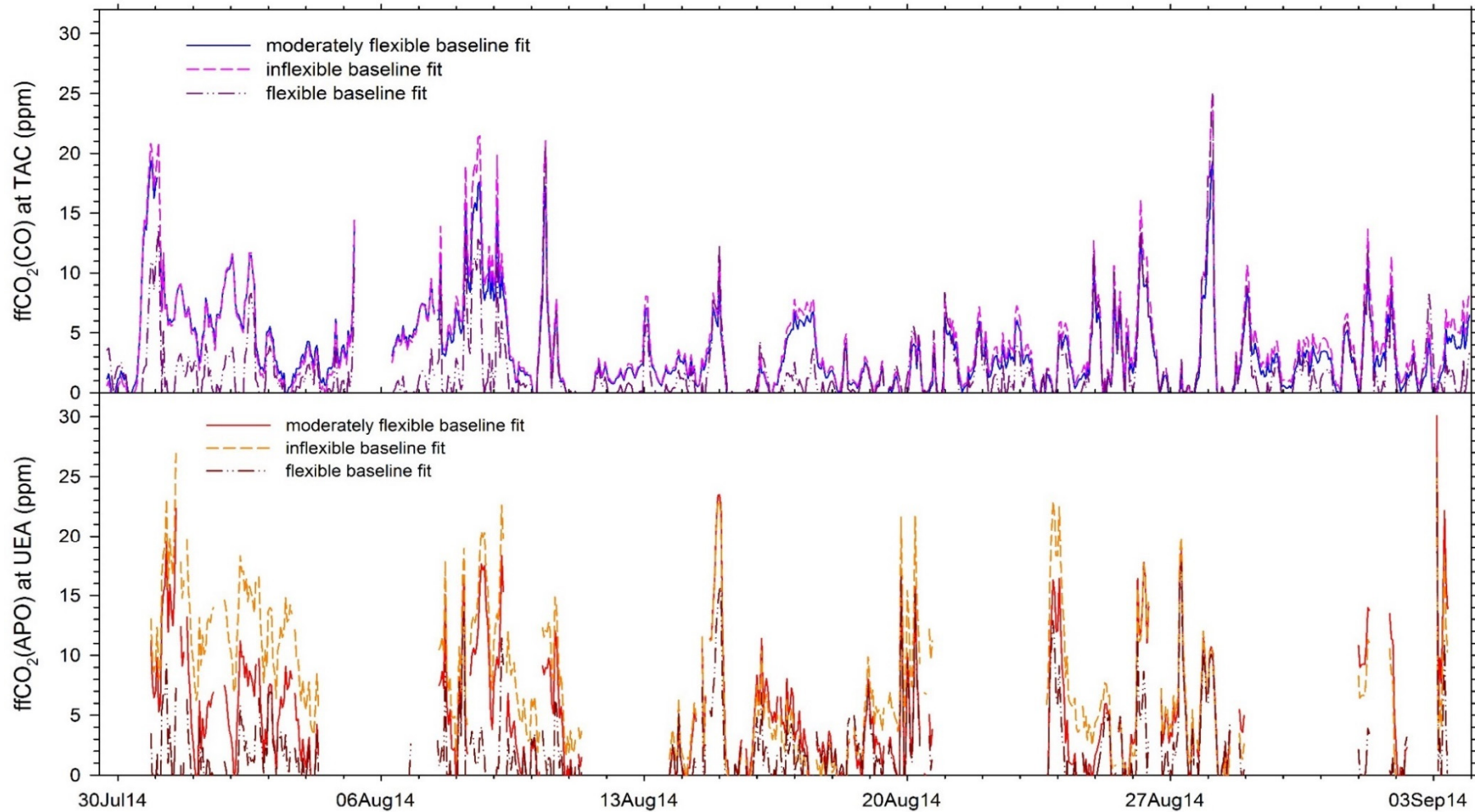


Figure 5.9. $ffCO_2$ calculated from Co at TAC (top panel) and APO at UEA (bottom panel) using the moderately flexible baseline fits used in Fig. 5.8, as well as inflexible baseline fits (dashed pink and orange lines) and flexible baseline fits (dotted-dashed dark purple and dark red lines).

APO and CO is assigned as 'background air' variability, and also very inflexible baselines, which hardly vary at all, thus almost all of the short-term variability in APO and CO is excluded from the baseline.

Fig. 5.9 demonstrates that at times, there is significant uncertainty associated with the statistical baseline fitting procedure for the CO and APO methods, as the magnitude of ffCO_2 is often dependent on the choice of baseline fit. It should be noted that the variability in ffCO_2 is not dependent on the choice of baseline fit. Figure 5.10 demonstrates the differences in the baseline fits used to calculate the ffCO_2 from CO and APO that is shown in Fig. 5.9. Since the numerator terms in Eqs. 5.2 and 5.4 are determined from the difference between the measurements and the baseline for each species, the flexible baseline fits tend to produce smaller ffCO_2 values, and the inflexible baseline fits tend to produce larger ffCO_2 values, with the moderately flexible baseline fits producing intermediate ffCO_2 values.

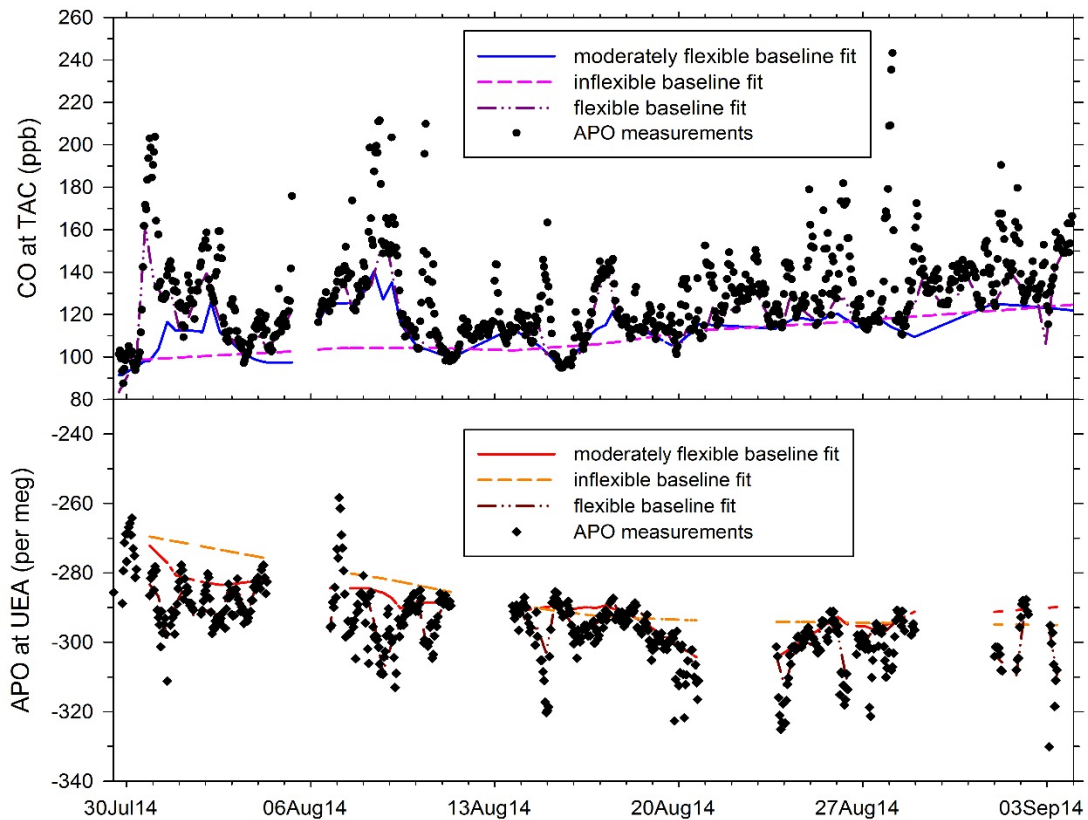


Figure 5.10. Moderately flexible, inflexible, and flexible baseline fits to CO from TAC (top panel) and APO from UEA (bottom panel).

The mean uncertainty in ffCO_2 associated with the choice of baseline fit is calculated to be $\pm 17.5\%$ and $\pm 27.5\%$ for the CO data and APO data respectively (based on the ffCO_2 differences using different baseline flexibilities), with no significant differences in the baseline uncertainties at each measurement site. These uncertainty estimates are based on the fact that the flexible baseline fits are probably not fit for purpose, given that they generally cause ffCO_2

to be underestimated, and that the most appropriate baseline fit lies between the standard fit and the inflexible fit: thus, the flexible baseline fit has not been accounted for in the baseline uncertainty estimates. In reality, the inflexible fit is likely to be the most appropriate baseline fit, assuming that ffCO₂ 'events' may be present in atmospheric time series data for periods of several days up to about a week, rather than for periods of only several hours up to a day or so; hence, the uncertainty estimates stated above are conservative.

The uncertainty associated with the CO and APO data is quantified from the $\pm 1\sigma$ standard deviation of the hourly-averaged atmospheric measurements during a period when the atmospheric variability in each species is low, and thus includes both the uncertainty of the measurement technique, and the uncertainty associated with some natural atmospheric variability. For CO, the measurement uncertainty is ± 5.54 ppb at TAC and ± 1.58 ppb at WAO. The larger measurement uncertainty at TAC is primarily due to greater imprecision in the measurement technique employed at TAC compared to that used at WAO, but is also partly due to the slightly greater CO variability observed at TAC compared to WAO.

For APO, the measurement uncertainty is determined from the $\pm 1\sigma$ standard deviation in both the hourly CO₂ and O₂ measurements, since $APO = O_2 + (-1.1 \times CO_2)$, where -1.1 is the oxidative ratio of the global terrestrial biosphere. Since the oxidative ratio of the terrestrial biosphere can vary regionally, an uncertainty of ± 0.05 is assigned, which is then summed in quadrature with the uncertainties of the O₂ and CO₂ measurements to obtain an overall uncertainty estimate for the APO data, which is ± 13.80 per meg at UEA and ± 12.35 per meg at WAO. The O₂ and CO₂ measurement uncertainties at UEA are actually smaller than those at WAO; however, the APO uncertainty at UEA is larger than that at WAO owing to the larger APO variability observed at UEA compared to WAO. As percentages, the measurement uncertainties are $\pm 4.29\%$ for CO at TAC and $\pm 1.28\%$ for CO at WAO, and $\pm 4.63\%$ for APO at UEA and $\pm 4.14\%$ for APO at WAO; thus, all of the measurement uncertainties are significantly smaller than the uncertainties associated with the choice of CO and APO baseline fits.

5.3.3. Using 'time-varying' fossil fuel emission ratios

In Fig. 5.8, I presented ffCO₂ from CO and APO data using fixed values for the fossil fuel emission ratios. In reality, the fossil fuel emission ratios observed at a measurement site can vary significantly, owing to changes in the emission ratios themselves prior to transportation to the measurement site, as well as changes in the atmospheric footprint of the measurement site. Hence, a much more appropriate way to calculate ffCO₂ from CO and APO data is to use time-varying fossil fuel emission ratios, which can be determined by combining fossil fuel

emission ratios from gridded databases with atmospheric transport model footprints, as shown in Equation 5.5:

$$R_t = \sum_{b_1 t_1}^{b_n t_n} E \times \frac{P}{T_P} \quad (\text{Eq. 5.5})$$

where R_t is the time-varying fossil fuel emission ratio at the measurement site from times t_1 to t_n , b_1 to b_n represent the individual grid boxes of the atmospheric transport model footprint, E is the fossil fuel emission ratio for each grid box of the atmospheric transport model, P is the number of atmospheric transport model particles in the grid box, and T_P is the total number of particles in the whole atmospheric footprint.

In order to calculate R_t in Eq. 5.5, I used the UK Met Office NAME (Numerical Atmospheric-dispersion Modelling Environment) model (Jones et al., 2007) to produce 2-day, backwards run atmospheric footprints every 3 hours, consisting of 10,000 inert particles, that were monitored from 0-200 m above the ground. The NAME runs were driven by the Met Office Unified Model meteorology, which has a spatial resolution of 17 km by 17 km. For E , the fossil fuel emission ratios, I used gridded O₂:CO₂ ratios from the COFFEE (CO₂ release and Oxygen uptake from Fossil Fuel Emissions Estimate) database (Steinbach et al., 2011) for the APO method, which were converted to APO:CO₂ ratios by subtracting the O₂:CO₂ ratio of global terrestrial biosphere-atmosphere exchange (-1.1) from all the values, and gridded CO:CO₂ ratios from the EDGAR (Emissions Database for Global Atmospheric Research) database for the CO method.

The EDGAR CO:CO₂ ratios are only available with annual time resolution (and are also only available up to 2010, not 2014), and therefore the time-varying CO:CO₂ ratios calculated at TAC and WAO only include variability from the changing NAME footprints (i.e. spatial variability). The COFFEE-derived APO:CO₂ ratios are available on hourly time resolution, and were converted into 3-hourly averages in order to match the time interval of the NAME footprints. Originally, the COFFEE database was only available up to 2010, however, COFFEE has recently been updated to 2014 by Christoph Gerbig (Max Planck Institute of Biogeochemistry, Jena, Germany), and now includes an updated set of O₂:CO₂ ratios for different fuel types (including better differentiation of light oil versus heavy oil ratios, and different ratios for different types of bioenergy), which I calculated. Both the time-varying CO:CO₂ and APO:CO₂ emission ratios were calculated on 3-hourly time intervals to be compatible with the NAME footprints, which were then interpolated to hourly time resolution to be compatible with the hourly-averaged APO and CO atmospheric data.

The uncertainty of the time-varying emission ratios is difficult to calculate, since neither the EDGAR or COFFEE databases assign uncertainties to the fossil fuel emissions estimates. Therefore, a proxy for the uncertainty of the time-varying emission ratios was determined by dividing R_t by the $\pm 1\sigma$ standard deviation of all of the emission ratios in the footprint. The mean uncertainties of the time-varying CO:CO₂ emission ratios at TAC and WAO are $\pm 78.3\%$ and $\pm 72.9\%$, respectively, and the mean uncertainties of the time-varying APO:CO₂ emission ratios at UEA and WAO are both $\pm 21.8\%$. The large difference between the CO and APO fossil fuel emission ratio uncertainties reflects the much larger spatial variability in the CO:CO₂ ratio values (since there is no temporal variability available in the EDGAR gridded databases), compared to both the spatial and temporal variability of the APO:CO₂ ratio values from the COFFEE database.

5.3.4. Comparison of CO and APO fossil fuel quantification methods

The total ffCO₂ uncertainty for both the CO and APO methods can be calculated by summing in quadrature the measurement, baseline, and emission ratio uncertainties. This produces mean total ffCO₂(CO) uncertainties of $\pm 87.5\%$ at TAC and $\pm 78.4\%$ at WAO, and mean ffCO₂(APO) uncertainties of $\pm 35.8\%$ at UEA and $\pm 35.6\%$ at WAO. At both locations, the mean ffCO₂(CO) uncertainty is much larger than the mean ffCO₂(APO) uncertainty (by more than a factor of 2). This is predominantly due to the much larger uncertainty in the CO:CO₂ emission ratios compared to the APO:CO₂ emission ratios. The ffCO₂ uncertainties at WAO are lower than those at TAC and UEA for both the CO and APO methods, owing to the smaller ffCO₂ signals that are observed at WAO in both species. Table 5.1 summarises the differences in uncertainty between ffCO₂(CO) and ffCO₂(APO) at each measurement site.

Table 5.1. Component and total uncertainties for the CO and APO ffCO₂ quantification methods at TAC, WAO and UEA, given to 2 significant figures for easier comparison.

	ffCO ₂ (CO)		ffCO ₂ (APO)	
	TAC	WAO	UEA	WAO
Baseline uncertainty	$\pm 18\%$	$\pm 18\%$	$\pm 28\%$	$\pm 28\%$
Measurement uncertainty	$\pm 4.3\%$	$\pm 1.3\%$	$\pm 4.6\%$	$\pm 4.1\%$
Emission ratio uncertainty	$\pm 78\%$	$\pm 73\%$	$\pm 22\%$	$\pm 22\%$
Total uncertainty	$\pm 88\%$	$\pm 78\%$	$\pm 36\%$	$\pm 36\%$

As shown in Table 5.1, for the CO method, the total ffCO_2 uncertainty at both locations is dominated by the CO:CO₂ emission ratio uncertainty, with the CO baseline uncertainty contributing far less, and the CO measurement uncertainty contributing the least. In contrast, the APO method total ffCO_2 uncertainty is most strongly influenced by the APO baseline uncertainty, closely followed by the APO:CO₂ emission ratio uncertainty, with the APO measurement uncertainty contributing the least. It is clear that the CO method is far less precise than the APO method, owing to the large uncertainty associated with the CO:CO₂ emission ratios. It should be noted that the total $\text{ffCO}_2(\text{CO})$ uncertainties do not include the uncertainty associated with potential natural CO sources and sinks, which would be very difficult to quantify. Additionally, neither the total $\text{ffCO}_2(\text{CO})$ nor the total $\text{ffCO}_2(\text{APO})$ uncertainties include the uncertainty associated with potential bioenergy influences, which would also be difficult to quantify, and will have a greater influence on the CO method than the APO method, because the APO method is conservative with respect to solid bioenergy and biomass burning.

$\text{ffCO}_2(\text{CO})$ from TAC and WAO and $\text{ffCO}_2(\text{APO})$ from UEA and WAO calculated using time-varying fossil fuel emission ratios (using Equation 5.4) are presented in Figure 5.11. In contrast to Fig. 5.8, the ffCO_2 data in Fig. 5.11 have been calculated using inflexible baselines, rather than moderately flexible baselines, as the latter can lead to underestimation of the ffCO_2 variability, particularly for ffCO_2 events lasting several days, as shown in Fig. 5.10 and described previously. The ffCO_2 uncertainties are represented by the shaded regions, and were calculated by summing the measurement, baseline and emission ratio uncertainties in quadrature. Also shown is the ffCO_2 calculated from discrete ¹⁴CO₂ measurements made at TAC. Overall, the ffCO_2 calculated from CO and APO appear to agree more closely in Fig. 5.11 than previously, in Fig. 5.8. There are still some periods where the two continuous methods do not agree within the uncertainties of each other, such as 31 July at WAO, for example. The ffCO_2 from ¹⁴CO₂ at TAC is normally also in agreement with the ffCO_2 from CO and APO, although as before, the $\text{ffCO}_2(^{14}\text{CO}_2)$ values tend to be lower than the $\text{ffCO}_2(\text{APO})$ and $\text{ffCO}_2(\text{CO})$ values. Fig. 5.11 illustrates the difference in uncertainty between the CO and APO methods that I have numerically presented in Table 5.1, and shows that the APO method is significantly more precise than the CO method. An analysis of the air mass history using NAME footprints reveals that most of the ffCO_2 during the summer 2014 period I have analysed is from the south of the UK and London, with some from the north of the UK, and very occasional ffCO_2 from France, the Netherlands and the North Sea (presumably from oil platforms). There is no apparent connection between the agreement of the CO and APO ffCO_2 quantification methods and the

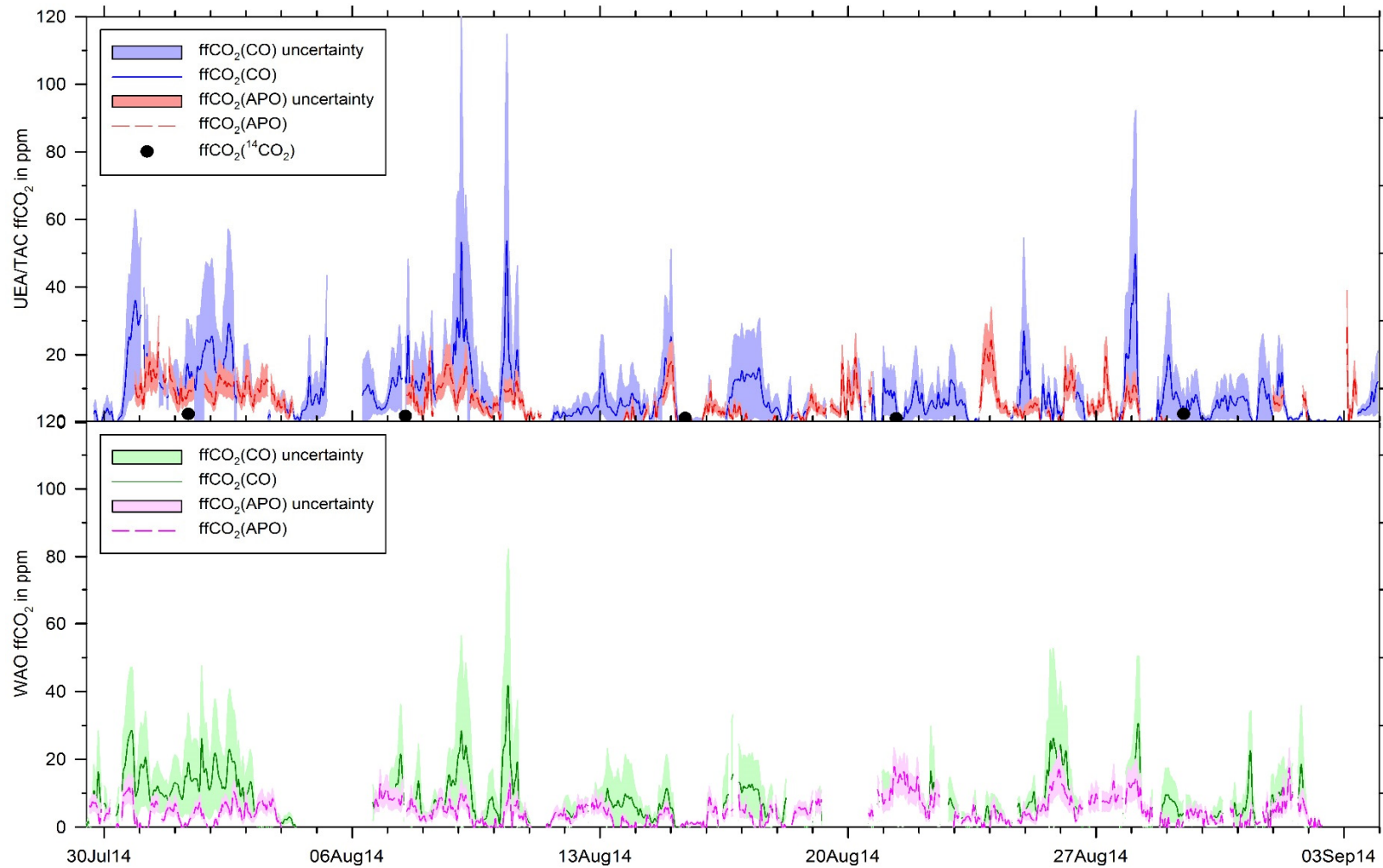


Figure 5.11. ffCO₂(CO) and ffCO₂(APO) at TAC and UEA, respectively (top panel), and ffCO₂(CO) and ffCO₂(APO) at WAO (bottom panel), calculated using time-varying emission ratios and inflexible baselines. Shaded areas denote the respective uncertainties of the calculated ffCO₂. ffCO₂ from ¹⁴CO₂ measurements at TAC are denoted by the black circles, of which the size represents the uncertainty of the ffCO₂(¹⁴CO₂) values.

origins of the NAME footprints. It is therefore likely that most of the disagreement between the two methods can be attributed to the fact that the TAC and UEA measurements are not co-located, as well as undiagnosed technical issues and differences in potential CO and APO influences that cannot easily be quantified, such as biomass burning (for CO).

In contrast to Fig. 5.7, where the anti-correlation in APO and CO was similar at WAO and at UEA and TAC, Fig. 5.11 indicates that ffCO_2 agreement is actually closer at WAO than at UEA and TAC. This is most likely due to the co-location of the CO and APO measurements at WAO, and adds confidence to both ffCO_2 quantification methods. Indeed, since ffCO_2 has been calculated using two entirely independent tracers, periods of strong agreement in ffCO_2 between the two methods are associated with extremely high confidence in the ffCO_2 accuracy (e.g. 21-28Aug2014 at WAO).

It is also clear from Fig. 5.11 that the CO method produces significantly higher ffCO_2 values than the APO method. This is largely due to the CO:CO₂ emission ratios from the EDGAR database, which are lower than expected, and cause the magnitude of the ffCO_2 from CO to be high. Table 5.2 shows typical ffCO_2 values from the literature, most of which also use the CO method, alongside the ffCO_2 range from the CO and APO methods shown above, and demonstrates that the ffCO_2 from CO at TAC and WAO is much higher than expected, when the values are compared to typical ffCO_2 observed in urban areas, such as Paris. In fact, it is not possible for some of the largest $\text{ffCO}_2(\text{CO})$ peaks at TAC and WAO to be accurate, since the ffCO_2 values are larger than the CO₂ enhancement above the baseline, shown in Fig. 5.6. This suggests that the EDGAR CO inventory data are incorrect (too low), since the COFFEE APO:CO₂ ratios are derived from EDGAR CO₂ data (see Steinbach et al., 2011 for details), and the $\text{ffCO}_2(\text{APO})$ values are within the expected range for a relatively rural area. It should also be noted that the TAC CO data are known to have an on-going calibration issue that is affecting the accuracy of the high CO values. It is possible that once corrected, the highest $\text{ffCO}_2(\text{CO})$ values at TAC may reduce by as much as 30% (Grant Forster, personal communication, 2016), although this correction will not affect the pattern of variability, nor the fact that the CO method still produces higher ffCO_2 values overall than the APO method, and unrealistically high values at WAO, where the CO data have been quality controlled and are deemed accurate.

Table 5.2. Typical ffCO₂ ranges from the literature, shown alongside the ffCO₂ ranges for TAC, UEA and WAO presented in this work, calculated using CO, APO and ¹⁴CO₂ atmospheric data.

Publication	Location	Species used	Typical ffCO ₂ range	ffCO ₂ uncertainty
van der Laan et al. (2010)	Lutjewad, The Netherlands	¹⁴ CO ₂ and CO	0 – 30 ppm	±2.5 ppm
Lopez et al. (2013)	Paris, France	¹⁴ CO ₂ , CO, NO _x and ¹³ CO ₂	0 – 40 ppm	Not given for most species. ±1.0 ppm for ¹⁴ CO ₂
Graven et al. (2009)	California, U.S.A.	¹⁴ CO ₂ and CO	0 – 10 ppm	±1.6 – 2.9 ppm
Turnbull et al. (2006)	New England and Colorado, U.S.A.	¹⁴ CO ₂ , CO and SF ₆	0 – 15 ppm	±2 – 4 ppm
This work	Norfolk, U.K.	CO (TAC)	0 – 70 ppm	±5.8 ppm
		CO (WAO)	0 – 40 ppm	±4.5 ppm
		APO (UEA)	0 – 20 ppm	±1.2 ppm
		APO (WAO)	0 – 15 ppm	±1.1 ppm
		¹⁴ CO ₂ (TAC)	1.2 – 2.5 ppm	±1.6 ppm

Fig. 5.11 suggests that using inventory data combined with an atmospheric transport model to estimate the emission ratios may lead to inaccurate ffCO₂, mainly due to inaccuracies with the inventory data, but also due to potential atmospheric transport model inaccuracies. Therefore, it is important to consider other methods of determining the fossil fuel emission ratios for the CO and APO methods. Figure 5.12 shows ffCO₂ from UEA and TAC calculated using the time-varying emission ratios (as shown Fig. 5.11, with uncertainties omitted for visual clarity), as well as ffCO₂ using the previous fixed emission ratios of 0.3 mol mol⁻¹ for APO:CO₂ and 5 ppb ppm⁻¹ for CO:CO₂ (very similar to ffCO₂ shown in Fig. 5.8, only using an inflexible baseline). Also shown is ffCO₂ calculated using emission ratios that have been ‘calibrated’ by the TAC ¹⁴CO₂ data, and for the APO method only, ffCO₂ calculated using the mean APO:CO₂ ratio of the atmospheric measurements at UEA during the summer 2014 period. ffCO₂(CO) was calculated using the mean CO:CO₂ ratio of the atmospheric measurements as well, but the values produced were extremely high (up to 350 ppm) and not realistic; hence, these data are not shown in Fig. 5.12. The reason why the mean measured CO:CO₂ ratio is too low, causing ffCO₂ to be biased too high, is due to large non-fossil fuel related

CO₂ signals from the terrestrial biosphere coinciding with fossil fuel related CO signals. In contrast, the mean APO:CO₂ ratio during this period is not so severely affected by the activity of the terrestrial biosphere.

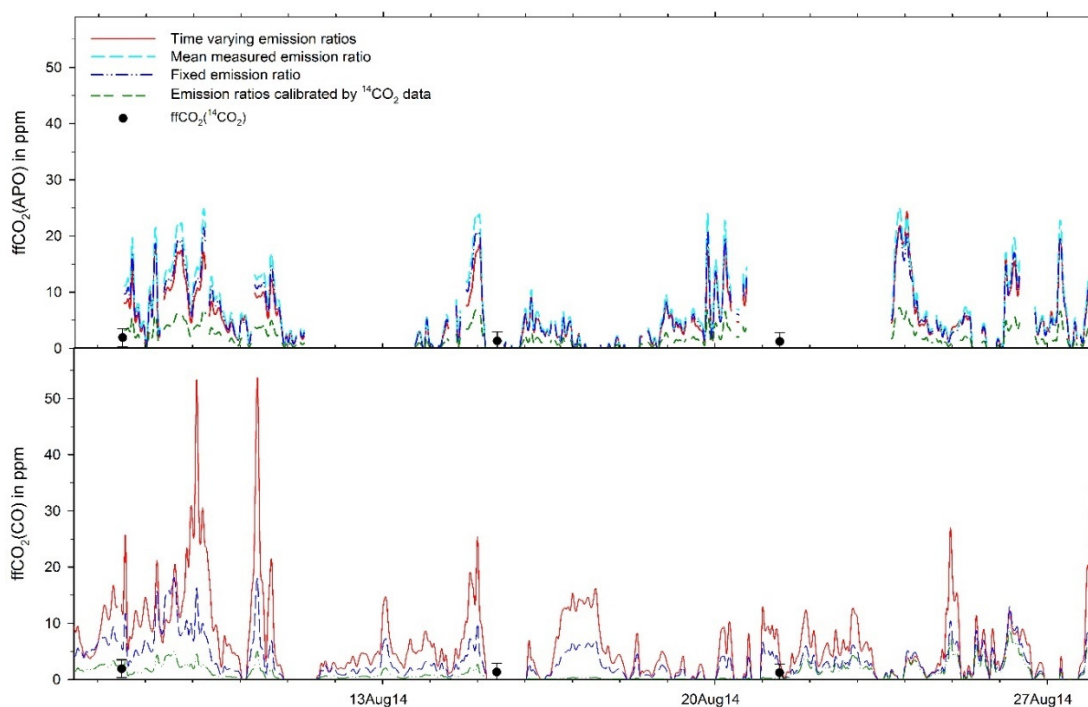


Figure 5.12. ffCO₂ from APO at UEA (top panel) and CO at TAC (bottom panel) calculated using a variety of emission ratios (see text above and figure legends). The ffCO₂ from time-varying ratios is the same as the ffCO₂ shown in Fig. 5.11 (top panel), only without the uncertainty shading, to aid visual comparison with the ffCO₂ calculated using the other emission ratios. Also shown is ffCO₂ from TAC ¹⁴CO₂ data (black symbols).

Fig. 5.12 demonstrates that the ffCO₂(APO) values (top panel) are all quite similar to each other, despite using different fossil fuel emission ratio sources. The only exception is the ffCO₂(APO) calculated from the emission ratios that were calibrated using the TAC ¹⁴CO₂ data, which is lower than that calculated using the other three types of emission ratios, which is lower than that calculated using the other three types of emission ratios. The ¹⁴CO₂ calibrated APO:CO₂ emission ratio had to be adjusted to the highest possible value for fossil fuel emissions (0.9 mol mol⁻¹) in order to be able to calculate ffCO₂ that was low enough to match the ffCO₂ from the ¹⁴CO₂ data. In fact, in some cases, it was not possible to match the ffCO₂(¹⁴CO₂) value without using an APO:CO₂ emission ratio that is higher than the maximum possible fossil fuel emission ratio value, which suggests that even though the ffCO₂(¹⁴CO₂) was corrected for nuclear influences, the values are still affected and are biased low. This is supported by the ffCO₂(CO) calculated using the ¹⁴CO₂ calibrated emission ratios, where it was also often necessary to use extremely high emission ratios (up to 100 ppb ppm⁻¹) in order to produce a low enough ffCO₂ value that would match the ffCO₂(¹⁴CO₂) value.

Unlike APO, the $ffCO_2(CO)$ shown in Fig. 5.12 is highly dependent upon the emission ratios used, with the time-varying ratios, fixed ratios, $^{14}CO_2$ calibrated ratios, and mean measured ratios (not shown) producing very different $ffCO_2$ values. As mentioned before, the mean measured ratios and time-varying ratios from the EDGAR database produce $ffCO_2$ from CO that is too high for a relatively rural location such as TAC or WAO, and the $^{14}CO_2$ calibrated ratios produce $ffCO_2$ values that are biased low by nuclear power plant emissions, given that sometimes very high CO:CO₂ emission ratios are required to reproduce the $ffCO_2(^{14}CO_2)$ values. The fixed emission ratios produce the $ffCO_2$ values that most closely match those calculated using the APO method (from different types of emission ratios) at UEA, and are also in the expected range, considering the location of TAC. Thus, Fig. 5.12 suggests that as well as the APO method being more precise than the CO method for quantifying $ffCO_2$, it is also very likely that the APO method is also more accurate than the CO method, given that the magnitude of $ffCO_2$ calculated from CO is so variable, depending on the choice of emission ratios used.

5.3.5. Comparison of $ffCO_2$ from 'top-down' atmospheric measurements with $ffCO_2$ from 'bottom-up' inventories

It is also interesting to compare the $ffCO_2$ calculated from APO and CO at TAC, UEA and WAO to modelled $ffCO_2$ from both the COFFEE and UK NAEI (National Atmospheric Emissions Inventory) bottom up inventories, as shown in Figures 5.13 (TAC and UEA) and 5.14 (WAO). Note that at the time of writing, only the NAEI inventory CO₂ values up to 2013 are available. The NAEI fossil fuel CO₂ emissions have a spatial resolution of 1 km, but are only available as annual averages. The modelled $ffCO_2$ was calculated by combining the NAME atmospheric footprints with the gridded inventory fossil fuel CO₂ emissions and modelled boundary layer height from the Met Office Unified Model, as shown in Equation 5.6, below.

$$ffCO_2 = \left(\sum_{t_1}^{t_n} \sum_{b_1}^{b_n} I \times \frac{P}{BLH} \right) \times 1000 \times 22.4 \quad (\text{Eq. 5.6})$$

where $ffCO_2$ is the modelled fossil fuel CO₂, t_1 to t_n represent the time intervals of the NAME footprints, b_1 to b_n represent the individual grid boxes of the NAME footprints, I is the inventory fossil fuel CO₂ in mol m⁻² hr⁻¹, P is the number of particles per grid box divided by the total number of particles in the NAME footprint and multiplied by 100, BLH is the modelled boundary layer height in metres, and 22.4 is the number of litres per mole of an ideal gas at standard temperature and pressure. Note that the modelled $ffCO_2$ values at TAC were

diluted to be representative of ffCO_2 at 100 m above the ground, using the ratio of the difference in TAC CO_2 enhancement above the background at 54 m and 100 m.

Figs. 5.13 and 5.14 show that the modelled ffCO_2 from the two inventories agree quite well with each other in terms of magnitude, although the UK NAEI does produce slightly higher values than COFFEE overall. The two inventories also generally agree with the ffCO_2 from both the CO and APO methods for the period of comparison in terms of the amount of ffCO_2 (within the uncertainties of the ffCO_2 from the atmospheric data), but there are large differences in the short-term variability. The inventory-derived modelled ffCO_2 for both COFFEE and NAEI do not produce values as high as the largest $\text{ffCO}_2(\text{CO})$ peaks at TAC, which is a positive result, given that the largest $\text{ffCO}_2(\text{CO})$ peaks are too large in magnitude to be accurate. At WAO, the modelled ffCO_2 from both inventories does occasionally produce unrealistically high values similar to those from the CO method. This might be caused by inaccuracies in the modelled boundary layer height used to model the ffCO_2 (because WAO is a coastal site), or could be caused by over-estimation of the inventory ffCO_2 emissions. Re-calculating the modelled ffCO_2 using a fixed boundary layer height of 500 m (an approximation of the mean boundary layer height during this time period) did not eliminate the largest peaks in the modelled ffCO_2 , which suggests that both the COFFEE and NAEI inventories sometimes over-estimate the fossil fuel CO_2 emissions in Norfolk.

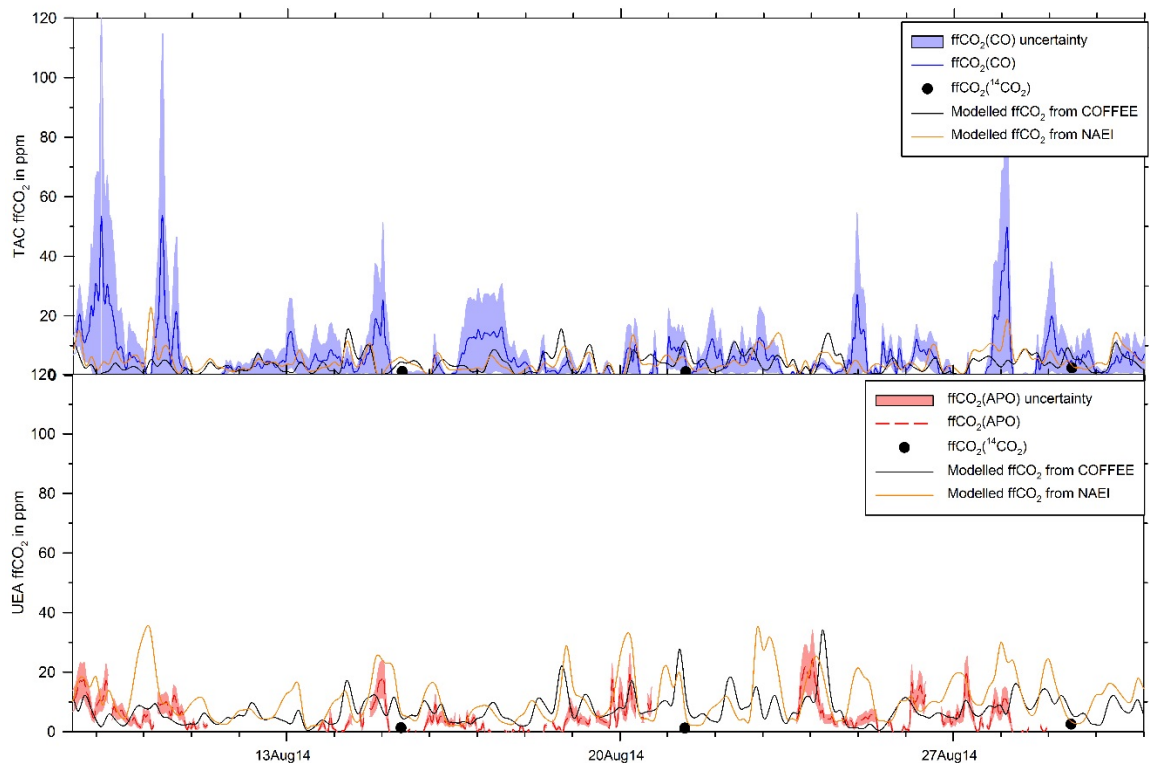


Figure 5.13. $\text{ffCO}_2(\text{CO})$ at TAC (top panel) and $\text{ffCO}_2(\text{APO})$ at UEA (bottom panel) compared to modelled ffCO_2 from COFFEE (black lines) and the UK NAEI (orange lines).

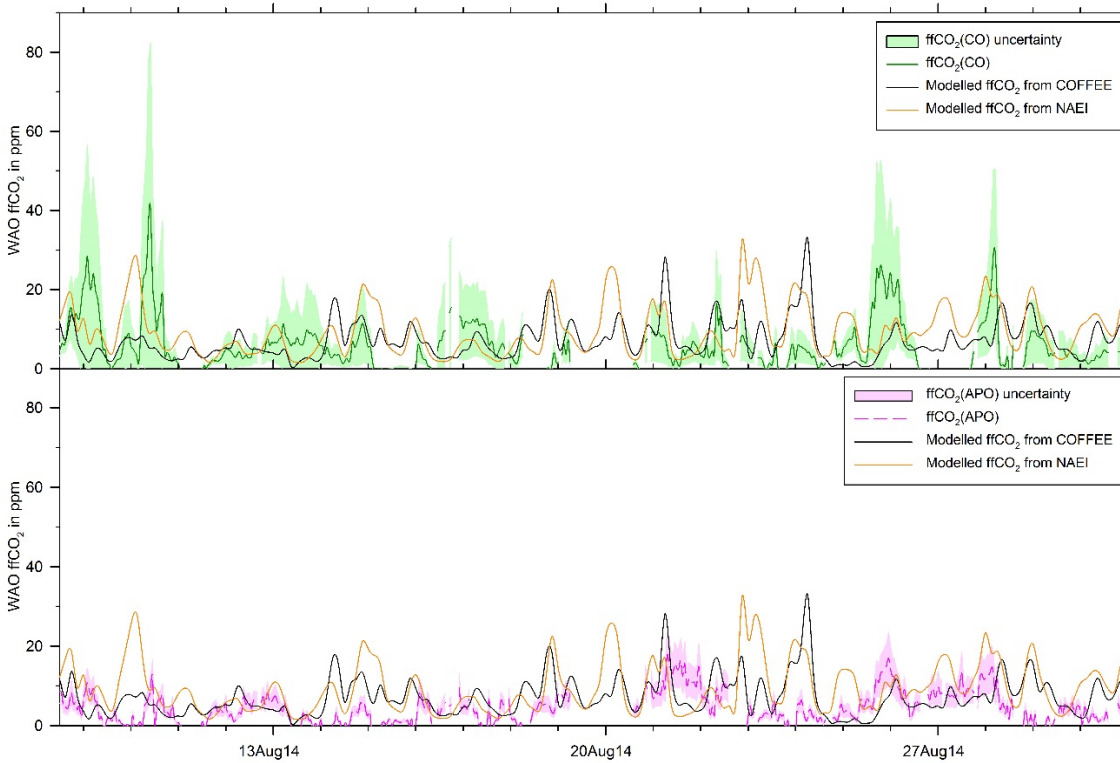


Figure 5.14. WAO fCO₂(CO) (top panel) and fCO₂(APO) (bottom panel) compared to modelled fCO₂ from COFFEE (black lines) and the UK NAEI (orange lines).

Table 5.3. Comparison of TAC fCO₂ values using the ‘top-down’ CO method and ‘bottom-up’ inventories. All units are in ppm. Average values are given ±1σ standard deviation.

	fCO₂(CO)	fCO₂(COFFEE)	fCO₂(NAEI)
Average fCO₂	6.9±7.3	5.7±3.9	8.4±5.6
Maximum fCO₂	53.3	27.5	26.5
Minimum fCO₂	0.0	0.3	1.2

Table 5.4. Comparison of UEA fCO₂ values using the ‘top-down’ APO method and ‘bottom-up’ inventories. All units are in ppm. Average values are given ±1σ standard deviation.

	fCO₂(APO)	fCO₂(COFFEE)	fCO₂(NAEI)
Average fCO₂	6.3±4.9	7.3±7.3	11.7±11.5
Maximum fCO₂	28.1	34.1	35.3
Minimum fCO₂	0.0	0.7	1.7

Table 5.5. Comparison of WAO fCO₂ values using the ‘top-down’ CO and APO methods and ‘bottom-up’ inventories. All units are in ppm. Average values are given ±1σ standard deviation.

	fCO₂(CO)	fCO₂(APO)	fCO₂(COFFEE)	fCO₂(NAEI)
Average fCO₂	6.8±6.3	4.7±3.5	7.2±7.2	9.9±9.7
Maximum fCO₂	40.0	17.4	33.2	37.1
Minimum fCO₂	0.0	0.0	0.6	1.6

A comparison of the overall fossil fuel values calculated using the atmospheric CO and APO data, as well as the COFFEE and NAEI inventory data at TAC, UEA and WAO is shown above in Tables 5.3 to 5.5. At all three locations, the NAEI average, maximum and minimum ffCO_2 values are all higher than those from COFFEE, with the only exception being the TAC COFFEE maximum value, which is slightly higher than the TAC NAEI maximum value. The CO method also consistently produces larger average and maximum ffCO_2 values than the APO method; this is largely caused by inaccuracies associated with the EDGAR CO:CO₂ ratios for fossil fuel, which result in over-estimated ffCO_2 values for the CO method, as discussed previously. The average ffCO_2 values from the inventories are larger than those from the CO and APO methods, with the exception of TAC, where the average ffCO_2 from the CO data is larger than the COFFEE value, but not the NAEI value. At TAC and WAO, the maximum ffCO_2 values from the CO method are much larger than the maximum ffCO_2 values from the inventories and from the APO method (at UEA and WAO respectively). Thus, Tables 5.3 to 5.5 indicate that the inventories generally over-estimate the ffCO_2 at UEA and WAO, although none of the differences in the average values are significantly different, given the relatively large variability in the ffCO_2 values during the time period of the comparison. If one assumes that the average ffCO_2 (APO) values at UEA and WAO are completely accurate, then the COFFEE inventory average ffCO_2 values are over-estimated by 16% and 53%, respectively, while the NAEI inventory average ffCO_2 values are over-estimated by 86% and 111%, respectively.

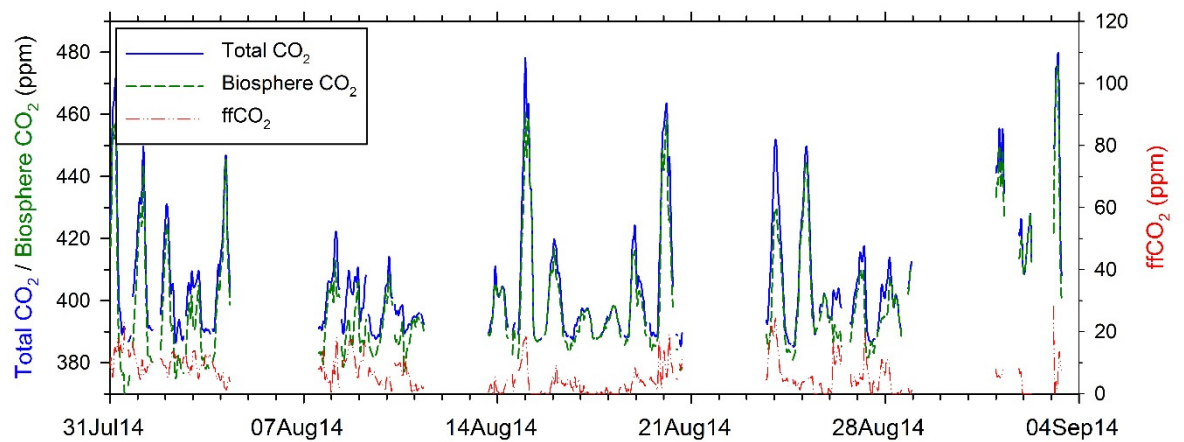


Figure 5.15. Total CO₂ (blue solid line), biosphere CO₂ (green dashed line) and ffCO_2 from APO (red dashed-dotted line) at UEA. Note that left and right y-axes are scaled to be visually comparable.

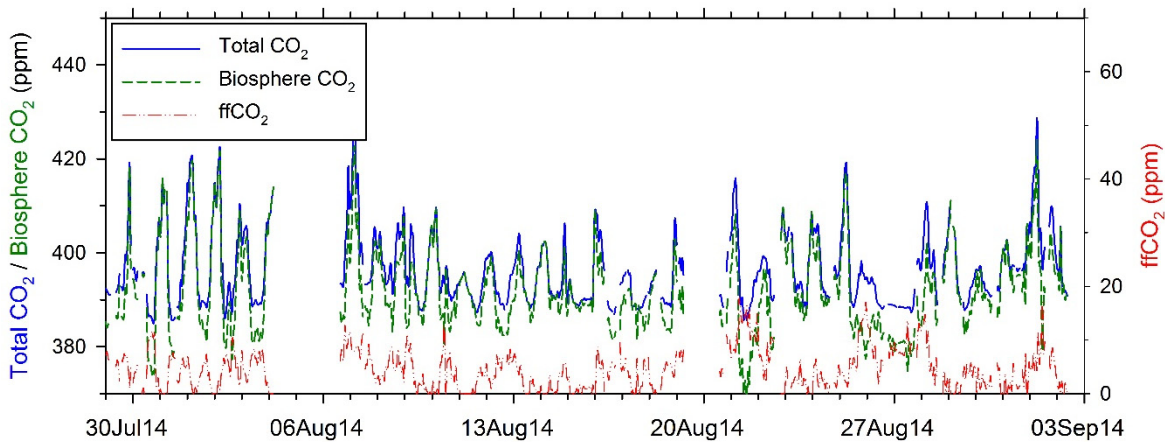


Figure 5.16. Total CO₂ (blue solid line), biosphere CO₂ (green dashed line) and ffCO₂ from APO (red dashed-dotted line) at WAO. Note that left and right y-axes are scaled to be visually comparable.

Figures 5.15 and 5.16 show the ffCO₂(APO) variability compared to total CO₂ variability and biosphere-only CO₂ variability (calculated by subtracting ffCO₂ from total CO₂) at UEA and WAO respectively. It is clear that total CO₂ variability is dominated by the activity of the terrestrial biosphere (and also some changes in atmospheric boundary layer height), particularly at UEA. At WAO, the dominance of the terrestrial biosphere and boundary layer height changes is weaker than at UEA, owing to the coastal location of the measurement station. It is also apparent that at both locations, the largest peaks in total CO₂ do not always correspond to peaks in ffCO₂, and therefore it would be very difficult to determine the ffCO₂ variability accurately by relying on total CO₂ measurements alone, or in combination with terrestrial CO₂ fluxes from a process model, unless the process model is able to accurately represent the day-to-day variability in terrestrial biosphere fluxes that are demonstrated in Figs. 5.15 and 5.16.

5.4 Summary and future work

In this chapter I have presented a new method for quantifying ffCO₂ using APO data, which I have compared to ffCO₂ calculated from CO and ¹⁴CO₂ data. Overall, I found the APO method to be significantly more precise than the CO method, which is largely owing to the reduced uncertainty in the APO:CO₂ fossil fuel emission ratios compared to the uncertainty in the CO:CO₂ fossil fuel emission ratios. The largest source of uncertainty in the APO method is currently the baseline fitting procedure. Future technical improvements in making high-precision O₂ measurements will help to reduce the APO baseline uncertainty. I would also expect that short-term deviations from the APO baseline will become easier to determine in a more urban setting, where the magnitude of the signals are larger, and that this will also help to

reduce the relative uncertainty in the APO baseline. In contrast to the two continuous methods, I found that relying on the $^{14}\text{CO}_2$ data alone led to significant underestimation of ffCO_2 in Norfolk, partly due to nuclear power plant influences that have not been adequately corrected for, and also partly due to clean air sampling (Angelina Wenger, personal communication, 2016).

When comparing the CO and APO methods, I found that the APO method was very likely to be more accurate than the CO method. This conclusion is largely based on a sensitivity analysis of four different emission ratio sources. For the APO method, I found that the range in ffCO_2 values associated with the four emission ratio sources was much smaller than the ffCO_2 range for the CO method. I was also able to determine that some of the largest ffCO_2 peaks from the CO method could not possibly be real, since they were larger than the measured CO_2 enhancement above the background CO_2 mole fraction. Ideally, I would have determined the accuracy of the APO and CO methods by comparing to ffCO_2 from $^{14}\text{CO}_2$ at a location that is not affected by gas-cooled nuclear power plant influences, because ffCO_2 from $^{14}\text{CO}_2$ is generally expected to be the most accurate way of determining ffCO_2 . As far as I am aware, however, there is no existing dataset of concurrent, high-precision APO, CO and $^{14}\text{CO}_2$ data at a location that also experiences polluted air, and is not affected by nuclear power plant influences. Despite this limitation, the results I have presented here indicate that it is very likely that the APO method is more accurate than the CO method. Most encouragingly, I have found that at WAO in particular (where the measurements are co-located), the ffCO_2 variability between the two methods is often very similar, and periods where the ffCO_2 magnitude is also in agreement affords me extremely high confidence in the ffCO_2 accuracy, given that the CO and APO methods are reliant on two completely independent tracers.

The UK government states that UK annual fossil fuel CO_2 emissions for 2013 are known to within $\pm 2\%$ uncertainty, based on bottom-up inventory methods and a 95% confidence level. While this uncertainty sounds very small, it is approximately equivalent to the UK mean annual CO_2 footprints of over 950,000 people. In addition, the uncertainties associated with the UK inventory are not quantified for higher spatial resolution than national, or for higher temporal resolution than annual (Stephen Forden, DECC; personal communication, 2016). Several studies have shown that emissions uncertainties increase with increasing spatial and temporal resolution, and can reach 100% or more for 1° latitude/longitude resolutions (also for a 95% confidence level) (Andres et al., 2012; Andres et al., 2016). Thus, even if national scale uncertainties in fossil fuel emissions are relatively small and are assumed to be well-known, large differences can be found at smaller scales, as demonstrated by (Ackerman and

Sundquist, 2008), who found differences of up to 25% in individual USA power plant CO₂ emissions compiled by different government agencies.

In order to be able to successfully reduce anthropogenic CO₂ emissions, we need to have access to high resolution (spatial and temporal) information that enables us to determine which behaviours cause increases and decreases in anthropogenic CO₂ emissions. For example, how do UK fossil fuel CO₂ emissions change if there is an unexpectedly cold winter, or if electric cars become dominant over petrol cars, or if house-hold electricity and gas smart meters are made compulsory in UK households? In this chapter, I have compared ffCO₂ from APO and CO measurements with modelled ffCO₂ from inventory estimates. The comparison indicates that both the COFFEE (derived from EDGAR) and the UK NAEI inventories may be over-estimating CO₂ emissions in Norfolk. In the case of the UK NAEI, some of this disparity may be explained by the fact that I have compared 2014 ffCO₂ from the atmospheric data to modelled ffCO₂ based on 2013 values, because the 2014 values are not currently available; however, the reduction in the Norfolk NAEI CO₂ emissions between summer 2013 and summer 2014 would need to be relatively large in order to bring the inventory ffCO₂ estimates in-line with the ffCO₂ from the atmospheric measurements. It should also be noted that the modelled ffCO₂ from the inventories that I have presented in this chapter are calculated using a single atmospheric transport model. Further sensitivity analysis on the modelled ffCO₂ emissions should be carried out using other atmospheric transport models, such as STILT (Stochastic Time-Inverted Lagrangian Transport model) (Lin et al., 2003) and TM3 (Heimann and Körner, 2003), to ensure that the modelled ffCO₂ is not biased by my choice of atmospheric transport model.

To my knowledge, there are currently no continuous high-precision atmospheric O₂ measurements made in urban settings for the purpose of ffCO₂ quantification, and yet ~70% of all anthropogenic CO₂ emissions are from cities (IEA, 2012a). I therefore propose a new direction for high-precision O₂ measurements, by advocating that atmospheric O₂ is a currently under-exploited tool for ffCO₂ quantification in urban environments, and has the potential to provide precise, accurate, high temporal and spatial resolution ffCO₂ quantification, which can also be used in regions that are severely affected by gas-cooled nuclear power plant emissions, such as western Europe, Japan, eastern USA and Canada. It should be noted that in order to use atmospheric O₂ measurements to successfully quantify ffCO₂, very precise measurements are required (on the order of ~5 per meg over 1-2 minutes) and a high level of data quality control is required. Nevertheless, as demonstrated in this chapter, it is currently possible to achieve such measurement precision and data quality control requirements in order to successfully quantify ffCO₂ even at rural and coastal locations, where ffCO₂ emissions are relatively low. I

therefore propose that a combination of atmospheric O₂ measurements and inverse modelling could enable robust top-down quantification of CO₂ emissions at both national, but also perhaps urban scales, and at sub-annual temporal resolutions, depending on the density of the atmospheric O₂ measurement network, and limitations of atmospheric transport models and inverse modelling methodologies.

References

- Ackerman, K. V. and Sundquist, E. T.: Comparison of two US power-plant carbon dioxide emissions data sets, *Environmental Science & Technology*, 42, 5688-5693, 2008.
- Andres, R. J., Boden, T. A., Breon, F. M., Ciais, P., Davis, S., Erickson, D., Gregg, J. S., Jacobson, A., Marland, G., Miller, J., Oda, T., Olivier, J. G. J., Raupach, M. R., Rayner, P., and Treanton, K.: A synthesis of carbon dioxide emissions from fossil-fuel combustion, *Biogeosciences*, 9, 1845-1871, 2012.
- Andres, R. J., Boden, T. A., and Higdon, D. M.: Gridded uncertainty in fossil fuel carbon dioxide emission maps, a CDIAC example *Atmospheric Chemistry and Physics Discussions*, 2016.
- Bergamaschi, P., Hein, R., Heimann, M., and Crutzen, P. J.: Inverse modeling of the global CO cycle 1. Inversion of CO mixing ratios, *Journal of Geophysical Research-Atmospheres*, 105, 1909-1927, 2000.
- Bergamaschi, P., Krol, M., Dentener, F., Vermeulen, A., Meinhardt, F., Graul, R., Ramonet, M., Peters, W., and Dlugokencky, E. J.: Inverse modelling of national and European CH₄ emissions using the atmospheric zoom model TM5, *Atmospheric Chemistry and Physics*, 5, 2431-2460, 2005.
- Breon, F. M., Broquet, G., Puygrenier, V., Chevallier, F., Xueref-Remy, I., Ramonet, M., Dieudonne, E., Lopez, M., Schmidt, M., Perrussel, O., and Ciais, P.: An attempt at estimating Paris area CO₂ emissions from atmospheric concentration measurements, *Atmospheric Chemistry and Physics*, 15, 1707-1724, 2015.
- Carslaw, D. C. and Ropkins, K.: Openair — an R package for air quality data analysis., *Environmental Modelling & Software*, 27-28, 52-61, 2012.
- Gammitzer, U., Karstens, U., Kromer, B., Neubert, R. E. M., Meijer, H. A. J., Schroeder, H., and Levin, I.: Carbon monoxide: A quantitative tracer for fossil fuel CO₂?, *Journal of Geophysical Research-Atmospheres*, 111, 2006.
- Graven, H. D.: Impact of fossil fuel emissions on atmospheric radiocarbon and various applications of radiocarbon over this century, *Proceedings of the National Academy of Sciences of the United States of America*, 112, 9542-9545, 2015.
- Graven, H. D. and Gruber, N.: Continental-scale enrichment of atmospheric ¹⁴CO₂ from the nuclear power industry: potential impact on the estimation of fossil fuel-derived CO₂, *Atmospheric Chemistry and Physics*, 11, 12339-12349, 2011.
- Gurney, K. R., Chen, Y. H., Maki, T., Kawa, S. R., Andrews, A., and Zhu, Z. X.: Sensitivity of atmospheric CO₂ inversions to seasonal and interannual variations in fossil fuel emissions, *Journal of Geophysical Research-Atmospheres*, 110, 2005.
- Heimann, M. and Körner, S.: *The Global Atmospheric Tracer Model TM3*, Max-Planck-Institut for Biogeochemistry, Jena, 2003.
- IEA: International Energy Agency: World energy outlook, 2012a.
- IEA: Technology Roadmap: Bioenergy for Heat and Power, International Energy Agency (IEA), 2012b.

- Jones, A. R., Thomson, D. J., Hort, M., and Devenish, B.: The U.K. Met Office's next-generation atmospheric dispersion model, NAME III In: Air Pollution Modeling and its Application Borrego, C. and Norman, A. L. (Eds.), XVII (Proceedings of the 27th NATO/CCMS International Technical Meeting on Air Pollution Modelling and its Application), Springer, 2007.
- Kossov, A., Peszko, G., Oppermann, K., Prytz, N., Klein, N., Blok, K., Lam, L., Wong, L., and Borkent, B.: State and Trends of Carbon Pricing 2015 (September), World Bank, Washington, DC., 2015.
- Levin, I., Hammer, S., Eichelmann, E., and Vogel, F. R.: Verification of greenhouse gas emission reductions: the prospect of atmospheric monitoring in polluted areas, Philosophical Transactions of the Royal Society a-Mathematical Physical and Engineering Sciences, 369, 1906-1924, 2011.
- Levin, I., Kromer, B., Schmidt, M., and Sartorius, H.: A novel approach for independent budgeting of fossil fuel CO₂ over Europe by ¹⁴CO₂ observations, Geophysical Research Letters, 30, 2003.
- Lin, J. C., Gerbig, C., Wofsy, S. C., Andrews, A. E., Daube, B. C., Davis, K. J., and Grainger, C. A.: A near-field tool for simulating the upstream influence of atmospheric observations: The Stochastic Time-Inverted Lagrangian Transport (STILT) model, Journal of Geophysical Research-Atmospheres, 108, 2003.
- Manning, M. R., Lowe, D. C., Melhuish, W. H., Sparks, R. J., Wallace, G., Brenninkmeijer, C. A. M., and McGill, R. C.: The use of radiocarbon measurements in atmospheric studies, Radiocarbon, 32, 37-58, 1990.
- Moxley, J. M. and Cape, J. N.: Depletion of carbon monoxide from the nocturnal boundary layer, Atmospheric Environment, 31, 1147-1155, 1997.
- Nisbet, E. and Weiss, R.: Top-Down Versus Bottom-Up, Science, 328, 1241-1243, 2010.
- Peylin, P., Houweling, S., Krol, M. C., Karstens, U., Rodenbeck, C., Geels, C., Vermeulen, A., Badawy, B., Aulagnier, C., Pregar, T., Delage, F., Pieterse, G., Ciais, P., and Heimann, M.: Importance of fossil fuel emission uncertainties over Europe for CO₂ modeling: model intercomparison, Atmospheric Chemistry and Physics, 11, 6607-6622, 2011.
- Ruckstuhl, A. F., Henne, S., Reimann, S., Steinbacher, M., Vollmer, M. K., O'Doherty, S., Buchmann, B., and Hueglin, C.: Robust extraction of baseline signal of atmospheric trace species using local regression, Atmospheric Measurement Techniques, 5, 2613-2624, 2012.
- Severinghaus, J. P.: Studies of the terrestrial O₂ and carbon cycles in sand dunes gases and in Biosphere 2, Ph.D. thesis, Columbia University, 1995.
- Staufer, J., Broquet, G., Breon, F. M., Puygrenier, V., Chevallier, F., Xueref-Remy, I., Dieudonne, E., Lopez, M., Schmidt, M., Ramonet, M., Perrussel, O., Lac, C., Wu, L., and Ciais, P.: A first year-long estimate of the Paris region fossil fuel CO₂ emissions based on atmospheric inversion, Atmospheric Chemistry and Physics Discussions, 2016.
- Steinbach, J., Gerbig, C., Rodenbeck, C., Karstens, U., Minejima, C., and Mukai, H.: The CO₂ release and Oxygen uptake from Fossil Fuel Emission Estimate (COFFEE) dataset: effects from varying oxidative ratios, Atmospheric Chemistry and Physics, 11, 6855-6870, 2011.
- Stephens, B. B., Keeling, R. F., Heimann, M., Six, K. D., Murnane, R., and Caldeira, K.: Testing global ocean carbon cycle models using measurements of atmospheric O₂ and CO₂ concentration, Global Biogeochemical Cycles, 12, 213-230, 1998.
- Turnbull, J., Rayner, P., Miller, J., Naegler, T., Ciais, P., and Cozic, A.: On the use of ¹⁴CO₂ as a tracer for fossil fuel CO₂: Quantifying uncertainties using an atmospheric transport model, Journal of Geophysical Research-Atmospheres, 114, 2009.
- Turnbull, J. C., Miller, J. B., Lehman, S. J., Tans, P. P., Sparks, R. J., and Southon, J.: Comparison of ¹⁴CO₂, CO, and SF₆ as tracers for recently added fossil fuel CO₂ in the atmosphere and implications for biological CO₂ exchange, Geophysical Research Letters, 33, 2006.
- van der Laan, S., Karstens, U., Neubert, R. E. M., Van der Laan-Luijkx, I. T., and Meijer, H. A. J.: Observation-based estimates of fossil fuel-derived CO₂ emissions in the Netherlands

- using $\Delta^{14}\text{C}$, CO and ^{222}Rn , *Tellus Series B-Chemical and Physical Meteorology*, 62, 389-402, 2010.
- Vogel, F. R., Hammer, S., Steinhof, A., Kromer, B., and Levin, I.: Implication of weekly and diurnal ^{14}C calibration on hourly estimates of CO-based fossil fuel CO_2 at a moderately polluted site in southwestern Germany, *Tellus B*, 512-520, 2010.
- Vogel, F. R., Levin, I., and Worthy, D. E. J.: Implications for deriving regional fossil fuel CO_2 estimates from atmospheric observations in a hot spot of nuclear power plant $^{14}\text{CO}_2$ emissions, *Radiocarbon*, 55, 1556-1572, 2013.
- Weiss, R. F. and Prinn, R. G.: Quantifying greenhouse-gas emissions from atmospheric measurements: a critical reality check for climate legislation, *Philosophical Transactions of the Royal Society a-Mathematical Physical and Engineering Sciences*, 369, 1925-1942, 2011.
- Zondervan, A. and Meijer, H. A. J.: Isotopic characterisation of CO_2 sources during regional pollution events using isotopic and radiocarbon analysis, *Tellus Series B-Chemical and Physical Meteorology*, 48, 601-612, 1996.

Chapter 6

Conclusions

6.1 Outline of major research findings

6.1.1 Shipboard atmospheric O₂ and CO₂ measurement system

- The measurement system compatibility of the Cap San Lorenzo data is 4.0 ± 2.9 per meg for O₂ and -0.045 ± 0.058 ppm for CO₂. These compatibility results are with reference to the UEA CRAM Laboratory calibration scales, which are traceable to the Scripps O₂ scale and the WMO NOAA CO₂ scale.
- The shipboard measurement system performs within both the northern and southern hemisphere WMO compatibility goals for CO₂ (± 0.1 ppm and ± 0.05 ppm, respectively), but does not achieve the WMO compatibility goal for O₂ of ± 2 per meg.
 - The WMO compatibility goal for O₂ is currently not routinely achievable in the high precision atmospheric O₂ community, even for most laboratories.
 - The shipboard measurement system does, however, perform well within the 'extended' WMO compatibility goal of ± 10 per meg, and is at the limit of what is currently achievable from a fuel cell O₂ analyser.
- Faster switching between the sample and reference air significantly improved the short-term precision of the Oxzilla II analyser (switching time reduced to 30 seconds, from 60 seconds typically used by other colleagues, e.g. Stephens et al. (2007)).
- High pressure calibration cylinders used for O₂ should be laid horizontally for at least 40 hours prior to being measured.
 - More thorough testing on cylinders of varying $\delta(\text{O}_2/\text{N}_2)$ ratios, and of different sizes and pressures is required.
- Making high-precision, fully-automated atmospheric O₂ measurements on a commercial container ship, with no human intervention for 8 week periods, is very challenging!
 - The main cause of measurement failure was from the 1st and 2nd stages of the drying system, which were unable to cope with the water-laden air caused by very high temperatures and humidity as the ship travelled through the tropical Atlantic.

6.1.2 Detecting short-term ocean O₂ fluxes in atmospheric O₂ data

- An unusually large, short-term APO 'event' in Sep 2013 (in the order of ~100 per meg), was observed during the JC090 research cruise in the North Atlantic Ocean.
 - This event cannot be explained by any of the complementary data collected during the cruise, or by features seen in satellite data for this time period.
 - According to the Jacob (1999) 'Puff' model it is theoretically possible that such an atmospheric event could have been caused by a change in ocean dissolved O₂ concentration.
- In ~1 year of shipboard O₂ measurements from the Cap San Lorenzo, however, there are no short-term events in APO larger than ~5 per meg that can be ascribed to air-sea fluxes or ocean processes, even though the Cap San Lorenzo passes through known active ocean upwelling regions.
- A re-analysis of data presented in Lueker et al. (2003) and Lueker (2004) reveals that the APO events discussed in these papers and attributed to ocean processes, are actually more likely to be of land origin than ocean origin.
 - The negative APO excursions observed most likely represent fossil fuel combustion.
- I have thus concluded that the large APO event during the JC090 cruise discussed in Chapter 3, was most likely caused by a previously undiagnosed technical issue, most probably O₂/N₂ fractionation within the gas handling system.
 - If the JC090 APO event is in fact real, then it must represent a very rare phenomenon.
- I propose that, contrary to the current view in the published literature, it is not possible to easily observe short-term (i.e. a few hours to a few days) air-sea exchanges of O₂ caused by ocean upwelling or marine biological activity in atmospheric APO data.
 - This appears to be because atmospheric mixing processes operate on much faster time scales than processes of O₂ exchange across the air-sea interface.
- One should exercise caution when attributing short-term variability in APO to localised/specific ocean events.
 - Unexplained variability in APO is often caused by technical issues.

- Negative excursions in APO can be caused by fossil fuel combustion.
- Long-range atmospheric transport can cause variability in APO.

6.1.3 The position of the ITCZ in the Atlantic Ocean

- The position of the ITCZ over the Atlantic Ocean seasonally migrates latitudinally towards the warming hemisphere.
- The position of the ITCZ over the Atlantic is biased towards the northern hemisphere more than the southern hemisphere.
 - A double maximum feature is apparent in the ITCZ position estimates from my Cap San Lorenzo data and also in the TRMM satellite data.
- The latitudinal range of the ITCZ position from my Cap San Lorenzo atmospheric data, and also from Royal Holloway atmospheric data, is larger than expected (by about 8° latitude), based on values from the published literature (e.g. Lefèvre et al., 2013; Schneider et al., 2014).
 - The atmospheric measurements are instantaneous, whereas the satellite-derived ITCZ position estimates are monthly averages.
 - Differences in the definition of the ITCZ position and short-term variability in atmospheric transport may also contribute to observed differences in the ITCZ latitudinal range.

6.1.4 Seasonal variability and annual mean latitudinal distribution of atmospheric O₂, CO₂ and APO across the Atlantic Ocean

- Seasonal variability in O₂, CO₂ and APO is as expected: O₂ seasonality reflects seasonal changes in both the terrestrial biosphere and the oceans, CO₂ seasonality reflects seasonal changes in the terrestrial biosphere only, and APO seasonality reflects seasonal changes in the oceans only.
- APO data over the Atlantic, for 2015, do not exhibit an equatorial APO 'bulge', as is apparent in western Pacific shipboard APO data (e.g. Tohjima et al., 2015).
 - From my single year of measurements, it is difficult to determine whether the non-existent APO bulge is a permanent feature over the Atlantic Ocean.
 - It is possible that the equatorial bulge was suppressed in 2015 owing to strong El Niño conditions, as has been observed in the western Pacific (Tohjima et al., 2012). The position of the ITCZ over the Atlantic during

2015, however, is not significantly different from previous years, suggesting that 2015 was not an unusual year for APO over the Atlantic Ocean.

- Modelled APO using both ‘high’ and ‘low’ resolution fluxes over-estimates the interhemispheric gradient in APO over the Atlantic Ocean.
 - The ocean general circulation models used in the ‘high-resolution’ model run I have examined may be over-estimating the southward sum of O₂ and CO₂ transport in the Atlantic Ocean, which is opposite to the conclusions of Stephens et al. (1998), who found that the models underestimated the southwards sum of O₂ and CO₂ transport in the Pacific Ocean.
- Modelled APO over the Atlantic Ocean using the ‘low resolution’ ocean fluxes exhibits an equatorial APO bulge.
 - The ocean fluxes used in the model may be too large in the tropical Atlantic.
 - There may be errors in the TM3 atmospheric transport over the Atlantic Ocean, such as under-estimated equator-wards transport, which enables a build-up of APO in the tropics.
 - The ‘high resolution’ ocean inversion fluxes do not produce an equatorial APO bulge.
- Northern hemisphere annual mean APO latitudinal distribution over the Atlantic Ocean is similar to that found over the western Pacific.
 - Spatial variability in annual mean APO is likely caused by a net O₂ sink in the western Atlantic, and the covariation of seasonal ocean O₂ fluxes and a seasonal rectifier effect over the mid-latitudes of the North Atlantic Ocean.

6.1.5 Quantifying ffCO₂ (fossil fuel-derived CO₂) using APO

- Quantifying ffCO₂ using APO data is a more precise method than quantifying ffCO₂ using CO data.
 - This is primarily owing to a smaller range of possible fossil fuel APO:CO₂ emission ratios compared to the range of possible fossil fuel CO:CO₂ emission ratios.

- Using CO to quantify ffCO₂ in Norfolk sometimes resulted in unrealistically high ffCO₂ values, largely because the EDGAR CO:CO₂ emission ratios seem to be unrealistically low.
- Using ¹⁴CO₂ to quantify ffCO₂ in Norfolk under-estimates the ffCO₂, owing to gas-cooled nuclear power plant influences on ¹⁴CO₂ that are not fully corrected for, and biases from ‘clean air’ sampling.
- The APO ffCO₂ method is very likely more accurate than the CO ffCO₂ method.
- Periods when the ffCO₂ estimates from both the APO and CO methods agree well with each other give very high confidence in the accuracy of the quantified ffCO₂.
- Modelled ffCO₂ from the COFFEE and UK NAEI CO₂ inventories suggests that both inventories are over-estimating fossil fuel emissions in Norfolk compared to ffCO₂ calculated from the atmospheric measurements, although the over-estimation is not significant, given the uncertainties associated with the modelling framework used here (mostly owing to atmospheric transport uncertainties).
 - The NAEI inventory consistently produces higher overall ffCO₂ values than the COFFEE inventory at all three Norfolk locations.

6.2 Summary of thesis and future work

In this thesis I have presented a new shipboard *in situ* O₂ and CO₂ measurement system that has been deployed on a commercial container ship across the Atlantic Ocean. The measurement system generally performs very well, although the air-drying components have struggled to cope with the relatively wet tropical air, which has resulted in some measurement system failures in the southern hemisphere and during the northwards bound transects. There is great potential to deploy other *in situ* O₂ and CO₂ measurement systems on board container ships, in order to help fill gaps in the global atmospheric O₂ measurement network; in particular, the eastern Pacific Ocean and Indian Ocean are regions that are currently not regularly sampled for atmospheric O₂ and CO₂, and also have major commercial shipping corridors. A key advantage of a shipboard *in situ* system on a commercial container ship, in contrast to both fixed stations and most research ships, is that, by ‘binning’ data into discrete latitude bands, time series from several ‘virtual stations’ can be collected

from just one measurement system, saving dramatically in costs, and avoiding common technical problems arising from potential calibration offsets between different measurement systems (particularly important when investigating relatively small latitudinal gradients in atmospheric signals).

The Cap San Lorenzo shipboard O₂ and CO₂ measurement system has provided initial insights into the seasonal variability and annual mean latitudinal distribution of O₂, CO₂ and APO over the Atlantic Ocean. As the dataset increases in length, these insights will become more robust, and new insights into interannual variability and long-term changes will also become apparent. This on-going Atlantic Ocean dataset will enable model-measurement comparisons in a region that was previously not possible, and can be used as a new tool for testing modelled estimates of air-sea O₂ and CO₂ fluxes, atmospheric transport over the Atlantic Ocean, and meridional transport of heat, O₂ and CO₂ in the Atlantic Ocean. Thus, I anticipate that these data will be of high scientific value, especially given the uncertainty regarding the Atlantic Ocean's ability to take up anthropogenic CO₂ in the future (Halloran et al., 2015), and projections of weakening ocean circulation in the North Atlantic Ocean (Perez et al., 2013).

The lack of short-term events in APO caused by air-sea O₂ fluxes in the Cap San Lorenzo dataset, after a full year of measurements, has led me to examine and question some previously reported APO short-term events from the literature. From experiences with my own datasets, I have found that unexplained variability in APO data is often a sign of a technical problem, which is often not immediately apparent in the O₂ data alone, and I suspect that some of the short-term APO events presented in the published literature reflect technical issues, rather than real events. An undetected technical issue, causing O₂/N₂ fractionation, is the most likely explanation of the JC090 research cruise's large negative APO event, which if real, must be an extremely rare phenomenon. Other short-term APO events that I have examined from the literature, such as those in Lueker (2004), do seem to reflect real events; however, I draw into question whether these events are of ocean origin, as an analysis of back-trajectories and CFC data indicates that these events are of land origin. I have also examined several un-published, multi-year APO datasets from coastal sites, which do not seem to exhibit any ocean-related short-term events, including Weybourne in the UK, Mace Head in Ireland, and Baring Head in New Zealand. The Southern Ocean shipboard dataset from the Laurence M. Gould research vessel is also lacking in short-term APO events of oceanic origin (Britton Stephens, personal communication, 2016).

I therefore propose that short-term or localised ocean events are not easily detectable in APO data using the currently available measurement techniques, most likely because atmospheric mixing processes operate much faster than the processes of O₂ exchange across the air-sea interface.

In addition to the shipboard atmospheric O₂ and CO₂ work of this thesis, I have also developed a new method for quantifying fossil fuel CO₂ from APO data. This new APO method is more precise than using CO data (a common method already used (e.g. van der Laan et al., 2010)), and very likely to be more accurate. The APO method can therefore be used independently of ¹⁴CO₂ measurements, which are expensive to analyse, and are severely affected by gas-cooled nuclear power plant emissions in the east of the USA and Canada, western Europe, and Japan.

Thus, I advocate a new, highly policy-relevant research direction for continuous APO data: using high-precision continuous measurements of O₂ and CO₂ to quantify fossil fuel CO₂ emissions in urban environments. This new application of APO data has the potential to improve 'top-down' fossil fuel CO₂ emissions estimates, and provide independent verification of the 'bottom-up' inventory estimates, which are reported to the United Nations Framework Convention on Climate Change (UNFCCC). Such independent verification, and quantifying the 'true' fossil fuel CO₂ emissions as observed in the atmosphere, is becoming increasingly essential, given global policy-makers' ambitions to ratify a climate mitigation treaty. The next steps needed in testing my APO method, are to carry out measurements in urban environments, and to use the measurements in an inverse atmospheric transport modelling framework to derive fossil fuel CO₂ emissions, which can be directly compared to the inventory emissions.

In this thesis, I have presented a new atmospheric O₂ and CO₂ dataset, and demonstrated a new application for APO data. The potential for using high-precision atmospheric O₂ data to learn more about carbon cycle processes is still very great. For example, further improvements in analytical measurement techniques, and in calibration and working tank stability would enable high-precision atmospheric O₂ measurements to become significantly more widespread. As one example future application, the development of high-precision O₂ eddy flux capability would enable improved understanding of land-atmosphere interactions, and may help to facilitate the separation of respiration and photosynthesis CO₂ fluxes (Alexander Knohl, personal communication, 2015). Some other potential applications of high-precision atmospheric O₂ measurements include: examining southern hemisphere

tropospheric-stratospheric transport (given that atmospheric O₂ exhibits much larger seasonal cycle amplitudes than CO₂ in the southern hemisphere); improved air-sea gas exchange velocity parameterisation using O₂ and CO₂ measurements in both the atmosphere and ocean; and the development of high-precision total column and satellite atmospheric O₂ measurements.

References

- Halloran, P. R., Booth, B. B. B., Jones, C. D., Lambert, F. H., McNeall, D. J., Totterdell, I. J., and Volker, C.: The mechanisms of North Atlantic CO₂ uptake in a large Earth System Model ensemble, *Biogeosciences*, 12, 4497-4508, 10.5194/bg-12-4497-2015, 2015.
- Jacob, D. J.: *Introduction to Atmospheric Chemistry*, Princeton University Press, 1999.
- Lefèvre, N., Caniaux, G., Janicot, S., and Gueye, A. K.: Increased CO₂ outgassing in February-May 2010 in the tropical Atlantic following the 2009 Pacific El Niño, *Journal of Geophysical Research-Oceans*, 118, 1645-1657, 10.1002/jgrc.20107, 2013.
- Lueker, T. J., Walker, S. J., Vollmer, M. K., Keeling, R. F., Nevison, C. D., Weiss, R. F., and Garcia, H. E.: Coastal upwelling air-sea fluxes revealed in atmospheric observations of O₂/N₂, CO₂ and N₂O, *Geophysical Research Letters*, 30, 10.1029/2002gl016615, 2003.
- Lueker, T. J.: Coastal upwelling fluxes of O₂, N₂O, and CO₂ assessed from continuous atmospheric observations at Trinidad, California, *Biogeosciences*, 1, 101-111, 2004.
- Perez, F. F., Mercier, H., Vazquez-Rodriguez, M., Lherminier, P., Velo, A., Pardo, P. C., Roson, G., and Rios, A. F.: Atlantic Ocean CO₂ uptake reduced by weakening of the meridional overturning circulation, *Nature Geoscience*, 6, 146-152, 10.1038/ngeo1680, 2013.
- Schneider, T., Bischoff, T., and Haug, G. H.: Migrations and dynamics of the intertropical convergence zone, *Nature*, 315, 45-53, 2014.
- Stephens, B. B., Keeling, R. F., Heimann, M., Six, K. D., Murnane, R., and Caldeira, K.: Testing global ocean carbon cycle models using measurements of atmospheric O₂ and CO₂ concentration, *Global Biogeochemical Cycles*, 12, 213-230, 10.1029/97gb03500, 1998.
- Stephens, B. B., Bakwin, P. S., Tans, P. P., Teclaw, R. M., and Baumann, D. D.: Application of a differential fuel-cell analyzer for measuring atmospheric oxygen variations, *Journal of Atmospheric and Oceanic Technology*, 24, 82-94, 10.1175/jtech1959.1, 2007.
- Tohjima, Y., Minejima, C., Mukai, H., Machida, T., Yamagishi, H., and Nojiri, Y.: Analysis of seasonality and annual mean distribution of atmospheric potential oxygen (APO) in the Pacific region, *Global Biogeochemical Cycles*, 26, 10.1029/2011gb004110, 2012.
- Tohjima, Y., Terao, Y., Mukai, H., Machida, T., Nojiri, Y., and Maksyutov, S.: ENSO-related variability in latitudinal distribution of annual mean atmospheric potential oxygen (APO) in the equatorial western Pacific, *Tellus Series B-Chemical and Physical Meteorology*, 67, 10.3402/tellusb.v67.25869, 2015.
- van der Laan, S., Karstens, U., Neubert, R. E. M., Van der Laan-Luijkx, I. T., and Meijer, H. A. J.: Observation-based estimates of fossil fuel-derived CO₂ emissions in the

Netherlands using $\Delta^{14}\text{C}$, CO and $^{222}\text{Radon}$, Tellus Series B-Chemical and Physical Meteorology, 62, 389-402, 10.1111/j.1600-0889.2010.00493.x, 2010.

Abbreviations

$^{14}\text{CO}_2$ – Radiocarbon content in CO_2

AAI – Aspirated Air Inlet

APO – Atmospheric Potential Oxygen

CFF – Cylinder Filling Facility at UEA

CH_4 - Methane

CO – Carbon monoxide

CO_2 – Carbon dioxide

COFFEE - CO_2 release and Oxygen uptake from Fossil Fuel Emissions Estimate

CRAM – Carbon Related Atmospheric Measurements laboratory at UEA

$\delta\text{O}_2/\text{N}_2$ – atmospheric O_2/N_2 ratio

EDGAR – Emissions Database for Global Atmospheric Research

ff CO_2 – fossil fuel CO_2

GC/TCD – Gas Chromatograph equipped with a Thermal Conductivity Detector

HYSPLIT – Hybrid Single Particle Lagrangian Integrated Trajectory model

ITCZ – Inter Tropical Convergence Zone

JC090 – James Cook 090 cruise

JT – Junk Tank

N_2O – Nitrous oxide

NAEI – National Atmospheric Emissions Inventory (UK)

NAME – Numerical Atmospheric-dispersion Modelling Environment

NDIR – Non-Dispersive Infra-Red

Nemo – the name of the measurement system software

NEMO-PlankTOM – Nucleus for European Modelling of the Ocean-Plankton Types Ocean Model

NERC – Natural Environment Research Council (UK)

NOAA – National Oceanic and Atmospheric Administration (USA)

per meg – a dimensionless unit equivalent to 0.001 per mil

PML – Plymouth Marine Laboratory (UK)

ppm – parts per million

PSS – Primary Secondary Standards

RRS – Royal Research Ship

SIO/Scripps – Scripps Institution of Oceanography

TAC – Tacolneston, UK

TM3 – Tracer transport model 3

TT – Target Tank

UEA – University of East Anglia

VUV – Vacuum-Ultraviolet

WAO – Weybourne Atmospheric Observatory, UK

WMO – World Meteorological Organization

WSS – Working Secondary Standard

WT – Working Tank

ZT – Zero Tank

Appendices

A. Pressure drop calculations for inlet lines

1. First, calculate the Reynolds number for the flow.

For flow in a pipe, the Reynolds number (Re) is generally defined as:

$$Re = \frac{\rho \times D_h}{\mu} = \frac{Q \times D_h}{vis \times A} \quad (\text{Eq. A.1})$$

where ρ is the density of the fluid in the inlet line in kg m^{-3} , D_h is the hydraulic diameter of the pipe in m, μ is the dynamic viscosity of the fluid in $\text{kg m}^{-1} \text{s}^{-1}$, Q is the volumetric flow rate in $\text{m}^3 \text{s}^{-1}$, vis is the kinematic viscosity (i.e. μ/ρ) in $\text{m}^2 \text{s}^{-1}$, and A is the pipe cross-sectional area in m^2 .

Using the values in Table A.1, the Reynolds number for the flow is calculated to be 33.8. The flow inside the inlet lines is laminar, because $Re < 2000$.

2. Now, calculate the friction factor f , using the equation for laminar flow.

$$f = \frac{64}{Re} \quad (\text{Eq. A.2})$$

The friction factor is therefore 1.89

3. Lastly, use the viscous head equation to calculate the pressure at the end of the tubing (P_B):

$$P_B = P_A - \rho \times g \times \frac{f \frac{L}{D_h}}{\frac{v^2}{2 \times g}} \quad (\text{Eq. A.3})$$

where P_A is the pressure at the beginning of the tubing (where the AAI is located) in pa, g is acceleration due to gravity in m s^{-2} , L is the length of the tubing in m, and V is the fluid velocity (Q/A) in m s^{-1} .

Again, using the values in Table A.1, P_B is calculated to be 101310 Pa, and hence the pressure drop in the inlet lines ($P_A - P_B$) is only 2.26 mbar.

Table A1. Ship system tubing properties used to calculate pressure drops within the inlet lines

Quantity	Value	Units
Tubing internal diameter (D_h)	0.0043	m
Volumetric flow rate (Q)	$1.66 * 10^{-6}$	$\text{m}^3 \text{s}^{-1}$
Kinematic viscosity (vis)	$1.45 * 10^{-5}$	$\text{m}^2 \text{s}^{-1}$
Tubing cross-sectional area (A)	$1.46 * 10^{-5}$	m^2
Tubing length (L)	65	m
Pressure at the beginning of the tubing (P_A)	101325	Pa

B. Oxyzilla II Allan deviation R script

```
#####
#
#   This script demonstrates how to do an Allan Variance plot in R, using code #
#
#                               Created by P.A.Pickers on 23Aug2013 #
#
#####

# Format of the inputfile: this should be a .csv file. The input file should have
# one header line, and can have multiple columns of signal output data if you want
# to compare the Allan variance of different instruments.

### PART 1: READING IN THE INPUT FILE ###

# In order to read in the file, set the working directory to the correct location
# using the following command:

setwd("C:/PhD/Programming/R/Working_directory")

# Note that R does not recognise "\" symbols in file pathways. Instead they must
# be replaced with "\\\" or "/".

# Next, read in the data into a variable called "data", and tell R that the input
# file has a header line. If there is no header line, type "header=F". Make sure
# that "filename" is replaced with the filename of the input data file.

data <- read.table("dO2_HAM_07Sep2014_shorter.txt",header=F)

### PART 2: CHECKING THE DATA (SKIP TO PART 3 IF THE DATA DO NOT NEED
CHECKING) ###

# To check that the data has been read into R correctly, look at the first 5 rows
# using the following command:
```

```
head(data)
```

```
names(data)[1] <- "Time"
```

```
names(data)[2] <- "dO2"
```

```
# Make a plot to visually check the data using the following commands.
```

```
plot(data$Time,data$dO2,xlab="Time (seconds)", ylab="dO2")
```

```
# Optional: add a line to the plot showing the mean of the data:
```

```
abline(h=mean(data$dO2),col="blue",lwd="2")
```

```
### PART 3: CALCULATING THE ALLAN VARIANCE ###
```

```
# Now calculate the Allan variance. First find the length of the data array,  
# and name it "end".
```

```
end <- length(data$Time)
```

```
# Then, use the length to find the average time step between samples and save  
# the inverse as the variable "frequency".
```

```
# frequency <- 1/mean(data$Time[2:end]-data$Time[1:(end-1)])
```

```
# Now call the package "allanvar" using the library command. The "allanvar"  
# package must be installed before loading the package using this command.
```

```
library("allanvar")
```

```
# Use the function "avar" to calculate the Allan variance for the data,  
# using the "frequency" variable that was calculated previously. Call this  
# "avar.data.x".
```

```

avar.data.x <- avarn(data$dO2,frequency(data$dO2))

# Check that the avar function has worked correctly using the head command:

head(avar.data.x)

### PART 4: PLOTTING THE ALLAN VARIANCE AND ALLAN DEVIATION ###

# Plot the variance for each size of time interval as follows:

plot(avar.data.x$time,avar.data.x$av,type="l",col="green",
     xlab="Sample Time (seconds, at 1 sample/sec)",
     ylab=expression(paste("Allan variance (sensor units squared)")))

# This is, however, not the most useful plot to look at for two reasons: firstly,
# the change in variance from the minimum point may happen very suddenly and it
# will therefore be difficult to read the ideal time interval from the plot;
# secondly, the y axis is in units of the sensor values squared, which is not
# very intuitive.

# Solve the first problem by making a log-log plot. Using the options
# function prevents the use of "1e00" notation up to 5 decimal places.

options(scipen=5)
plot(avar.data.x$time,avar.data.x$av,type="l",col="green",log="xy",
     xlab="Sample Time (seconds, at 1 sample/sec)",
     ylab=expression(paste("Allan variance (sensor units squared)")),
     main="Log-log Plot of Allan Variance")

# In order to solve the second problem, plot the Allan deviation rather than
# Allan variance, since standard deviation is the simply the square root
# of variance.

options(scipen=5)

```

```
plotCI(avar.data.x$time,sqrt(avar.data.x$av),uiw=avar.data.x$error,type="l",col="green",log="xy",
  xlab="Sample Time (Seconds, at 1 sample/second)",
  ylab="Allan Standard Deviation (in [%] * 10^4 equivalents)")
```

```
# Adding some grid lines and a title makes the plot look a bit more
# pretty:
```

```
grid(equilog=FALSE,lwd=1,col="orange")
title(main="Allan Deviation Plot for dO2 Cap San Lorenzo data on 07Sep2014")
# points(60,1.568757,col="red",cex=2,lwd=3)
# points(60,0.7843785,col="green",cex=2,lwd=3)
```

```
# There are two more commands that might be useful: the first helps to check that
# the data processing and plot are correct, by examining the standard deviation
# of the raw data, which should match the y axis intercept on the plot:
```

```
standard.dev <- sd(data$dO2)
print(standard.dev)
```

```
# And the second is that examining the error of the Allan deviation data shows
# that the error increases as the averaging time increases:
```

```
Allan.error <- avar.data.x$error
print(Allan.error)
```

```
# write a .jpeg file of the plot to the working directory
```

```
plotfile<-'Allan_variance_HAM_07Sep2014.jpg'
```

```
jpeg(filename=plotfile,width=800,height=800,units='px',pointsize=12,bg='white',quality=100)
options(scipen=5)
plotCI(avar.data.x$time,sqrt(avar.data.x$av),uiw=avar.data.x$error,type="l",col="green",log="xy",
```

```
xlab="Sample Time (Seconds, at 1 sample/second)",
ylab="Allan Standard Deviation (in [%] * 10^4 equivalents)")
grid(equilog=FALSE, lwd=1, col="orange")
title(main="Allan Deviation Plot for Cap San Lorenzo data on 07Sep2014")
# points(60,1.568757,col="red", cex=2, lwd=3)
# points(60,0.7843785,col="green", cex=2, lwd=3)
# 'dev.off()' shuts down the jpeg plotting device.
dev.off()

### THE END ###
```

C. Ship measurement system file structure

Example filename	Sub-directory	File description	When data can be recorded	Data acquisition frequency	File creation frequency
HAM20130220_SEC.csv	RAW	Records data every second	Whenever software is running	1 Sec	Daily
HAM20130220_DIG.csv	PRELIM	Records diagnostic data	Whenever software is running ¹	30 Sec ²	Daily
HAM201302_DIF.csv	PRELIM	Records 1 min averages of concentration data	Whenever software is running AND V23 is switching	1 Min ³	Monthly
HAM201302_DEF.csv	PRELIM	Records 1 min averages of concentration data but lines are written 1 min after DIF so we know if the data is used	Whenever software is running AND V23 is switching	1 Min ³	Monthly
HAM201302_AIR.csv	FINAL	Records 1 min averages of final air concentrations	During the air measurement macros when recording is on ("RC,1" or "RC,2") and software is in autorun	1 Min ³	Monthly
HAM201302_MET.csv	FINAL	Not currently recorded for HAM	Not currently recorded for HAM	N/A	N/A
HAM2013_SPAN.csv	CALIB	Records the calibration parameters defined by the WSS macro	At the end of each 'daily' calibration (WSS macro) and software is in autorun	~23 hours ⁴	Annually
HAM2013_WSS.csv	CALIB	Records 1 minute averages of each jog during a WSS run	During the WSS macro, when recording is on and software is in autorun	1 Min ³	Annually
HAM2013_TARGET.csv	CALIB	Records the final concentration of the Target cylinder	At the end of the target macro and software is in autorun	~10 hours ⁴	Annually
HAM2013_ZERO.csv	CALIB	Records the final concentration of the Zero cylinder	At the end of the zero macro and software is in autorun	~4 hours ⁴	Annually
HAM2013_OTHERS.csv	CALIB	Records 1 minute averages of any cylinder run as defined in the 'Others', 'LSS' or 'Next WSS' macros	During the 'Others', 'LSS' or 'Next WSS' macros, when recording is on and software is in autorun	1 Min ³	Annually
HAM20130906_AIR_SMALL	SMALL	Records a 'snapshot' of the AIR file once every 6 minutes (hard coded). Only the 'SMALL' files are written to the Dropbox location to reduce data	During the air measurement macros when recording is on ("RC,1" or "RC,2") and software is in autorun	6 Min	Daily

Example filename	Sub-directory	File description	When data can be recorded	Data acquisition frequency	File creation frequency
		transmission costs. New files are generated daily, not monthly.			
HAM20130906_DIG_SMALL	SMALL	Records a 'snapshot' of the DIG file once every hour (hard coded). Only the 'SMALL' files are written to the Dropbox location to reduce data transmission costs	Whenever software is running ¹	1 hour	Daily
HAM201302_SYS.csv	LOG	Records a log of system events	When triggered by a system event	Variable	Monthly
HAM2013_CYLLOG.csv	LOG	Records any changes to cylinder tab	When a change is made to info in the 'Cylinders' tab	Variable	Annually
HAM2013_ERRORS.csv	LOG	Records any data lines skipped due to system errors	When triggered by a system error	Variable	Annually
HAM2013_MNTLOG.csv	LOG	Records any maintenance events	When a change is made to the 'Maintenance' tab	Variable	Annually
HAM2013_USR.csv	LOG	Records user generated log entries	When a user makes a log entry in the 'User Log' tab	Variable	Annually
HAM201302_SKP.csv	LOG	Records any O ₂ data that is skipped due to an Oxzilla spike	Whenever software is running	5 lines per Sec	Monthly
nemo_settings.xml	SETTINGS	Records all current system software settings	When a system setting is changed the file is updated	Variable	Once only

Notes:

1. During the Oxzilla sweep out time (currently 15s after V23 switch) no O₂ data is collected and NaNs are recorded in the data files. During the cylinder purge and LiCor sweep out times no O₂ data and no CO₂ standard deviations are collected and NaNs are recorded in the data files.
2. This time period is hard-coded and is not linked to auto-switch time (V23 switching interval).
3. This is actually twice the auto-switch time, currently set to 30 seconds for HAM.
4. As currently defined in the 'Macros/Calibration' tab.

D. Detailed description of ship measurement system data files

Settings folder:

nemo_settings.xml: records all current system software settings. When a system file is changed, the file is updated

nemo_settings.xml.bak: a backup of the software system settings file

***date*_nemo_settings.xml:** a copy of the system settings file taken on a certain date

RAW folder:

SEC.csv file: records data every second when the software is running. Files are created daily. The file columns from left to right are as follows:

- **Date/Time:** the date and time of the measurement
- **Flags:** Not currently in use. Idea is to automatically flag data according to some diagnostic parameters
- **Oxcell:** which Oxzilla cell the sample was passing through at the time of the measurement (i.e. 1 or 2)
- **Cur Gas:** which inlet line the sample gas was passing through at the time of measurement (i.e. BL or RD), or which calibration cylinder is being run (e.g. ZT)
- **OX C1 [%]:** Oxzilla cell 1 oxygen measurement in percent
- **OX C2 [%]:** Oxzilla cell 2 oxygen measurement in percent
- **dO2[%] *10⁴:** delta oxygen measurement (i.e. difference between cell 1 and cell 2) in percent multiplied by 10⁴
- **dCO2 [mV]:** delta CO₂ measurement (i.e. difference between sample side and reference side) in mV
- **MKS 250 [mbar]:** MSK solenoid valve reading in mbar, indicating the difference in pressure between the sample and reference lines
- **FL20 [mL/min]:** sample side flow rate in mL/min
- **M20 [mL/min]:** reference gas flow rate in mL/min
- **P24 [mbar]:** Oxzilla internal pressure reading

PRELIM folder:

DIG.csv file: records diagnostic data when the software is running. The data frequency is 30 seconds, and files are created daily. The file columns from left to right are as follows:

- **Date/Time:** the date and time of the measurement.
- **Flags:** Not currently in use. Idea is to automatically flag data according to some diagnostic parameters
- **ID_CALIB:** records the ID of the calibration cylinder being run. If a calibration cylinder is not being run, then the software enters 'N.O.N.E' into this column.
- **ID_WT:** records the ID of the working tank cylinder being run.
- **Cur Gas:** which inlet line the sample gas was passing through at the time of measurement (i.e. BL or RD), or which calibration cylinder is being run (e.g. ZT)

- **Oxcell:** which Oxzilla cell the sample was passing through at the time of the measurement (i.e. 1 or 2)
- **V3V5V41Va40:** records a five digit code that indicates the valve positions of V3 (B or R, for blue or red line), V5 (C or S, for calibration or sample gas), V41 (Z or V, for ZT or Valco Valve), and Va40 (1-6, for the six Valco Valve positions).
- **V6V7V40V43:** records a three digit code that indicates the valve positions of V6 (S or O, for slow purge on or slow purge off), V7 (F or O, for fast purge on or fast purge off), and V40 and V43 (1-3, indicating which working tank cylinder is currently being used).
- **O2 Cell1 30s AV:** records the 30 second average of the Oxzilla cell 1 oxygen measurement. Note that due to the Oxzilla sweep out time, no O₂ data is recorded and so every other line is populated with NaN by the software.
- **O2 Cell2 30s AV:** records the 30 second average of the Oxzilla cell 2 oxygen measurement. Note that due to the Oxzilla sweep out time, no O₂ data is recorded and so every other line is populated with NaN by the software.
- **dO2 30s AV [%] *10⁴:** records the 30 second average of the delta O₂ measurement (difference between cell 1 and cell 2) in percent, multiplied by 10⁴
- **dO2 30s SD [%] *10⁴:** records the 30 second standard deviation of the delta O₂ measurement in percent, multiplied by 10⁴
- **dO2 30s n:** records the number of measurements used in the 30 second averages of the previous 4 columns
- **dCO2 30s AV [mV]:** records the 30 second average of the delta CO₂ measurement (difference between sample and reference cells) in mV
- **dCO2 30s SD [mV]:** records the 30 second standard deviation of the delta CO₂ measurement (difference between sample and reference cells) in mV
- **dCO2 30s n:** records the number of measurements used in the 30 second averages of the previous 2 columns
- **P1 [mbar] to P8 [mbar]:** records the pressure of the sample side gas handling system in mbar
- **P20 [mbar] to P24 [mbar]:** records the pressure of the measurement unit gas handling system in mbar
- **P24 RAW [mbar]:**
- **P40 [mbar] to P42 [mbar]:** records the delivery pressure of the working tank cylinders in mbar
- **FL1 [mL/min] to FL3 [mL/min]:** records the flow rate of the purging lines in mL/min
- **FL20 [mL/min] and M20 [mL/min]:** records the flow rate of the sample side and reference side gas handling lines, respectively, in mL/min
- **T1 [°C] to T3 [°C]:** records the temperatures of the Tropicool, chiller, and room, respectively, in °C
- **T20 [°C] and T21 [°C]:** records the temperatures of the LiCor and the Oxzilla, respectively, in °C

- **T40 [°C] to T45 [°C]:** records the Blue Box temperatures (front top left, front middle left, front bottom left, front middle right, middle left, back middle left, respectively) in °C
- **MSK sol(V):** records the MKS solenoid valve voltage
- **Blue Fan and Red Fan:** records the blue and red fan signals in volts
- **UPS status:** records the status of the UPS (line or battery mode)
- **CPUmx:** the maximum CPU over the DIG averaging period
- **CPUav:** the average CPU over the DIG averaging period
- **RAM:** records the free CPU RAM
- **Win Uptime:** records the time since the last Windows re-start
- **Prog Uptime:** records the time since the last software re-start
- **Latitude and Longitude:** records the GPS position of the system at the time of the measurement, in degrees and minutes
- **Speed [mph]:** records the speed of the ship, in miles per hour
- **Bearing:** records the direction the ship is travelling, in degrees
- **Satellites in use:** records the number of satellites that the GPS is able to connect to

DIF.csv file: records averages of mole fraction data, when the software is running and V23 is switching. Files are created monthly. The file columns from left to right are as follows:

- **Date/Time:** the date and time of the measurement.
- **Flags:** Not currently in use. Idea is to automatically flag data according to some diagnostic parameters
- **ID_CALIB:** records the ID of the calibration cylinder being run. If a calibration cylinder is not being run, then the software enters 'N.O.N.E' into this column.
- **ID_WT:** records the ID of the working tank cylinder being run.
- **Cur Gas:** which inlet line the sample gas was passing through at the time of measurement (i.e. BL or RD), or which calibration cylinder is being run (e.g. ZT)
- **DATA USED:** records whether data are used immediately, or whether this is currently unknown (indicated by a '?' symbol)
- **ST1 count:** the number of measurements used for calculating the ST1 dO₂ AV [%] x 10⁴ value
- **ST1 dO₂ AV [%] x10⁴:** step 1 delta O₂ average value in percent, multiplied by 10⁴
- **ST1 dO₂ SD [%] x10⁴:** step 1 delta O₂ standard deviation in percent, multiplied by 10⁴
- **ST2 count:** the number of measurements used for calculating the ST2 dO₂ AV [%] x 10⁴ value
- **ST2 dO₂ AV [%] x10⁴:** step 2 delta O₂ average value in percent, multiplied by 10⁴
- **ST2 dO₂ SD [%] x10⁴:** step 2 delta O₂ standard deviation in percent, multiplied by 10⁴

- **ST3 count:** the number of measurements used for calculating the ST3 dO₂ AV [%] x 10⁴ value
- **ST3 dO₂ AV [%] x10⁴:** step 3 delta O₂ average value in percent, multiplied by 10⁴
- **ST3 dO₂ SD [%] x10⁴:** step 3 delta O₂ standard deviation in percent, multiplied by 10⁴
- **ddO₂ [%] x 10⁴:** the double delta O₂ value in percent, multiplied by 10⁴
- **ddO₂ SD [%] x 10⁴:** the double delta O₂ standard deviation in percent, multiplied by 10⁴
- **O₂ [ppmEq]:** the O₂ measurement value in ppm equivalent units
- **O₂ SD [ppmEq]:** the O₂ measurement standard deviation in ppm equivalent units
- **O₂ [per meg]:** the O₂ measurement value in per meg units
- **O₂ SD [per meg]:** the O₂ measurement standard deviation in per meg units
- **dCO₂ count:** the number of measurements used for calculating the dCO₂ AV, dCO₂ SD, CO₂ AV and CO₂ SD columns
- **dCO₂ AV [mV]:** the delta CO₂ average in mV
- **dCO₂ SD [mV]:** the delta CO₂ standard deviation in mV
- **CO₂ AV [ppmv]:** the CO₂ average value in ppmv units
- **CO₂ SD [ppmv]:** the CO₂ standard deviation in ppmv units
- **O₂ CALIB Date/Time:** the date and time of the last accepted O₂ calibration
- **CO₂ CALIB Date/Time:** the date and time of the last accepted CO₂ calibration
- **CO₂ ZT CALIB Date/Time:** the date and time of the last accepted CO₂ zero tank calibration

DEF.csv file: records averages of mole fraction data, but lines are written 2 minutes after the DIF file lines, so that we know if the data is used or not. The file records data when the software is running and V23 is switching, and files are created monthly. The file columns are exactly the same as for the DIF.csv file.

FINAL Folder:

***station_name_and_date*_AIR.csv file:** records averages of final air mole fractions. Data are recorded when the air measurement macros are running and recording is turned on ('RC, 1' or 'RC,2'). Files are created monthly. The file columns from left to right are as follows:

- **Date/Time:** the date and time of the measurement.
- **Latitude and Longitude:** records the GPS position of the system at the time of the measurement, in degrees and minutes
- **Speed [mph]:** records the speed of the ship, in miles per hour
- **Bearing:** records the direction the ship is travelling, in degrees
- **Flags:** Not currently in use. Idea is to automatically flag data according to some diagnostic parameters
- **ID_WT:** records the ID of the working tank cylinder being run
- **Cur Gas:** which inlet line the sample gas was passing through at the time of measurement (i.e. BL or RD), or which calibration cylinder is being run (e.g. ZT)

- **ddO2 [%] x 10⁴**: the double delta O₂ value in percent, multiplied by 10⁴
- **ddO2 SD [%] x 10⁴**: the double delta O₂ standard deviation in percent, multiplied by 10⁴
- **O2 [ppmEq]**: the O₂ measurement value in ppm equivalent units
- **O2 SD [ppmEq]**: the O₂ measurement standard deviation in ppm equivalent units
- **O2 AV [per meg]**: the O₂ measurement value in per meg units
- **O2 SD [per meg]**: the O₂ measurement standard deviation in per meg units
- **dCO2 AV [mV]**: the delta CO₂ average in mV
- **dCO2 SD [mV]**: the delta CO₂ standard deviation in mV
- **CO2 AV [ppmv]**: the CO₂ average value in ppmv units
- **CO2 SD [ppmv]**: the CO₂ standard deviation in ppmv units
- **O2 CALIB Date/Time**: the date and time of the last accepted O₂ calibration
- **CO2 CALIB Date/Time**: the date and time of the last accepted CO₂ calibration
- **CO2 ZT CALIB Date/Time**: the date and time of the last accepted CO₂ zero tank calibration

***station_name_year*_flags.csv file**: a csv version of the 'flags' tab in the station logbook. Is used to apply flags to the data when running the AIR IDL program.

***station_name_year*_MET.csv file**: meteorological data file, obtained from ECMWF. Files are generated manually.

CALIB folder:

***station_name_year*_SPAN.csv file**: records the calibration parameters defined by the WSS macro. Data is recorded at the end of each 'daily' calibration (WSS macro), and the file is created annually. The file columns from left to right are as follows:

- **Date/Time**: the date and time of the measurement.
- **Flags**: Not currently in use. Idea is to automatically flag data according to some diagnostic parameters
- **O2 CAL FLAG**: records if the O₂ calibration was flagged as 'bad' (1 indicates flagged)
- **CO2 CAL FLAG**: records if the CO₂ calibration was flagged as 'bad' (1 indicates flagged)
- **ID_Wss1**: ID of the Wss1 cylinder
- **ID_Wss2**: ID of the Wss2 cylinder
- **ID_Wss3**: ID of the Wss3 cylinder
- **ID_Wss4**: ID of the Wss4 cylinder
- **ID_WT**: records the ID of the working tank cylinder being run
- **n Wss1**: number of jogs over which the Wss1 cylinder was measured during the calibration
- **n Wss2**: number of jogs over which the Wss2 cylinder was measured during the calibration
- **n Wss3**: number of jogs over which the Wss3 cylinder was measured during the calibration

- **n Wss4:** number of jogs over which the Wss4 cylinder was measured during the calibration
- **CO2 A-Term:** value of the CO₂ A-Term
- **CO2 B-Term:** value of the CO₂ B-Term
- **CO2 C-Term:** value of the CO₂ C-Term
- **CO2 R^2:** CO₂ R squared value
- **O2 SLP:** value of the O₂ slope
- **O2 INTCP:** value of the O₂ intercept
- **O2 R^2:** O₂ R squared value

***station_name_year*_WSS.csv file:** records averages of each jog during a WSS run. The data is recorded during the WSS macro when recording is turned on. The files are created annually. The file columns from left to right are as follows:

- **Date/Time:** the date and time of the measurement.
- **Flags:** Not currently in use. Idea is to automatically flag data according to some diagnostic parameters
- **ID_CALIB:** records the ID of the calibration cylinder being run
- **ID_WT:** records the ID of the working tank cylinder being run
- **Cur Gas:** which calibration cylinder is being run (e.g. W1)
- **ddO2 [%] x 10^4:** the double delta O₂ value in percent, multiplied by 10⁴
- **ddO2 SD [%] x 10^4:** the double delta O₂ standard deviation in percent, multiplied by 10⁴
- **dCO2 AV [mV]:** the delta CO₂ average in mV
- **dCO2 SD [mV]:** the delta CO₂ standard deviation in mV

***station_name_year*_TARGET.csv file:** records the final concentration of the Target cylinder. Data are recorded at the end of the target macro, and files are created annually. The file columns from left to right are as follows:

- **Date/Time:** the date and time of the measurement.
- **Flags:** Not currently in use. Idea is to automatically flag data according to some diagnostic parameters
- **O2 TT flag:** records if the O₂ TT calibration was flagged as 'bad' (1 indicates flagged)
- **CO2 TT flag:** records if the CO₂ TT calibration was flagged as 'bad' (1 indicates flagged)
- **ID_TARGET:** records the ID of the target cylinder being run
- **ID_WT:** records the ID of the working tank cylinder being run
- **n (No. Points):** records the number of jogs over which the target tank cylinder was measured
- **O2 AV [per meg]:** the O₂ measurement value in per meg units
- **O2 SD [per meg]:** the O₂ measurement standard deviation in per meg units
- **dO2 AV (n; measured - quoted) [per meg]:** the difference between the measured and quoted O₂ measurement value in per meg units
- **CO2 AV [ppmv]:** the CO₂ average value in ppmv units

- **CO₂ SD [ppmv]:** the CO₂ standard deviation in ppmv units
- **dCO₂ AV [ppmv]:** the difference between the measured and quoted CO₂ average value in ppmv units
- **O₂ CALIB Date/Time:** the date and time of the last accepted O₂ calibration
- **CO₂ CALIB Date/Time:** the date and time of the last accepted CO₂ calibration
- **CO₂ ZT CALIB Date/Time:** the date and time of the last accepted CO₂ zero tank calibration

***station_name_year*_ZERO.csv file:** records the final concentration of the Zero cylinder. Data are recorded at the end of the zero macro, and files are created annually. The file columns from left to right are as follows:

- **Date/Time:** the date and time of the measurement.
- **Flags:** Not currently in use. Idea is to automatically flag data according to some diagnostic parameters
- **ZT flag:** Indicates if the ZT calibration was flagged as 'bad' (1 indicates flagged)
- **ID_ZERO:** records the ID of the zero tank cylinder being run
- **ID_WT:** records the ID of the working tank cylinder being run
- **n (No. Points):** records the number of jogs over which the zero tank cylinder was measured
- **No of runs since calibration:** records the number of times the zero tank cylinder has been run since the last calibration was done
- **CO₂ AV [ppmv]:** the CO₂ average value in ppmv units
- **CO₂ sigma [ppmv]:** the CO₂ standard deviation in ppmv units
- **Base Zero CO₂ [ppmv]:** the CO₂ measurement of the zero tank run that followed immediately after the calibration run in ppmv units
- **CO₂ C-Term:** the current value of the C-term in the quadratic equation used to calibrate the CO₂ analyser
- **(Current-Base) CO₂ [ppmv]:** the current CO₂ measurement of the zero tank minus the base CO₂ measurement of the zero tank in ppmv units
- **(Current-Prev) C-Term:** the current value of the C-term minus the previous value of the C-term
- **O₂ AV [per meg]:** the O₂ measurement value in per meg units
- **O₂ SD [per meg]:** the O₂ measurement standard deviation in per meg units
- **dO₂ AV (n; measured - quoted) [per meg]:** the difference between the measured and quoted O₂ measurement value in per meg units

***station_name_year*_OTHERS.csv file:** records averages of any cylinder run as defined in the 'Others', 'LSS' or 'Next WSS' macros. Data are recorded during the 'Others', 'LSS' or 'Next WSS' macros when recording is turned on, and files are created annually. The file columns from left to right are as follows:

- **Date/Time:** the date and time of the measurement
- **Flags:** Not currently in use. Idea is to automatically flag data according to some diagnostic parameters

- **ID_CALIB:** records the ID of the calibration cylinder being run
- **ID_WT:** records the ID of the working tank cylinder being run
- **Cur Gas:** which calibration cylinder is being run (e.g. W1)
- **ddO2 [%] x 10⁴:** the double delta O₂ value in percent, multiplied by 10⁴
- **ddO2 SD [%] x 10⁴:** the double delta O₂ standard deviation in percent, multiplied by 10⁴
- **O₂ [ppmEq]:** the O₂ measurement value in ppm equivalent units
- **O₂ SD [ppmEq]:** the O₂ measurement standard deviation in ppm equivalent units
- **O₂ AV [per meg]:** the O₂ measurement value in per meg units
- **O₂ SD [per meg]:** the O₂ measurement standard deviation in per meg units
- **dCO₂ AV [mV]:** the delta CO₂ average in mV
- **dCO₂ SD [mV]:** the delta CO₂ standard deviation in mV
- **CO₂ AV [ppmv]:** the CO₂ average value in ppmv units
- **CO₂ SD [ppmv]:** the CO₂ standard deviation in ppmv units
- **O₂ CALIB Date/Time:** the date and time of the last accepted O₂ calibration
- **CO₂ CALIB Date/Time:** the date and time of the last accepted CO₂ calibration
- **CO₂ ZT CALIB Date/Time:** the date and time of the last accepted CO₂ zero tank calibration

LOG folder:

***station_name_date*_SYS.csv file:** records a log of system events. The file records whenever a system event occurs, and files are created monthly. The file columns from left to right are as follows:

- **Date/Time:** the date and time of the entry
- **Event:** description of the system event
- **Value:** value of the system event

***station_name_year*_CYLLOG.csv file:** records any changes to the cylinder tab. The file records whenever a change is made to the information on the cylinders tab. Files are created annually. The file columns from left to right are as follows:

- **Date/Time:** the date and time of the entry
- **Valco pos:** position of the cylinder on the Valco Valve
- **Old Reg:** old regulator position
- **New Reg:** new regulator position
- **Old ID:** old cylinder ID
- **New ID:** new cylinder ID
- **Old Code:** old cylinder code
- **New Code:** new cylinder code
- **Old [O₂] (per meg):** oxygen concentration of the old cylinder in per meg units
- **New [O₂] (per meg):** oxygen concentration of the new cylinder in per meg units
- **Old [CO₂] (ppm):** CO₂ concentration of the old cylinder in ppm
- **New [CO₂] (ppm):** CO₂ concentration of the new cylinder in ppm

***station_name_year*_ERRORS.csv file:** records any data lines skipped due to system errors. The file records whenever a system error occurs, and files are created annually. The file columns from left to right are as follows:

***station_name_year*_MNTLOG.csv file:** records any maintenance events. The file records whenever a change is made to the information on the maintenance tab. Files are created annually. The file columns from left to right are as follows:

- **Date/Time:** date and time of maintenance
- **Entry:** description of maintenance carried out

***station_name_year*_USR.csv file:** records user generated log entries. The file records whenever a user makes a log entry in the user log tab. Files are created annually. The file columns from left to right are as follows:

- **Date/Time:** the date and time of the entry
- **Log entry:** entry from user log tab

***station_name_date*_SKP.csv file:** records any O₂ data that are skipped due to an Oxzilla spike. The file records data every 0.2 seconds whenever the software is running, and files are created monthly. The file columns from left to right are as follows:

- **Date/Time:** the date and time of the entry
- **O2 diff:** difference between cell 1 and cell 2
- **Skip no:** the number of successive 0.2 second frequency data that are skipped. The maximum is 5, as there can only be a maximum of 5 data points skipped per second interval (due to logging frequency of 0.2 seconds). If 5 data points are successively skipped, a change in concentration is assumed instead of a spike, and the software starts accepting values until the next skip occurs.
- **Last 5 av:** Average of the last five reading from the Oxzilla. The Oxzilla output frequency is 5 readings per second.
- **3 sigma:** the 3 sigma value of the last 5 average readings
- **spike thresh:** O₂ spike threshold value (settable in the software)
- **Oxz Cell1:** O₂ concentration of Oxzilla cell 1
- **Oxz Cell2:** O₂ concentration of Oxzilla cell 2

Logging procedure: only skipped data are logged in the file (currently the non-skipped 0.2 second frequency data are not recorded anywhere). Data are skipped if the following conditions are met: the difference between the 'O2 diff' value and the 'Last 5 av' value is greater than the 'spike thresh' value, **and** the difference between the 'O2 diff' value and the 'Last 5 av' value is greater than the '3 sigma' value, **and** 5 data points have not already been skipped within the last second.

***station_name_date*_SETTINGS.csv file:** records any changes in the software settings. The file records whenever the software is running and a tab is changed, and files are created annually. The file columns from left to right are as follows:

- **Date/Time:** records the date and time that the setting is changed
- **Setting:** records which setting is changed

- **Value:** describes the setting change (e.g. from ... to ...)

SMALL Folder:

***station_name_and_date*_AIR_SMALL.csv file:** records 6 minute 'snapshots' of final air mole fractions. Data are recorded when the air measurement macros are running and recording is turned on ('RC, 1' or 'RC,2'). Files are created daily. The file columns from left to right are the same as for the AIR file. Only the SMALL files are sent to the Dropbox location to try and reduce data transfer costs.

***station_name_and_date*_DIG_SMALL.csv file:** records hourly 'snapshots' of diagnostic data. Data are recorded when the software is running, and files are created daily. The file columns from left to right are the same as for the DIG file. Only the SMALL files are sent to the Dropbox location to try and reduce data transfer costs.

E. A rather unexpected short-term ocean 'event'

Cap San Lorenzo Runs Aground Off Zeebrugge

By Milton Stuards, April 24, 2015.

The Cap San Lorenzo vessel was sailing from Antwerp en route to Le Havre when it ran aground on April 23rd, at approximately 7 kilometers off the Zeebrugge coast. There were 29 crew members aboard the ship at the time when the accident occurred.



At 2:30 a.m. the vessel had departed from the DP World terminal that is located in the Deurganck Dock, and was headed to South America. At approximately 7:30 a.m. the vessel was unable to continue its voyage due to getting stuck on a sand bar in close proximity to Scheur between buoys 6 and 8, right outside of Zeebrugge's main fairway.

The first attempt to salvage the vessel proved to be unsuccessful due to being prevented by the low tide and present fog. The 2nd attempt was initiated at 3:30 p.m. and was managed by the ariem Reddings- en Coördinatiecentrum (MRCC). At roughly 4:00 p.m. four Antwerp-based URS and Smit Salvage tugs managed to pull the vessel off.

The ship was then escorted to an anchorage area near Ostend in order for divers to conduct the necessary inspection procedures before permitting it to berth in Zeebrugge.

